Interdiffusion at polymer-polymer interfaces

Kim . Houghton

How to cite:

Houghton, Kim . (2005) Interdiffusion at polymer-polymer interfaces. Doctoral thesis, Durham University.

INTERDIFFUSION AT POLYMER-POLYMER INTERFACES

Kim A. Houghton

Durham
University

2005

Submitted in conformity with the requirements
for the degree of Doctor of Philosophy

Declaration

The material contained within this thesis has not previously been submitted for a degree at the University of Durham or any other university. The research reported within this thesis has been conducted by the author unless indicated otherwise.

Copyright Notice

Abstract

Interdiffusion at polymer-polymer interfaces

Kim A. Houghton

There is not an extensive understanding of diffusion behaviour between chemically different polymers, especially where polymers are partially compatible. Nuclear reaction analysis has been used to observe the diffusion of molten DPEO into glassy PMMA where both polymers are above their entanglement molecular weight. The observed slowing down of diffusion of DPEO may be due to concentration dependent changes in interaction parameter or blend glass transition temperature, T_g. Small angle neutron scattering was used to find the interaction parameter χ, at the temperatures above the melting temperature (T_m) of DPEO but below the T_g of PMMA. The blend exhibited upper critical solution temperature behaviour, enthalpic interactions were dominant and χ was found to be concentration dependent.

Elastic recoil detection showed that glassy PMMA was quickly dissolved into molten DPEO and subsequently into the evolving DPEO/PMMA blend. The rate of increase of blend PMMA volume fraction (φ_{PMMA}) decreases with increasing volume fraction. DPEO/PMMA diffusion couples can be described by both Fickean and limited supply case II diffusion. PMMA was substituted with a block copolymer polystyrene-b-poly(methylmethacrylate) (PS-PMMA). Polystyrene is immiscible with DPEO and PMMA, however diffusion behaviour was similar to that of pure PMMA with DPEO. PS-PMMA flux into the growing blend was similar to a higher molecular weight than the PMMA block present.

Neutron reflectivity was employed to analyse interfacial concentration profiles with better resolution than is possible with ion beam analysis. For the anneal times utilized the diffusion was limited to movement of only a portion of the polymer chain. Bilayers were fitted by a model which included a growing precursor layer with $\varphi_{DPEO}\sim 0.1$ and a developing broadening between this layer and DPEO. The copolymer did not diffuse to a distance greater than the radius of gyration of the polymer components.

Acknowledgements

My thanks to Randal Richards, who despite orphaning me was a wonderful support and motivator. I would also like to express my gratitude to Nigel Clarke for adopting me and managing to make my most obvious questions seem intelligent. My special thanks to Richard Thompson, for his insight, patience and brilliance (and forgiveness) at fixing my mistakes on the ion beam.

Thanks to Steve King, Stephen Holt, and John Webster for help and support at ISIS. I am also grateful to Imtiaz Ansari for his work with the TEM, Doug Carswell for running the DSC, and Lian Hutchings for GPC work, synthesising my polymers and answering a litany of basic organic chemistry questions.

I would like to thank Stephen Collins and Julian Bent for their advice and company and the denizens of the MC building for subjecting me to some of the worst jokes spoken by human kind. I would finally like to thank Tom for providing me with the perfect retreat.

Dedication

For my mother.
I'm sorry you never got to tell the staff room about this.

Contents

1 BACKGROUND THEORY..1
1.1 Diffusion..1
1.1.1 Fick's laws of diffusion..1
1.1.2 Case II diffusion..4
1.1.3 Boltzman-Matano method..5
1.2 Diffusion in polymers..7
1.2.1 Entanglement molecular weight..7
1.2.2 Types of diffusion coefficient..8
1.2.3 Unentangled melts and the Rouse model..8
1.2.4 Entangled molecular weights in blends..9
1.2.5 Constraint release..12
1.3 Polymer blends..14
1.3.1 Miscibility of polymer blends..14
1.3.2 Entanglement molecular weights in blends..16
1.3.3 Mutual diffusion..17
1.3.3.1 Slow Theory..18
1.3.3.2 Fast theory..19
1.3.4 Thermodynamic slowing down of blends..20
1.4 The glass transition temperature of blends..21
1.5 Previous diffusion studies in blends..22
1.5.1 PS/PVME (Polystyrene and Poly(vinyl methyl ether))..22
1.5.2 PS/PXE (Polystyrene and Poly(xylenyl ether))..23
1.5.3 PVC/PCL (Polyvinyl chloride and Polycaprolactone)..23
1.5.4 PVC/PMMA (Polyvinyl chloride and Poly(methylmethacrylate))..24
1.6 PEO/PMMA (Poly(ethylene oxide) and Poly(methylmethacrylate))..24
1.6.1 Miscibility..24
1.6.2 Diffusion and dynamics..26
1.6.3 Conformation in the blend..27
1.7 Objectives..28
1.8 Presentation of this thesis..28
1.9 References..29

2 EXPERIMENTAL METHODS..33
2.1 Introduction..33
2.2 IBA Instrument..34
2.2.1 Data collection..37
2.3 Elastic recoil detection (ERD)..37

2.3.1 Introduction....37
2.3.2 ERD....37
2.3.3 Interaction of matter and energy loss....38
2.3.4 Kinematic factor and particle energy....39
2.3.5 Data analysis....42
2.3.5.1 Depth scale conversion....42
2.3.5.2 Normalised yield and volume fraction....43
2.4 Nuclear reaction analysis (NRA)....43
2.4.1 Introduction....43
2.4.2 NRA....45
2.4.3 Energy optimization and geometry....45
2.4.4 Energy optimization and depth resolution....46
2.4.5 Data analysis....48
2.4.5.1 Depth scale conversion....48
2.4.5.2 Normalised yield and volume fraction....49
2.4.5 Comparison of NRA and ERD....50
2.5 Small angle neutron scattering (SANS)....50
2.5.1 LOQ....53
2.6 Neutron reflectivity....54
2.6.1 SURF....60
2.7 DMA and DSC....61
2.7.1 Dynamic mechanical analysis (DMA)....61
2.7.2 Differential scanning calorimetry (DSC)....64
2.8 Atomic Force microscopy (AFM)....65
2.9 Transmission electron microscopy (TEM)....66
2.10 References....67

3 NUCLEAR REACTION ANALYSIS OF THIN DPEO FILMS DIFFUSING INTO PMMA....69
3.1 Introduction and aims....69
3.2 Experimental refinement....70
4.3 Experimental....71
3.3.1 Materials....71
3.3.2 Bilayer preparation....71
3.3.3 NRA measurements....73
3.3.4 Calculating diffused depth....73
3.5 Results....74
3.5.1 Sample roughness....74
3.5.2 Surface roughness experiment and NRA simulation....75
3.5.3 Graphs of volume fraction against depth....80
3.6 Discussion....85
3.7 Summary....88
3.8 Speculative theory....89
3.9 References....92

4 BULK PROPERTIES OF BLENDS OF DPEO AND PMMA....94

4.1 Introduction 94
4.2 Measurement of T_g 95
4.3 Experimental 95
4.4 Results 97
4.5 Discussion 99
4.6 Copolymer results and discussion 101
4.7 Summary 103
4.8 SANS measurement of χ 103
4.9 Experimental 105
4.10 Data analysis 106
4.11 Results and discussion 109
4.12 Summary 119
4.13 References 119

5 ELASTIC RECOIL DETECTION OF DIFFUSION OF DPEO AND PMMA 121
5.1 Introduction 121
5.2 Experimental refinement 122
5.2.1 Experimental geometry 122
5.2.2 Stopping powers 122
5.2.3 Beam energy 123
5.2.4 Energy per channel 123
5.2.5 Stopper foil 124
5.2.6 Resolution and beam damage 125
5.2.7 Effect of surface roughness 130
5.3 Experimental 132
5.3.1 Materials 132
5.3.2 Bilayer construction 132
5.3.3 ERD measurements 133
5.4 Data analysis 132
5.4.1 Depth scale conversion and normalized yield 133
5.4.2 Raw data and interface definitions 134
5.4.3 Calculating diffusion profile 141
5.5 Discussion 144
5.5.1 Rubbery/glassy diffusion couples 144
5.5.2 Diffusion regimes for rubbery/glassy bilayers 144
5.5.3 Blend volume fraction 147
5.5.4 Application of Fickean diffusion 160
5.5.5 Application of case II diffusion 169
5.6 Summary 174
5.7 References 175

6 ELASTIC RECOIL DETECTION ANALYSIS OF BILAYERS OF DPEO AND PS-PMMA BLOCK COPOLYMER 177
6.1 Introduction 177
6.2 Copolymer background 178

6.3 Experimental 180
6.3.1 Materials 180
6.3.2 Bilayer construction 180
6.3.3 Transmission electron microscopy 180
6.3.4 ERD measurements 180
6.4 Data analysis 181
6.4.1 Depth scale conversion and normalized yield 181
6.4.2 Surface roughness, resolution and beam damage........182
6.4.3 Raw data and interface definitions........182
6.4.4 Calculating diffusion profile........188
6.5 Discussion 189
6.5.1 TEM results........189
6.5.2 Rubbery/glassy diffusion couples 190
6.5.3 Dewetting of small molecular weight DPEO........191
6.5.4 Blend volume fraction 192
6.5.5 Application of Fickean diffusion 203
6.5.6 Application of case II diffusion 205
6.6 Summary........208
6.7 References........208

7 NEUTRON REFLECTIVITY STUDIES OF THE INTERFACE BETWEEN DPEO AND PMMA AND PMMA COPOLYMERS 210

7.1 Introduction 210
7.2 Experimental refinement........211
7.3 Experimental 212
7.3.1 Materials 212
7.3.2 SURF measurements........213
7.4 Data analysis 214
7.4.1 Data reduction and raw data........214
7.4.2 PARRATT........216
7.4.3 Interfacial models........217
7.5 PMMA bilayer results 222
7.6 PS-PMMA bilayer results 226
7.7 Discussion........229
7.7.1 PMMA bilayers........231
7.7.2 PS-PMMA bilayers........244
7.8 Summary........255
7.9 References........256

8 CONCLUSIONS AND FURTHER WORK 258

8.1 Conclusions and further work........258
8.2 References........261

APPENDIX I-POLYMERS UTILISED........262
APPENDIX II-GLOSSARY OF TERMS........264
APPENDIX III-GLOSSARY OF ACRONYMS........269

Chapter 1

Background theory

1.1 Diffusion

There are several methods and models for describing diffusion. These vary according to the parameters that are assumed to control the diffusion rate. As polymers diffuse in a different manner to small molecules not all mathematical models are applicable to polymer systems.

1.1.1 Fick's laws of Diffusion

Fick recognized that there were similarities between the transfer of heat due to random molecular motions and the transfer of matter. By analogy between the two processes, and adopting the equation relating to heat conduction derived by Fourier he showed that the rate of transfer of a diffusing substance through unit area of a section is proportional to the concentration gradient measured normal to the section.[1]

$$F = -D\frac{\partial C}{\partial x} \qquad \text{Equation 1.1}$$

F is the rate of transfer per unit area, C is the concentration of the diffusing substance, x is the distance measured in the direction of diffusion and D is the diffusion coefficient, which is taken to be constant. The negative sign occurs because diffusion occurs in the direction opposite to that of increasing concentration. If we start with $C=\infty$ at $x=0$ and $C=0$ elsewhere, then defining the distribution of C evolves according to Fick's first law of diffusion, the physical basis of which is that any diffusion process results in a uniform concentration distribution. It is worth noting that for polymer systems, D is often dependent on concentration and should not therefore be treated as a constant.

Fick's second law of diffusion shows that, for constant diffusion coefficient, the rate of change in concentration with time is proportional to the rate at which the concentration gradient changes with distance in a given direction, i.e.

$$\frac{\partial C}{\partial t} = D\frac{\partial^2 C}{\partial x^2} \qquad \text{Equation 1.2}$$

The solution of which is,

$$C = \frac{A_1}{t^{0.5}} e^{\frac{-x^2}{4Dt}} \qquad \text{Equation 1.3}$$

where A_1 is a normalisation constant and t is time. This expression is symmetrical with respect to x =0, it tends to zero as x approaches infinity, positively or negatively for $t > 0$. The total amount of substance present M_g, is given by,

$$M_g = \int_{-\infty}^{\infty} C dx \qquad \text{Equation 1.4}$$

If the concentration distribution is that of Equation 1.3 and defining ξ_C through,

$$\frac{x^2}{4Dt} = \xi_C{}^2 \qquad \text{Equation 1.5}$$

so that,

$$dx = 2(Dt)^{0.5} d\xi_C \qquad \text{Equation 1.6}$$

then we find,

$$M_g = 2A_1 D^{0.5} \int_{-\infty}^{\infty} e^{-\xi_C{}^2} d\xi_C = 2A_1 (\pi D)^{0.5} \qquad \text{Equation 1.7}$$

Thus,

$$C = \frac{M_g}{2(\pi Dt)^{0.5}} e^{\frac{-x^2}{4Dt}} \qquad \text{Equation 1.8}$$

This describes the spreading by diffusion of an amount of substance M_g deposited at time t=0 in the plane x=0.This expression applies when the diffusing species moves in either direction, i.e. towards both positive and negative x. For the case when diffusion only occurs in the direction of positive x, the solution for negative x can be considered to be reflected in the plane x=0 and superimposed on the original distribution in the region x=0 so that,

$$C=\frac{M_g}{(\pi Dt)^{0.5}}e^{\frac{-x^2}{4Dt}}$$ Equation 1.9

The above equations apply when the diffusing species is originally restricted to an infinitely thin plane. This is rarely an adequate approximation to normal experimental conditions. If the diffusing substance in an element of width $d\xi_C$ is considered to be a line source of strength $C_0\ \delta\xi_C$ (see Figure 1.1 below), then the concentration at point P, distance ξ_C from the element, at time t is given by,

$$C_P=\frac{C_0}{2(\pi Dt)^{0.5}}e^{\frac{-\xi_C^2}{4Dt}}$$ Equation 1.10

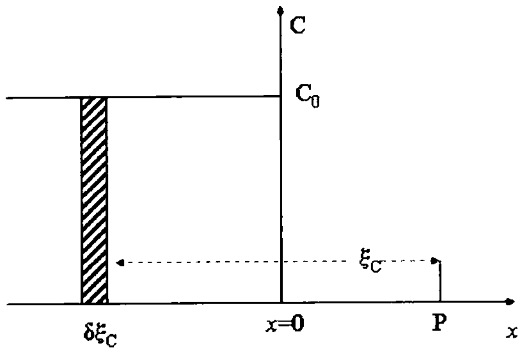

Figure 1.1 Diagram of system described by Fickean diffusion

The complete solution, due to the initial distribution,

$C=C_0, x<0,\quad C=0, x>0,\quad t=0$ Equation 1.11

is given by integrating over successive elements $d\xi_C$,

$$C(x,t)=\frac{C_0}{2(\pi Dt)^{0.5}}\int_x^{\infty}e^{\frac{-\xi_C^2}{4Dt}}d\xi_C=\frac{C_0}{\pi^{0.5}}\int_{\frac{x}{2}\sqrt{(Dt)}}^{\infty}e^{-\eta^2}d\eta$$ Equation 1.12

Where $\eta=\xi_C/2\sqrt{(Dt)}$. Since no analytical result exists for the final integral on the right hand side of Equation 1.12, it is useful to introduce mathematical error function $erf\,(z)$ defined by,

$$erf\,z=\frac{2}{\pi^{0.5}}\int_0^z e^{-\eta^2}d\eta$$ Equation 1.13

which has the following properties,

$$erf(-z) = -erf\,z, \quad erf(0) = 0, \quad erf(\infty) = 1, \qquad \text{Equation 1.14}$$

Hence

$$\int_z^{\infty} e^{-\eta^2}\,d\eta = \int_0^{\infty} e^{-\eta^2}\,d\eta - \int_0^{z} e^{-\eta^2}\,d\eta = 1 - erf\,z = erfc\,z \qquad \text{Equation 1.15}$$

where *erfc(z)* is the error-function complement. Hence,

$$C(x,t) = \frac{1}{2} C_0 erfc \frac{x}{2\sqrt{(Dt)}} \qquad \text{Equation 1.16}$$

Looking at the form of the concentration distribution for this expression, $C=0.5C_0$, at $x=0$ for all $t > 0$.For a substance initially confined to the region $-h_0 < x < +h_0$, the summing over successive elements (integration) is from $x\text{-}h_0$ to $x+h_0$ instead of from x to ∞, leading to

$$C = \frac{1}{2} C_0 \left\{ erf \frac{h_0 - x}{2\sqrt{(Dt)}} + erf \frac{h_0 + x}{2\sqrt{(Dt)}} \right\} \qquad \text{Equation 1.17}$$

It is often more useful to consider volume fraction of a given substance φ_i rather than concentration

$$\varphi_A = \frac{1}{2} \left\{ erf \frac{h_0 - x}{2\sqrt{(Dt)}} + erf \frac{h_0 + x}{2\sqrt{(Dt)}} \right\} \qquad \text{Equation 1.18}$$

This expression can therefore be used to calculate a diffusion coefficient for the interdiffusion of two polymers films, where $\varphi_A=1$ within one film and $\varphi_A=0$ in the other film at $t=0$.

1.1.2 Case II diffusion.

For some cases of diffusion between two components, the swelling caused by the penetrating component and the subsequent stress developed, influences the diffusion. The flux, F of a penetrant component can be described in terms of a gradient in chemical potential and the stress of the penetrant,

$$F = -B_{mob} C \left(\frac{\partial \mu}{\partial x} - \frac{1}{C} \frac{\partial S_p}{\partial x} \right) \qquad \text{Equation 1.19}$$

where B_{mob} is a mobility coefficient, μ is the chemical potential, S_p is the partial stress tensor in one dimension and C is the concentration. If S_p is proportional to the total uptake of penetrant molecules the generalised diffusion equation is obtained,[1]

$$\frac{\partial C}{\partial t}=\frac{\partial}{\partial x}\left\{D(C,x,t)\frac{\partial C}{\partial x}-B_{mob}(C,x,t)sC\right\} \qquad \text{Equation 1.20}$$

where s is a constant. If the diffusion is controlled by the stress gradient, so that $\partial\mu/\partial x << \partial S_p/\partial x$, then Equation 1.20 leads to case II diffusion. The linear form of Equation 1.20 for diffusion into a semi-infinite medium with a constant surface concentration, C_0 is given by,

$$C(x,t)=\frac{1}{2}C_0\left[\exp(xv_1/D)erfc\left\{\frac{x+v_1t}{2\sqrt{Dt}}\right\}+erfc\left\{\frac{x-v_1t}{2\sqrt{Dt}}\right\}\right] \qquad \text{Equation 1.21}$$

where $v_1=B_{mob}s$ is a constant.

1.1.3 Boltzman-Matano method

Fick's second law for time-dependent linear flow with variable diffusivity $D(C)$ can be described by the non-linear diffusion equation, [2]

$$\frac{\partial C}{\partial t}=\frac{\partial}{\partial x}\left(D(C)\frac{\partial C}{\partial x}\right) \qquad \text{Equation 1.22}$$

where x is the distance over which the component described travels. This equation can be transformed to an ordinary differential equation by introducing ψ, the Boltzman similarity variable,

$$\psi\equiv\frac{x-X_M}{2\sqrt{t}} \qquad \text{Equation 1.23}$$

X_M is a constant that describes a reference plane between diffusing couples. Fick's second law in its non-linear form reduces to a non-linear ordinary differential equation,

$$-2\psi\frac{dC}{d\psi}=\frac{d}{d\psi}\left(D(C)\frac{dC}{d\psi}\right) \qquad \text{Equation 1.24}$$

To apply this equation, for a diffusion couple such as two molten metal blocks put next to each other, the initial boundary conditions below are selected,

$$C=\begin{cases}C_L(x<0,t=0)\\ C_R(x>0,t=0)\end{cases} \qquad \text{Equation 1.25}$$

where C_L and C_R are the concentrations of the blocks on left and right hand side respectively. The first integral of Equation 1.24 with the boundary conditions above gives,

$$-2\int_{C_R}^{C'} \psi \, dC = \int_{C_R}^{C'} d\left(D(C)\frac{dC}{d\psi} \right)$$ Equation 1.26

Integration of the right hand side gives,

$$-2\int_{C_R}^{C'} \psi \, dC = \left[D(C)\frac{dC}{d\psi} \right]_{C_R}^{C'}$$ Equation 1.27

where *C'* is illustrated in Figure 1.2. The solute distribution in the Matano distribution, as shown in Figure 1.2, provides a gradient *dC/dψ*, that vanishes as $C \rightarrow C_R$. This boundary condition means that Equation 1.27 becomes,

$$-2\int_{C_R}^{C'} \psi \, dC = D(C')\frac{dC}{d\psi} \Big|_{C=C'}$$ Equation 1.28

so that,

$$D(C') = -2\left(\frac{d\psi}{dC}\right)_{C'} \int_{C_R}^{C'} \psi \, dC$$ Equation 1.29

If Equation 1.29 is transformed back into *(x, t)* space-time coordinates, the Boltzman-Matano solution is found, [3]

$$D(C') = \left(-\frac{1}{2t}\frac{dx}{dC}\right)_{C'} \int_{C_R}^{C'} (x - X_M) dC$$ Equation 1.30

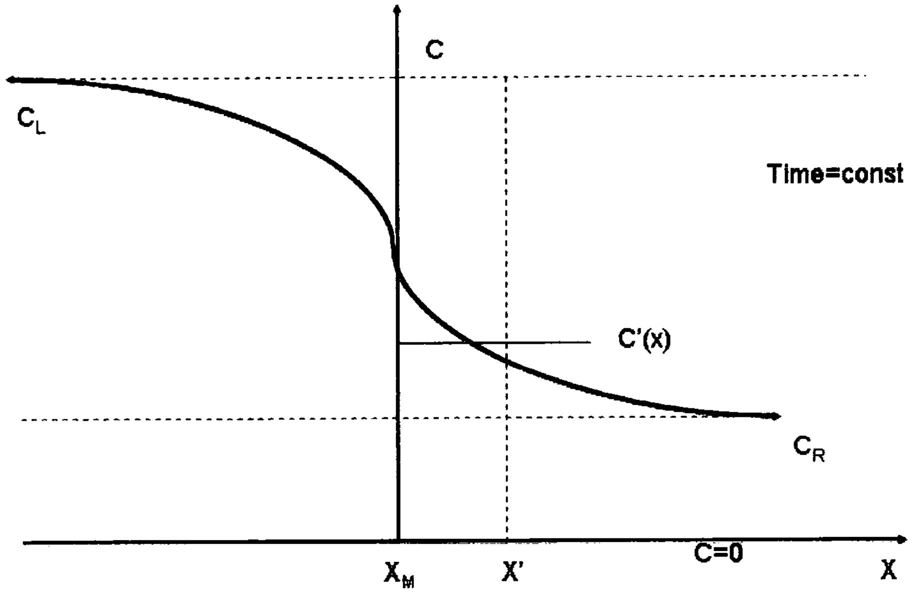

Figure 1.2 Illustration of Boltzman-Matano geometry for a diffusion couple

The Matano interface therefore describes a plane within a diffusion couple, X_M. Across this interface equal amounts of mass diffuse in either direction. The location of the Matano interface can be found through a conservation of mass condition, where the gain of diffusant on the right is balanced by its loss on the left. Figure 1.2 shows the Matano interface with equal area either side of gain and loss, which can be described as,

$$\underbrace{\int_{-\infty}^{X_M}[C_L - C(x)]dx}_{loss} = \underbrace{\int_{X_M}^{\infty}[C(x) - C_R]dx}_{gain} \qquad \text{Equation 1.31}$$

1.2 Diffusion in polymers

Diffusion in a polymer melt differs from diffusion of a polymer in a dilute solution. In a melt the polymer diffuses into an identical region, the melt being at a temperature sufficiently far above the glass transition temperature (T_g) and/or the melting temperature (T_m) for the polymers to be mobile. The diffusion of a polymer in the melt is influenced by its surroundings. Interactions between segments in polymers are dominated by dispersive interactions and in general the mixing of chemically different monomers is energetically unfavourable.

2.2.1. Entanglement molecular weight

A polymer has an entanglement molecular weight M_e, a critical value that defines the molecular weight at which a polymer is sufficiently long enough that it may no longer move without negotiating another polymer that restricts movement. One manifestation of entanglements is the appearance of a wide region of frequency (or time) where the modulus, the constant of proportionality between stress and strain, is almost constant in a oscillatory shear (or stress relaxation) experiment. The molecular entanglement weight M_e, can be related to this plateau modulus G_N^0 via,[4]

$$M_e = \frac{(\rho_d T N_a k_B)}{G_N^0} \qquad \text{Equation 1.32}$$

where ρ_d is the polymer density, N_a is the Avagadro constant, T is the absolute temperature and k_B is the Boltzman constant. It has been proposed[5] that the plateau modulus is related to molecular properties: number of chains per unit volume v_n, chain length L and the effective bond length or Kuhn step length Λ.

$$G_N^0 = K_1 (v_n L)^2 \Lambda k_B T \qquad \text{Equation 1.33}$$

1.2.1 Types of diffusion coefficient

A polymer diffusion coefficient describes the mean-squared displacement per second. The tracer diffusion coefficient D^* is a measure of the mobility and movement of a single probe molecule, into a sample of polymers that are chemically different or have a different degree of polymerisation, where diffusion is driven purely by the combinatorial entropy of mixing.[6] The 'self-diffusion' coefficient is a measure of the movement of molecules in a chemically uniform environment; the 'tracer diffusion' coefficient for a single component system. For chemically similar polymers diffusing into different molecular weight a chemical potential driving force is not required for interdiffusion.[7,8] Mutual diffusion is the interdiffusion of chemically dissimilar polymers in a melt; and is dominated by the excess enthalpy and entropy of the species mixing.

1.2.2 Unentangled melts and the Rouse model

The Rouse model can be used to describe the translational dynamics of unentangled polymer chains in melts.[9,10] The Rouse model assumes that the dynamics of a chain are governed by localised interactions along the chain. Each polymer chain is considered to consist of a string of 'beads', which contain several monomers, connected by Hookean springs, as shown in Figure 1.3.

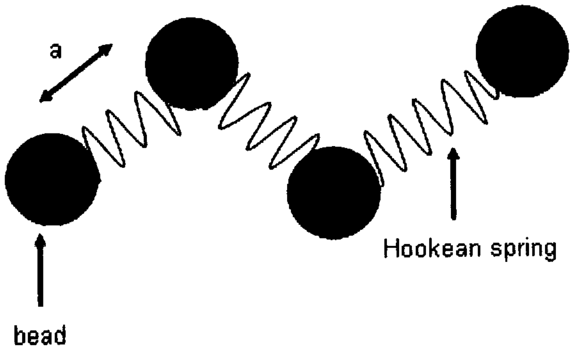

Figure 1.3 Diagram of simplified Rouse model

Each spring has a force constant of magnitude $3k_BT/a^2$; where a is the separation between beads (step length). The Rouse model describes the Brownian motion of a series of coupled oscillators, whose positions are described by a position vector R_N. When each bead moves with a velocity v relative to its surroundings it is assumed to experience a 'frictional' drag force; ζ_0 **v.** ζ_0 is the monomeric friction coefficient for a given polymer.[11] The friction coefficient of the entire chain will be the sum of the friction coefficient of all the monomers,

$$\zeta = \zeta_0(M / M_0) \qquad \text{Equation 1.34}$$

where M is the molecular weight of the entire chain and M_0 is the molecular weight of the monomer. Each chain is considered to undergo centre of mass motion in any direction subject only to the drag force of it's monomers by the surroundings, the Rouse model neglects intramolecular excluded volume and hydrodynamic interactions present in solutions, which are assumed to be screened in melts. The motion of the polymer and its beads can be described by normal mode co-ordinates where each mode is independent of others. This model can be solved to provide N_r relaxation times with relaxation time τ_l corresponding to each normal mode. The resultant diffusion coefficient is therefore described by Equation 1.35.

$$D_{Ro} = k_B T(N_r \zeta)^{-1} \qquad \text{Equation 1.35}$$

which is in essence, the Einstein fluctuation-dissipation relation.[12] Polymer chains diffusing by the Rouse dynamics have a self-diffusion coefficient D_{Ro} with a molecular weight dependence M^1.The Rouse model works reasonably well for unentangled polymer systems.

1.2.3 Entangled melts and reptation

The Rouse model does not consider the topological constraints exerted on long chains by their neighbours and it fails to explain the viscoelasticity and diffusion of polymers above the entanglement molecular weight. One method of describing the process of diffusion for entangled linear polymers is the reptation model. Reptation[13] is the process by which a long polymer chain 'crawls' along a primitive path defined by the topological constraints of the other chains present in the polymer melt as shown in Figure 1.4.

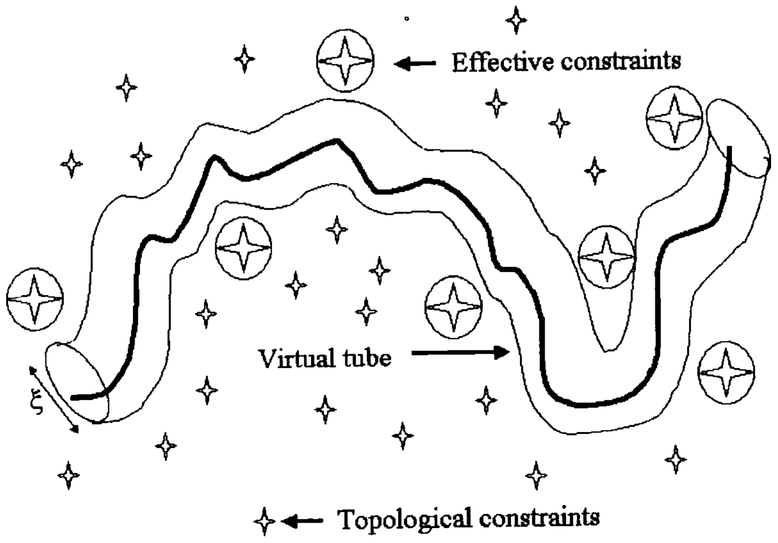

Figure 1.4 Illustration of reptation of a polymer in a virtual tube

The motion of a given chain A, as shown in Figure 1.5 is confined to the axis of a tube[14] (its primitive path) defined by the surrounding constraining long chains. These constraints were initially thought to be frozen. The chain A, with molecular weight M_A, has a random coil configuration and therefore a mean end-to end distance given by,

$$\langle R_A^2 \rangle = K_A M_A \qquad \text{Equation 1.36}$$

where K_A is a constant for the A species. The virtual tube has the same end to end distance as the diffusing chain.[14] Hence the tube can be described as a primitive chain which coincides with the centre line of the virtual tube as shown in Figure 1.5. The contour length of the primitive chain or virtual tube is,

$$L_c = a_2 N_i \qquad \text{Equation 1.37}$$

where a_2 is the length of the step, shown in Figure 1.5 and N_i the number of primitive chain steps. N_i can be expressed in terms of the entanglement molecular weight, M_e, which is related to the plateau modulus G^0_N [15](Equation 1.32). The number of primitive steps N_i of a tube which surrounds an A chain is,

$$N_i = \left(\frac{M_A}{M_e} \right) \qquad \text{Equation 1.38}$$

and the length of each primitive step a_2 is,

$$a_2 = \sqrt{K_A M_e} \qquad \text{Equation 1.39}$$

The tube diameter ξ is an indicator of the lateral freedom of the diffusing chain. It has been estimated to be several nanometres for linear polymer melts.[16]

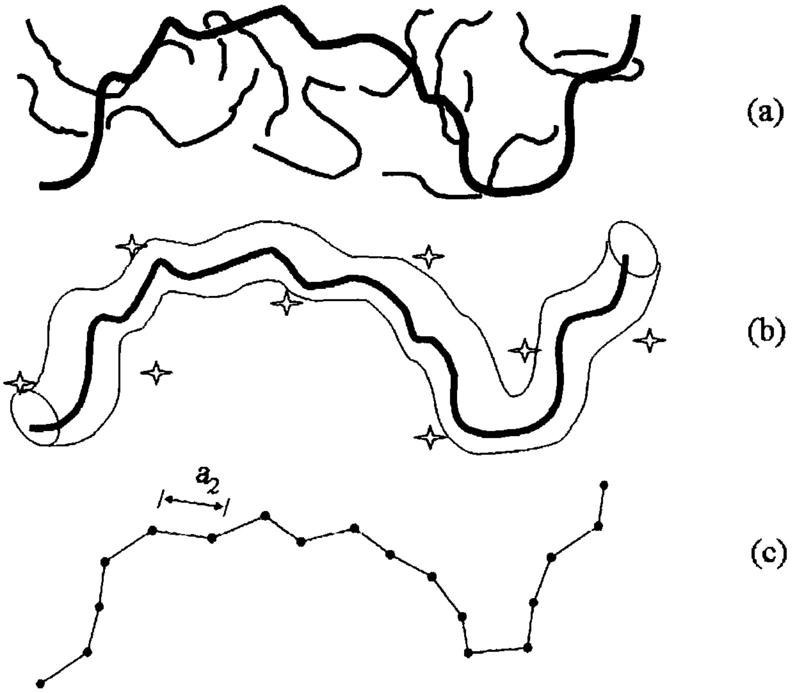

Figure 1.5 Illustration of an A chain diffusing by reptation, a) an A chain in a matrix, b) an A chain in virtual tube defined by constraints (stars), c) primitive chain coinciding with centreline of the virtual tube, consisting of N steps each of length a.

The centre of mass movement of the reptating A chain occurs via a one-dimensional curvilinear diffusion.[17] Following Graessley's[18] approach, the reptation diffusion coefficient $D_{R,A}$ of A can be expressed in terms of the Rouse diffusion coefficient for the A chain, $D_{Ro,A}$ and the number of primitive path steps of the tube surrounding A, N_A.

$$D_{R,A} = D_{Ro,A} / 3N_A \qquad \text{Equation 1.40}$$

Substituting Equation 1.35 into Equation 1.40 the reptation diffusion coefficient becomes,

$$D_{R,A} = D_{0,A} M_A^{-2} \qquad \text{Equation 1.41}$$

where $D_{0,A}$ is the reptation constant of polymer A

$$D_{0,A} = \left(\frac{M_0 M_e k_B T}{\zeta_{0,A}} \right) \qquad \text{Equation 1.42}$$

Hence, $D_{R,A}$ should scale as M^2, however experimentally a scaling of $M^{2.4}$ has been found for tracer diffusion.[8,12,19,20] The tube relaxation time τ, for reptation or the time taken for the polymer to abandon its original tube can be described by,

$$\tau_{R,A} = \frac{L_c^{\ 2}}{\pi^2 D_{Ro,A}} \qquad \text{Equation 1.43}$$

Equations 1.35, 1.37, 1.38 and 1.39 can be substituted into Equation 1.43 to give[18] Equation 1.44 and express the relaxation time with measurable properties.

$$\tau_{R,A} = \frac{K_A}{3\pi^2}\frac{M_A^3}{D_{O,A}} \qquad \text{Equation 1.44}$$

1.2.4 Constraint release

A polymer with a molecular weight higher than the entanglement value will diffuse via reptation in a polymer melt as long as the constraints remain fixed for a time longer than the time it takes for the chain to abandon it's original path ($\tau_{R,A}$). When the polymer molecules surrounding the tube are diffusing themselves, the constraints will not remain static and the tube itself will diffuse.[18,21] Constraints that are likely to diffuse faster than the relaxation time of the diffusing A chain will be those due to lower molecular weight polymers. If reptation and constraint release mechanisms are independent, the centre of mass tracer diffusion coefficient D^*_A of the A chain is then defined by,[20]

$$D^*{}_A = D_{R,A} + D_{CR,A} \qquad \text{Equation 1.45}$$

In a one component system of A chains, as a given chain reptates through the matrix a new portion of the virtual tube is created. The function $F_A(t)$ describes the fraction of the original tube still occupied by the reptating polymer chain after time t,[22]

$$F_A(t) = \frac{8}{\pi^2}\sum_{n\ odd}\frac{1}{n^2}\exp\left\{\frac{-n^2 t}{\tau_{R,A}}\right\} \qquad \text{Equation 1.46}$$

Because the $n=1$ term dominates the summation in Equation 1.46 and initially $F_A(0)=1$, a good approximation for $F_A(t)$ is

$$F_A(t) \equiv \exp\left\{\frac{-t}{\tau_{R,A}}\right\} \qquad \text{Equation 1.47}$$

Hence for topological constraints due to a matrix of polydisperse A chains,

$$F_A(t) = \sum_i W_i \exp\left\{\frac{-t}{\left(\tau_{R,A}\right)_i}\right\} \qquad \text{Equation 1.48}$$

where W_i is the weight fraction and $(\tau_{R,A})_i$ the reptation time of an A chain with degree polymerisation i. For a two component matrix, the probability of any constraint being due to an A chain is equal to the volume fraction of A chains, φ, hence $F(t)$ for that system becomes

$$F(t) = \varphi F_A(t) + (1-\varphi)F_B(t) \qquad \text{Equation 1.49}$$

If the virtual tube is defined by z molecules at each step acting as constraints, (or the number of 'suitably placed constraints' per M_e), the release of one constraint will allow the tube to drift or diffuse, normal to the primitive path, a distance a_p, or the diameter of the path. The time taken for the release of a constraint is called the waiting time τ_w,

$$\tau_w = \int_0^\infty dt\left[F_A(t)\right]^z \qquad \text{Equation 1.50}$$

As the number of constraints z increases the probability that a constraint release step occurs will increase, therefore the waiting time will decrease. For a 2 component system the waiting time is dependent upon the reptation times of the individual components and,

$$\tau_w = \int_0^\infty dt\left[\varphi F_A(t) + (1-\varphi)F_B(t)\right]^z \qquad \text{Equation 1.51}$$

Graessley describes the general expression for constraint release diffusion coefficient, for an A chain in a homogeneous matrix as,[18]

$$D_{CR,A} = \frac{1}{12}\frac{a_p^{\;2}}{N\tau_w} \qquad \text{Equation 1.52}$$

Taking into account Equation 1.38 and Equation 1.39, the constraint release diffusion coefficient is described by

$$D_{CR,A} = \frac{1}{12}\frac{K_A M_e^2}{M_A \tau_w} \qquad \text{Equation 1.53}$$

The waiting time in Equation 1.51 is a complex function of reptation times however it has been simply expressed[18] for a monodisperse system in which an A chain diffuses into a matrix of A chains as,

$$\tau_{w,A} = \left(\frac{\pi^2}{12}\right)\tau_{R,A} \qquad \text{Equation 1.54}$$

The constraint release diffusion coefficient $D_{CR,A}$ for a sample of one A chain diffusing into a matrix of chemically identical chains with molecular weight P_A can be found from Equations 1.44, 1.53 and 1.54,

$$D_{CR,A} = \alpha_{CR} \frac{D_{0,A} M_e^2}{M_A P_A^3} \qquad \text{Equation 1.55}$$

where

$$\alpha_{CR} = (48/25)Z(12/\pi^2)^{Z-1} \qquad \text{Equation 1.56}$$

By combining equations Equations 1.41, 1.45 and 1.55[23] the tracer diffusion, D_A^* can be found. When $M_e < P_A << M_A$ constraint release occurs and the diffusion coefficient has only a minor reliance on M_A and D_A^* will vary with P_A^{-3} at low molecular weight [20]. Thus for self-diffusion, where $M_A >> M_e$ and $M_A = P_A$ the diffusion should be dominated by reptation. The following relationship has been found by Composto using blends of poly(xylenyl ether) and polystyrene,[22].

$$D_A^* = \frac{D_{0,A}}{M_A^2} + \alpha_{CR} \frac{D_{o,A} M_e^2}{M_A P_A^3} \qquad \text{Equation 1.57}$$

1.3 Polymer Blends

1.3.1 Miscibility of polymer blends

In general chemically different polymers are not miscible and when mixed they will phase separate. A signature of the few examples that are thermodynamically compatible is a single glass transition temperature, T_g. The thermodynamics of phase separation in polymer mixtures is, in principle the same as that for the phase separation of mixtures of small molecules. If an expression for the free energy of mixing can be obtained, the phase boundaries in terms of temperature, pressure and volume fraction can be obtained. The free energy (ΔG^M) of an A-B mixture of polymers may be described by the Flory-Huggins theory,

$$\Delta G^M = \frac{1}{N_A} \varphi_A \ln \varphi_A + \frac{1}{N_B} \varphi_B \ln \varphi_B + \chi \varphi_A \varphi_B \qquad \text{Equation 1.58}$$

χ is the interaction parameter, a measure of the strength of unfavourable monomeric interactions between polymers, N_A and N_B are the number of monomers per polymer and the volume fractions in the blend[5] are φ_A and φ_B. The last term represents the interaction energy. The first two terms represent the entropy of mixing, acting to mix polymers of different types. Normally $\chi > 0$ and this term acts to separate the chemically different molecules. For a mixture of small molecules $N_A=N_B=1$, for polymers in solution $N_A=N$, $N_B=1$.For these systems the entropy dominates the interaction energy and the components can mix. To understand polymer blends, it is useful to consider the case when $N_A=N_B=N$,

$$\Delta G^M = \frac{1}{N}[\varphi \ln \varphi + (1-\varphi)\ln(1-\varphi)] + \chi\varphi(1-\varphi) \qquad \text{Equation 1.59}$$

$\varphi_A = \varphi$, $\varphi_B = (1-\varphi)$. This equation is symmetric about φ=0.5 and when $\chi > \chi_C$ gives a curve with two minima that can be joined by a common tangent. The coexistence curve for this phase diagram is determined by the positions of the minima, ($\Delta G^M = 0$) ,

$$\frac{1}{1-2\varphi}\ln\frac{\varphi}{1-\varphi} = -N\chi \qquad \text{Equation 1.60}$$

If $N\chi >> 1$, this gives the following solutions

$$\varphi = \exp(-N\chi), \quad 1-\varphi = \exp(-N\chi)$$

This gives two phases of essentially pure A and pure B. Mixing will occur when χ or the number of unfavourable monomeric interactions drops below χ_C. This 'critical point' can be found by solving,

$$\frac{\partial^2 G}{\partial \varphi^2} = \frac{\partial^3 G}{\partial \varphi^3} = 0 \qquad \text{Equation 1.61}$$

Thus, for polymers A and B to mix, $\chi < 2/N$, therefore the dimensionless interaction energy must be of the order $1/N$, The interaction energy is therefore very small, so unless χ is very small or negative, most polymers do not mix. If N_A and N_B are different the critical point can be expressed as,

$$\varphi_C = \left(1 + \sqrt{\frac{N_A}{N_B}}\right)^{-1}, \quad \chi_C = \frac{1}{2}\left(\frac{1}{\sqrt{N_A}} + \frac{1}{\sqrt{N_B}}\right)^2 \qquad \text{Equation 1.62}$$

Hence the critical concentration φ_C is weighted towards the lower molecular weight component. The phase diagram of a polymer blend in T-φ space can be determined if the temperature dependence of χ is known. Two schematic examples are shown in Figure 1.6. The spinodal curve encloses the region within which a homogeneous mixture is thermodynamically unstable. The binodal describes the locus of compositions of the two phases in thermodynamic equilibrium with each other. The value of χ, at the critical point where the spinodal and binodal meet, (χ_C) is described by Equation 1.62.

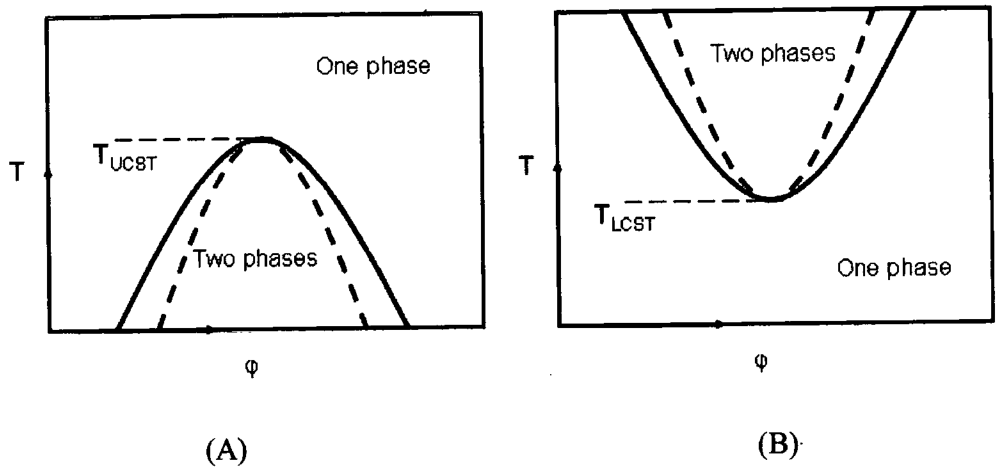

Figure 1.6 Schematic diagrams of two types of phase boundaries commonly encountered with polymer blends. Dashed lines indicate the spinodal and the solid curve the binodal A) showing UCST behaviour and B) LCST behaviour.

If an increase in temperature leads to an increase in miscibility, this behaviour is referred to as upper critical solution temperature behaviour (UCST) behaviour. The reverse of this behaviour, where an increase in temperature, leads to an increase in χ and hence lower miscibility, leads to lower critical solution temperature behaviour (LCST).

1.3.2 Entanglement Molecular weights in blends

For pure components A and B, the plateau modulus can be described by Equation 1.33 as shown below,

$$G_{N,A}^0 = K_1 (\nu L_C)_A^2 \Lambda_A k_B T$$
$$G_{N,B}^0 = K_1 (\nu L_C)_B^2 \Lambda_B k_B T \qquad \text{Equation 1.63}$$

For a blend with volume fraction φ of polymer type A, the total chain length per unit volume is,

$$(\nu L_C)_{blend} = \varphi(\nu L_C)_A + (1-\varphi)(\nu L_C)_B \qquad \text{Equation 1.64}$$

Hence the plateau modulus for the blend is given by,

$$G_N^0 = \Lambda_{blend}\left[\varphi\sqrt{\frac{G_{N,A}^0}{\Lambda_A}} + (1-\varphi)\sqrt{\frac{G_{N,B}^0}{\Lambda_B}}\right]^2 \qquad \text{Equation 1.65}$$

The Kuhn step lengths should be different for the two types of polymers. However, as most polymers are very similar in size Λ_A and Λ_B can be considered to be equal, hence,[22]

$$M_e^{-1} = \left[\varphi (M_{e.A})^{-\frac{1}{2}} + (1-\varphi)(M_{e,B})^{-\frac{1}{2}} \right]^2 \qquad \text{Equation 1.66}$$

where $M_{e,i}$ is the entanglement molecular weight for component *i*.

1.3.3 Mutual diffusion

Mutual diffusion is important for testing the thermodynamics of blends and their diffusion behaviour as well as understanding and controlling phase separation. De Gennes showed that as the combinatorial entropy of mixing polymers is small, scaling as N^{1}, the mutual diffusion of chemically dissimilar polymers will be dominated by the excess enthalpy and entropy of segment-segment mixing. As can be seen from Equation 1.58, in the mean field approximation, the excess Gibbs free energy of mixing per segment ΔG_{mix}^{ex}, in a blend of A and B, is given by,[24]

$$\Delta G_{mix}^{ex} = \chi \varphi_A \varphi_B k_B T \qquad \text{Equation 1.67}$$

The mutual diffusion coefficient D_M is given by,[8,25-27]

$$D_M = 2(\chi_S - \chi)\varphi_A \varphi_B D^* \qquad \text{Equation 1.68}$$

which is the product of the thermodynamic term $2(\chi_s-\chi)$ and the intrinsic mobility term ($\varphi_A\varphi_B D^*$, the Onsager transport coefficient). The latter includes the tracer diffusion coefficient D_T, the driving force for D^* is dominated by the combinatorial entropy of mixing (ΔG^{ex}_{mix}=0). χ_s is the Flory segment-segment interaction parameter at the spinodal point,

$$\chi_S = \frac{1}{2}\left(\frac{1}{\varphi_A N_A} + \frac{1}{\varphi_B N_B} \right) \qquad \text{Equation 1.69}$$

The transport coefficient is believed to be a function of the tracer diffusion coefficients of the two species present. Two theories for relating these parameters are the 'slow' and 'fast' theory.

1.3.3.1 Slow Theory

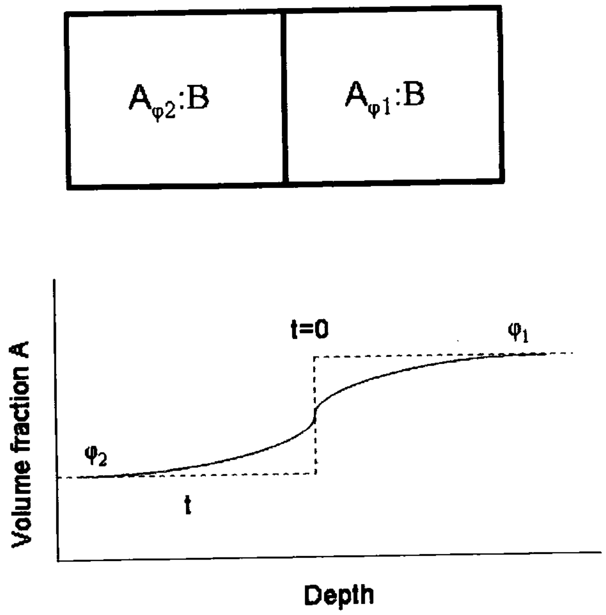

Figure 1.7 Diagram of a diffusion couple, where two blocks of A and B are placed next to each other and diagram of volume fraction against depth plot for the couple at t=0, (dashed) and t, (solid).

If a block of A and a block of B were placed next to each other the fluxes of A and B chains are equal and opposite. The diffusion of chains will require an osmotic pressure gradient across the initial interface of A and B.[26] This leads to the expression,

$$\frac{1}{D^*} = \frac{\varphi_B}{D_A^* N_A} + \frac{\varphi_A}{D_B^* N_B}$$ Equation 1.70

Where D^*_n is the self-diffusion coefficient for the n component. The diffusion will be controlled by the slower moving component if A and B mobilities vary and this theory has been dubbed ‘slow theory’. Small angle X-ray studies between Poly(methylmethacrylate) (PMMA) and Poly(vinylidene fluoride) (PVDF) support this ‘slow theory’.[28]

1.3.3.2 Fast theory

Kramer et al [29] assumed that a backflow flux will occur in a diffusion couple that is equal to the difference between the fluxes of A and B chains, such that there is no build up of osmotic pressure gradient. Sillescu arrived at a similar description for diffusion separately[30] by removing the pressure gradient by invoking the Gibbs-Duhem equation, (essentially the chemical potential of one component of a mixture cannot change independently of the chemical potential of other components). The mutual diffusion coefficient for both theories is defined with respect to a reference system that moves by backflow relative to the laboratory system yielding,

$$D_T = \varphi_B D_A^* N_A + \varphi_A D_B^* N_B \qquad \text{Equation 1.71}$$

This 'fast theory' predicts that diffusion is controlled by the faster moving component. These two theories have been hybridised into a 'fast-slow' theory;[31] for a characteristic diffusion distance, less than l, where l is described by

$$l = \sqrt{D_A^* \tau_{R,B}} = <R_B^2>^{1/2} \sqrt{\frac{D_A^*}{3\pi^2 D_B^*}} \qquad \text{Equation 1.72}$$

where $\tau_{R,B}$ is the reptation time for B chains and $<R_B^2>^{0.5}$ is the root mean square end-to-end distance of the B chains. The fast molecules swell the slower moving component over small distances, similar to the swelling of gels, as described in 'fast theory'. For greater distances an osmotic pressure gradient develops so that diffusion similar to 'slow theory' develops. This theory seems to agree with results from marker displacement experiments. The transport diffusion coefficient D_T and the self-diffusion coefficients of the components can be used to extract the Flory-Huggins parameter χ,

$$\chi = \chi_s - \frac{D^*}{2\varphi_A \varphi_B D_T} \qquad \text{Equation 1.73}$$

This relationship between χ, D^* and D_T accounts for the phenomenon of thermodynamic slowing down and acceleration of diffusion between miscible polymer couples. A further hybridisation of the slow and fast theories has been discussed by Akcasu.[32] The 'ANK theory' can match the fluctuations of a finite number of vacancies, but states that the interdiffusion cannot be expressed only in terms of the tracer diffusion coefficients of the components. Therefore 'ANK theory' includes the cooperative diffusion coefficient which is characteristic of the relaxation of total density fluctuations.

$$\frac{1}{\chi_C} = \frac{N}{S_{coop}D_{coop}} - \frac{1}{\varphi_A N_A D_A^* + \varphi_B N_B D_B^*} \qquad \text{Equation 1.74}$$

Here D_{coop} is the cooperative diffusion coefficient and $S_{coop}=S_{AA}+2S_{AB}+S_{BB}$ where S is the static structure factor for combinations of AA, AB and BB respectively, defined by $S_{ij}=<\varphi_i(q)\varphi_j(q)>$ where $\varphi_i(q)$ represents equilibrium fluctuations in Fourier space about the mean concentration φ_i.

1.3.4 Thermodynamic slowing down of blends

As noted previously, chemically different polymers can mix when their interaction parameter, χ, which represents unfavourable interactions, falls below a critical value, χ_C.[24] χ is temperature dependent, such that when dispersive forces are dominant, χ decreases with increasing temperature. The condition $\chi_C = \chi$ occurs at a critical temperature T_C. For most polymers T_C exceeds the thermal decomposition point. Cases where this does not occur include chemically identical but isotopically different polymers such as polybutadiene and deuterated polybutadiene[33], having small positive value of χ, or, in rare cases where there are specific non-dispersive forces between polymers and χ is negative, such as polystyrene and poly(vinyl methylether).[34]

When polymers are fully miscible, the driving force for mixing may still be decreased by monomeric repulsions, i.e. where $0 < \chi < \chi_s$. Hence there will be a thermodynamic slowing down of interdiffusion (or mutual diffusion). For a blend of deuterated and hydrogenous polystyrene, a system which has a small positive χ, it has been shown that the rate of diffusion reaches a minimum at a critical concentration φ_{dc},[35,36] therefore exhibiting thermodynamic slowing down. The depression of the interdiffusion coefficient is more pronounced at lower temperatures, which are closer to the upper critical solution temperature (UCST). The minimum interdiffusion coefficient was found to be at $\varphi_{dc}=0.5$, which is where repulsive monomeric interactions are greatest in number.

Interdiffusion of polymers that have negative χ can experience thermodynamic 'acceleration',[37] where mixing is promoted by the weak entropy of mixing and by the attractive interactions between different monomers. The diffusion of the polymers is 'accelerated' compared to the individual self-diffusion coefficients. For example, PVC and PCL have a weak dipole-dipole type interaction and χ=-0.38.[38] The driving force for this interdiffusion, due to the monomeric attractions is much greater than that due to combinatorial entropy (proportional to $1/N$).

1.4 The glass transition temperature of blends

At sufficiently low temperatures (T) all polymers are rigid solids (glassy). For an amorphous polymer, as T rises each polymer gains enough thermal energy to enable it's chains to move freely, enough for it to behave like a viscous liquid (assuming no thermal degradation). The transition between glassy and rubbery behaviour is the glass transition temperature T_g, which marks a major change in mechanical properties. A perfectly crystalline polymer without disordered material should become a viscous liquid past T_m, the melting temperature and this transition should be sharp. However, all polymers that crystallise exhibit both T_g and T_m, corresponding to the behaviour of ordered and disordered portions and are known as semi-crystalline polymers. T_m often represents a melting range because the semi-crystalline polymer contains a spectrum of chain lengths and crystallites of various sizes with many defects. When two polymers A and B are fully miscible a single glass transition T_{gblend} is observed between the T_gs of the parent materials. The position of T_{gblend} can be predicted by the Fox equation,[39]

$$\frac{1}{T_{gblend}} = \frac{W_A}{T_{gA}} + \frac{W_B}{T_{gB}} \qquad \text{Equation 1.75}$$

where W_A *and* W_B are the weight fraction of each polymer whose glass transition temperatures are T_{gA} ,and T_{gB} respectively. When the polymers do not form a miscible blend two glass-rubber transitions will be observed corresponding to those of the parent polymers. Intermediate cases exist where the polymers are partially miscible so that two T_gs are still observed but they are both between that of a fully phase separated blend.

The melting temperature of pure crystalline solid T_m and its melting temperature in a blend T_{mblend} can be related by the Nishi-Wang equation [40](Equations 1.76 and 1.77) if the second component in the blend is non-crystalline.

$$\frac{1}{\varphi_{Amorph}}\left[\frac{1}{T_{mblend}}-\frac{1}{T_m}\right]=-\frac{B_w V_{Crys}}{\Delta H_{Crys}}\bullet\frac{\varphi_{Amorph}}{T_m}$$ Equation 1.76

$$\chi=\frac{B_w V_{Amorph}}{RT}$$ Equation 1.77

φ_{Amorph} is the volume fraction of the amorphous polymer V_{Amorph} and V_{Crys} are the molar volume of the amorphous and crystalline polymer respectively. ΔH_{Crys} is the heat of fusion per mole of the crystalline polymer. In contrast to fusion , T_g is a kinetic effect. It is dependent on thermal prehistory and the physical method by which it is determined. T_g can be measured among other methods by differential scanning calorimetry (DSC) and dynamic mechanical analysis (DMA). Both rely on measuring the change in physical properties associated with T_g.

1.5 Previous diffusion studies in blends

1.5.1 PS/PVME (Polystyrene and Poly(vinyl methyl ether))

The interdiffusion of PS and PVME has been measured using attenuated total reflection infrared spectroscopy (ATR-FTIR).[41] The diffusion both above and below the glass transition temperature of PS was measured for a sample of pure PS next to a sample of pure PVME. To analyse the diffusion coefficient the data collected was fitted using both case II and Fickian diffusion, with a hybrid model of both types required to describe experimental data. The diffusion coefficient for blend of PS of M_w= 105000 gmol^{-1} and PVME M_w=99000 gmol^{-1} at 378 K (5 K above the glass transition temperature) of PS was of the order 1.1×10^{-12} cm^2/s, which is intermediate between the diffusion coefficients for the single components. Diffusion was found not to be dominated by either component. At 358 K, below the T_g for PS, the diffusion coefficient was found to be non-Fickian and time dependent, with a diffusion coefficient of the order 4.2×10^{-14} cm^2/s. The data at 378 K and 358 K was fitted to a model that included 20% and 70% non-Fickian components respectively. It was theorised that the faster diffusing component swells the slower diffusing one prior to interdiffusion across the interface.

1.5.2 PS/PXE (Polystyrene and Poly(xylenyl ether))

Mutual diffusion coefficients have been measured by preparing several pairs of blended films of PS and PXE (PS:PXE) placed next to each other such that their composition only differed by 10%. Strictly, the mutual diffusion coefficient varies continuously with volume fraction. However, a small jump in composition across the interface of such a couple allows it to be assumed that the mutual diffusion is governed by a single mutual diffusion coefficient, corresponding to the average composition of the couple, and thus D_M can be measured. The molecular weight dependence has been analysed as well as the temperature dependence. The tracer diffusion coefficients were also measured by making couples of d-PS/PS:PXE and d-PXE/PS:PXE. These tracer diffusion coefficients can be used to calculate the monomeric friction coefficients. The movement of deuterium and hydrogen was profiled using elastic recoil detection analysis (ERD).[11,42,43] The mutual diffusion coefficient varied as N^{-1}. As the D^*N attributed to the faster component was found to dominate the value of the mutual diffusion coefficient, the results are thought to support 'fast theory'. Thermodynamic 'slowing down' is observed for φ_{PS}=0.55. The value of χ was found to have weak composition dependence. Work has also been done on analysing the mutual diffusion coefficient of PS:PXE blends below the glass transition temperature of the PXE. These have been measured with attenuated total reflectance fourier spectroscopy (ATR-FTIR), Rutherford back-scattering (RBS)[44], ERD[7] and dynamic secondary ion mass spectrometry (SIMS)[45]. Data were described using both case II and Fickean diffusion.

1.5.3 PVC/PCL (Polyvinyl chloride and Polycaprolactone)

Several pairs of blends of PVC/PCL (M_w=83500 gmol^{-1} and M_w=33000 gmol^{-1} respectively) were prepared and placed next to each other such that their composition only differed by 10%, these were then heated to 364 K. The mutual diffusion coefficient for blends of PVC/PCL was measured using X-ray microanalysis in a scanning electron microscope to measure the concentration of chlorine atoms across the sample.[46] The mutual diffusion coefficients were of the order 1×10^{-10} cm^2/s and an increase in diffusion rate was found at volume fractions of 0.5.

1.5.4 PVC/PMMA (Polyvinyl chloride and Polymethylmethacrylate)

The interdiffusion of PVC and PMMA has been followed using external reflection infrared spectroscopy and ATR-FTIR[47] for a bilayer of PVC (M_w=55000 gmol^{-1}) and PMMA(M_w=100000 gmol^{-1}) heated at 423 K.

1.6 PEO and PMMA

Poly(ethylene oxide), (PEO) is a semi-crystalline polymer synthesised using anionic ring opening polymerisation. It has a glass transition temperature well below room temperature (approx 253 K) and a melting temperature of approximately 337 K. Poly(methyl methacrylate) (PMMA) is an amorphous polymer normally synthesised using free radical vinyl polymerisation. It has a T_g of approximately 393 K. PMMA can be both atactic and syndiotactic and this can affect the physical properties such as T_g.

1.6.1 Miscibility

The miscibility, melting behaviour, the glass transition temperature and structural parameters of PEO/PMMA blends have been found to be strongly dependent on tacticity and blend composition.[48] The free energy of mixing consists of three main contributions; the combinatorial entropy of mixing, the exchange interaction and the free volume contribution. A change in tacticity of a blend component leads to a change in the free volume contribution. The number and strength of exchange interactions will be influenced by conformation and the radius of gyration and hence tacticity. Theoretically PEO and atactic PMMA (aPMMA) have been found to be compatible at $T > 55$ °C using solubility parameters. PEO has shown a preference to form miscible blends with isotactic PMMA (iPMMA) instead of syndiotactic PMMA (sPMMA).[49] Conversely a preference for sPMMA over iPMMA has been reported,[50] this contradiction is attributed to different conclusions about the lowest energy conformations of PMMA in the blend.[48] The total number and strength of exchange interactions are almost identical for PEO with iPMMA and sPMMA. Hence the differences in miscibility are attributed to the differences in free volume and thermal expansivity in blends between the tactic forms.[48]

PEO and atactic PMMA have been found to be miscible at all volume fractions in the blend above the T_m of PEO.[51,52] A single T_g was observed by differential scanning calorimetry (DSC) for directly quenched molten blends.[51] The T_g of PEO/PMMA blends decrease as the PEO content increases. For a given concentration the effect of PEO molecular weight was negligible.[52] Blends[53] with $\geq 0.8\varphi_{PMMA}$ exhibited a single T_g, which moved to lower temperatures with increasing PEO content. Conversely two T_gs have been observed for blends containing $0.25 < \varphi_{DPEO} < 0.50$.[51] No single T_g could be established for blends of PEO with aPMMA and sPMMA,[48] this was accounted for by the T_g transition being masked by the PEO endothermic peak. Using DSC[48] PEO/iPMMA was found to have a T_g of -40 °C for all concentrations of DPEO. This is smaller than that predicted by the Fox equation, and is believed to indicate two phases, one rich in PEO the other in iPMMA. The T_g associated with the second phase is lost in the PEO melting endotherm peak. A decrease in T_m in a blend can be attributed to morphological effects (PEO lamellar thickness) and thermodynamic effects such as polymer-polymer interactions. Lamellar thickness for PMMA and PEO blends has been found to be independent of concentration so a change in T_m with PMMA concentration is attributed to interactions between polymers[48].

From melting point depression methods, the interaction parameter (χ/volume of DPEO monomer) for PEO and PMMA blends was found to be χ=-0.131 and -0.139 at 333 K, indicating miscibility in the molten state[54]. The interaction parameter is known to be influenced by isotopic labelling (deuteration). χ has also been found to be small and negative by small angle neutron scattering (SANS) for DPEO and PMMA at temperatures above the PMMA T_g[55]. χ was found to be temperature and composition dependent and dominated by enthalpic contributions. An upper critical solution temperature (UCST) was consequently predicted for the system. This is in contrast to other SANS work[56] where χ was found to change from a small negative value when the composition exceeds $0.8 = \varphi_{DPEO}$ at 353 K for both DPEO/PMMA and PEO/DPMMA blends. Hence entropic contributions were considered to be dominant for the blends and above the DPEO T_m, DPEO/PMMA form a homogeneous blend. A lower critical solution temperature (LCST) was also consequently expected. LCST [57] has also been predicted for PEO/PMMA from thermodynamic values found using a modified pressure dilatometer where χ was also found to have a weak temperature dependence. Corresponding states of matter theory[58] predicted a LCST of 350 °C for aPMMA and PEO (molecular weight 130000 $\mathrm{gmol^{-1}}$ and 20000 $\mathrm{gmol^{-1}}$ respectively), experimental results showed complete miscibility of DPEO and aPMMA over 120 °C < T < 60 °C.[59] At room temperature, amorphous blends ($\varphi_{DPEO} < 0.3$) were found to be homogeneous down to 50 nm. Below this length scale structures with average sizes larger than 2 nm existed, heterogeneities were later found to only exist below 40 nm[60]

1.6.2 Diffusion and dynamics

Rheology has been used to investigate the behaviour of PEO and PMMA in the blend. In contrast to the behaviour of the pure components, time-temperature superposition (section 2.7.1) failed for φ_{DPEO}=0.2 blend and individual friction coefficients and relaxations for each component in the blend were identifiable. An effective tube diameter of ~40Å was calculated for both pure components.[61] Failure of time-temperature superposition was also observed using forced Rayleigh scattering.[62] The terminal dynamics of each component for a PEO tracer/PMMA matrix blend, maintained temperature dependence. This indicated that the failure of time temperature superposition has an intramolecular origin. If considered at the same (T-T_g) PMMA relaxes slower in the blend than in pure PMMA and PEO relaxes faster than in pure PEO[61], this discrepancy in the relaxation times of PEO was attributed to uncertainity in the T_g of PEO. Dynamic measurements from NMR[63] indicate two dynamic responses from PEO/PMMA blends which are due to the large difference in T_g between components (180 K). The mobility of PEO is reduced by the presence of PMMA and remains mobile when the blend temperature is below the glass transition of the blend. Quasi-elastic neutron scattering techniques have shown that the dynamics of PMMA molecules in PEO blends resembles behaviour in pure PMMA. Taking into account the change in glass transition temperature on blending, segmental mobility on short time scales was found to be controlled by the distance from T_g,[64] this scaling is limited to early stages of relaxation behaviour.

The segmental dynamics of PEO over the entire range of blend compositions, as measured, for example, by NMR, are hardly influenced by the presence of the considerably slower moving PMMA. This was confirmed from NMR studies for a blend with $0.03=\varphi_{DPEO}$ (a near tracer composition). The segmental dynamics of DPEO in the blend are retarded by less than one order of magnitude compared to pure DPEO. This relationship continues at temperatures well below the glass transition of the PMMA matrix, where the segmental relaxation times of PMMA are up to 12 orders of magnitude greater than the rapid PEO relaxation times for the PEO tracer blend.[65] The local mobility of amorphous PEO was found from ^{13}C NMR to decrease in proportion to the concentration of PMMA in a blend.[60] Other work that showed an invariance of PEO dynamics to composition has been considered to be a consequence of the high temperature and frequency of NMR experiments.[66]

Monomeric friction coefficients calculated from forced Rayleigh scattering measurements were in contrast to other literature results.[67] Global dynamics of the PEO molecules were found to be a stronger function of temperature than segmental dynamics and could not be directly related. By comparing with small molecules diffusing in PMMA, the polyethylene oxide repeat unit was found to have a high degree of local conformational freedom due to the details of molecular packing.[62]

1.6.3 Conformation in the blend

Small angle X-ray scattering (SAXS) has confirmed a pseudo-lamellar structure for PEO in PMMA. For PEO/aPMMA and PEO/sPMMA when ($\varphi_{PEO} > 0.6$) PEO crystalline lamellae are separated by amorphous regions of PEO and PMMA. PEO/PMMA $\varphi_{PEO} > 0.6$ contains alternate and amorphous lamellae of PEO with iPMMA separated into interfibbular regions. iPMMA in the blend is considered to form a 3/1 helix whilst sPMMA forms a planar zigzag conformation.[50] Vibrational spectroscopy has been used to investigate structure in the blend. Upon blending, PMMA ‘forces’ PEO to be coplanar. To interact via hydrogen bonding, PEO has to act as a proton acceptor through the negative oxygen whilst PMMA is a proton donor via the positive carbonyl atom. This is weakened by repulsive forces from the two negative charges on PMMA. Many authors therefore believe that PEO and PMMA compatibility is mostly attributed to physical rather than chemical intermolecular interactions.[50]

1.7 Objectives

- To develop a method for investigating the diffusion of DPEO and PMMA using ion beam analysis.
- To investigate whether the diffusion observed supports 'fast' or 'slow' theory by investigating the effect of component molecular weight on diffusion.
- To determine any differences in the diffusion mechanism of DPEO and PMMA due to partial miscibility of PMMA and DPEO and the disparate glass transition temperatures.
- To develop a suitable model for the movement of DPEO and PMMA.
- To seek evidence for thermodynamic slowing down or acceleration.
- To determine whether this diffusion can be related to the temperature at which the couples diffuse.
- To investigate the interaction parameter and glass transition temperature of the DPEO/PMMA blend to assist in understanding diffusion behaviour.
- To try to distinguish between kinetic and thermodynamic driving forces for diffusion by altering one of the components in the blend.
- To investigate the behaviour of the polymer bilayer at the interface during the early stages of diffusion using neutron reflectometry.

1.8 Presentation of this thesis

Chapter 2 covers the various experimental techniques utilised in the following chapters. Ion beam analysis and neutron reflectivity provide information about polymer interfaces and hence interdiffusion behaviour, on differing complementary depth scales. Film surface roughness influences these techniques and can be analysed using atomic force microscopy. Small angle neutron scattering can be used to measure polymer interactions from particle scattering. Dynamic mechanical analysis and differential scattering calorimetry can also be used to establish pure and blend polymer thermal behaviour and transmission electron microscopy can be used to study bulk organisation. A review of the theory behind each of these techniques and a brief overview of the instrumentation and operation are included.

The tracer diffusion of PEO into PMMA has not previously been studied. Chapter 3 covers the calculation of this tracer diffusion coefficient and an investigation into whether this diffusion can be related to the molecular weight of PEO and PMMA and the temperature at which the couples diffuse. The effect of the 'partial miscibility' of PMMA and PEO blends on diffusion and evidence for thermodynamic slowing down is discussed. The chapter includes an evaluation of the effect of surface roughness on experimental data.

The understanding of mutual or interdiffusion behaviour requires knowledge of the composition and temperature dependence of the interaction parameter and glass transition temperature for molten DPEO and glassy PMMA. Chapter 4 discusses the measurement and analysis of 'bulk' properties of PEO/PMMA blends. This includes the measurement of the variation of the glass transition temperature with composition using dynamic mechanical analysis. The variation of the interaction parameter with concentration, temperature and molecular weight at temperatures above the melting temperature of DPEO but below the T_g of PMMA were measured using small angle neutron scattering. Results of scattering data are evaluated to establish whether entropic or enthalpic interactions dominate in the blend as well as whether the system exhibits UCST or LCST behaviour.

Elastic recoil detection is a suitable tool for looking at the mutual or interdiffusion of both DPEO and PMMA. Theories of case II diffusion often rely upon one component acting as a 'well', displaying no dilution. Hence chapter 5 covers analysis of bilayers with a greater depth of DPEO than that used for tracer diffusion measurements, so that case II diffusion assumptions can to be made and thin film effects minimised. A discussion of experimental refinements and establishing various parameters for data analysis is incorporated and the effect of beam damage and surface roughness assessed. The diffusion behaviour of both DPEO and PMMA is then compared to Fickean and case II diffusion and the effect of composition variation on blend behaviour considered.

In chapter 6 a diblock copolymer of polystyrene and PMMA (PS-PMMA), is used instead of PMMA as the glassy matrix. The PMMA and DPEO components should still have favourable enough interactions for interdiffusion whilst the PS portion of the chain should slow the diffusion process. The copolymer is characterised using transmission electron microscopy to establish the morphology of PS and PMMA in thin films. By utilising the same DPEO molecular weights to make PS-PMMA/DPEO bilayers, comparisons are then made to the interdiffusion behaviour of the PMMA/DPEO system. Chapter 7 discusses the neutron reflectometry analysis of the interface between molten DPEO and glassy PMMA. Whether DPEO molecules initially enter the glassy matrix before PMMA is sufficiently mobile to move into the molten DPEO, or whether exposure of PMMA chains at the interface the mobile DPEO is sufficient to loosen PMMA chains is addressed.

1.9 References

(1) Crank, J. *'The Mathematics of Diffusion'*; 2nd ed., 1975.
(2) Shewmon, P. G. *Diffusion in Solids*; McGraw-Hill, 1963.
(3) Matano, C. *Japanese Journal of Physics* **1933**, *8*, 109.
(4) Graessley, W. W.; Edwards, S. F. *Polymer* **1981**, *22*, 1329-1334.
(5) Doi, M. *Introduction to Polymer Physics*; Oxford University Press, 1996.
(6) Composto, R. J.; Kramer, E. J.; White, D. M. *Macromolecules* **1988**, *21*, 2580-2588.
(7) Composto, R. J.; Mayer, J. W.; Kramer, E. J. *J. Phys.Rev.Lett.* **1986**, *57*.
(8) Kramer, E. J.; Green, P.; Palmstrom, C. J. *Polymer* **1984**, *25*, 473.
(9) Doi, M.; Edwards, S. F. *The Theory of Polymer Dynamics*; Oxford University Press, 1986.
(10) Rouse, P. *J. Chem. Phys.* **1953**, *21*.
(11) Composto, R. J.; Kramer, E. J.; White, D. M. *Polymer* **1990**, *31*, 2320-2328.
(12) Klein, J. *Macromolecules* **1978**, *11*, 852.
(13) de Gennes, P. G. *Scaling Concepts in Polymer Physics Cornell University Press* **1979**.
(14) Doi, M.; Edwards, S. F. *J. Chem. Soc. Faraday Trans.2.* **1978**, *74*, 1789,1802,1818.
(15) Graessley, W. W. *Faraday Symposia of the Chemical Society* **1983**, 7-27.
(16) Graessley, W. W. *J. Polym. Sci. Polym. Phys. Ed.* **1980**, *18*.
(17) deGennes, P. G. *J. Chem. Phys.* **1971**, *55*.
(18) Graessley, W. W. *Advances in Polymer Science* **1982**, *47*, 67-117.
(19) Antonietti, M.; Coutandin, J.; Grutter, R.; Sillescu, H. *Macromolecules* **1984**, *17*.
(20) Green, P. F.; Mills, P. J.; Palmstrom, C. J.; Mayer, J. W.; Kramer, E. *J. Phys. Rev. Lett* **1984**, *53*.

(21) Daoud, m.; de Gennes, P. G. *J. Polym. Sci. Phys. Ed.* **1979**, *17*.

(22) Composto, R. J.; Kramer, E. J. *Macromolecules* **1992**, *25*.

(23) McKenna, G. B. *Polymer Communications* **1985**, *26*.

(24) Flory, J. P. *Principles of Polymer Chemistry*; Cornell University Press: New York, 1953.

(25) Composto, R. J.; Kramer, E. J.; White, D. M. In *New Trends in Physics and Physical Chemistry of Polymers*; Lee, L.-H., Ed.; Plenum Press, 1989.

(26) Brochard, F.; Jouffroy, J.; Levinson, P. *Macromolecules* **1983**, *16*, 1638-1641.

(27) Sillescu, H. *Makromolekulare Chemie-Rapid Communications* **1987**, *8*, 393-399.

(28) Garbella, R. W.; Wendorff, J. H. *Makromolekulare Chemie-Rapid Communications* **1986**, *7*, 591-597.

(29) Kramer, E. J.; Green, P.; Palmstrom, C. J. *Polymer* **1984**, *25*, 473-480.

(30) Sillescu, H. *Makromolekulare Chemie-Rapid Communications* **1984**, *5*, 519-523.

(31) Brochard, F.; Degennes, P. G. *Europhysics Letters* **1986**, *1*, 221-224.

(32) Akcasu, A. Z. *Macromolecular Theory and Simulations* **1997**, *6*, 679-702.

(33) Bates, F. S.; Hartney, M. A. *Macromolecules* **1985**, *18*, 2478.

(34) Hammouda, B.; Briber, R. M.; Bauer, B. J. *Polymer Communications* **1992**, *33*, 1785.

(35) Green, P. F.; Doyle, B. L. *Macromolecules* **1987**, *20*, 2471-2474.

(36) Green, P. F.; Doyle, B. L. *Physical Review Letters* **1986**, *57*, 2407-2410.

(37) de Gennes, P. G. *J. Chem. Phys* **1980**, *72*, 4756.

(38) Klein, J. *Science* **1990**, *250*, 640-646.

(39) Fox, T. G. *Bull. Am. Phys. Soc* **1956**, *1*, 123.

(40) Nishi, T.; Wang, T. T. *Macromolecules* **1975**, *8*, 909.

(41) Jabbari, E.; Peppas, N. A. *Macromolecules* **1993**, *26*, 2175-2186.

(42) Composto, R. J.; Kramer, E. J.; White, D. M. *Macromolecules* **1992**, *25*, 4167-4174.

(43) Composto, R. J.; Mayer, J. W.; Kramer, E. J.; White, D. M. *Physical Review Letters* **1986**, *57*, 1312-1315.

(44) Composto, R. J.; Kramer, E. J. *Journal of Materials Science* **1991**, *26*, 2815-2822.

(45) Lin, H. C.; Tsai, I. F.; Yang, A. C. M.; Hsu, M. S.; Ling, Y. C. *Macromolecules* **2003**, *36*, 2464-2474.

(46) Jones, R. A. L.; Klein, J.; Donald, A. M. *Nature* **1986**, *321*, 161-162.

(47) Boven, G.; Brinkhuis, R. H. G.; Vorenkamp, E. J.; Schouten, A. J. *Macromolecules* **1991**, *24*, 967-969.

(48) Silvestre, C.; Cimmino, S.; Martuscelli, E.; Karasz, F. E.; Macknight, W. J. *Polymer* **1987**, *28*, 1190-1199.

(49) Martuscelli, E.; Silvestre, C.; Addonizio, M. L.; Amelino, L. *Makromolekulare Chemie-Macromolecular Chemistry and Physics* **1986**, *187*, 1557-1571.

(50) Rao, G. R.; Castiglioni, C.; Gussoni, M.; Zerbi, G.; Martuscelli, E. *Polymer* **1985**, *26*, 811-820.

(51) Li, X.; Hsu, S. L. *Journal of Polymer Science Part B-Polymer Physics* **1984**, *22*, 1331.

(52) Liberman, S. A.; Gomes, A. D.; Macchi, E. M. *Journal of Polymer Science Part a-Polymer Chemistry* **1984**, *22*, 2809-2815.

(53) Jin, X.; Zhang, S. H.; Runt, J. *Macromolecules* **2004**, *37*, 8110-8115.

(54) Cortazar, M. M.; Calahorra, M. E.; Guzman, G. M. *European Polymer Journal* **1982**, *18*, 165-166.

(55) Hopkinson, I.; Kiff, F. T.; Richards, R. W.; King, S. M.; Farren, T. *Polymer* **1995**, *36*, 3523-3531.

(56) Ito, H.; Russell, T. P.; Wignall, G. D. *Macromolecules* **1987**, *20*, 2213-2220.

(57) Privalko, V. P.; Petrenko, K. D.; Lipatov, Y. S. *Polymer* **1990**, *31*, 1277-1282.

(58) Cimmino, S.; Martuscelli, E.; Silvestre, C. *Polymer* **1989**, *30*, 393-398.

(59) Pedemonte, E.; Polleri, V.; Turturro, A.; Cimmino, S.; Silvestre, C.; Mmartuscelli, E. *Polymer* **1994**, *35*, 3278-3281.

(60) Schantz, S. *Macromolecules* **1997**, *30*, 1419-1425.

(61) Colby, R. H. *Polymer* **1989**, *30*, 1275-1278.

(62) Haley, J. C.; Lodge, T. P. *Journal of Chemical Physics* **2005**, *122*, art. no.-234914.

(63) Lartigue, C.; Guillermo, A.; CohenAddad, J. P. *Journal of Polymer Science Part B-Polymer Physics* **1997**, *35*, 1095-1105.

(64) Sakai, V. G.; Chen, C.; Maranas, J. K.; Chowdhuri, Z. *Macromolecules* **2004**, *37*, 9975.

(65) Lutz, T. R.; He, Y. Y.; Ediger, M. D.; Cao, H. H.; Lin, G. X.; Jones, A. A. *Macromolecules* **2003**, *36*, 1724-1730.

(66) Ngai, K. L.; Roland, C. M. *Macromolecules* **2004**, *37*, 2817-2822.

(67) Wesson, J. A.; Noh, I.; Kitano, T.; Yu, H. *Macromolecules* **1984**, *17*, 782-792.

Chapter 2

Experimental methods

2.1 Introduction

Ion beam techniques can be used to follow polymer diffusion over a range of depth scales and can also be used for ion implantation and elemental analysis. After looking at the technical details relating to the generation and control of the ion beam, an overview of the various ion beam techniques used to probe polymeric materials and to understand interdiffusion behaviour will be discussed. It is also relevant to review small angle neutron scattering as a technique for measuring polymer interactions from particle scattering. Neutron reflectivity is a method which can provide information about polymer interfaces, on a scale smaller than those possible with ion beam analysis and is relevant in understanding diffusion near the polymer length scale. Other techniques reviewed include thermal analysis such as dynamic mechanical analysis and differential scattering calorimetry. PEO is known to be semi-crystalline and hence thin films should have a rough surfaces and these can be analysed using atomic force microscopy. Segregation within a polymer blend or copolymer can be imaged using transmission electron microscopy.

2.2 IBA Instrument

The NEC 5SDH Pelletron accelerator at Durham can be used to produce a monoenergetic beam of helium ions. At the helium ion source, a radio frequency field of approximately 100 kHz is used to convert either ^{3}He or ^{4}He gas to a plasma of positive helium ions. The source is insulated and held under a potential of 6 kV. The helium ions in the plasma are extracted towards the Pelletron accelerator, with a typical current of 2 mA. The helium ions come into contact with rubidium vapour resulting in helium particles with neutral or negative charge, which are steered with a gap lens and einzel lens towards the Pelletron accelerator. The accelerator works like a Van de Graff generator, a positive field is set up using a belt of metal pellets with non-conducting nylon links; the negative helium ions accelerate towards the positive terminal. Here collisions with a nitrogen stripper gas held inside the positive terminal, change the negative ions to neutral or positive ions, the latter are in turn accelerated away from the positive centre of the accelerator chamber. As several species have been produced those required (^{3}He^{++} for NRA and ^{4}He^{++} for ERD) need to be selected. This is achieved by using a bending magnet, similar to that found in a mass spectrometer, to separate species according to their charge to mass ratio. The magnet's field can be fine-tuned to direct the required species down the beam line. The beam of positive ions produced needs to be focussed by using quadropole electromagnets that can be fine-tuned to achieve the correct beam shape. The beam of ions is steered and focused towards the end station, which holds the samples to be analysed. The beam is directed by further bending magnets and is focussed using quadropole magnets. Along the beam's path, beam profile monitors allow the size and shape of the beam to be monitored by passing a helical wire through the beam and analysing the resultant current from charge flowing within the wire. As the beam enters the end station with a current of typically 30-40nA the 2mm aperture defines the beam spot size. Within the accelerator, the ion beam is under high vacuum from the ion source to the end chamber where the samples are mounted.

The samples are held in a moveable vertical rack, controlled by a sample manipulator, run from a computer. A beam line valve allows only the end station

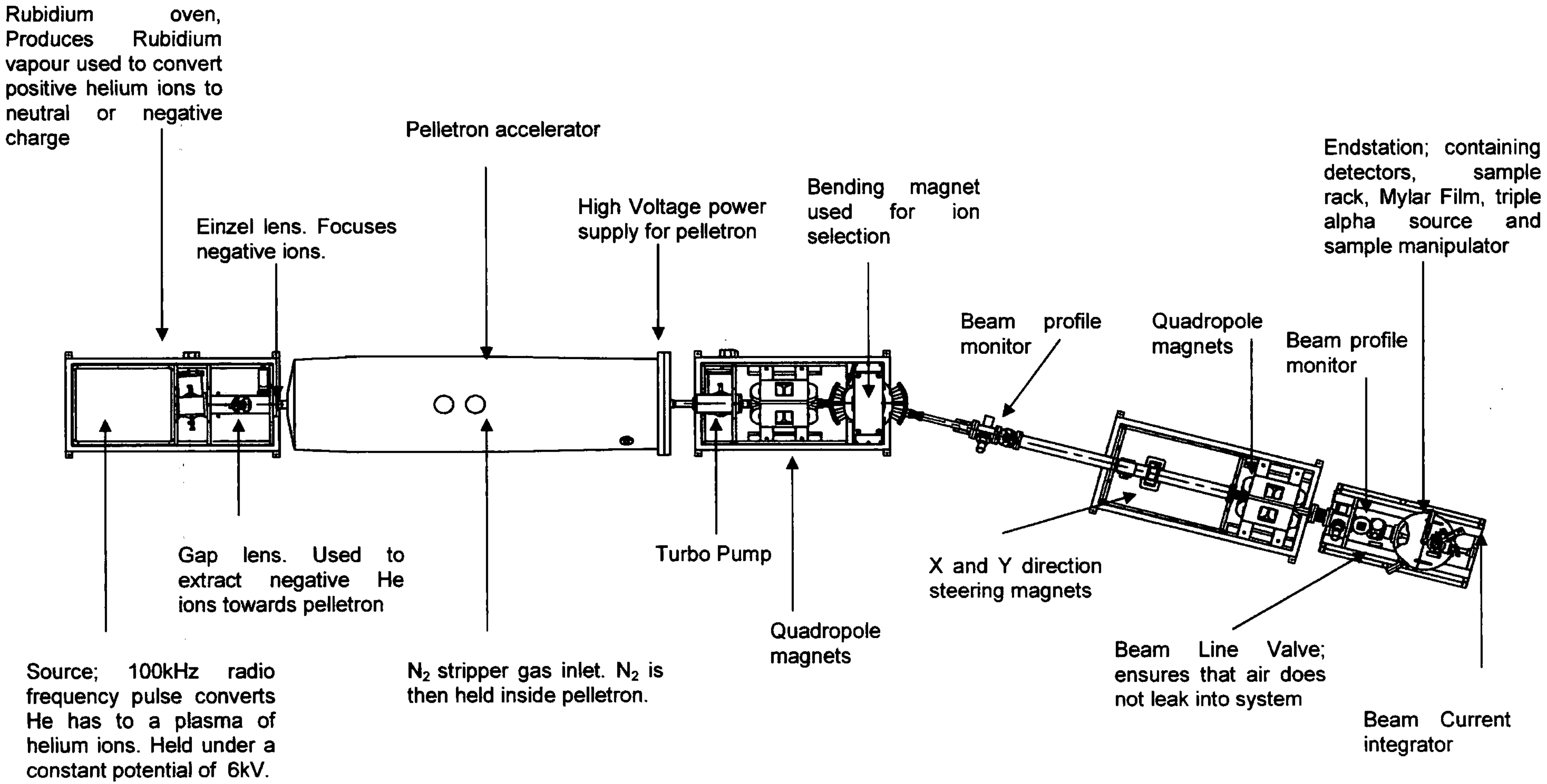

Figure 2.1. Schematic of 5SDH accelerator in Materials Chemistry Building, Durham.

to be opened to the air. There are two moveable silicon surface barrier (SSB) detectors that record the energy of species that are scattered from the sample. Mylar^{TM} foils of various thicknesses can be moved in front of the detectors to prevent unwanted species from reaching the detectors. An aperture in front of the detectors ensures that geometric broadening from recoiled particles at different angles to that being analysed is minimized. The detectors contain a crystal with a potential across it. When an ion hits the crystal in the aperture of the detector, the energy of the impact promotes electrons and holes into the conduction band for the crystal; these electrons and holes do not recombine due to the voltage present. The number of electron hole pairs created is proportional to the energy of the incident particle. The electrons in the conduction band cause an electric current to flow that can be measured. Hence the energy and yield of particles interacting with the detector can be measured and the counts for a given energy of particle can be recorded. The two detectors for the two techniques work in the same way, however the detector used for NRA utilises a thicker crystal (1.5 mm) than the ERD detector (0.3 mm) because this greater thickness is required to completely stop high energy protons generated by nuclear reactions. The energy and current of the beam is measured using a beam current integrator. The end station is insulated from the ground, apart from one wire connected to the beam current integrator which allows the charge of the beam to be measured.

Operation.

Samples are placed in the end station via a load lock, the rack and samples can be cooled using the liquid nitrogen cooling system. The temperature of the holder can be calculated by measuring the resistance of a platinum wire attached to the holder. Temperatures as low as -80 °C can be readily achieved. A sample on the rack can then be lined up with the beam and the angle of incidence of the beam set up. The RC43 software* allows various geometries for a rack to be stored and then each sample exposed to the beam in turn, the ejected or reflected particles measured by the detectors. As the sample rack moves the beam is cut off from the end station by the beam line valve until the sample rack has finished moving. The extent to which a given sample is exposed to the beam is selected by choosing a certain amount of charge to be collected for that sample.

---

* Automated ion beam analysis programme v. 4.3.15 (National electrostatics corporation)

2.2.1 Data collection

Two methods of ion beam analysis were used in this study; Elastic Recoil Detection (ERD) and Nuclear Reaction Analysis (NRA). The geometry for each method was optimised for the system as described in sections 3.2 and 5.2. In most cases samples of the same type but different annealing times were placed on the same rack. The results for each sample were then directly comparable because samples had been exposed to a beam of the same energy, size and charge. The area exposed to the ion beam was lined up using a mechanical manipulator and a camera inside the vacuum chamber. The data files produced give the counts per channel for the detector of back scattered (NRA) or forward recoiled (ERD) ions. These files include the beam energy, geometry, resolution and charge for the particular experiment.

2.3 *Elastic Recoil Detection (ERD)*

2.3.1 Introduction

Ion beam analysis using forward recoil spectroscopy, also termed elastic recoil detection (ERD) is a technique used to detect the depth and type of a species by measuring the energy of the recoiled target atoms following impact with a heavier ion[1]. This is useful when the target ions are light, such as hydrogen or deuterium[2] and use of a low energy ^{4}He beam has proved advantageous in measuring ^{1}H depth distribution,[3-5] diffusion coefficients in polymer/solvent[6] and polymer/polymer systems.[7-9] ERD is particularly useful because it allows measurement of the volume fraction of a deuterated polymer diffusing into a chemically identical non-deuterated matrix. It is a fast technique compared to nuclear reaction analysis (NRA)(section 2.4), neutron reflectivity (section 2.6) and dynamic secondary ion mass spectrometry (SIMS) and utilises comparatively simple, robust equipment.[10]

2.3.2 ERD

As shown in Figure 2.2 a monoenergetic beam of ^{4}He^{++} ions with energy E_0 is directed at a sample that includes both hydrogenous and deuterated polymer at a glancing angle α with respect to the sample surface. The ion then travels into the sample, the energy of particles travelling through materials change with depth,

(E_0 becomes E_1). Subsequent collision with a target nucleus occurs within the sample; in this case the target nuclei are hydrogen or deuterium. The collision is elastic and thus the deuterium and hydrogen atoms receive a constant fraction of the energy of the ^{4}He ion. Collisions with carbon and other heavy elements present are possible but result in ejected nuclei of lower energy that are not normally detected. Collisions with hydrogen or deuterium nuclei may result in the ejection of the target nuclei with energy E_2, which has energy E_3 upon leaving the sample. The ejected nuclei will then be detected as shown in Figure 2.2. However, many of the incident $^4He^{++}$ ions are also deflected and these could mask the signals from the recoiled hydrogen and deuterium. The helium ions are thus removed before they reach the detector by placing a Mylar (PET) stopper foil in front of it (E_3 becomes E_4). The detector records the number of particles (counts) with a given energy range (energy channel), hence the density of a given species at a certain depth can be calculated. The straggling in the stopper foil of the hydrogen and deuterium nuclei means that the energy and therefore the depth resolution of the experiment are limited.[3]

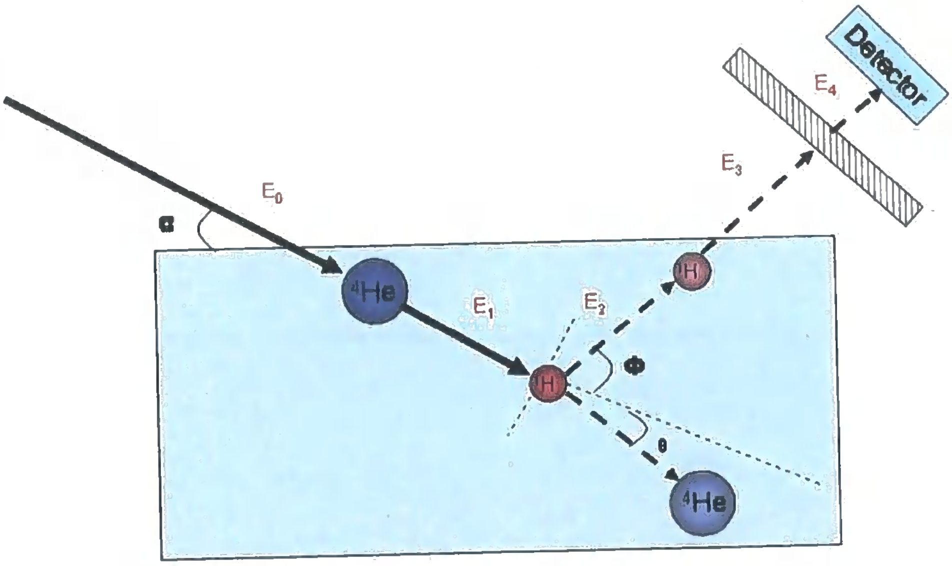

Figure 2.2 Diagram of the basic process of ERD.

2.3.3 Interaction of matter and energy loss

As an energetic ion moves through matter it loses energy through processes associated with the Coulomb force;[11] where the ion collides with target nuclei and excites or ejects electrons from nearby atoms. For ions with energies of approximately 1-3 MeV, such as those used in ion beam analysis, the energy loss due to interactions with nuclei are about three orders smaller than the energy loss from interactions with electrons. Hence the main mechanism of energy loss, for particles utilised in ion beam analysis, passing through a sample is from electronic interactions. Due to the relative size of the electron and the incident ion the path of the ion does not change significantly. Due to the high density of electrons within the sample the incident ion is slowed down by interaction with electrons almost continuously. As the change in energy with depth, $-(dE/dx)$ decreases with increasing incident energy and dE/dx varies systematically with $1/E$ at high energies, the detected energy range can be converted into a depth profile. The energy loss per unit path length, $-(dE/dx)$, due to momentum transfer between the incident ion and target electrons can be calculated for any given sample. There is also a second contribution to ion slowing which is due to the incident ions outside the electron orbit undergoing small momentum transfers from electron excitation.[12] This can be expressed as,

$$\frac{-dE}{dx} = \frac{2\pi Z^2 e^4}{E_{in,0}} N_d Z_t \left(\frac{M_p}{m_e}\right) \ln\left(\frac{2m_e v^2}{I}\right)$$ Equation 2.1

where N_d is the atomic density, m_e and m_p are the electron mass and particle mass respectively, Z_t is the target ion's atomic number, $E_{in,0}$ is the incident particle energy, v is the ion velocity, and I is the excitation energy of an electron. For a target sample that is not a pure element, such as a polymer, Bragg's rule is used to calculate the material's stopping power. This assumes that the target atoms contribute independently to the total energy loss, regardless of bonding. This allows the stopping powers to be calculated from the elemental stoichiometry and the density. A software program called SRIM®† (Stopping range of ions in matter), developed by Ziegler et al,[13] can be used to calculate the stopping powers[14] of various polymers. Alternatively, the stopping powers can also be determined experimentally from a film of known thickness and density.[15,16]

2.3.4 Kinematic factor and particle energy

From Figure 2.2, when a monoenergetic beam of ^{4}He ions impinges on a sample, the lighter element undergoes an elastic collision with the ^{4}He ion and is forward

---

† SRIM® v.2003.26 (James F. Ziegler)

scattered at an angle Φ with respect to the incident beam direction. The energy of the recoiled light particle, either deuterium or hydrogen, E_2, can be determined from the energy of the incident ion, due to the conservation of momentum and energy. Hence E_1 relates to E_2 as shown in Equations 2.2 and 2.3,[12]

$$E_2 = KE_1 \qquad \text{Equation 2.2}$$

$$\frac{E_{2t}}{E_1} = K = \left[\frac{4m_{He}m_t}{(m_{He}+m_t)^2}\right]\cos^2\Phi \qquad \text{Equation 2.3}$$

where m_{He} and m_t are the masses of the helium ions and the target nuclei. The Mylar stopper foil removes the heavier He nuclei, since the energy loss is greater for He ions passing through material than the lighter recoiled target nuclei, which can pass through the foil with only a small loss in energy. From Figure 2.2 it follows that the energy of the nuclei that is measured by the detector E_4, will be described by,

$$E_4 = E_3 - \delta E_s \qquad \text{Equation 2.4}$$

where δE_s is the energy that the ion loses passing through the Mylar stopper foil. This energy loss will be dependent on both the thickness of the foil and the elements present in the foil. The energy of the recoiled nuclei that reach the stopper foil will not however be that which was present at the initial collision of the beam and target. The recoiled ^{4}He, ^{1}H and ^{2}D will also lose energy due to electronic interactions within the sample. The energy of the nuclei detected can be described by,

$$E_4 = E_3 - \delta E_s = (E_2 - \delta E_{ss}) - \delta E_s \qquad \text{Equation 2.5}$$

where δE_{ss} is the energy lost by the nuclei whilst travelling out of the sample. Stopping powers are relatively constant in thin films, δE_{ss} can often be calculated[12] using Equation 2.1 and its variation with $1/E$. This is called the thin film approximation. As stopper foils are of the order of μm, δE_s can be calculated by using thick target approximation.[17] The sample is divided into N layers, each with thickness Δx and the total thickness of the sample will be $N\Delta x$ (Figure 2.3). For sufficiently small Δx the stopping power in that layer can be considered to be constant. The energy to depth conversion can thus be performed sequentially for each layer.

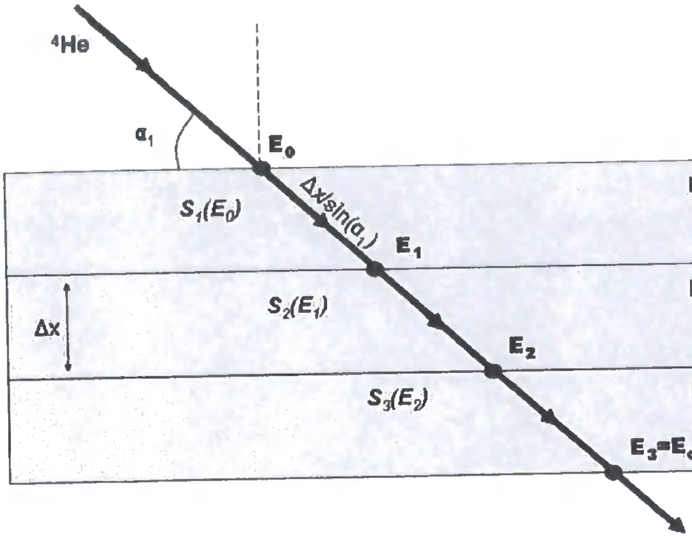

Figure 2.3 Diagram describing the thick target approximation for ERD

The energy of an ion entering layer *j+1,* is E_j, the energy of an ion passing through a layer can be evaluated from the recurrent relation,[12]

$$E_{j+1} = E_j - \frac{\Delta x}{\sin \alpha_2} S_j E_j \qquad \text{Equation 2.6}$$

where S_j is a function of energy loss with depth as evaluated at E_j.

Typical ERD spectra for a polymer bilayer diffusing are shown in Figure 2.4. Ion energy is a linear function of channel number, where higher energies occur at higher channel numbers. The two peaks are discrete; the far right peak is attributed to recoiling ^{2}H, the highest energy of which is the surface of the bilayer. The peak to the left is the ^{1}H peak, the highest energy indicating the deuterated/hydrogenous polymer interface.

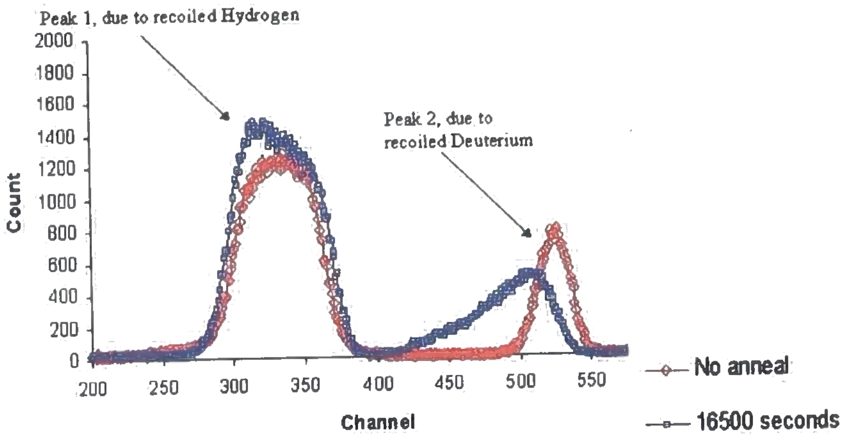

Figure 2.4 Illustration showing typical ERD spectra for a bilayer with a deuterated polymer on top of a hydrogenous polymer before and after heating

2.3.5 Data analysis

2.3.5.1 Depth scale conversion

A typical ERD spectrum is shown in Figure 2.4. It is necessary to convert channel number into depth. The energy per channel can be found from a calibration experiments as shown in sections 5.2.4 and 2.4.5.1. The energy of a particle as it is detected by the detector will depend on the depth within the sample from which it originated. The leading edge (that of highest channel number and thus energy) of the deuterium peak in a ERD spectrum indicates the channel for a deuterium ion leaving the surface of the sample, as shown in Figure 2.4. This 'surface channel' is therefore considered to be zero depth. Using kinematics, the resultant energy of a deuterium ion recoiling after collision with an incident ion at the surface of the sample can be calculated, using Equation 2.3. The energy for every subsequent channel from the zero depth can then be determined.

Equation 2.5 can be used to find the depth of origin of recoiled particles. A spreadsheet can be developed to take known values such as beam energy, resolution, energy per channel, experimental geometry and foil thickness as well as functions of SRIM® calculated stopping powers with depth for ^4He, ^1H and ^2H ions in substrate and stopper foils. The thick target approximation is used to establish δE_{ss} and the thin film approximation for δE_{ss}. Theoretically, samples on the same rack in an experiment should have the same surface channels. This is not always the case and is attributed to the samples attached to the rack with double sided tape not lying completely flat, or curvature in the sample rack. This can cause a variation of ± 2° in the nominal forward scattering angle. When calculating a depth scale for a given sample, the surface channel can first be defined by using least squares fitting of raw data. This can be used to indicate the true forward scattering angle and hence enable calculation of a depth scale accordingly.

2.3.5.2 Normalised yield and volume fraction

Counts need to be converted into volume fraction of component. The volume fraction of a given species at a given depth was required. This can be achieved by dividing the collected spectra by the spectrum obtained for a thick homogeneous sample. Experimental data for a well characterised copolymer of hydrogenous and deuterated polystyrene can be fitted using the simulation programme SIMNRA[‡]. This allows a theoretical target to be built up and the spectrum is simulated after the energy, geometry, charge and other detector parameters are specified. The simulation also accounts for straggle, resolution and finite beam size. The experimental spectrum is therefore smoothed so that statistical roughness is not transferred to the spectra being analysed. As the experimental spectrum is divided by the simulated mixed spectrum, the widths of the deuterium and hydrogen peaks needed to be as broad as possible to account for large depths of each element. Hence the simulated spectra should be broadened as much as possible without the hydrogen and deuterium peaks overlapping. This simulation can then be converted to an axis with a depth scale using a spreadsheet similar to that discussed above.

2.4 Nuclear Reaction Analysis (NRA)

2.4.1 Introduction

Nuclear Reaction Analysis (NRA) is a alternative ion beam technique for depth profiling deuterium, first used to detect trace amounts of deuterium in materials such as silicon[18] and later for studying polymers. Nuclear reaction analysis unlike

---

[‡] SIMNRA v.5.07 (Dr. Matej Mayer, Max Planck Institute für Plasmaphysik)

ERD relies upon detecting the products of a nuclear reaction between the incident ion and the target nucleus. An incident ^{3}He ion reacts with deuterium in a sample according to the following exothermic reaction,

$$^3He + {}^2H \rightarrow {}^4He + {}^1H + Q \qquad \text{Equation 2.7}$$

where Q=18.352 MeV. The reaction proceeds by formation of a ^{5}Li nucleus, which decays to the products shown. Conservation of momentum requires that the velocities of the proton and alpha particle (^{4}He) be related by the following equation, using terms defined in Figure 2.5.

$$V_p^c = -4V_\alpha^c \qquad \text{Equation 2.8}$$

The velocity of the centre of mass V_{cm} is found from,

$$V_{cm} = \frac{3}{5} V_{^3He} \qquad \text{Equation 2.9}$$

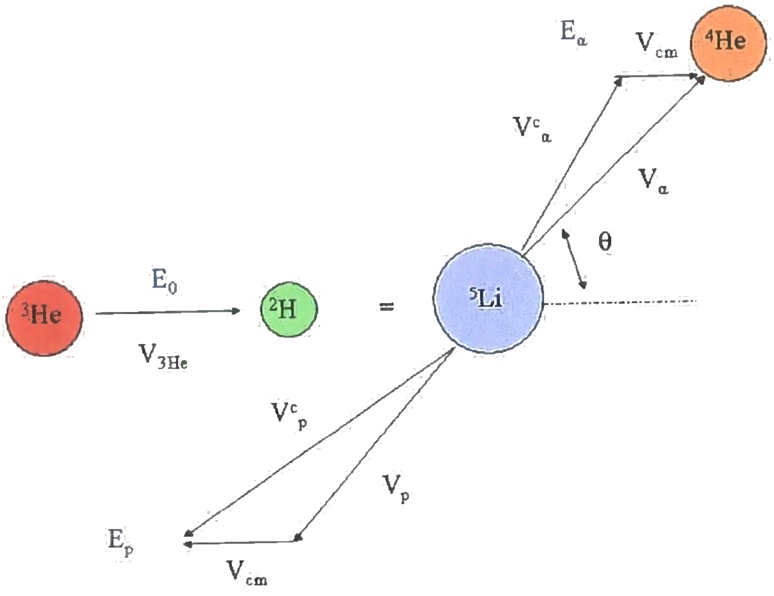

Figure 2.5 Diagram of nuclear reaction involved in NRA measurements

The protons and alpha particles are ejected from the sample and their energy and number collected using a particle detector. The energy loss of nuclei travelling through a given medium is described in section 2.3.3, Ziegler stopping powers,[13] can be used in a similar way to ERD analysis, to relate depth scale within a medium to energy, as described in section 2.3.4. NRA has been used to analyse polymer diffusion,[18] surface dewetting[19] and surface decomposition.[20]

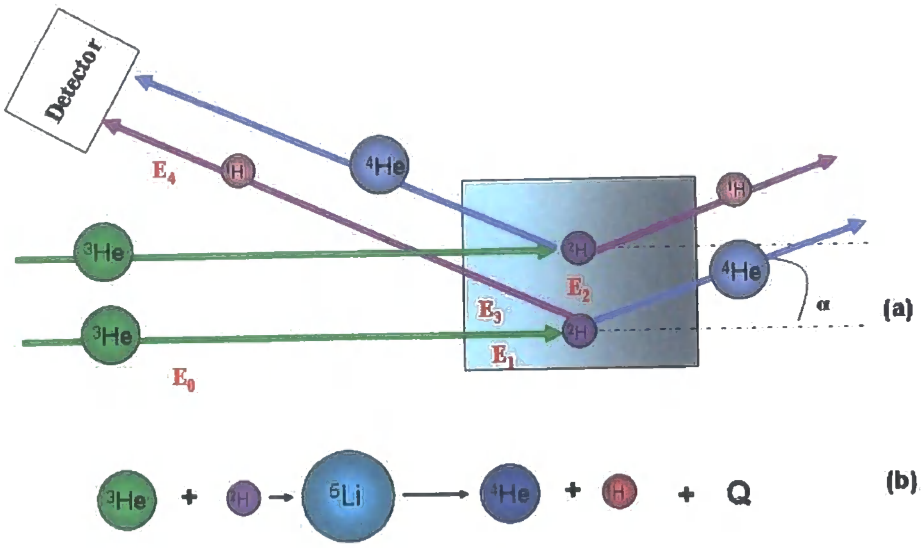

Figure 2.6 (a) Diagram of experimental setup for NRA (b) and nuclear reaction utilized for NRA.

2.4.2 NRA

As the incident ion ^{3}He, with energy E_0, collides with the sample, the single electron is stripped, leaving a doubly charged nucleus. Subsequent to reaction with deuterium, the outgoing ^{4}He and ^{1}H have energies much higher than the incident ion energy E_0. In a typical experimental set up with E_0=700 KeV the outgoing ^{4}He and ^{1}He have differing energies.[12] The energy of the ejected particles will be dependent on the energy of the incident ^{3}He ion at the depth of collision and reaction.[10] The high energy protons produced exit the sample in either geometry with negligible energy loss due to electronic interactions. The ejected ^{4}He ions will be influenced by the electronic interactions and their energy at the detector will be dependent upon the depth of the reaction and ^{4}He stopping powers within the sample.

2.4.3 Energy optimisation and geometry

In the geometry used by Klein[21] the detector was at an angle of Φ=30°.This allows forward scattered particles to be detected. Whilst ^{4}He are forward scattered towards the detector after nuclear reaction, ^{3}He and ^{1}H can be elastically forward scattered from collision with particles without reaction in a similar way to ERD. A magnet in front of the detector can remove all particles except ^{4}He; this prevents the signal being swamped by the elastically scattered ^{3}He. A depth profile of the ^{2}H can then be obtained from a distribution of the outgoing ^{4}He. Due to ^{4}He energy losses during travel through the sample, the forward scattering geometry is only appropriate for depth profiling near the surface.

Since ^{1}H travels through the sample with very little loss in energy, ^{1}H originating from greater depths than those measured in the forward recoil direction can be detected and the ^{2}H distribution probed. In a technique developed by Payne[18] the detector is placed at $\Phi = 160°$, so that the energy of particles in the back scattered geometry can be analysed. Elastically scattered ^{3}He from collisions with carbon or other large nuclei are present but at lower energies and not in significant amounts to saturate the signal. ^{4}He ejected from the upper layers of the sample will also be present, but no magnetic separation or stopper foil is necessary to remove these particles. To achieve the best resolution; ^{4}He ions from forward scattering geometry experiments can be used to probe near surfaces whilst ^{1}H from back scattering geometry experiments can be used to probe greater depths. The resolution is approximately 10% of the depth probed.[22]

2.4.4 Energy optimisation and depth resolution

Several factors influence the depth resolution of ion beam techniques. The depth resolution can be defined as δx,

$$\delta x = \frac{\Delta E_{tot}}{(dE/dx)_{eff}} \qquad \text{Equation 2.10}$$

where, if they are uncorrelated and can be characterised by a Gaussian distribution,[12,23]

$$\Delta E_{tot}^2 = \Delta E_D^2 + \Delta E_M^2 + \Delta E_S^2 + \Delta E_F^2 + \Delta E_G^2 \qquad \text{Equation 2.11}$$

ΔE_D, detector energy resolution

ΔE_M, energy broadening due to multiple scattering

ΔE_S, energy straggling in the sample

ΔE_F, energy straggling in the stopper foil for ERD only

ΔE_G, geometrical broadening due to beam divergence and finite acceptance angle of detector.

The energy resolution of the detector, ΔE_D can be considered to be constant. The energy broadening due to multiple scattering ΔE_M is due to the repeated collision of the incident ions with other nuclei. A beam of ions passing through a sample will also have multiple small angle collisions with electrons in the sample, this will lead to a broadening of the beam diameter.[24] This lateral and angular spread, including path-length fluctuations of incoming and outgoing particles have been estimated from theories of multiple scattering.[25] As these events are statistical in nature the energy loss to the ions has a Gaussian distribution with a width corresponding to the energy straggling. Bohr theory[26] can be used to approximate the energy spread due to straggling. Straggling is independent of beam energy and increases as the square root of target (film) thickness[12].

Geometric broadening[27] occurs because both the beam and detector have a finite diameter. The kinematic factor has a strong reliance on the recoil angle (Equation 2.3). Different spots on the sample targeted will have different values of recoil angle and thus different kinematic broadening which can introduce an error ΔE_G. This effect can be reduced by having an aperture in front of the detector to allow only particles from a small solid angle to enter the detector. The largest error affecting the depth resolution in ERD is the straggling in the Mylar™ stopper foil, ΔE_F. The straggling process is the same as in the sample. Whilst removing the ^{4}He ions it slows and increases the energy spread of the ^{1}H and ^{2}H ions.

For some samples, lateral inhomegenities, such as surface roughness can also affect resolution. For ion beam analysis a rough surface will affect the energies of particles entering and emerging from the sample. The peaks and troughs will give different distances of travel for particles and therefore will provide a wider spread of energies for particles that have recoiled from same distance within the sample. If a substrate or layer within a sample is rough, the roughness will be perturbated through layers that lie above, leaving a rough upper surface. A sample with two smooth interfaces causes a symmetrical peak in the spectra. Roughness at the surface of a sample should manifest itself in both ERD and NRA spectra as a tail indicating a greater distribution of energies of recoiled particles. This 'tail' causes a problem for analysis as it occupies the same energy range as that occupied by diffusion of molecules to greater depths.

2.4.5 Data Analysis

2.4.5.1 Depth scale conversion

To calculate a depth profile, the volume fraction of a given species at a given depth is required. For forward scattering NRA this means plotting the movement of the peak for the proton particles ejected. It is therefore necessary to convert channel number into depth. A calibration experiment can be carried out to determine the energy per channel. An RBS spectrum of a silicon wafer with a thin layer of gold is collected and analysed using an analysis software programme RUMP[§]. RUMP allows a simulation to be built and fitted to experimental ion beam data. It is most suited to elemental analysis and RBS but not polymer systems. Because the kinematic factors for pure elements are known, the energy difference and the number of channels between the two peaks can be found and the detector calibration calculated. This is a reasonable method for calculating the energy per channel for ion beams up to about 3 MeV, The energy per channel can also be calculated from NRA spectrum using the triple alpha source[28] present in the end station. This can provide accurate values for keV/Channel up to 30 MeV

[§] RUMP (Computer Graphic Service, Ithaca, NY)

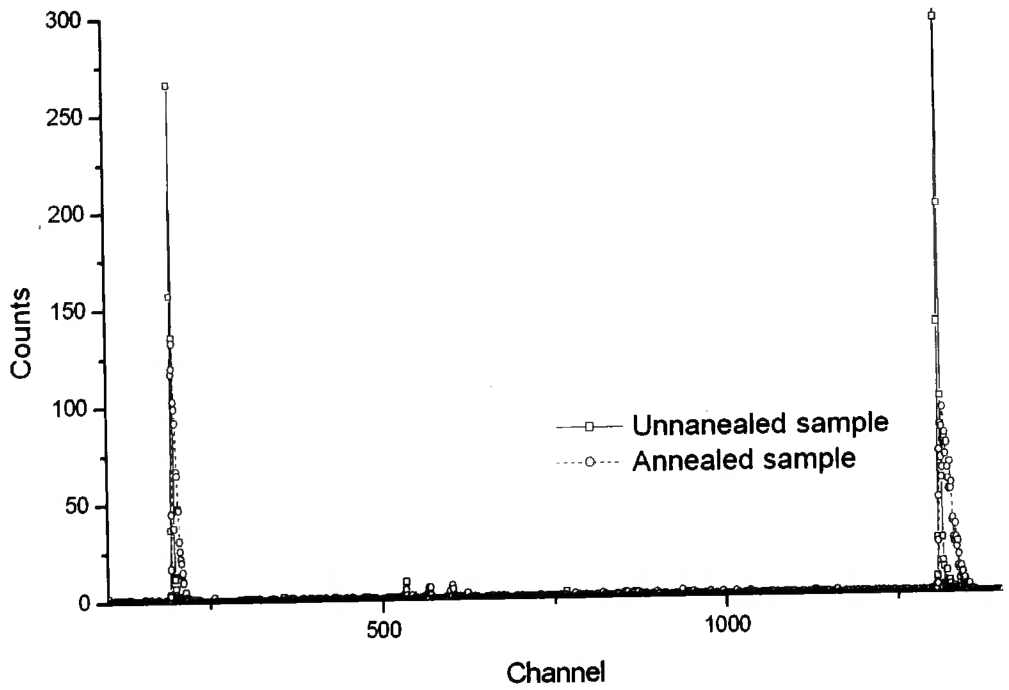

Figure 2.7 Showing typical raw NRA data using forward scattering geometry.[29] Peaks from the left to right are attributed to; alpha particles, triplet peak from calibration alpha source in endstation and proton peak. The straight edge on left of proton peak represents the surface channel.

For NRA, the back edge of the alpha peak provides the channel for a nuclear reaction at the surface or 'zero' depth (see Figure 2.7). For NRA, kinematics are used to find the amount of energy a nuclear reaction at the surface would provide an ejected alpha particle. Once zero depth and energy per channel are known the energy for all channels can be found. To establish the energy before and after the nuclear reaction (section 2.3.4) the thick film approximation and SRIM® stopping powers can be used to establish δE_{ss}. A spreadsheet can be used to account for the detector angle, beam energy, resolution and geometry and convert energy to depth.

2.4.5.2 Normalised yield and volume fraction

The volume fraction of a given species at a given depth is required. For NRA the proton peak can be divided by data from a thick sample of deuterated polymer collected at the same energy and geometry. The experimental spectrum was smoothed and converted to an axis with a depth scale in the same way described in section 2.3.5.2.

2.4.6 Comparison of NRA and ERD

NRA analysis is advantageous by virtue of its good surface resolution and simple analysis; however, NRA is marginally more expensive than ERD as it requires ^{3}He instead of ^{4}He. Unlike ERD, NRA only allows the profiling of deuterium; this prevents the tracing of any movement of the hydrogenous polymer, which may be significant. NRA can probe greater depths with better resolution than ERD; however data takes longer to collect. The depth range for NRA is less limited than for ERD.[10] The lack of a stopper foil improves depth resolution of NRA set up with the Payne geometry.

2.5 Small angle neutron scattering

Small angle neutron scattering (SANS) is a diffraction technique that utilises the wave property of neutrons to provide information about the size and shape of molecules and their assemblies. SANS measures the interference between pairs of scattered waves from different scattering centres. Neutron scattering techniques utilise the scattering length densities of the elements in the sample. Only the coherently scattered neutrons, where phase is conserved, contain the structural information about the sample. Coherent scattering length varies irregularly between nuclei.

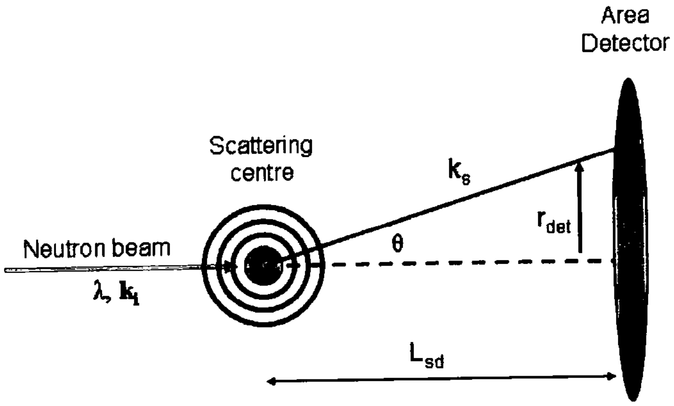

Figure 2.8 Geometry of a SANS experiment.

Figure 2.8 shows the geometry of the SANS experiment. Neutrons with wavelength λ are scattered spherically from the nuclei, the scattered neutrons emanate from the sample with equal intensity in all directions so the scattering centres can be considered point scatterers. A fraction of the neutrons scattered through an angle θ are recorded on the area detector. L_{sd} is the distance from the sample to the detector. $\boldsymbol{k}_s$ is the scattered wavevector and $\boldsymbol{k}_i$ is the incident wavevector. The scattering vector $\boldsymbol{Q}$ describes the relationship between $\boldsymbol{k}_s$ and $\boldsymbol{k}_i$. The modulus of $\boldsymbol{Q}$, Q, is the independent variable in a SANS experiment and has dimensions of (length)$^{-1}$ as shown by,

$$Q = |\mathbf{Q}| = |\mathbf{k}_s - \mathbf{k}_i| = \frac{4\pi n}{\lambda}\sin\left(\frac{\theta}{2}\right) \approx \frac{4\pi}{\lambda}\frac{r_{\det}}{L_{sd}} \qquad \text{Equation 2.12}$$

n, the neutron refractive index, can be taken to be unity for a SANS experiment; however under certain conditions such as in neutron reflectivity experiments this is not true. By substituting Equation 2.12 into the Bragg equation, relating spacing, d, with the scattering angle and wavelength,

$$\lambda = 2d\sin\frac{\theta}{2} \qquad \text{Equation 2.13}$$

the following important relation between lengthscales within the sample and the scattering vector, is obtained,

$$d = \frac{2\pi}{Q} \qquad \text{Equation 2.14}$$

The typical Q range available using SANS means that d is a polymer length scale. $(d\Sigma(Q)\ /d\Omega)$ is the dependent variable (units of length^{-1}) measured in a SANS experiment. The detector measures the number of neutrons of a given wavelength, scattered through a particular angle, that arrive on an area of the detector in unit time. This flux of neutrons is expressed as $I(Q)$,

$$I(Q) = I_0(\lambda)\Delta\Omega\eta_d(\lambda)I_T(\lambda)V_s\frac{\partial\Sigma}{\partial\Omega}(Q) \qquad \text{Equation 2.15}$$

$\Delta\Omega$ is the solid angle element defined by the size of a detector pixel, η_d is the detector efficiency, I_T is the transmission of the sample and V_s is the volume of the sample exposed to the beam. $(d\Sigma(Q)/d\Omega)$ contains information on the size, shape and interactions between scattering centres in the sample as described by.

$$\frac{\partial\Sigma}{\partial\Omega}(Q) = N_{conc}V^2(\Delta\rho)^2 P(Q)S(Q) + B$$ Equation 2.16

N_{conc} is the number concentration of scattering centres with an individual volume V and B is the background signal. ρ is the neutron scattering length density of a molecule and depends on the number density $n_{d,i}$ of the atomic species i and b_i the coherent scattering length which describes the interaction between the neutron and the atomic nucleus i. $\Delta\rho$ is the difference between scattering length densities for components in the blend. The large difference in b for ^{1}H and ^{2}H, as shown in Table 2.1, is very important to polymer studies, as isotopic labelling of polymer components allows a strong contrast between polymers of interest.

$$\rho = \sum_i n_{d,i} b_i$$ Equation 2.17

Nucleus	b/10^{-15}m
^{1}H	-3.741
^{2}H	+6.671
O	+5.803
C	+6.646
Si	+4.153

Table 2.1 Coherent scattering lengths *b* for selected nuclei

P(Q) is a dimensionless function called the form factor, which describes how *(dΣ(Q)/dΩ)* is modulated by interference effects between neutrons scattered by different parts of the same scattering centre. For example, The form factor is dependent on both the size and shape of the scattering centre. As many particle sizes are present in a sample the form factor is convoluted with a particle size distribution. A homogeneous sphere of radius R is described by,[30]

$$P(Q) = \left[\frac{3(\sin(QR) - QR\cos(QR))}{(QR)^3} \right]^2$$ Equation 2.18

and a Gaussian distribution of segment density about a centre of mass characterised by the radius of gyration R_g is described by,[30]

$$P(Q) = \frac{2\left(\exp\left(-Q^2 R_g^2\right) + Q^2 R_g^2 - 1\right)}{\left(Q^2 R_g^2\right)^2}$$ Equation 2.19

S(Q) is another dimensionless function called the structure factor, which describes how *(dΣ(Q) /dΩ)* is modulated by different scattering centres in the sample. It is dependent on the amount of local order and interaction potential between scattering centres,

$$S(Q) = 1 + \frac{4\pi N}{QV} \int_0^{\infty} [g(r) - 1] r \sin(Qr) dr$$ Equation 2.20

where *g(r)* is a density distribution function related to the radial distribution function, typically a damped oscillatory function whose maxima corresponds to the distance r of the nearest neighbour co-ordination shell. If *P(Q)* is invariant with concentration *S(Q)* can be found by measuring *(dΣ(Q) /dΩ)* at two different concentrations.

2.5.1 LOQ

Reactor sources of neutrons produce a neutron flux that does not change with time and thus the wide range of neutron wavelengths available is monochromated to a single wavelength. The Q range for an experiment using such a fixed wavelength source is expanded by altering the distance of the sample to the detector L_{sd}. The velocity of a neutron is related to the distance travelled L_{sd}, and time taken t. The neutron wavelength λ can be related by the mass of the neutron m_n and Planck constant, h.

$$v_n = \frac{L_{sd}}{t} \qquad \lambda = \frac{h}{m_n v_n}$$ Equation 2.21

Pulsed sources of neutrons, where a variety of neutron wavelengths are produced, utilise fixed geometry experiments and can use time of flight methods to measure the time taken for neutrons to travel a set distance.

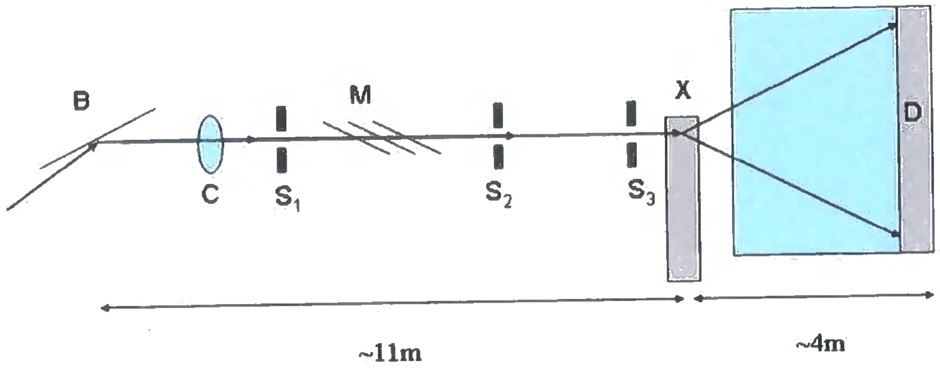

Figure 2.9 Schematic diagram of LOQ

LOQ is a fixed geometry neutron scattering instrument at the UK pulsed spallation source; ISIS. The available Q range on LOQ is 0.006 Å^{-1} to 0.22 Å^{-1}, limited at high Q by the size of the detector and at lower Q by the size of the beam stop. A Soller bending mirror (**B**) deflects all but the shortest wavelength neutrons. The LOQ disc chopper (**C**) operates at 25Hz, selecting alternate pulses of neutrons from the target, providing a useful wavelength range of 2.0-9.8 Å. The neutron beam is collimated by three apertures (**S_1, S_2, S_3**) to a beam size of 11mm in diameter. The beam passes through low efficiency detectors (monitors) that allow the rate at which neutrons reach the sample to be measured. Integrated count can be used to put data on a per neutron basis. Longer wavelengths (13.7 Å), which would interfere with neutrons from preceeding pulses are removed using overlap mirrors (**M**). The sample mount (**X**) is in ambient conditions and can be fitted with a temperature controlled multiple sample rack. Scattered neutrons pass through a vacuum chamber to minimise scattering from air before reaching the detector (**D**). The ^{3}He-CF_4 filled area (64 cm x 64 cm) detector is arranged so that the direct beam falls on the middle of the area. The vacuum tank and detector are heavily shielded to reduce background radiation. The direct (transmitted) beam is blocked by a neutron absorbing beam stop.

2.6 Neutron reflectivity

Neutron reflection allows the composition variation with depth perpendicular to the surface to be measured. This information can be gained by ion beam analysis, X-ray reflectivity and light ellipsometry. However, X-ray reflection is sensitive to contrasts the electron density of molecules and light ellipsometry to the refractive index and this contrast is not available for all polymer bilayers. Ion beam analysis techniques have limited depth resolution compared to neutron reflectometry. Neutrons can penetrate a variety of materials allowing various sample environments to be utilised. No vacuum system is required so experiments can be carried out under atmospheric conditions.

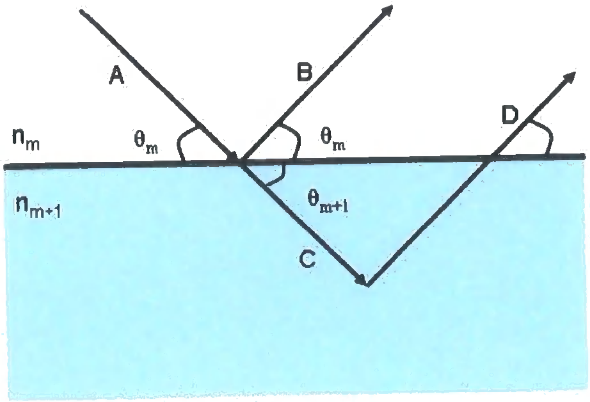

Figure 2.10 Diagram of incident neutron beam on a flat interface between two media, *j* and *m+1*, showing reflection, refraction and transmission.

The wave behaviour of neutrons allows an analogy with classical optics to be used to describe their reflection, refraction and interference. Like light, a beam of neutrons as shown in Figure 2.10, can reflect specularly (**B**), refract (**C**) and be transmitted through the material. The processes can be described by Snell's law,

$$n_m \cos\theta_m = n_{m+1} \cos\theta_{m+1}$$ Equation 2.22

$$\mathbf{n}_m = 1 - \frac{\lambda^2 N_d b}{2\pi} + \frac{i N_d \sigma_a}{4\pi}$$ Equation 2.23

where n_m is the neutron refractive index of medium m and is given by Equation 2.24. N_d is the atomic number density, λ is the neutron wavelength and b_i is defined in section 2.5. The coherent scattering lengths allow a contrast in neutron refractive index to be created by the presence of different elements or most advantageously by isotopic substitution of one element. As already noted the large difference in b_i for ^1H and ^2H in particular is useful in studying polymers where one species can be deuterated. In Equation 2.23 σ_a is the absorption cross section. For materials such as polymers, that do not contain the elements Li, B, Cd, Sm or Gd, the absorption cross section is effectively zero, ($\sigma_a \approx 0$), hence for most polymeric materials, Equation 2.23 becomes,

$$\mathbf{n}_j = 1 - \frac{\lambda^2 N_d b_m}{2\pi} = 1 - \frac{\lambda^2 \rho_m}{2\pi}$$ Equation 2.24

where ρ_m is the scattering length density; the product of the atomic number density and the coherent scattering length, b_m. At a critical angle θ_c the beam can refract and the reflectivity drops from unity. In a plot of $R(q)$ vs. θ, θ_c is called the critical edge and occurs at a wavelength given by the relationship

$$\theta_c \approx \lambda \sqrt{\left(\frac{N_d b}{\pi}\right)}$$ Equation 2.25

When $\theta_j < \theta_c$ total external reflection of the incident beam is observed, for $\theta_j > \theta_c$ refraction into the sample accompanies the external reflection. The ratio of incident to refracted beam intensity defines the transmissivity. The reflectivity is the ratio of reflected to incident beam intensity. The reflected beam contains parallel and perpendicular elements with relation to the surface. For the specular reflection of neutrons only the perpendicular component (z) contains information about the composition of the material. For the interface shown in Figure 2.10, between m and $m+1$, the perpendicular reflectivity $\boldsymbol{R}$ can be defined by the Fresnel reflection coefficient $r_{m,m+1}$,

$$\mathbf{R} = r_{m.m+1} r^*_{m.m+1}$$ Equation 2.26

and $r^*_{m,m+1}$ is the complex conjugate of $r_{m,m+1}$.

$$r_{m,m+1} = \frac{n_m \sin\theta - n_{m+1}\sin\theta_{m+1}}{n_m \sin\theta + n_{m+1}\sin\theta_{m+1}}$$ Equation 2.27

For most materials there is no complex component, so Equation 2.26 simplifies to

$$\mathbf{R} = r^2_{m,m+1}$$ Equation 2.28

As with SANS neutron momentum transfer ***q*** is related to the wavelength and incident angle as,

$$\mathbf{q} = 2\mathbf{k} = \frac{4\pi}{\lambda}\sin\theta$$ Equation 2.29

$r_{m,m+1}$ and hence ***R*** can be defined in terms of q_{zm} the momentum transfer normal to the surface,

$$q_{z,i} = 2\sqrt{\left(\frac{q_z^2}{4} - \frac{q_c^2}{4}\right)}$$ Equation 2.30

where q_z is the z component of the wavevector ***q***, and q_c is the critical value, above which refraction occurs. Hence,

$$r_{m,m+1} = \left(\frac{q_{zm} - q_{zm+1}}{q_{zm} + q_{zm+1}}\right).$$ Equation 2.31

The reflectivity due to a sharp interface as a function of q_z is thus given by the Fresnel reflectivity,

$$R(q_z) = \left[\frac{1-\sqrt{\left[1-\left(\frac{q_c}{q_z}\right)^2\right]}}{1+\sqrt{\left[1-\left(\frac{q_c}{q_z}\right)^2\right]}} \right]^2$$ Equation 2.32

Most systems of interest cannot be described as two discrete layers; hence it is necessary to consider the consequences of more complex arrangements. Figure 2.11 shows a sample with *m* discrete layers, where *m+1* is the substrate and layer 0 is the medium that surrounds the sample, e.g. air. The reflection coefficient for reflection at the substrate is given by Equation 2.27.

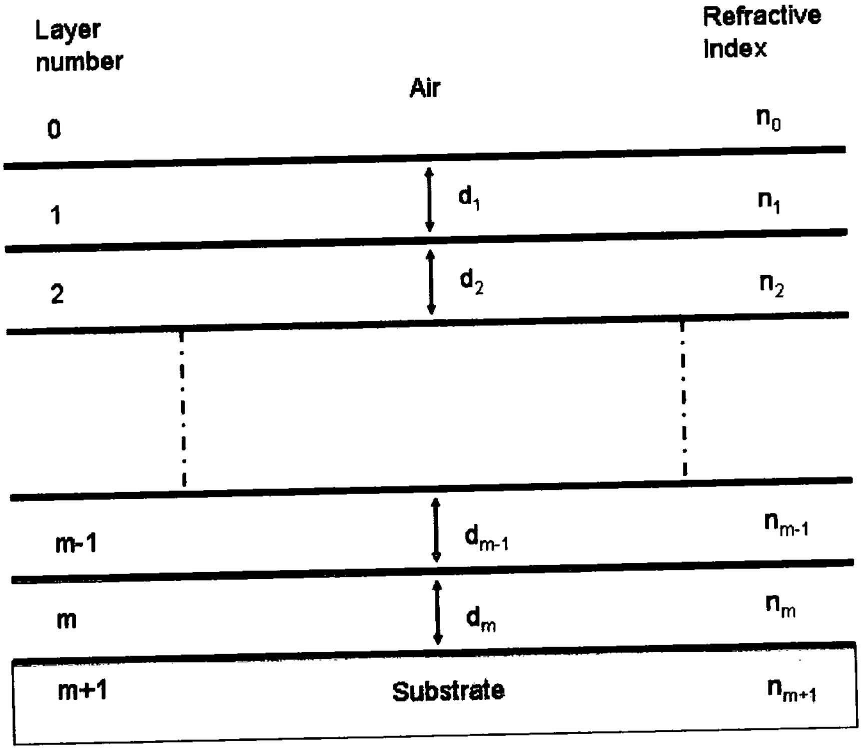

Figure 2.11 Diagram to show two layers divided into discrete layers for calculation of reflectivity[31].

The reflection coefficient $r'_{m-1,m}$ between the m^{th} and m-1^{th} layer should contain internal reflections (denoted by the prime) as shown by Figure 2.12 between the *m-1* ,*m*, *m+1*interfaces,

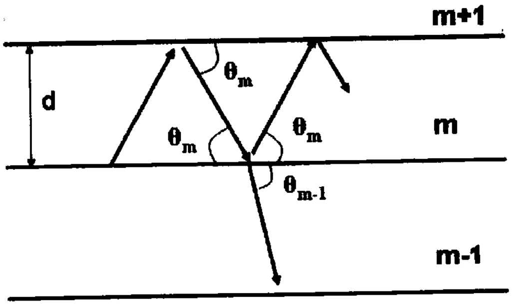

Figure 2.12 Diagram to show internal reflections within a sample.

$$r'_{m-1,m} = \frac{r_{m-1,m} - r_{m,m+1}e^{2i\beta_m}}{1 + r_{m-1,m}r_{m,m+1}e^{2i\beta_m}}$$ Equation 2.33

where β_m is a phase factor,

$$\beta_m = \left(\frac{2\pi}{\lambda}\right)n_m d_m \sin\theta$$ Equation 2.34

The phase factor introduces a path length d_m as shown in Figure 2.11 and the refractive index n_m of a given discrete layer. When the neutron wavelength or angle satisfies the Bragg equation constructive interference occurs and maxima and minima are characteristic of the layer thickness occur. Hence,

$$d_i = \frac{2\pi}{\Delta q_i}$$ Equation 2.35

where Δq_i is the difference between successive high frequency fringes are from thicker layers and at low frequencies from thin layers. The reflectivity is proportional to the sum of the squares of the reflectances at each interface, where reflectance is proportional to scattering length density, ρ_i, as defined in Equation 2.24,

$$Rq_z^4 = 16\pi^2 \sum_{ij} \left(\rho_i^2 - \rho_j^2\right)$$ Equation 2.36

Calculating reflectivity in this way is exact but mathematically cumbersome. A characteristic matrix for each discrete layer,[32] can be constructed,

$$c_m = \begin{bmatrix} \cos\beta_m & -\left(\frac{i}{\kappa_m}\right)\sin\beta_m \\ -i\kappa_m \sin\beta_m & \cos\beta_m \end{bmatrix}$$ Equation 2.37

where ($\kappa_m = n_m \sin\theta_m$). An overall sample matrix, M, is the product of all c_m

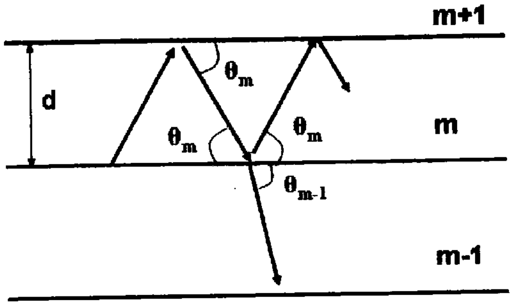

Figure 2.12 Diagram to show internal reflections within a sample.

$$r'_{m-1,m} = \frac{r_{m-1,m} - r_{m,m+1}e^{2i\beta_m}}{1 + r_{m-1,m}r_{m,m+1}e^{2i\beta_m}}$$ Equation 2.33

where β_m is a phase factor,

$$\beta_m = \left(\frac{2\pi}{\lambda}\right) n_m d_m \sin\theta$$ Equation 2.34

The phase factor introduces a path length d_m as shown in Figure 2.11 and the refractive index n_m of a given discrete layer. When the neutron wavelength or angle satisfies the Bragg equation constructive interference occurs and maxima and minima are characteristic of the layer thickness occur. Hence,

$$d_i = \frac{2\pi}{\Delta q_i}$$ Equation 2.35

where Δq_i is the difference between successive high frequency fringes are from thicker layers and at low frequencies from thin layers. The reflectivity is proportional to the sum of the squares of the reflectances at each interface, where reflectance is proportional to scattering length density, ρ_i, as defined in Equation 2.24,

$$Rq_z^4 = 16\pi^2 \sum_{ij} \left(\rho_i^2 - \rho_j^2\right)$$ Equation 2.36

Calculating reflectivity in this way is exact but mathematically cumbersome. A characteristic matrix for each discrete layer,[32] can be constructed,

$$c_m = \begin{bmatrix} \cos\beta_m & -\left(\frac{i}{\kappa_m}\right)\sin\beta_m \\ -i\kappa_m \sin\beta_m & \cos\beta_m \end{bmatrix}$$ Equation 2.37

where ($\kappa_m = n_m \sin\theta_m$). An overall sample matrix, M, is the product of all c_m

$$M = \prod_{m=0}^{m} c_m = \begin{bmatrix} M_{11} & M_{12} \\ M_{21} & M_{22} \end{bmatrix}$$ Equation 2.38

The reflectivity for the sample is then given by,

$$R = \left| \frac{(M_{11} + M_{12}\kappa_{m+1})\kappa_0 - (M_{21} + M_{22})\kappa_{m+1}}{(M_{11} + M_{12}\kappa_{m+1})\kappa_0 + (M_{21} + M_{22})\kappa_{m+1}} \right|^2$$ Equation 2.39

2.6.1 SURF

Neutron reflectivity can be measured as a function of θ and λ. The fixed geometry instrument SURF at the ISIS pulsed neutron source at the Rutherford-Appleton Labs, allows reflectivity to be measured for several fixed geometries over a range of incident neutron wavelengths[33].

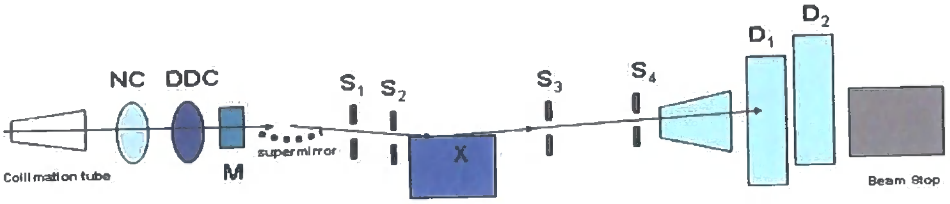

Figure 2.13 Schematic illustration of SURF. Side elevation.

Neutrons from the hydrogen moderator pass down a neutron shielded collimation tube, which defines the beam 1.5° to the horizontal. The nimonic chopper **(NC)** removes fast neutrons and gamma rays that occur at the start of each pulse from the source. A further double disc chopper **(DDC)** can select neutron wavelengths between 0.5 and 14Å and the beam passes through two rough collimation jaws. A supermirror focuses the beam on the sample position such that the illuminated length of the beam is reduced by a factor of 3 without loss of neutron intensity. To reduce background noise the supermirror is separated from the sample and detector by sheilding. Computer controlled cadmium/B_4C slits **(S_1, S_2, S_3, S_4)** are used for collimation before and after the sample. The beam monitor **(M)**, measures the incident beam flux used to ensure useable neutrons reach the sample. The samples sit on a moving sample holder **(X)**, whose height, angle and lateral position can be controlled by computer. Neutrons are then reflected from the sample and pass through further slits and the funnel before reaching the detector. The funnel reduces the level of background radiation reaching the detector. Both the detector and the funnel are coated in boron impregnated resin, a strong absorber of neutrons. Two detectors are available; a single shielded He_3 gas detector for specular reflection (**D_1**), and a two dimensional area detector for off specular reflection (**D_2**).

2.7 *DMA and DSC*

2.7.1 DMA

Dynamic Mechanical Analysis (DMA) measures the properties of materials while they are subjected to periodic stress, usually applied sinusoidally. Stress σ is the force (F) applied per unit area A and an applied stress will cause a deformation measured by strain ε,

$$\sigma = \frac{F}{A} \qquad \varepsilon = \frac{\Delta l}{l}$$ Equation 2.40

l is the original length and Δl is the change in length. An elastic material will obey Hooke's law,

$$E = \frac{\sigma}{\varepsilon}$$ Equation 2.41

where E is the tensile modulus. During a DMA experiment a low amplitude stress is applied so that the sample is within the linear region of it's stress-strain behaviour. For a perfectly elastic material the stress and strain are in phase and Equation 2.41 applies.

Under dynamic loading for a material exhibiting pure flow, the stress and strain are out of phase by 90° and stress is proportional to the rate of change of the strain. This allows viscosity η to be defined by the relation,

$$\sigma = \eta \frac{d\varepsilon}{dt}$$ Equation 2.42

Polymeric materials show both elasticity and flow, hence, 'viscoelasticity', where the stress and strain curves are out of phase by a value less than 90°. DMA applies a stress and measures the strain as well as the phase angle δ between them. The modulus can then be resolved into an in-phase storage component *(E')* and an out of phase loss component (E''). The damping factor, which is the ratio E''/E' or loss tangent ($\tan\delta$), is the amount of energy dissipated as heat during the loading/unloading cycle exerted on the sample by the DMA. As illustrated in Figure 2.14.

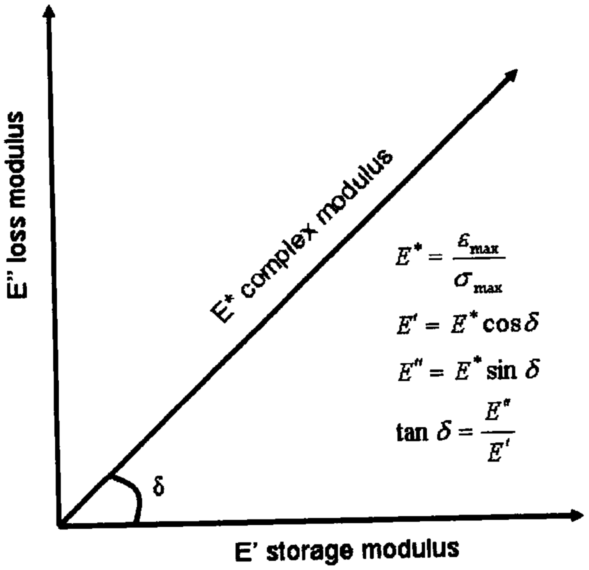

Figure 2.14 Schematic of relationship between loss and storage modulus

During a DMA experiment stress is applied to the sample using a force motor, while the resulting strain is measured by a position transducer. Figure 2.15 shows a schematic of a DMA curve for a typical amorphous polymer. A drop in loss modulus E'' (B) and a peak in *tan δ* (A) indicates the glass transition T_g. Once the material begins to flow, mechanical integrity is lost and the response signal drops away. The local motions of polymers in the glassy state; the alpha, beta and gamma transitions (C) can occasionally be observed below the glass transition temperature.

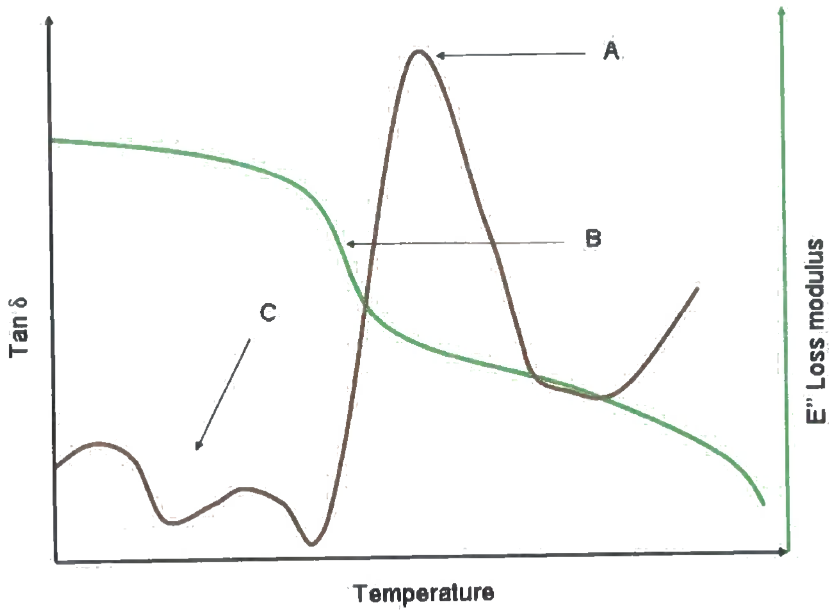

Figure 2.15 Schematic of typical DMA curve measured at 1Hz for a polymer sample.

Some investigators[34] use the loss tangent (*tan δ*) peak and others use the loss modulus (E'') peak or the elastic modulus (E') decrease onset to define T_g. DMA measurements are inherently frequency dependent and peak temperatures increase 6-8°C for every decade increase in test frequency.

A curve of logarithmn of modulus against time and temperature provides useful information about the movement of polymers. The practical time scale for most stress-relaxation measurements range from 10^1 to 10^6 s, but a wider time range is often desirable. For viscoelastic materials, processes with different time scales can be accessed by varying temperature. A composite isothermal curve covering the required extensive time scale can be constructed from data at different temperatures. This is accomplished by translation of the curves from small time scales along *log t* until they are superimposed to form a large composite curve. An arbitrary temperature T_0 is chosen to serve as a reference, as the values of the relaxation modulus $E_r(t)$ have been measured at widely different temperatures, they are corrected to $[E_r(t)]_{red}$, for changes in the sample density with temperature to give a reduced modulus, where $\rho_{d,0}$ and ρ_d are the polymer densities at T_0 and T respectively,

$$[E_r(t)]_{red} = \left(\frac{T_0 \rho_{d,0}}{T_\rho}\right) E_r(t)$$ Equation 2.43

Each curve of reduced modulus is shifted with respect to the curve at T_0 until all fit to form one master curve. The curve at each temperature is shifted by,

$$(\log t - \log t_0) = \log\left(\frac{t}{t_0}\right) = \log a_T$$ Equation 2.44

a_T is the shift factor and is a function of temperature only, it decreases with increasing temperatures and by definition is unity at T_0. The shift factor has been defined as the ratio of relaxation times at temperatures, T and T_0 and is related to the viscosities η and η_0 by,

$$a_T = \frac{\tau}{\tau_0} = \left(\frac{\eta}{\eta_0}\right)\left(\frac{T_0 \rho_0}{T \rho}\right)$$ Equation 2.45

If the temperature dependence of the viscosity obeys the Arrenhius equation, a_T can be expressed in an exponential form,

$$a_T = \exp b_1 \left(\frac{1}{T} - \frac{1}{T_0}\right)$$ Equation 2.46

where b_1 is a constant. The variation of polymer free volume with T alters after the glass transition temperature, this process is not included in the behaviour of Equation 2.46 but is accounted for in the WLF equation,

$$\log_{10} a_T = \frac{-C_1(T - T_g)}{C_2 + (T - T_g)}$$ Equation 2.47

where C_1, C_2 are constants that can be found experimentally.

2.7.2 Differential Scanning Calorimetry

The operation of a differential scanning calorimeter (DSC) is based on the measurement of the thermal response of an unknown specimen as compared with a standard when the two are heated uniformly at a constant rate. When a polymer undergoes a chemical and physical change, a change in enthalpy can be observed. In DSC a sample is placed in a pan on a heating block alongside a reference sample, often just an empty pan. Both samples are heated, the computer ensures that the polymer sample is heated at the same rate as the reference sample, the difference in electrical energy needed to allow the polymer sample to be heated at the same rate is measured. The DSC scans obtained show the amount of electrical energy supplied to the system as a function of temperature, so areas under the peaks are proportional to the change in enthalpy. It is preferable to record both heating and cooling curves and to optimise the rate of heating.

A change in heat capacity is associated with the glass transition temperature, hence there will be a noticeable change in change in heat flow at the glass transition temperature. The mid-point of this transition typically defines the glass transition temperature. The crystallization temperature for certain polymers can be found from the exothermic peak at that temperature. The melting temperature can also be found from the endothermic peak at the latent heat for melting T_m. Decomposition and cross linking can also be analysed using a DSC trace.

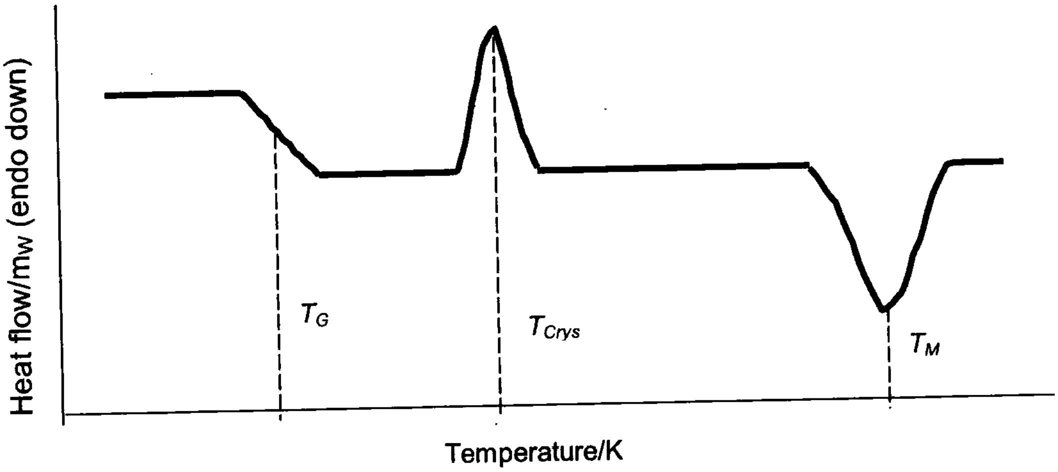

Figure 2.16 Illustration of a DSC trace. Showing T_g (glass transition) T_{crys} (crystallisation temperature) and T_m (melting temperature)

In general T_{gDMA} defined by the *tan δ* peak are reported to be 10-30°C higher than T_{gDSC}. It has been proposed that the average of the two peaks, (*tan δ* and E'') measured at 1 rad/s defines the same T_g as measured by DSC[35]. It has also been proposed that for several polymeric samples when the DMA response is measured at 1Hz, $T_{gDSC} \approx T_{gE'}$.

2.8 Atomic Force Microscopy (AFM)

Atomic force microscopy (AFM) is an imaging technique that allows the surfaces of samples to be measured and analysed. A sharp tip is scanned over a surface with feedback mechanisms that enable the piezo-electric scanners to maintain the tip at a constant force (to obtain height information), or height (to obtain force information). Tips are made of silicon nitride and are extended down from the end of a cantilever. The Nanoscope IV AFM head employs an optical detection system in which the tip is attached to the underside of a reflective cantilever. A laser is focused onto the back of a reflective cantilever. As the tip scans the surface of the sample, moving up and down with the contour of the surface, the laser beam is deflected off the attached cantilever into a dual element photodiode. The photodetector measures the difference in light intensities between the upper and lower photodetectors, and then converts to voltage. Feedback from the photodiode difference signal, through software control from the computer, enables the tip to maintain either a constant force or constant height above the sample. To ensure accurate results a vibration isolation platform is needed and the tip is brought close to the sample with the aid of a microscope.

Several modes are available for imaging the surface of a sample. Although forces used in AFM are extremely small, approximately nanonewtons, different modes can damage some samples. Contact mode imaging, where the tip is pulled along the surface is heavily influenced by frictional and adhesive forces. Tapping mode AFM, where the tip oscillates gently across the surface was developed as a method to achieve high resolution without inducing destructive frictional forces both in air and on very soft and fragile samples.

2.9 Transmission Electron Microscopy

Transmission electron microscopy (TEM) works in a similar fashion to an optical microscope, utilising an electron beam instead of light. The monochromatic electrons are focussed using metal apertures and magnetic lenses. The electrons then pass through the sample and are affected by the structure and objects in the sample. The transmitted beam is then projected on to a screen (photographic film or fluorescent screen). Staining can improve resolution and enhance structural detail; compounds of heavy metals such as ruthenium can be selectively deposited within the sample. The high electron densities of these heavy metals interact strongly with the electron beam, providing contrast in the transmitted image.

2.10 References

(1) L'Ecuyer, J.; Brassard, C.; Cardinal, C. *Nucl. Instrum. Methods* **1978**, *111*.

(2) Coyle, B. L.; Peercy, P. S. *Appl. Phys. Lett.* **1979**, *34*.

(3) Genzer, J.; Rothman, J. B.; Composto, R. J. *Nucl. Instr. And Methods in Phys. Res. B* **1994**, *86*.

(4) Turos, A.; Meyer, O. *Nucl. instrum. Methods* **1984**, *92*.

(5) Doyle, B. L.; Peercy, P. S. *Appl. Phys. Lett.*, *34*, 811.

(6) Mills, P. J.; Palmstrom, C. J.; Mayer, J. W. *J. Mater. Sci* **1986**, *21*.

(7) Green, P. F.; Palmstrom, C. J.; Mayer, J. W.; Kramer, E. J. *Polymer* **1986**, *27*.

(8) Green, P. F.; Palmstrom, J. W.; Kramer, E. J. *Macromolecules* **1985**, *18*.

(9) Mills, P. J.; Green, P. F.; Palmstrom, C. J.; Mayer, J. W.; Kramer, E. J. *Polym. Sci. Part B Polym. Phys* **1986**, *24*.

(10) Kramer, E. J. *Physica. B* **1991**, *173*.

(11) Davies, J. A. *Mrs Bulletin* **1992**, *17*, 26-29.

(12) Composto, R. J.; Walters, R. M.; Genzer, J. *Materials Science & Engineering R-Reports* **2002**, *38*, 107-180.

(13) J.F.Ziegler, J. P. B., U. Littmark, *The Stopping Powers and Ranges of Ions in Solids*; Pergamon Press, 1975.

(14) In *Handbook of Modern Ion Beam Materials Analysis*; Nastasi, M., Ed.; Materials Research Society: Pittsburgh, 1995.

(15) Wallace, W. E.; Rothman, J. B.; Composto, R. J. *Journal of Applied Physics* **1994**, *75*, 2312-2316.

(16) Wallace, W. E.; Rothman, J. B.; Composto, R. J. *Nuclear Instruments & Methods in Physics Research Section B- Beam Interactions with Materials and Atoms* **1994**, *84*, 1-4.

(17) Green, P. F.; Doyle, B. L. In *New Characterization Techniques for Thin Polymer Films*; Nguyen, L. T., Ed.; Wiley: New York, 1990.

(18) Payne, R. S.; Clough, A. S.; Murphy, P.; Mills, P. J. *Nucl. Instrum. Methods. In Phys. Res. B* **1989**, *42*, 130.

(19) Steiner, U.; Klein, J.; Fetters, L. J. *Physical Review Letters* **1994**, *72*, 1498-1501.

(20) Geoghegan, M. In *Polymer Surfaces and Interfaces III*; Peace, S. K., Ed.; Wiley, 1999.

(21) Chaturvedi, U. K.; Steiner, U.; Zak, O.; Krausch, G.; Schatz, G.; Klein, J. *Applied Physics Letters* **1990**, *56*, 1228-1230.

(22) Kramer, E. J. *Physica B* **1991**, *173*, 189-198.

(23) Szilagyi, E.; Paszti, F.; Amsel, G. *Nuclear Instruments & Methods in Physics Research Section B- Beam Interactions with Materials and Atoms* **1995**, *100*, 103-121.

(24) Nagata, S.; Yamaguchi, S.; Fujino, Y.; Hori, Y.; Sugiyama, N.; Kamada, K. *Nuclear Instruments & Methods in Physics Research Section B- Beam Interactions with Materials and Atoms* **1985**, *6*, 533-537.

(25) Sigmund, P.; Winterbon, K. B. *Nuclear Instruments & Methods in Physics Research Section B- Beam Interactions with Materials and Atoms* **1975**, *119*, 541.

(26) Bohr, N. *K Dan Vidensk Selsk* **1948**, *18*, 8.

(27) Turos, A.; Meyer, O. *Nuclear Instruments & Methods in Physics Research Section B- Beam Interactions with Materials and Atoms* **1984**, *232*, 92-97.

(28) Gooda, P. H.; Gilboy, W. B. *Nuclear Instruments & Methods in Physics Research* **1987**, *A255*, 222.

(29) Kerle, T.; Scheffold, F.; Losch, A.; Steiner, U.; Schatz, G.; Klein, J. *Acta Polymerica* **1997**, *48*, 548-552.

(30) Roe, R.-J. *Methods of X-Ray and Neutron Scattering in Polymer Science*; 1st ed.; Oxford University Press, 2000.

(31) Bucknall, D. G.; Higgins, J. S. In *Polymers and Surfaces. A Versatile Combination*; Hommel, H., Ed.; Research Signpost, 1998.

(32) Heavens, O. S. *Optical properties of thin films*; Butterworth: London, 1955.

(33) Penfold, J.; Richardson, R. M.; Zarbakhsh, A.; Webster, J. R. P.; Bucknall, D. G.; Rennie, A. R.; Jones, R. A. L.; Cosgrove, T.; Thomas, R. K.; Higgins, J. S.; Fletcher, P. D. I.; Dickinson, E.; Roser, S. J.; McLure, I. A.; Hillman, A. R.; Richards, R. W.; Staples, E. J.; Burgess, A. N.; Simister, E. A.; White, J. W. *Journal of the Chemical Society-Faraday Transactions* **1997**, *93*, 3899-3917.

(34) Achorn, P. J.; Ferrillo, R. C. *Journal of Applied Polymer Science* **1994**, *54*, 2033-2043.

(35) Rieger, J. *Polymer Testing* **2001**, *20*, 199-204.

Chapter 3

Nuclear Reaction Analysis of thin DPEO films diffusing into PMMA

3.1 *Introduction and aims*

Ion beam analysis, as noted in chapter 2 can be used to measure polymer diffusion. The tracer diffusion of PEO into PMMA has not previously been studied. A method for calculating the tracer diffusion coefficient for PEO into PMMA, using ion beam analysis needs to be developed, to investigate the conflicting results of other probes of PEO and PMMA relaxations in the blend (section 1.6.2). This method can then be used investigate whether this diffusion can be related to the molecular weight of PEO and PMMA and the temperature at which the couples diffuse and thus comment on the accuracy of the fast and slow models for mutual diffusion between polymers. It may be possible to determine whether the diffusion mechanism of PEO and PMMA is influenced by the 'partial miscibility' of PMMA and PEO blends and consequently develop a suitable model for the movement of PEO and seek evidence of thermodynamic slowing down or acceleration. This requires refining ion beam experimental methods to suit the system, such as selecting beam energies, geometries and suitable bilayer dimensions. As DPEO is semi-crystalline, bilayers need to be checked for the degree of surface roughness and the impact this has on the data and how it needs to be considered. The relationship between interfacial width and times can then be discussed in terms of diffusion coefficients.

3.2 *Experimental refinement*

The deuteration of one component is considered to not influence the chemical behaviour of polymers and hence such blends can be considered to represent the diffusion of hydrogenous blends. The tacticity of PMMA has been found to influence miscibility and conformation in the blend.[1] The PMMA utilised here is mostly atactic. All PMMA samples were made by the same method so may be assumed to have a similar variation in tacticity, therefore displaying a similar miscibility variation with tacticity.

To allow for the measurement of tracer DPEO molecules into PMMA a comparatively thin layer of DPEO was placed on a PMMA substrate. Previous experiments[2], analysing polymer/polymer bilayers with nuclear reaction analysis have found the relation between depth resolution and the incident energy and geometry. The results are shown in Table 3.1, the angle *α*, is defined in section 2.4.1.

Depth/µm	E_0(MeV)	Angle α (°)	Resolution at depth (nm)	Resolution at surface (nm)
0.1	0.7	15	30	30
0.25	0.8	15	50	35
0.5	0.75	30	80	60
1	0.75	90	125	105
2	1	90	180	150
3	1.2	90	225	195
4	1.4	90	270	240
5	1.55	90	310	275
6	1.7	90	345	310
7	1.85	90	380	350
8	2	90	420	395

Table 3.1 Optimum values of ^{3}He beam energy (E_0) and sample geometry (relative to the incident beam) α when profiling to various depths.[2]

For a sample approximately 600 nm in depth an incident energy E_0=700 KeV, with a geometry where α =15°, is ideal. PMMA is known to be degraded by ion beams, especially when they are focussed onto a small area.[3] Beam damage was minimised by limiting total exposure to 2.5 μC charge and using a diffuse beam spot size of ~3mm^2 which still provides statistically significant data.

3.3 Experimental

3.3.1 Materials

The polymers utilised, along with their characteristics are shown in Table 3.2. More complete characterisation data are shown in Appendix I. All polymers are above their individual entanglement molecular weight (M_{ePMMA}=10000 gmol^{-1}and M_{ePEO}=1700 gmol^{-1}) [4]

Polymer	M_w/gmol^{-1}	M_n/ gmol^{-1}	M_w/ M_n	T_g/K	T_m/K
DPEO	77800	75400	1.03	215	330
DPEO	17300	16900	1.03	227	337
PMMA	16000	14800	1.08	408	
PMMA	213400	178000	1.2	404	

Table 3.2 Showing polymers and polymer properties as measured by GPC and DSC

3.3.2 Bilayer preparation

A thick film (approximately 900 nm) of PMMA was spun onto a silicon wafer from a toluene solution. PMMA films were then heated overnight at 413 K to relax the PMMA polymers to unperturbed dimensions. After cooling, a thin film of DPEO approximately 50 nm thick was spun directly onto the PMMA from a solution in methanol. Care was taken when handling samples to minimise contact with water and dust.

The thickness of the PMMA layer was measured using optical reflectometry. The thickness of the DPEO layer could not be measured directly with optical methods due to DPEO's semi-crystalline nature and resultant rough surface. The thickness of DPEO was measured using X-ray reflectometry. A layer was spun directly onto a silicon wafer and the depth was measured using a D-5000 reflectometer and layer thickness analysed using the software program (Win-Refsim* version 1.2) to fit the fringes. As the same spinning speed and solution concentration were used for bilayer preparation, the depth of the DPEO film could be assumed to be the same as that spun onto the PMMA layer. DPEO films were therefore considered to be 50-60 nm thick. Only approximate values for the film depths were needed; therefore the effect of spinning onto silicon instead of PMMA was considered to be minimal.

Coated silicon wafers were then broken up into smaller pieces and heated in a vacuum oven at different temperatures and for different times. Samples were checked for dewetting or damage using an optical microscope. Initially, the samples were annealed at temperatures above the glass transition temperature of both DPEO and PMMA. The fastest and the slowest diffusing combinations were analysed first, to ensure a reasonable heating time regime could be employed for further molecular weight combinations. The slowest and fastest combinations were assumed to be the bilayers comprising the two highest molecular weight (DPEO, M_w =77800 gmol^{-1} and PMMA, M_w =216000 gmol^{-1}) and the two lowest molecular weight (DPEO, M_w=17300 gmol^{-1} and PMMA, M_w =16000 gmol^{-1}) polymers. The bilayers were heated at 423 K and 443 K for times of approximately 10, 20, 40 and 60 minutes.

Homogeneous concentration profiles were found for all these anneal temperatures and times; showing that at these temperatures, DPEO molecules were able to diffuse throughout the film in 10 minutes. This was observed for both the largest molecular weight and smallest molecular weight combinations of DPEO and PMMA. The samples were annealed at a range of temperatures above the T_m of DPEO and below the T_g of PMMA; 373 K, 363 K, 353 K, 344 K, and at temperatures approximately the same as, and below, the T_m for DPEO; 338 K and 323 K. The samples were heated for a range of times for approximately 10, 20, 40, 80 and 160 minutes.

---

* Win-Refsim v.1.2 (AGFG, Bruker AXS GmbH)

3.3.3 NRA measurements

Bilayers of the same type were placed on the same sample racks. Samples were analysed using a 0.700MeV beam of ^{3}He ions. θ=70° and θ=60°and $\alpha\approx 30°$. Each sample was exposed to 2.5μC of charge on separate areas for each value of θ. The bulk of the sample was considered to be PMMA, hence the stopping powers found from SRIM® and consequently utilised in depth calculations were for PMMA alone.

3.3.4 Calculating diffused depth

Volume fraction with depth profiles were constructed using spreadsheets and experimental parameters as described in sections 2.4.5.1 and 2.4.5.2. A theoretical fit to depth profiles found experimentally was constructed by using a version of (Equation 1.18),

$$\varphi_A = \frac{1}{2}\left\{ erf\frac{h_0 - x}{w_{width}} + erf\frac{h_0 + x}{w_{width}} \right\} \qquad \text{Equation 3.1}$$

where x is the depth and interfacial width w_{width}, is related to the tracer diffusion coefficient by, $w_{width}=2\sqrt{(D^*t)}$. A FORTRAN program[†] was used to convolute Equation 3.1 with the Gaussian instrumental resolution function, the total width of the sample and the resolution. As all samples of the same bilayer construction were placed on the same sample rack in the end station, they were assumed to have the same resolution and the same original thickness of DPEO layer, h_0. Error fitting of non-annealed sample data was first used to find h_0 and the resolution, (w_{width} was assumed to be zero for no anneal time). The values for h_0 and resolution found were then fixed for the rest of the samples of the same bilayer. When the diffused thickness, w_{width} approached the limit of reasonable depth resolution width the data becomes difficult to analyse. Hence all thicknesses of w_{width} within 10% of the total thickness of the sample were ignored. Once the data was fitted and the values of w_{width} obtained, a plot of $w_{width}{}^2/4$ against time t results in a straight line with a gradient equal to D^*, the tracer diffusion coefficient for that molecular weight sample if the diffusion coefficient is independent of concentration.

[†] 'Errfit', using FITFUN. (R.Thompson, University of Durham)

3.4 Results

3.4.1 Sample Roughness

Roughness at the surface of a sample affects ion beam data and should manifest itself, in NRA spectra, as a tail towards higher energies for backscattered protons, a smooth sample giving a nearly symmetrical peak. The 'tail' causes a problem for analysis as it occupies the same region of the energy scale as the diffusing component. NRA spectra of unannealed DPEO/PMMA shows a characteristic tail for all depths and molecular weights of DPEO, as can be seen in Figure 3.3 and Figure 3.4.

The tails present could be due to either surface roughness, dewetting of the polymer surface or instantaneous diffusion of PEO and PMMA, either through compatibility or by solvent assisted diffusion from the sample preparation. DPEO is crystalline and may be expected to be 'rough', this roughness may vary with anneal time, as the concentration of DPEO is diluted or by the melting and quenching of the crystalline components. Dewetting is the process by which a thin film breaks up into droplets.[5] This can be due to the differences in surface tension between the thin film and substrate. These droplets can be visible to the naked eye or under a microscope. The droplets will have a characteristic volume related to the amount of polymer in the initial film layer. Examination of the bilayers with a microscope showed no sign of dewetting. Although diffusion at room temperature during sample preparation is possible, movement by the polymers would not be expected, as PMMA is below the T_g and PEO, although above its T_g is below its T_m. Solvents can assist diffusion, PMMA has been relaxed by heating, so should not contain any solvent and methanol used to spin coat DPEO is a very poor solvent for PMMA. Therefore the tail could be considered to be due to surface roughness.

It is reasonable to assume that surface roughness is probably due to the crystallisation of the pure DPEO. DPEO when spun from methanol crystallised and spherulites several millimetres across were observed on the surface. In order to assess the effect of sample roughness, the thickness distribution of the sample surface needs to be found. Atomic force microscopy (AFM) probes the surface of a sample and the surface morphology measured

3.4.2 Surface roughness experiment and NRA simulation

A small piece of each sample annealed or unannealled was cut off using a glass cutter, these were kept in sealed containers to minimize damage to the PEO surface from exposure to water. Samples were scanned using a Digital Instrument Nanoscope IV AFM. Sections were scanned using tapping mode. Very little difference was observed between contact and tapping mode results, although for consistency tapping mode was employed for all samples. Scan rates of 1.09-1.31 Hz were utilized and several 1μm^2 scans were typically selected from parts of 10μm^2 scans.

Scans were analysed using the Nanoscope IV version 5.12 analysis software. The 'Roughness' command generates a wide variety of statistics for surfaces (Figure 3.1). The analysis software allows statistics for both the entire image and a selected box area to be calculated. Large scans (>1μm^2) often exhibit bowing, due to the fact that the piezos responsible for scanning in the horizontal phase tilt the sample slightly. Prior to roughness analysis, this effect must be removed from the raw scan data using the 'flatten' command. The 'flatten' command calculates a second order plane fit for the individual scan lines which is then subtracted. Two values were recorded for scans of 1μm^2 and 10μm^2: $I_{mg}Rms$ and $I_{mg}Ra$. $I_{mg}Ra$ is the arithmetic average of the absolute values of the surface height deviations measured from the mean plane,

$$I_{mg}Ra = \frac{1}{n}\sum_{i=1}^{n}|Z_J| \qquad \text{Equation 3.2}$$

$I_{mg}Rms$ is the root mean square average of height deviations taken from the mean data plane, expressed as,

$$\sqrt{\frac{\sum Z_i^2}{n}} = I_{mg}\ Rms \qquad \text{Equation 3.3}$$

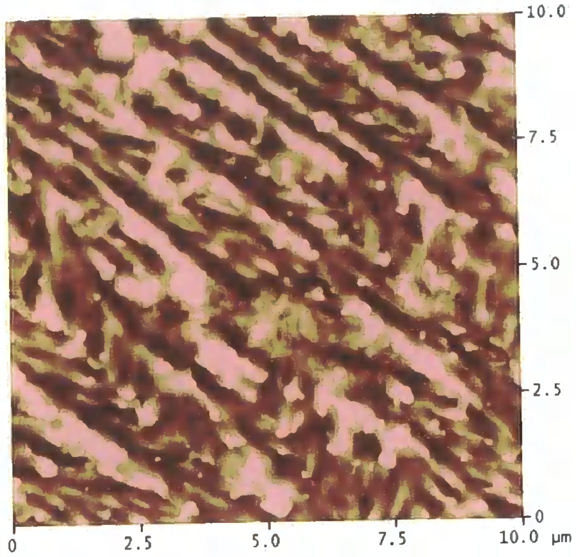

Figure 3.1 AFM scan of 10 µm^2 section of a bilayer of DPEO (50 nm) M_w= 17300 gmol^{-1} and PMMA (950 nm) M_w= 16000 gmol^{-1} unannealled.

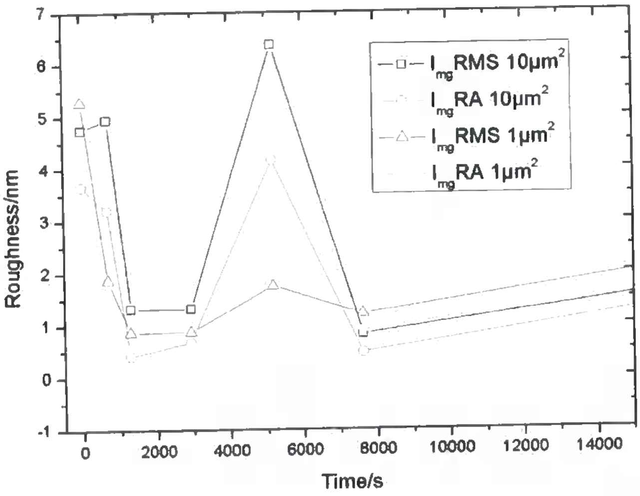

(A)

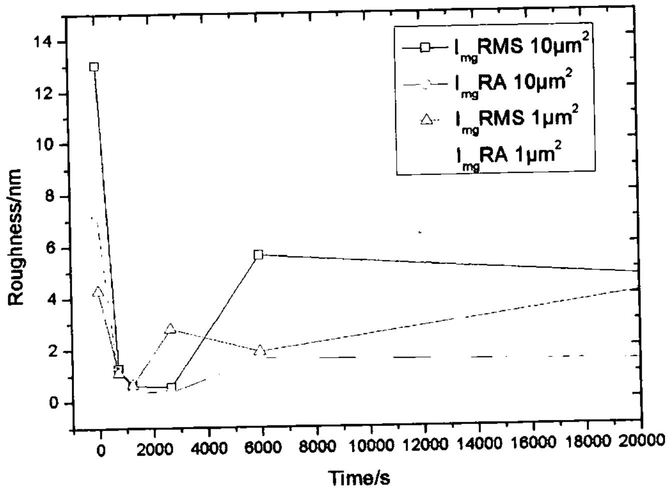

(B)

Figure 3.2 Plot of FWHM roughness against annealing time at 373 K for (A) ≈50 nm DPEO, M_w= 17300 gmol^{-1}, on ≈950 nm relaxed PMMA M_w=16000 gmol^{-1} and (B) ≈50 nm DPEO, M_w= 77800 gmol^{-1}, on ≈950 nm relaxed PMMA M_w=16000 gmol^{-1}

It has been well recorded that PEO dissolves in water and degradation in thin films can occur with exposure to moisture (breath or touch give noticeable changes in appearance visible to the naked eye). Therefore it is possible that changes in roughness visible with the AFM can be attributed to environmental factors as well as changes in PEO concentration at the surface. The rate of quenching molten polymers affects the crystallisation and hence the roughness. All samples when removed from the oven were placed on an aluminium block at ambient temperature in an attempt to give the same quenching conditions.

Figure 3.2 shows the variation in surface roughness values with time heated. In general the roughness decreased upon annealing, the increase in roughness at 5000s in Figure 3.3A, may not be present if further sections were analysed and averages taken. If surface roughness is only attributed to the crystallisation of DPEO, then the dilution of DPEO bulk to a thinner surface film by chains diffusing into PMMA should change the kinetics and therefore extent of DPEO crystalisation.[6] The presence of PMMA in the DPEO would also inhibit crystallisation[7] and therefore decrease surface roughness. Eventually the surface roughness decreases to a uniform value. This may be considered to be the suppression of crystallinity, possibly by dilution of DPEO by PMMA.

From Figure 3.2 it can be seen that the surface roughness was never more than approximately 10% of the initial DPEO depth. SIMNRA allows the roughness of a sample or the roughness of a substrate to be accounted for in an NRA spectrum.[8-11] Experimental data from the samples were compared to simulations built using; film depths as calculated from optical and X-ray techniques, film roughness values gained from AFM and known experimental parameters. Simulations with SIMNRA using the largest surface roughness simulations, with a thickness distribution the same size as the original DPEO film, allow the 'worst case scenario' to be analysed. This 'worst case scenario' fits the experimental unannealled data closest (Figure 3.3-3.4).

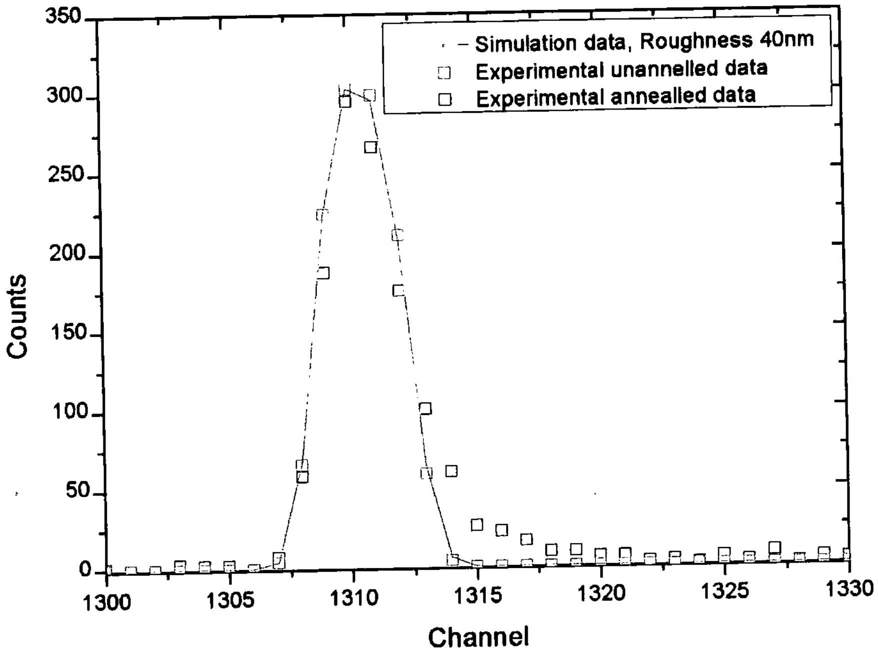

Figure 3.3 Simulated and experimental plots of a bilayer of DPEO (50 nm) M_w= 77800 gmol^{-1} and PMMA (950 nm) M_w= 213400 gmol^{-1} heated at 363 K.

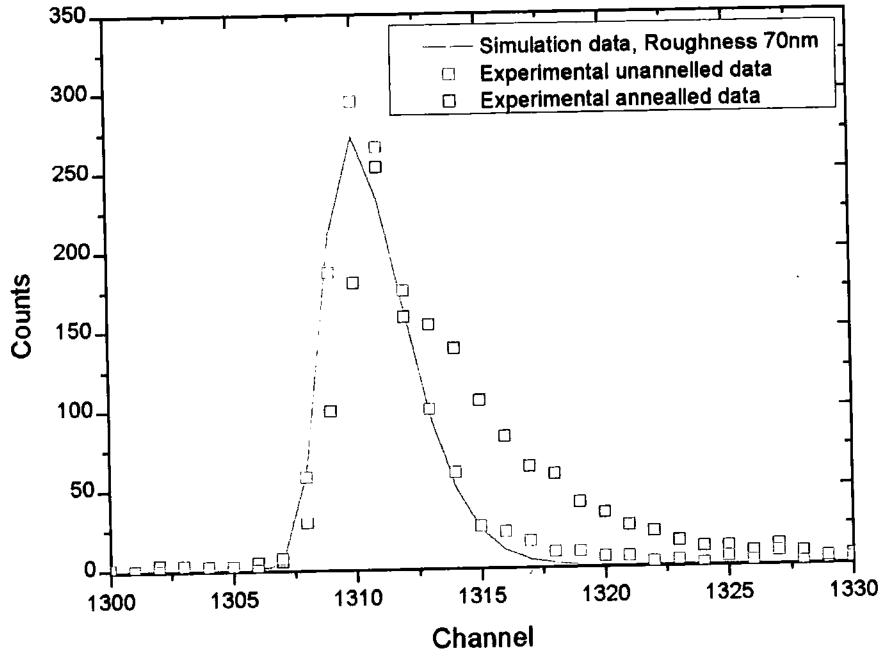

Figure 3.4 Simulated and experimental plots of. a bilayer of DPEO (50 nm) M_w=17300 gmol^{-1} and PMMA (950 nm) M_w= 16000 gmol^{-1} heated at 344 K

The surface roughness is an important factor in the shape of unannealed profiles and profiles after heating, but is not the major contribution to the 'tail' (channels >1313) that could indicate a statistical error in annealed samples. As the change in surface roughness is not predictable with increasing heating times and therefore PEO distribution, it cannot be continuously accounted for when looking at diffusion widths. Compared to the shape of diffused data, the surface roughness only accounts for a very small part of the diffused tail as shown in Figure 3.3 and Figure 3.4, and hence could be dismissed as being a similar source of error in calculating width to statistical noise.

3.4.3 Graphs of volume fraction against depth

Figure 3.5 and Figure 3.6 show typical depth profiles for the two bilayers analysed. The peak due to ^2H from DPEO decreases in volume fraction and diffuses to greater depths with time. The peak volume fraction should ideally be 1 for the unannealed sample. An artefact of normalisation means that this is not always true, however since interfacial width values are independent of the absolute volume fractions the results for w_{width} and the diffusion coefficient are unaffected by this artefact.

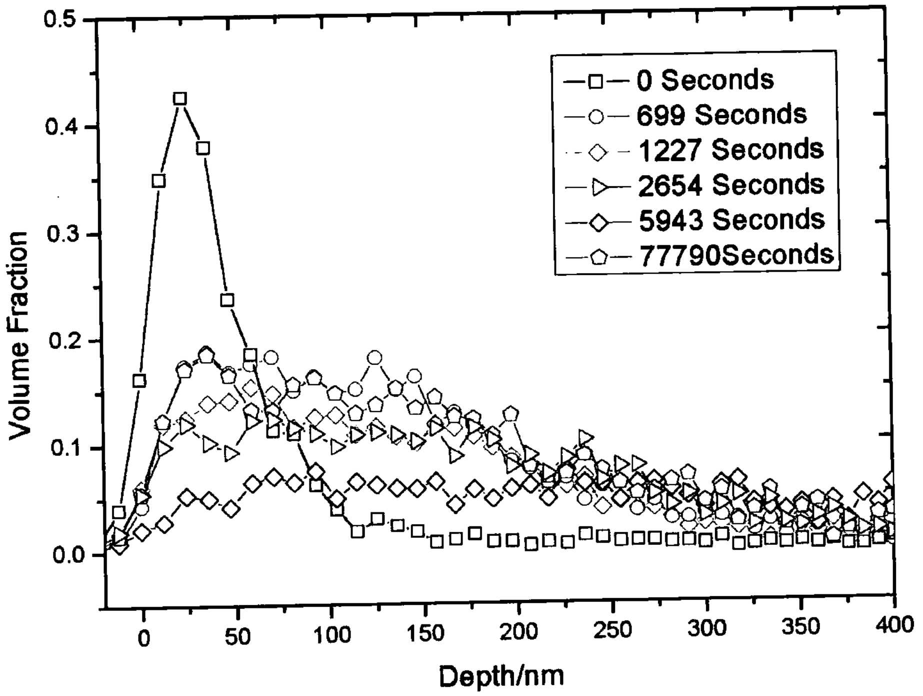

Figure 3.5 Depth profile of DPEO (50 nm) M_w= 17300 gmol^{-1} diffusing into PMMA (950 nm) M_w= 16000 gmol^{-1} heated at 373 K for various times.

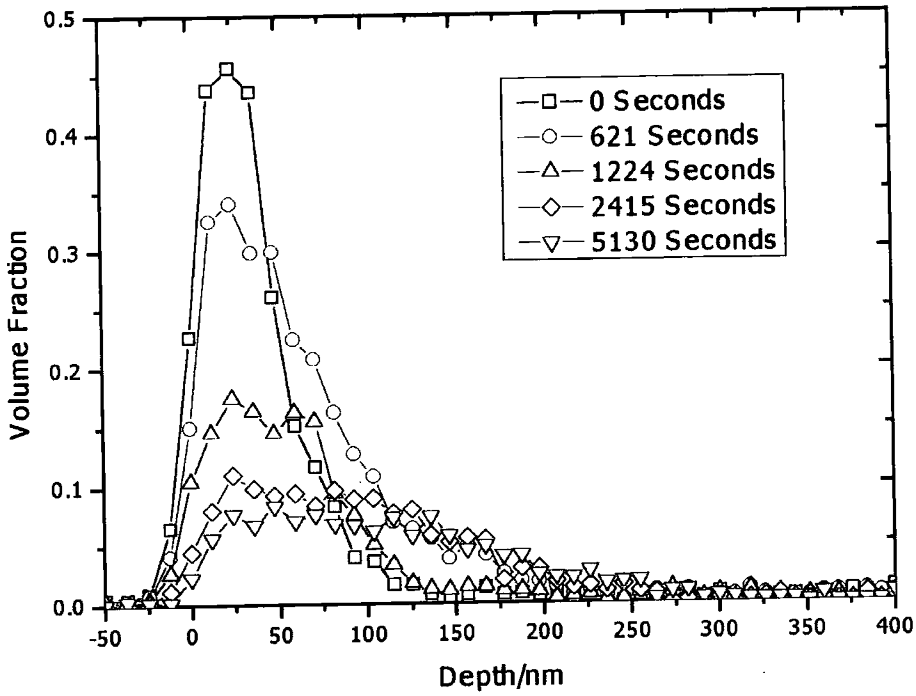

Figure 3.6 Depth profile of DPEO (50 nm) M_w= 77800 gmol^{-1} diffusing into PMMA (950 nm) M_w= 213400 gmol^{-1} heated at 353 K for various times.

An example of a fit using a FORTRAN program described in section 3.3.4 is shown in Figure 3.7. Fits were in general imperfect, with the model failing to account perfectly for a slight shoulder or bump next to the main Gaussian peak. Examples of good fits are shown in Figure 3.7 and Figure 3.8 for heated samples. Surface roughness could not account for the imperfect fits, as surface roughness decreases upon annealing.

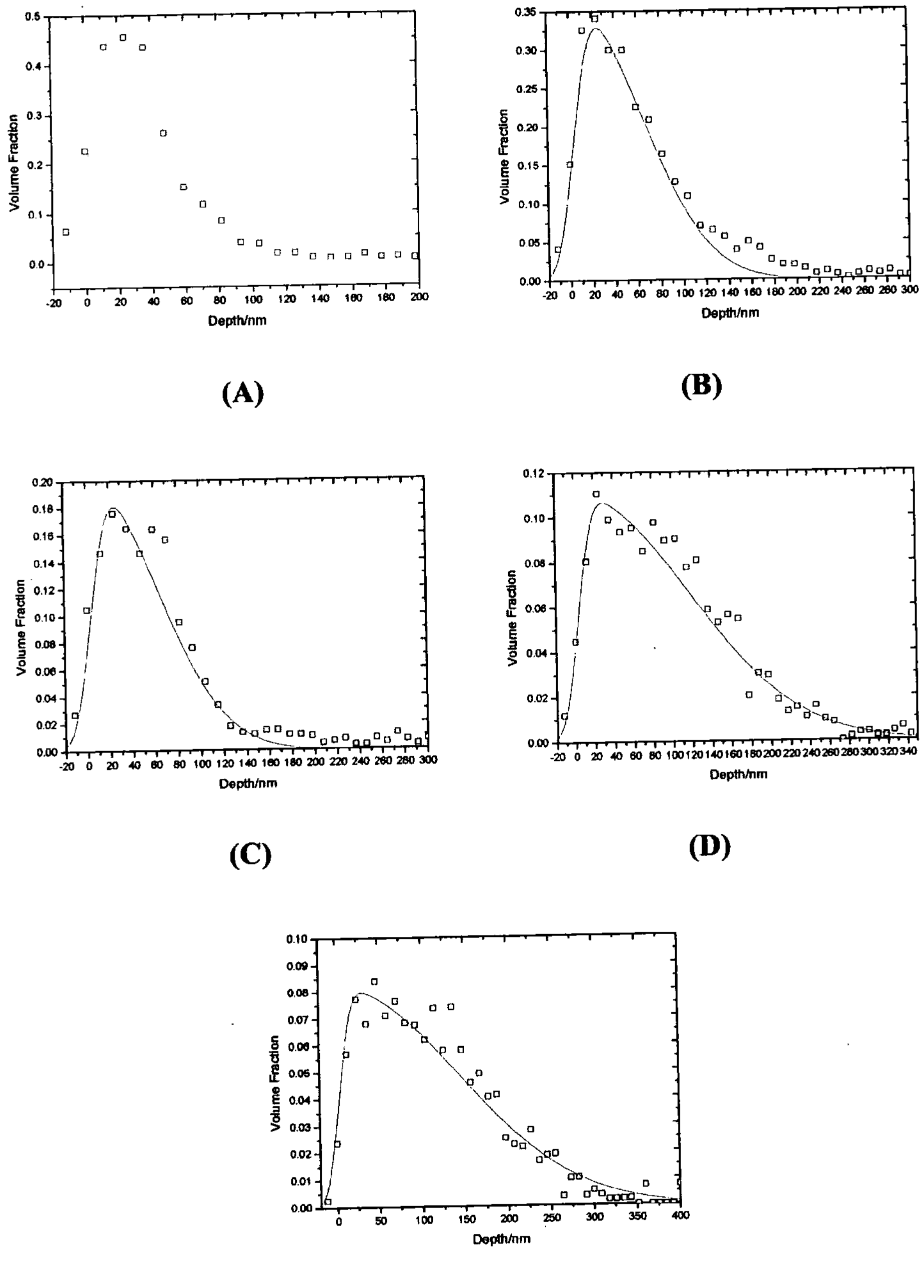

(A)

(B)

(C)

(D)

(E)

Figure 3.7 Depth profiles and fits of DPEO (50 nm) M_w= 77800 gmol^{-1} diffusing into PMMA (950 nm) M_w= 213400 gmol^{-1} heated at 353 K for various times: (A) 0 seconds, (B) 621 seconds, (C) 1224 seconds, (D) 2415 seconds and (E) 5130 seconds.

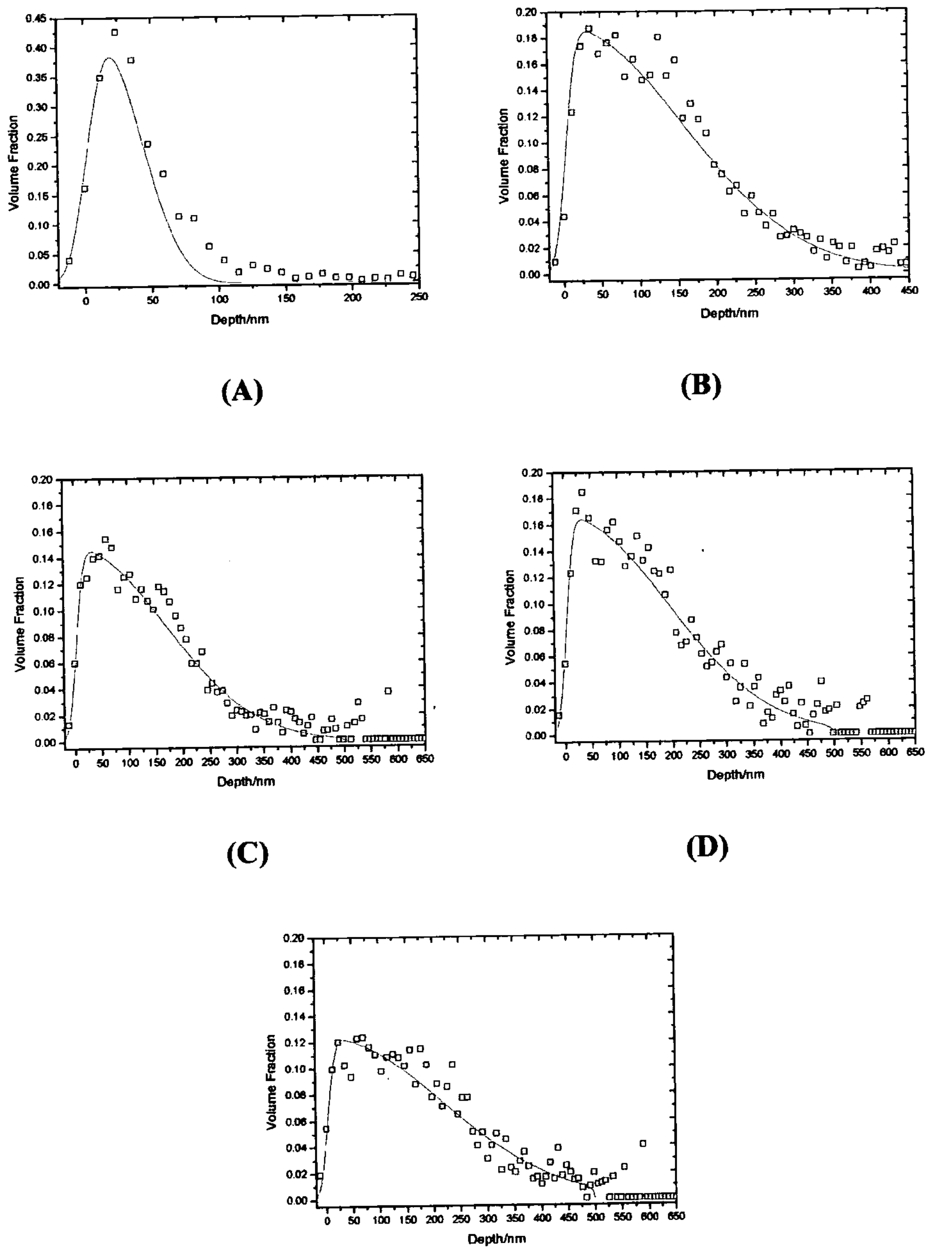

(A)

(B)

(C)

(D)

(E)

Figure 3.8 Depth profile of DPEO (50 nm) M_w= 17300 gmol^{-1} diffusing into PMMA (950 nm) M_w= 16000 gmol^{-1} heated at 373 K for various times: (A) 0 seconds, (B) 699 seconds, (C) 1227 seconds, (D) 2654 seconds and (E).5943 seconds

If $D*$ is independent of concentration and time, plots of $w_{width}^2/4$ against anneal time should produce straight lines with a gradient equivalent to the tracer diffusion coefficient of DPEO into PMMA. However, as shown in Figure 3.9 and Figure 3.10 the graphs did not produce straight lines, but rather curves. For both molecular weight combinations the higher temperatures produced steeper increases in $w_{width}^2/4$ with time and achieved a plateau in $w_{width}^2/4$ at later anneal times. Unsuprisingly, the diffusion processes were faster for higher temperatures. Measurement at 323 K showed no change in $w_{width}^2/4$ with time indicating that below the T_m of DPEO diffusion did not occur at times utilised for these experiments. Whilst at first this result may seem obvious, it is not necessarily the case since even below the melt temperature a reasonable fraction of the DPEO is in the amorphous liquid state, when $T > T_g$. For both 60° and 70° incident beam angles, NRA data provided similar results, although 60° results give better resolution at greater depths.

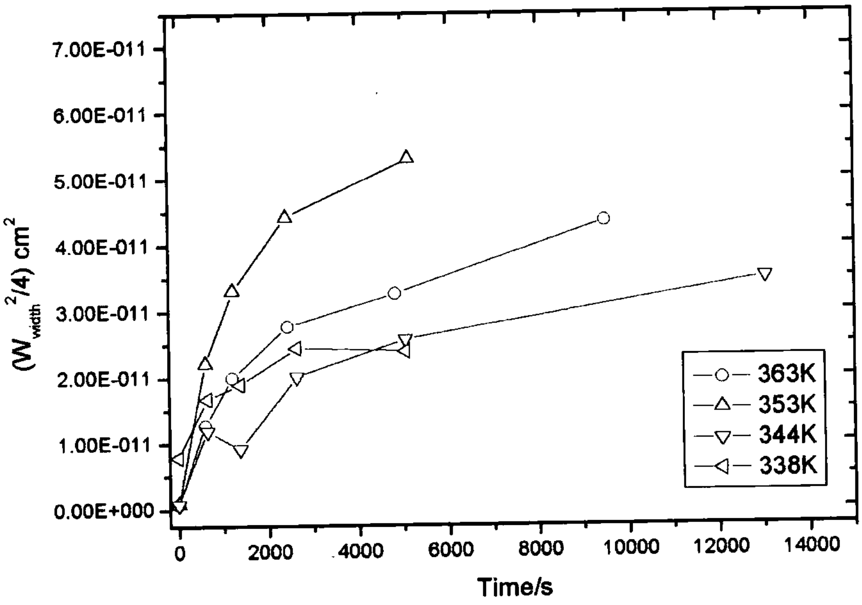

Figure 3.9 Plot of $w_{width}\,^2/4$ against diffusion time for a sample of DPEO (≈50 nm) M_w= 17300 gmol^{-1} and PMMA (≈950 nm) M_w=16000 gmol^{-1} at various temperatures. Plot shows data one NRA geometry (60°) for each temperature. Points at higher $w_{width}^2/4$ have been removed to allow comparison at early times.

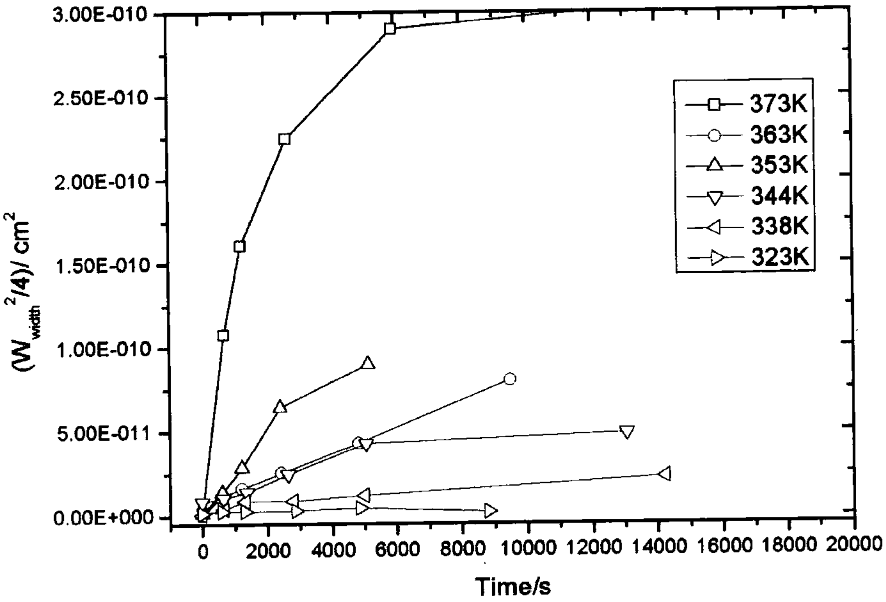

Figure 3.10 Plot of $w_{width}{}^2/4$ against diffusion time for a sample of DPEO (≈50 nm) M_w= 77800 gmol^{-1} and PMMA (≈950 nm) M_w=213400 gmol^{-1} at various temperatures. Plot shows data one NRA geometry (60°) for each temperature. Points at higher $w_{width}{}^2/4$ have been removed to allow comparison at early times.

3.5 Discussion

For all raw NRA data, the profile due to the deuterium moved to greater depths with heating, indicating that the diffusion of molten DPEO into glassy PMMA had occurred. The movement of DPEO into PMMA could be explained by DPEO plasticizing the PMMA; DPEO enters the PMMA and interrupts the PMMA interactions; hence the mobility of the surrounding PMMA chains can be higher than for pure PMMA and thus assist with DPEO diffusion. NRA as a technique cannot analyse whether the PMMA chains have sufficient mobility to then diffuse towards the surface. It is worth noting that a 50 nm DPEO film may display thin film effects such as decreased T_g compared to the bulk[12] and stronger interfacial effects. This may indicate that behaviour of the bilayer is different to that expected for bulk DPEO and PMMA placed into contact with each other.

There have been a few studies of molten polymers diffusing into glassy matrices. The diffusion of rubbery poly(vinylmethylether) (PVME) into glassy PS[13] has been observed. Further studies of this diffusing pair have only included one entangled polymer with the rubbery component below the entanglement molecular weight.[14,15] The method of diffusion for these couples has been analysed by various methods. Some[13,16] extend case II processes to describe the diffusion of rubbery polymers into glassy polymers above the entanglement molecular weight and of similar size to here (~100000 gmol^{-1}), showing that the process is controlled by the mechanical response of the glassy polymer. Others point out that large molecules in the liquid state are associated with low osmotic pressures, insufficient to trigger a mechanism of mechanically controlled penetration at the glassy interface[15]. The diffusion of liquid styrene oligomers into glassy PPO has been analysed using Raman spectra. The molecular weights utilised were small for PS (850 gmol^{-1} and 740 gmol^{-1}) and large for PPO (15500 gmol^{-1}) .[14] It was proposed that the PS rapidly dissolved the glassy PPO at the interface due to a favourable interaction parameter. This process could be described by case II diffusion, the subsequent movement of the polymers can then be described by Fickean diffusion. The diffusion process for liquid polymer (PS) into a PS/PPO couple does not change when the temperature is greater than the T_g of the PPO so that diffusion processes were similar for liquid/glassy and liquid/liquid couples.[15,17] Case II diffusion should be characterised by a 'moving front' not apparent in the NRA profiles analysed here.

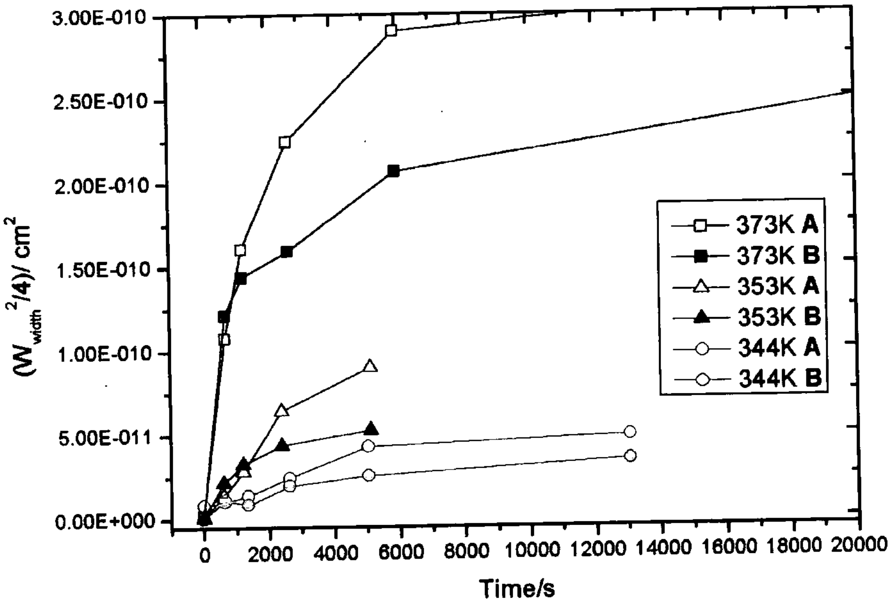

Figure 3.11 Plot of $w^2/4$ against diffusion time for samples of DPEO (≈50 nm) on PMMA (≈950 nm) at various temperatures. Solid symbols (A) represent DPEO M_w= 17300 gmol^{-1} and PMMA M_w=16000 gmol^{-1} open symbols (B) M_w= 77800 gmol^{-1} and PMMA M_w=213400 gmol^{-1}

The non-linear relationship between $w_{width}^2/4$ and time could be attributed to the surface roughness or the data being fitted to the wrong type of diffusion model. Surface roughness decreased with anneal time, where as deviation from linear behaviour increased, implying that the main mechanism for diffusion is not Fickean and the tracer diffusion coefficient is not constant. A straight line drawn through the early section of the data gives the slope at early stages of diffusion, the resulting tracer diffusion coefficients D^*_{DPEO} for DPEO into PMMA are shown in Table 3.3.

Temperature/K	D^*_{DPEO}/cm^{2}s^{-1} for DPEO, M_w =77800in PMMA , M_w =213400	D^*_{DPEO}/cm^{2}s^{-1} for DPEO, M_w =17300in PMMA M_w =16000
373	7.96E-14	3.02E-14
363	8.26E-15	7.09E-15
353	1.75E-14	2.81E-14
344	7.05E-15	4.41E-15
338	2.14E-15	3.06E-15

Table 3.3 Showing the DPEO tracer diffusion coefficients for various temperatures

The previous study of PMMA and DPEO blends,[18] at lower molecular weights than studied here ≈ 7500 gmol^{-1}, gave a mutual diffusion coefficient of the order 10^{-8} cm^{2}s^{-1}. Such a high value of mutual diffusion may explain why heating at higher temperatures gave diffusion so fast it could not be followed using ion beam techniques.

All the samples showed a slowing down of diffusion of DPEO, visible from both raw data in Figure 3.5 and Figure 3.6 and from plots of $w_{width}^2/4$. The depths at which the DPEO stopped moving were less than the depths at which NRA resolution became unreliable. The interaction parameter χ is known to be concentration dependent for blends of DPEO and PMMA. The slowing down observed may be due to the DPEO reaching some critical concentration within the PMMA leading to thermodynamic slowing down[1] as described in section 1.3.4. If the diffusion is controlled by penetrant DPEO molecules changing the T_g and hence mobility in the PMMA bulk, then the changing concentration of the resultant blend and the associated T_g may also explain this deceleration. However it would be expected that a higher volume fraction DPEO would decrease the blend T_g, thus accelerating diffusion. The depth of the plateau regions in Figure 3.9 and Figure 3.10 are similar for temperatures between 338 K and 363 K but very different for 373 K. The difference in plateau for high and low molecular weight combinations was small and they follow a similar change with temperature. It is possible that the depth of penetration for DPEO into PMMA may be an indicator of a critical concentration or critical blend T_g.

For both molecular weight combinations, the higher temperatures gave greater initial diffusion coefficients. The difference in D^* could be due to the extra mobility of the DPEO or PMMA at elevated temperatures. There was some movement when the DPEO was heated to near its melting point (338 K) indicating DPEO was mobile. The change in diffusion width still exhibited the same curvature. At 323 K (Figure 3.10) neither polymer should be mobile, the slight difference in $w_{width}^2/4$ exhibited could be evidence of the errors of fitting and the effects of sample handling.

Figure 3.11 shows the diffusion behaviour of both molecular weight combinations. The smaller combination couple could be expected to move faster, however there was no distinguishable pattern in behaviour. This may indicate that the diffusion is independent of molecular weight of either component. If DPEO is molten, its behaviour may be independent of its molecular weight, moving in a similar fashion to unentangled oligomers. Temperature was far more influential in determining the limit of diffusion range and this may support oligomer-like behaviour as oligomer mobility would still be influenced by temperature. However, PMMA should behave like a reptating polymer, thus providing molecular weight dependence to the diffusion. Hence diffusion must be dominated by the molecular weight independent movement of DPEO, obeying 'fast' theory.[19] Further molecular weight combinations may yield clearer relations between molecular weight and diffusion.

3.6 Summary

NRA has been used to observe the diffusion of molten DPEO into glassy PMMA where both components were entangled. Depth profiles showed unusual shape and the diffusion cannot be described well by Fickean diffusion. Slowing down of the diffusion of DPEO was observed and may be due to changes in interaction parameter in the resultant blend or to concentration dependent changes in blend T_g. The relationship between volume fraction and diffusion may be extracted by calculations utilising the behaviour of the blend glass transition with volume fraction.

3.7 Speculative Theory

Starting from the assumption that diffusion process observed here is concentration dependent, a method is required to quantify this relationship. The diffusion coefficient D is related to molecular properties by,

$$D \approx \frac{\left\langle R_g^2 \right\rangle}{\tau_R} \qquad \text{Equation 3.4}$$

where $\left\langle R_g^2 \right\rangle$ is the mean squared radius of gyration. τ_R is the relaxation time of the chain, (the Rouse time for unentangled polymers, the reptation time for entangled polymers). Assuming $\left\langle R_g^2 \right\rangle$ remains constant, a variation in D originates from a variation of τ_R with composition. The relaxation time τ_R is proportional to ζ_o, the monomeric friction coefficient, the temperature dependence of the latter is given by the WLF equation[20],

$$\log \zeta_o(T) = \log \zeta_0(T_g) + \log_{10} a_T \qquad \text{Equation 3.5}$$

Where T is the temperature of the system and a_T is found from,

$$\log_{10} a_T = \frac{-c_1(T - T_g)}{c_2 + T - T_g} \qquad \text{Equation 3.6}$$

where c_1 and c_2 are WLF parameters. In 1989 Colby[21] proposed that for blends, the WLF description of the temperature dependence of the monomeric friction coefficient holds if c_1 and c_2 have pure component values but the value of the glass transition is that of the blend; $T_g(\varphi_{PEO})$, so for a pure sample,

$$\zeta_o\left(T_g, \varphi_{PEO} = 1\right) = \zeta_0\left(T_g^{PEO}\right)a_T(PEO)$$ Equation 3.7

where,

$$\log\ a_T\ (PEO\ ) = \frac{-c_1\left(T - T_g^{PEO}\right)}{c_2 + T - T_g^{PEO}}$$ Equation 3.8

If $\varphi_{PEO} \neq 1$, then,

$$\zeta_o\left(T_g, \varphi_{PEO}\right) = \zeta_0\left(T_g\left(\varphi_{PEO}\right)\right)a_T\left(\varphi_{PEO}\right)$$ Equation 3.9

where,

$$\log a_T\left(\varphi_{PEO}\right) = \frac{-c_1\left(T - T_g\left(\varphi_{PEO}\right)\right)}{c_2 + T - T_g\left(\varphi_{PEO}\right)}$$ Equation 3.10

which is essentially Colby's proposal, where $T_g(\varphi_{PEO})$ is the glass transition of a blend with composition φ_{PEO} and is related to the glass transition of the pure components by the Fox equation[22],

$$\frac{1}{T_g\left(\varphi_{PEO}\right)} = \frac{\varphi_{PEO}}{T_g^{PEO}} + \frac{1 - \varphi_{PEO}}{T_g^{PMMA}}$$ Equation 3.11

Using the proportionality of τ_R to ζ_o and assuming that any constants of proportionality are irrelevant, Equation 3.7 and Equation 3.9 can show,

$$\frac{\tau_R\left(\varphi_{PEO} = 1\right)}{\tau_R\left(\varphi_{PEO}\right)} = \frac{\zeta_o\left(T, \varphi_{PEO} = 1\right)}{\zeta_o\left(T, \varphi_{PEO}\right)} = \frac{\zeta_o\left(T, \varphi_{PEO} = 1\right)}{\zeta_o\left(T, \varphi_{PEO}\right)} \times \frac{a_T(PEO)}{a_T\left(\varphi_{PEO}\right)}$$ Equation 3.12

Using the relationship in Equation 3.4,

$$\frac{\tau_R\left(\varphi_{PEO} = 1\right)}{\tau_R\left(\varphi_{PEO}\right)} = \frac{D\left(\varphi_{PEO} = 1\right)}{D\left(\varphi_{PEO}\right)}$$ Equation 3.13

And hence

$$D\left(\varphi_{PEO}\right) = D_0 \frac{\zeta_o\left(T, \varphi_{PEO} = 1\right)}{\zeta_o\left(T, \varphi_{PEO}\right)} a_T'$$ Equation 3.14

where,

$$a_T' = 10^{\left[\frac{-c_1\left(T - T_g^{PEO}\right)}{c_2 + T - T_g^{PEO}} + \frac{-c_1\left(T - T_g\left(\varphi_{PEO}\right)\right)}{c_2 + T - T_g\left(\varphi_{PEO}\right)}\right]}$$ Equation 3.15

$D(\varphi_{PEO})$ needs to be related to a measurable quantities. A crude assumption is that the average environment for the PEO depends on the width of the broadening interface between PEO and PMMA as shown in Figure 3.12.

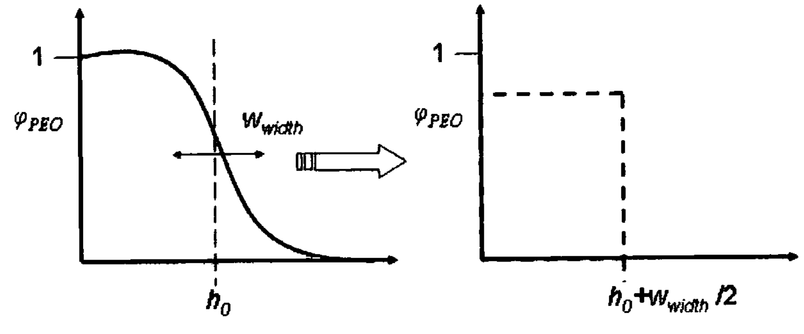

Figure 3.12 Schematic of broadening interface between PEO and PMMA, with original depth h_0 and broadening width w_{width}.

w_{width} can be simplified as shown in Figure 3.12 and hence φ_{PEO} can be described by,

$$\varphi_{PEO} = \frac{h_0}{h_0 + \frac{w_{width}}{2}} \qquad \text{Equation 3.16}$$

Since D is known as a function of φ_{PEO} (Equation 3.14) and φ_{PEO} is known as a function of w_{width}, D is known as a function of w_{width},

$$\frac{{w_{width}}^2}{4} = D(w_{width})\,t \qquad \text{Equation 3.17}$$

$$\frac{{w_{width}}^2}{4} = D_0\,\frac{\zeta_o(T,\varphi_{PEO}=1)}{\zeta_o(T,\varphi_{PEO})}\times 10^{\left\{\frac{-c_1\left(T-T_g(\varphi_{PEO})\right)}{c_2+T-T_g(\varphi_{PEO})}+\frac{-c_1\left(T-T_g^{PEO}\right)}{c_2+T-T_g^{PEO}}\right\}} \bullet t \qquad \text{Equation 3.18}$$

A further proposition of Colby is that the monomeric friction coefficient for PEO at the glass transition temperature is independent of the composition,

$$\zeta_o(T,\varphi_{PEO}=1) = \zeta_o(T,\varphi_{PEO}) \qquad \text{Equation 3.19}$$

therefore

$$\frac{{w_{width}}^2}{4} = D_0 10^{\left\{\frac{-c_1\left(T-T_g(\varphi_{PEO})\right)}{c_2+T-T_g(\varphi_{PEO})}+\frac{-c_1\left(T-T_g^{PEO}\right)}{c_2+T-T_g^{PEO}}\right\}} \bullet t \qquad \text{Equation 3.20}$$

Experimentally the relationship between the diffusion coefficient and concentration can be found. Using nuclear reaction analysis, for a given annealed bilayer w_{width} can be calculated and hence φ_{PEO} as a function of time can be found using Equation 3.16. The glass transition of the blend can be found from Equation 3.11 and the glass transition temperatures of the pure polymers, are given by either DMA or DSC. The WLF parameters c_1 and c_2 can be found from rheology measurements of the pure components, hence a_T' can be found. D_0 can be found by fitting a curve to the data of $w_{width}{}^2/4$ against t,

$$\frac{w_{width}{}^2}{4} = D_0 a_T'\left(w_{width}\right)t \qquad \text{Equation 3.21}$$

In more sophisticated theories of the monomeric friction coefficient in blends φ_{PEO} needs to be replaced with an effective composition $\varphi_{eff,i}$,[23]

$$\varphi_{eff,i} = \varphi_{s,i} + \left(1-\varphi_{s,i}\right)\varphi_i \qquad \text{Equation 3.22}$$

where φ_i is the macroscopic volume fraction and $\varphi_{s,i}$ is the self composition from chain connectivity at the scale of the Kuhn length[24].

3.8 References

(1) Silvestre, C.; Cimmino, S.; Martuscelli, E.; Karasz, F. E.; Macknight, W. J. *Polymer* **1987**, *28*, 1190-1199.

(2) Payne, R. S.; Clough, A. S.; Murphy, P.; Mills, P. J. *Nuclear Instruments & Methods in Physics Research Section B- Beam Interactions with Materials and Atoms* **1989**, *42*, 130-134.

(3) Hutchings, L. R.; Richards, R. W.; Thompson, R. L.; Clough, A. S.; Langridge, S. *Journal of Polymer Science Part B-Polymer Physics* **2001**, *39*, 2351.

(4) Fetters, L. J.; Lohse, D. J.; Richter, D.; Witten, T. A.; Zirkel, A. *Macromolecules* **1994**, *27*, 4639-4647.

(5) Reiter, G. *Physical Review Letters* **1992**, *68*, 75.

(6) Dalnoki-Veress, K.; Forrest, J. A.; Massa, M. V.; Pratt, A.; Williams, A. *Journal of Polymer Science Part B-Polymer Physics* **2001**, *39*, 2615-2621.

(7) Cimmino, S.; Martuscelli, E.; Silvestre, C.; Canetti, M.; Delalla, C.; Seves, A. *Journal of Polymer Science Part B-Polymer Physics* **1989**, *27*, 1781-1794.

(8) Mayer, M. *Nuclear Instruments & Methods in Physics Research Section B- Beam Interactions with Materials and Atoms* **2002**, *194*, 177-186.

(9) Kitamura, A.; Tamai, T.; Taniike, A.; Furuyama, Y.; Maeda, T.; Ogiwara, N.; Saidoh, M. *Nuclear Instruments & Methods in Physics Research Section B- Beam Interactions with Materials and Atoms* **1998**, *134*, 98-106.

(10) Yesil, I. M.; Assmann, W.; Huber, H.; Lobner, K. E. G. *Nuclear Instruments & Methods in Physics Research Section B- Beam Interactions with Materials and Atoms* **1998**, *138*, 623-627.

(11) Sajavaara, T.; Arstila, K.; Laakso, A.; Keinonen, J. *Nuclear Instruments & Methods in Physics Research Section B- Beam Interactions with Materials and Atoms* **2000**, *161*, 235-239.

(12) Hamon, L.; Grohens, Y.; Holl, Y. *Langmuir* **2003**, *19*, 10399-10402.

(13) Jabbari, E.; Peppas, N. A. *Macromolecules* **1993**, *26*, 2175-2186.

(14) Tomba, J. P.; Carella, J. M.; Garcia, D.; Pastor, J. M. *Macromolecules* **2001**, *34*, 2277-2287.

(15) Tomba, J. P.; Carella, J. M.; Pastor, J. M. *Macromolecules* **2005**, *38*, 4355-4362.

(16) Lin, H. C.; Tsai, I. F.; Yang, A. C. M.; Hsu, M. S.; Ling, Y. C. *Macromolecules* **2003**, *36*, 2464-2474.

(17) Tomba, J. P.; Carella, J. M.; Garcia, D.; Pastor, J. M. *Macromolecules* **2004**, *37*, 4940-4948.

(18) Xia, J. L.; Wang, C. H. *Journal of Chemical Physics* **1991**, *94*, 3229-3234.

(19) Composto, R. J.; Kramer, E. J.; White, D. M. *Nature* **1987**, *328*, 234-236.

(20) Ferry, J. D. *Viscoelastic Properties of Polymers*; 3rd ed.; Wiley: New York, 1980.

(21) Colby, R. H. *Polymer* **1989**, *30*, 1275-1278.

(22) Fox, T. G. *Bull. Am. Phys. Soc* **1956**, *1*, 123.

(23) Pathak, J. A.; Kumar, S. K.; Colby, R. H. *Macromolecules* **2004**, *37*, 6994.

(24) Lodge, T. P.; McLeish, T. C. B. *Macromolecules* **2000**, *33*, 5278-5284.

Chapter 4

Bulk properties of blends of DPEO and PMMA

4.1 Introduction

To understand the diffusion behaviour of molten DPEO into PMMA the composition and temperature dependence of the interaction parameter at these temperatures and alteration of the glass transition temperature, with blend composition need to be known. The glass transition has been variously measured for blends of DPEO and PMMA, but not by dynamic mechanical analysis (DMA). The variation of glass transition temperature with composition can be measured using DMA. Results can be compared to behaviour with the Fox equation by measuring the T_g for pure components. Previous comparisons between DMA and DSC values for polymer glass transitions are limited, however will be attempted.

The interaction parameter, χ has been found from melting point depression[1,2] and small angle neutron scattering (SANS) .[3,4] However, the composition dependence and temperature dependence of χ at the temperatures utilised for ion beam experiments (above the T_m of DPEO but below the T_g of PMMA) have not previously been found. Calculations of χ from melting point depression require the measurement of the equilibrium melting points for the pure component and the blend. These measurements can be influenced by lamellar thickening during heating,[4] modification of crystalline structure and superheating of the crystals and therefore were not the most suitable method for blends of PEO and PMMA. The variation of the interaction parameter with concentration, temperature and molecular weight can be measured using small angle neutron scattering. The handling of scattering data which allows thermodynamic properties to be extracted will be reviewed before results of scattering data are evaluated to establish whether entropic or enthalpic interactions dominate as well as whether the system exhibits UCST or LCST behaviour. The results can then be compared to previous work.

4.2 Measurement of T_g

The glass transition temperature of polymers can be measured using both differential scattering calorimetry (DSC) and dynamic mechanical analysis (DMA). Initial attempts to study polymer blends using DSC were not successful, with peaks on the trace becoming indistinguishable upon blending. The variation of mechanical behaviour in the bilayers, with change in concentration, may be important in understanding the behaviour of DPEO and PMMA, DMA was therefore used to provide clearer T_g values.

4.3 Experimental

Both pure samples and blends were prepared for DMA analysis. Pure samples are listed in Table 4.1. PMMA samples were pressed into a mould approximately 40 mm×9 mm×0.8 mm using a heated press at 160 °C under a nitrogen atmosphere. DPEO samples were pressed into a similar mould at 80 °C.

Polymer	M_w/ gmol^{-1}	M_n / gmol^{-1}	Polydispersity
DPEO	121100	119100	1.02
DPEO	17300	16900	1.03
DPEO	170700	165000	1.04
PMMA	182400	153400	1.19
PMMA	96200	93000	1.03
PMMA	60200	59600	1.01
PMMA	2016000	1903000	1.06
PS-PMMA	PS= 29200 PMMA=285100		1.08

Table 4.1 Showing polymers utilised in DMA experiments

Two molecular weight combination blends were prepared; 96200 gmol^{-1} and 182400 gmol^{-1} PMMA with 121100 gmol^{-1} DPEO. Various volume fractions were constructed for each molecular weight combination. Polymers were accurately weighed then solvated in chloroform. This solution was solvent cast and the resulting films dried in a vacuum oven at 150 °C for > 48hours. Due to the small mass of polymer available, samples were recycled, by constructing different volume fraction blends by further addition of DPEO and repeating the steps outlined above. The re-use of samples may introduce errors, as the heating used during sample preparation may have degraded the polymers. Dynamic mechanical analysis measurements were taken, using a dual cantilever, multifrequency strain experiment, on a TA instruments DMA Q800. The frequency was fixed at 1 Hz and a heating ramp of 3 °C/minute utilised. Samples were maintained for 3 minutes at either end of the heating cycle to establish thermal equilibration. Pure DPEO samples were measured between -150 °C to 70°C, pure PMMA and blends were treated between -70 °C to 170 °C. Differential scanning calorimetry results are taken from experiments run on a Perkin Elmer Pyris DSC/TGA and the data analysed using Pyris* software.

---

* Pyris v.3.81 (Perkin Elmer)

4.4 Results

Typical scans and fits for values of the T_g found using TA instruments fitting program[†] are shown in Figure 4.1-4.3. Some investigators[5] use the loss tangent (*tan δ*) peak and others use the loss modulus (E'') peak or the elastic modulus (E') decrease onset to define T_g. T_gs were consequently found from both the loss modulus and *tanδ*. Figure 4.1 shows a typical scan for pure PMMA, the large peak in *tanδ* indicates the T_g at 141 °C whilst the loss modulus demonstrates a T_g at 132 °C. Peaks at lower temperatures are assumed to indicate alpha or beta transitions as described in section 2.7.1. Figure 4.2 shows a typical scan for DPEO. The peak at ~-60 °C in both *tanδ* and the loss modulus indicates the glass transition temperature. The trailing signal towards 50 °C is due to the sample melting within the DMA clamp.

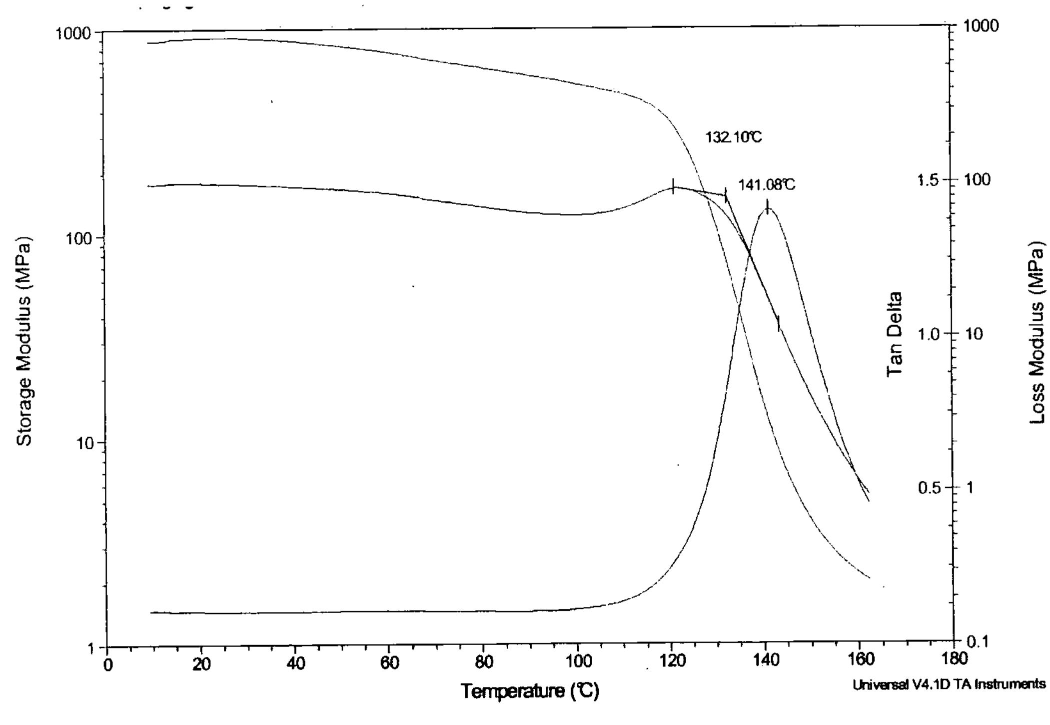

Figure 4.1DMA scan and fitted values for T_g for 182400 gmol^{-1} PMMA.

[†] TA Universal Analysis v.4.1D (TA instruments-Waters LLC)

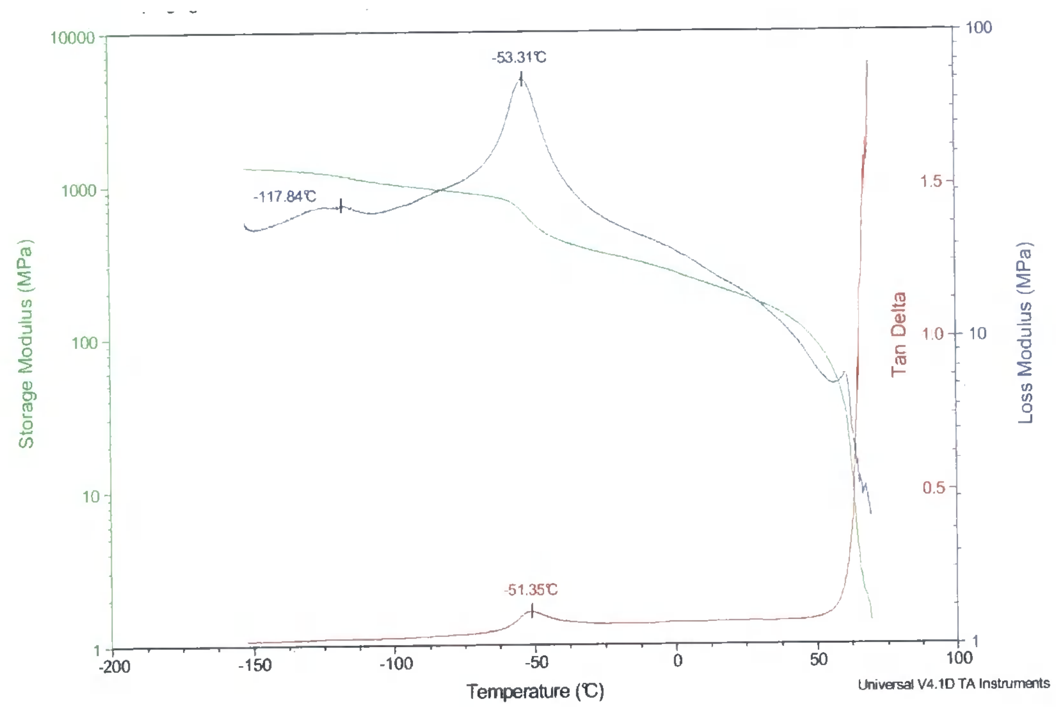

Figure 4.2 DMA scan and fitted values for T_g for 170700 gmol^{-1}DPEO.

A typical scan of a blend of DPEO and PMMA is shown in Figure 4.3. A single glass transition, $T_{g,blend}$ is observed in both the loss modulus and *tanδ*.

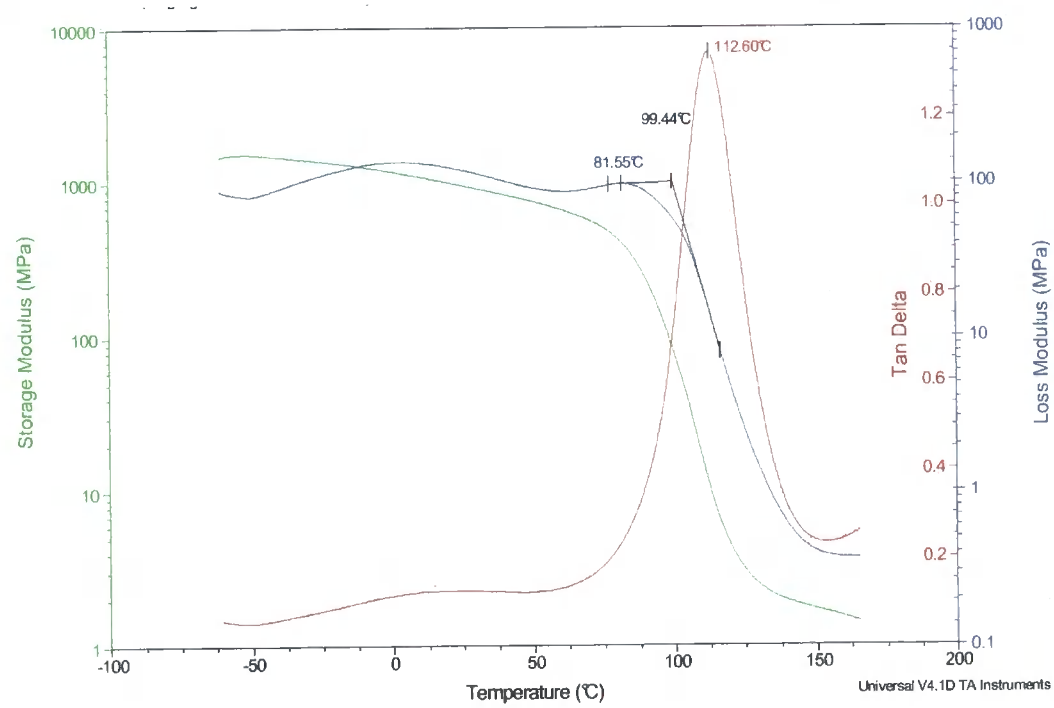

Figure 4.3 DMA scan and fitted values for T_g for a blend of 182400 gmol^{-1} PMMA and 20% 170700 gmol^{-1} DPEO

4.5 Discussion

A single peak in *tan δ* attributed to T_g was observed for all volume fractions analysed, including those where $\varphi_{DPEO} > 0.3$, the concentration at which the blend is believed to no longer be homogeneous. It might be expected, in line with previous experiments[6] that for these blends two peaks would be observed, for each phase of the blend DPEO. Figure 4.4 and Figure 4.5 show the relationship between T_{gblend} and volume fraction DPEO as calculated from the Fox equation (section 1.4) with pure sample DMA measurements, and the experimental blend data. Experimental data differs from the calculated relationship, which may indicate that the blend is not homogenous or that the theory is inadequate. More data points may provide better correlation.

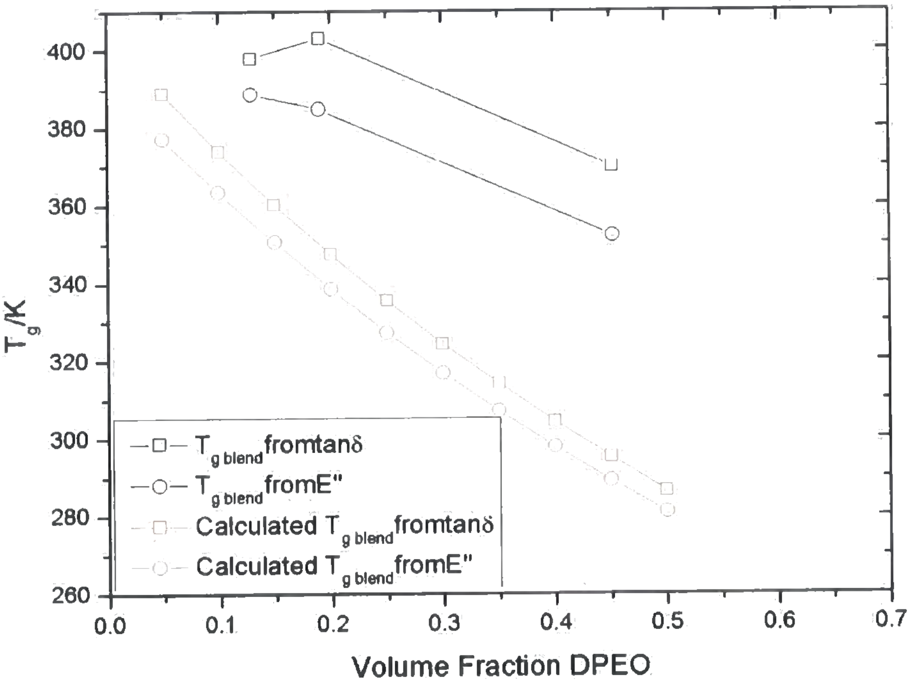

Figure 4.4 T_{gblend} against blend composition for a blend of 96200g mol^{-1} PMMA and 121100 gmol^{-1} DPEO, with T_{gblend} calculated from values found by DMA for pure samples and the Fox equation.

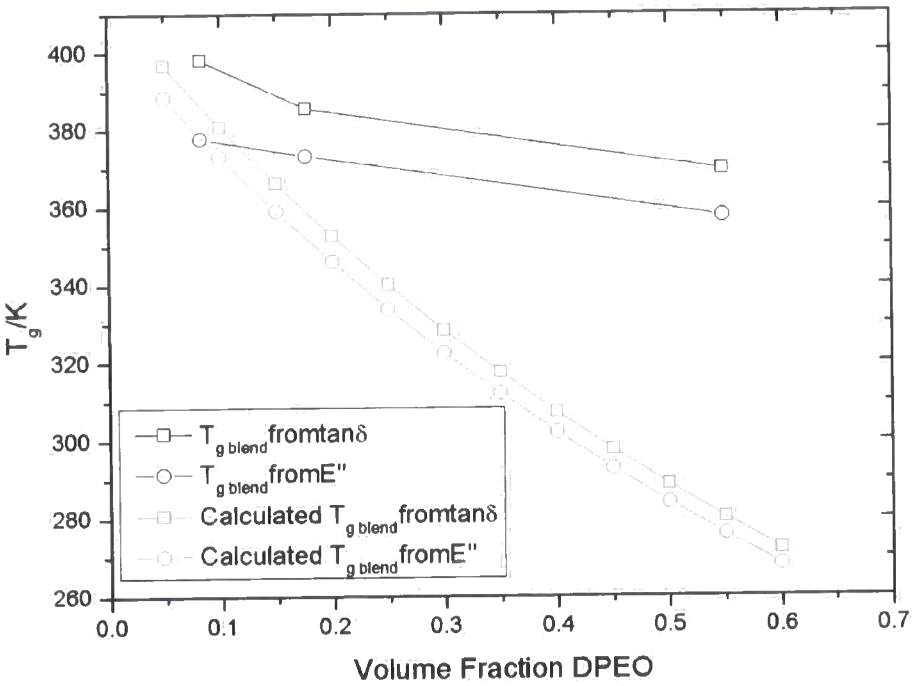

Figure 4.5 T_{gblend} against blend composition for a blend of 182400 gmol^{-1} PMMA and 121100 gmol^{-1} DPEO with T_{gblend} as calculated from values found by DMA for pure samples and the Fox equation.

T_g found from E'' and *tanδ* for the pure samples are shown in Table 4.2. The variation in T_{gblend} found from E'' and *tanδ for* a given concentration can be seen in Figure 4.4-4.5. Table 4.2 shows the difference between T_gs found from E'' and *tanδ* was 6 K. The deviation between the average T_g and values as measured by DSC was 6 K. It has been proposed, that the average of the two peaks, (*tan δ* and E'') measured at 1 rad/S defines the same T_g as measured by DSC[7] but this is not supported by the results of this section.

Polymer	Molecular weight/ gmol^{-1}	T_g from DSC/K	T_g from *Tan* δ /K	T_g from E''/K	Average T_g from DMA/K	Difference between *Tan* δ and E''/K	Difference between DMA T_g and DSC T_g /K
DPEO	121100		222	219	220	2	
DPEO	17300	227.2	243	249	246	4	13
DPEO	170700		220	222	221	1	
PMMA	182400	404.8	414	405	410	6	3
PMMA	96200	404.9	405	392	399	9	4
PMMA	60200	406.0	413	401	407	9	1
PMMA	2016000		420	409	414	8	
PS-PMMA	PS= 29200 PMMA=285100		417	409	413	6	
						6	6

Table 4.2 Showing T_g as found from DSC and DMA and the average standard deviation between *Tan δ* and E''/K and DMA T_g and DSC T_g

4.6 Copolymer Results and Discussion

DMA scans for pure and blended copolymer are shown in Figure 4.6 and Figure 4.7.

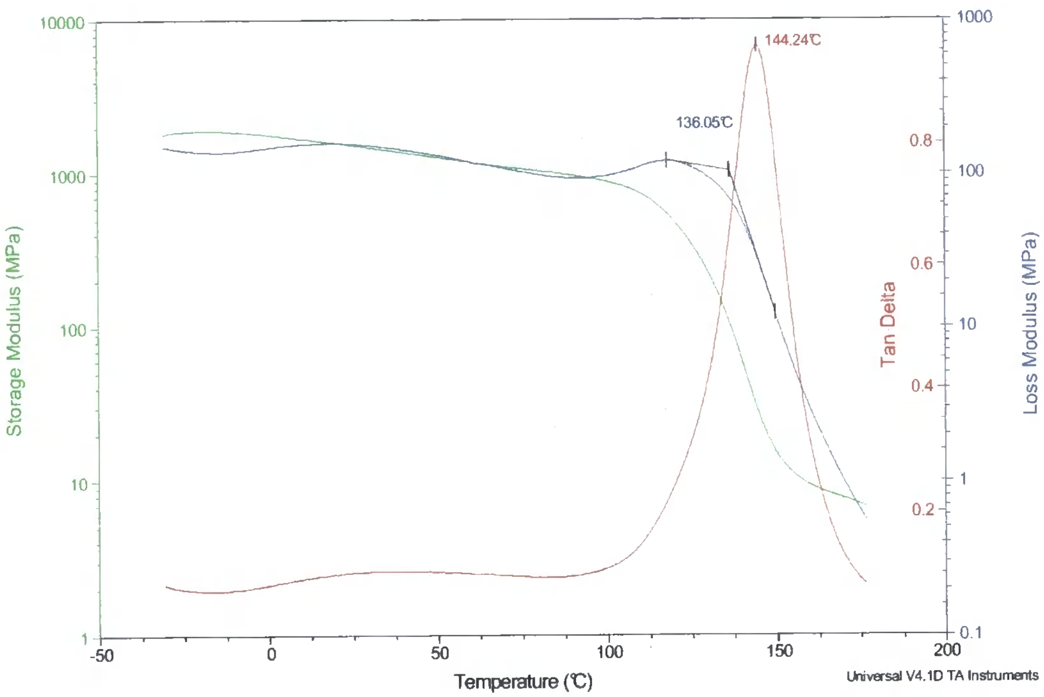

Figure 4.6 DMA scan and fitted values for T_g for PS-PMMA copolymer

The DMA scan for blended copolymer (Figure 4.7), displays a peak at ~10°C, believed to be due to alpha or beta transitions, which are elevated compared to the pure copolymer. The peak at $T_{g,tan\delta}$=108 °C in Figure 4.7, is believed to be due to the glass transition of the blend between the PMMA block in the copolymer and DPEO. The peak at 149 °C is due to the glass transition temperature of polystyrene block in the copolymer. The T_g of a blend of 28% DPEO in PMMA can be extrapolated from Figure 4.5, a blend of PMMA and DPEO should provide, $T_{gtan\delta}$=111 °C, which is in reasonable agreement.

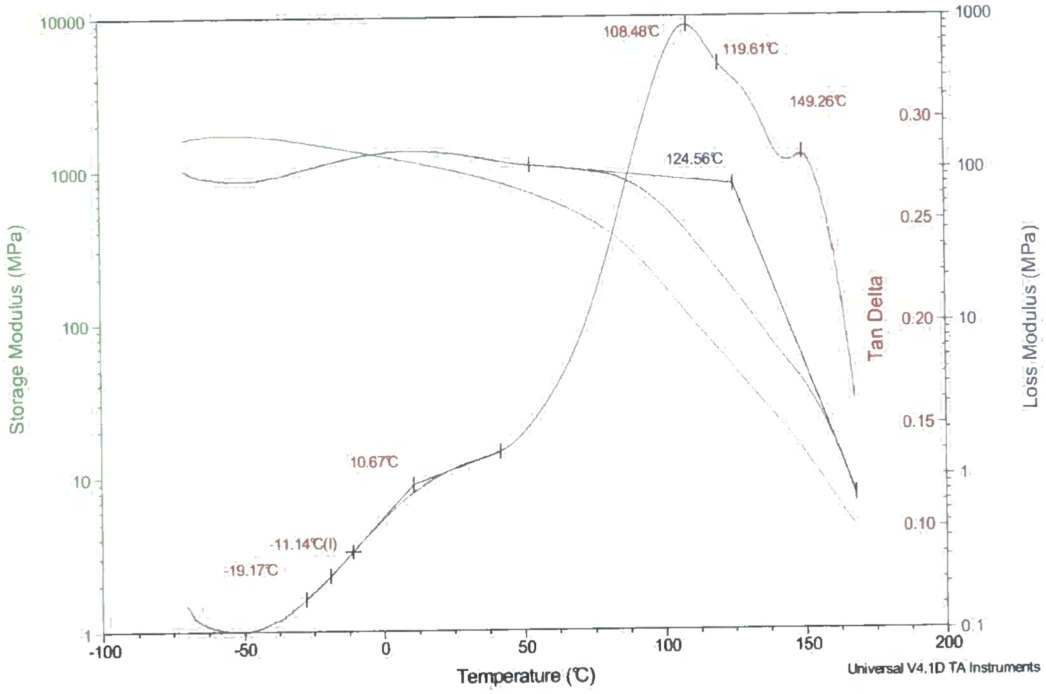

Figure 4.7 DMA scan and fitted values for T_g for a blend of PS-PMMA and 27.5% 121100 gmol^{-1} DPEO

4.7 Summary

The glass transition temperature of both pure components and blends has been analysed using dynamic mechanical analysis. Values are in reasonable agreement with those found from DSC. The T_{gblend} was found to vary with concentration but this variation could not be described by the Fox equation.

4.8 SANS measurement of χ

The interaction parameter for a polymer blend can be related to the coherent scattering intensity. Using the random phase approximation deGennes[8,9] derived the expression for $I(q)_r$,

$$\frac{V(\Delta\rho)^2}{I(q)_r} = \frac{1}{v_A\varphi_A D(q^2R_{g1}^2)} + \frac{1}{v_B\varphi_B D(q^2R_{g2}^2)} - \frac{2\chi}{v_u} \qquad \text{Equation 4.1}$$

The blend described has two polymers A and B, where R_{gA} and R_{gB} are the radii of gyration of polymers in the blend. φ_A and φ_B are the volume fractions of the polymers in the blend v_A and v_B are the volumes of the polymer repeat units. In the original Flory formulation, v_u is equated to the volume of a solvent molecule, in a blend it is commonly taken to be equal to be the monomeric volume of one of the polymers or the geometric mean, $v_u = \sqrt{(v_A v_B)}$. χ must be proportional to the volume used and only χ/v_u is physically meaningful. V is the scattering volume and $\Delta\rho$ is the difference in scattering length density between the polymers,

$$(\Delta\rho)^2 = (\rho_A - \rho_B)^2 \qquad \text{Equation 4.2}$$

$D(x)$ is the Debye function,

$$D(x) = \frac{2\left(e^{-x_D} + x_D - 1\right)}{x_D^{\ 2}} \qquad \text{Equation 4.3}$$

The Debye function arises if it is assumed that the chain conformations can be described using Gaussian statistics. An idealised polymer chain can be modelled as $(N+1)$ segments connected by N bonds of fixed length l,

$$R_g^2 = \frac{Nl^2}{6} \qquad x_D = \frac{q^2 Nl^2}{6} \qquad \text{Equation 4.4}$$

The behaviour of the Debye function describing polymer chains in comparison to the scattering functions for a sphere and thin disk is shown in Figure 4.8.

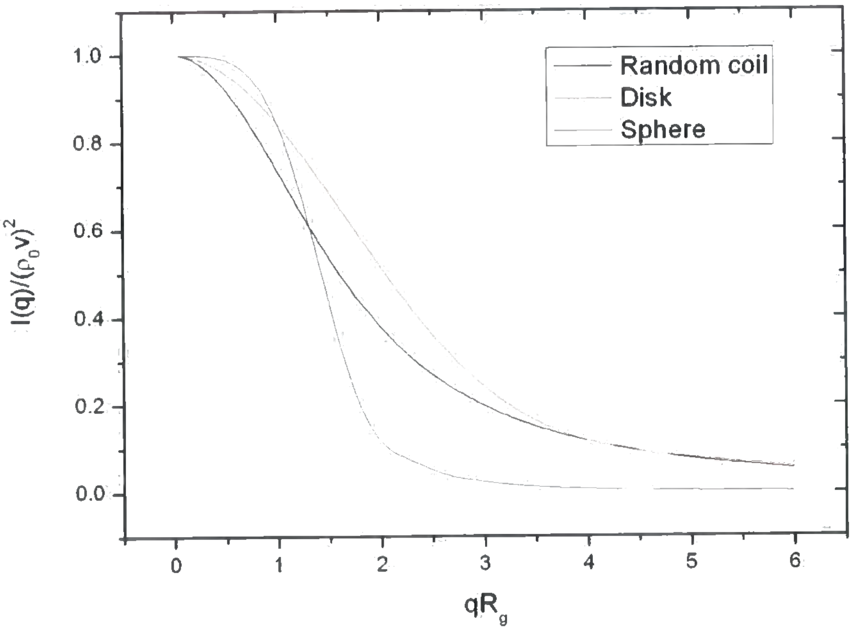

Figure 4.8 The Debye function, for a random coil compared with the independent scattering function for a sphere and a thin circular disk.[10]

In the limit of $q \rightarrow 0$, Equation 4.1 becomes,

$$\frac{V(\Delta p)^2}{I(0)} = \frac{1}{v_A}\frac{1}{\varphi_A} + \frac{1}{v_B}\frac{1}{\varphi_B} - 2\frac{\chi}{v_u}$$ Equation 4.5

If the scattering function is expanded to include the q^2 term then,

$$\frac{V(\Delta p)^2}{I(q)_r} = \frac{1}{S(q)} = \frac{1}{S(0)}\left(1 + q^2 \xi_l^2\right)$$ Equation 4.6

where ξ_l is the correlation length, a measure of the distance over which the concentration fluctuations remain correlated. It is described by,

$$\xi_l^2 = \frac{S(0)}{2}\left(\frac{R_{gA}^2}{v_A \varphi_A} + \frac{R_{gB}^2}{v_B \varphi_B}\right)$$ Equation 4.7

S(q) is the structure factor; the scattered intensity per unit volume per unit contrast factor,

$$I(q) = V(\Delta p)^2 S(q)$$ Equation 4.8

The structure factor is thus related to the effective interaction parameter by,

$$\frac{1}{S(0)} = \frac{1}{v_{PMMA}\varphi_{PMMA}} + \frac{1}{v_{DPEO}\varphi_{DPEO}} - \frac{2\chi_{eff}}{v_u}$$ Equation 4.9

Since an assumption is made over which monomer volume to use for v_u, χ can only described by χ_{eff} the effective interaction parameter. Hence it is essential when quoting values of χ to include the reference volume used. This also allows any concentration dependence and any other influences not incorporated in the original Flory-Huggins theory.

4.9 Experimental

To optimise the time required for each sample to be in the neutron beam a suitable transmission I/I_0 is required,

$$\frac{I}{I_0} = \exp(-n\sigma_T t_h)$$ Equation 4.10

where I is the transmitted flux, I_0 the incident flux, n is the monomer units per unit volume, σ_T is the total cross section (the sum of incoherent and coherent cross sections for each atom) and t_h the thickness of the sample. I must be less than I_0, hence a desirable thickness of samples with a range of DPEO concentrations $0 < \varphi_{DPEO} < 1$ were calculated and the required samples should be 1.5 mm to 0.5 mm thick. Polymers utilised are characterised in Appendix I.

Samples were prepared by co-dissolving the appropriate polymers in chloroform, pouring the solution into the mould and allowing chloroform to evaporate. Samples were then heated to 363K in a vacuum oven for 48 hours to ensure removal of solvent and a homogeneous blend. The volume fraction of DPEO in the blend mixtures explored was in the range $0.05 < \varphi_{DPEO} < 0.4$. The films were free of macroscopic air bubbles and uniform in thickness, measured using an average of micrometer screwguage readings. Each specimen so prepared was placed between two quartz windows with an aluminium spacer in a brass cell, which could be placed in a temperature controlled sample changer. The temperature was monitored using a single thermocouple at the centre of the rack. The samples were placed in LOQ, the small angle neutron diffractometer at the UK pulsed spallation source, ISIS, at the Rutherford Appleton Laboratory, Chilton, UK. Positions on the rack were aligned using a laser coincident to the neutron beam. Rack position, temperature and sample exposure time were controlled automatically using a command file on the LOQ front end computer. For each sample two measurements were made; the transmission and the small angle scattering. By placing the scintillation monitor immediately after the sample position and a collimation aperture to the incident beam the transmission as a function of wavelength was measured. The transmission of the sample was measured in comparison to a similar measurement of 'direct beam' where no sample is present. Small angle neutron scattering data were collected for 85μA hours and transmission for 15μAhours using the area detector, (μAhours are proportional to the integrated neutron flux). Each blend and the individual homopolymers were measured at temperatures of 373K, 363K, 353K and 343K.

4.10 Data analysis

Calibration data were collected by running transmission and scattering runs for direct beam measurement and a well-defined polymer blend and copolymer. A mask file is a computer file built using calibration data that establishes the default conditions for the reduction of the raw time of flight data into SANS cross section versus scattering vector data. It includes detector to spectrum mapping tables and applies necessary detector and time masks and coordinate corrections, it also ensures the reduced data is scaled by an appropriate calibration factor. The 'Collette[‡]' program was used to reduce experimental data; the raw data was divided by the monitor count, scaled by the direct beam for the detector efficiency, then scaled by radially averaging and the transmission and sample volume, weighting the masked data by zero and finally rebinning the data as a function of q.

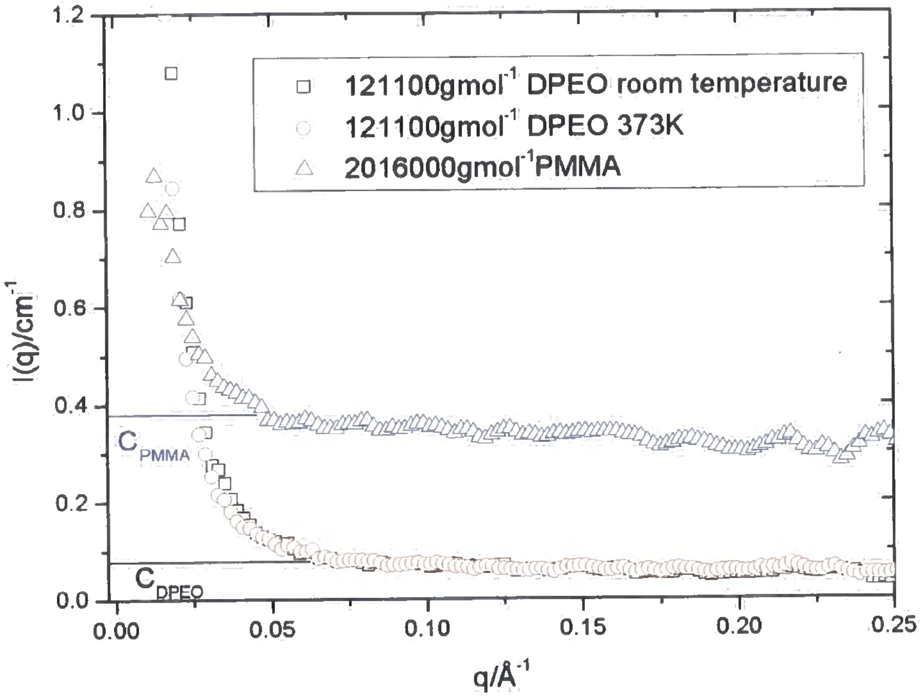

Figure 4.9 Scattering from pure DPEO and PMMA

The reduced elastic coherent scattering intensity $I(q)_r$ of the blend is required. Initially the total scattering of the sample is measured $I(q)$, which is the sum of elastic coherent, and background scattering (elastic incoherent and inelastic incoherent scattering). To correct for the background scatter, pure samples of the polymers in the blends were run at each temperature. The pure polymers produce coherent scattering but also provide a measure of the incoherent processes that the blend exhibits. A weighted sum of the background scattering from each pure component (C_i) should match that of the blend as described in by,

$$I(q)_r = I(q) - \varphi_{PMMA} C_{PMMA} - \varphi_{DPEO} C_{DPEO} \qquad \text{Equation 4.11}$$

The C_i value can be calculated but as the data show a clear horizontal plateau can be extracted directly, by taking an average of values between

---

[‡] Collette. (Various, ISIS)

$0.101 < q < 0.201$ Figure 4.9 shows that the background scattering arises substantially from the PMMA as there is greater incoherent scattering from hydrogen compared to deuterium. The background scattering from the DPEO and PMMA appeared to be temperature independent, indicating no change in polymer conformation or crystallinity, so only one value of C_i is required for all temperatures. Table 4.3 shows the values and standard deviation as extracted from Figure 4.9.

	C_i / cm^{-1}
DPEO room temperature	0.060 ± 0.007
DPEO 373K	0.062 ± 0.005
2016000 gmol^{-1} PMMA room temperature	0.333 ± 0.014

Table 4.3 Values of C_i as calculated from Figure 4.9, C_i is the average taken from $0.101 < q < 0.201$

A plot of $V(\Delta\rho)^2/I(q)_r$ against q^2 (an Ornstein-Zernike plot) should yield a straight line (Equation 4.6) where the intercept is related to the effective interaction parameter by Equation 4.9. The scattering volume V is calculated from the depth of the sample as measured by micrometer and the beam radius. $(\Delta\rho)^2$ is found from Equation 4.2, where polymer A is DPEO and polymer B is PMMA. The scattering length ρ_i of a given polymer is described by,

$$\rho_i = \frac{\sum b_i \rho_{d,i} N_a}{R_i} \qquad \text{Equation 4.12}$$

where R_i is the molecular mass of the monomer, b_i the coherent scattering lengths of the polymer, $\rho_{d,i}$ the density of the polymer and N_a Avagadro's constant. The densities of crystalline and amorphous DPEO are known.[11] As the samples are analysed above the melting temperature of DPEO the amorphous densities were used in all calculations. The mass composition is known for each blend hence, using the density, the volume fraction of each component within the blend can be calculated. An example of a plot of $V(\Delta\rho)^2/I(q)_r$ against q^2 is shown in Figure 4.10, a linear fit was typically found for $0 < q^2 < 0.01$.

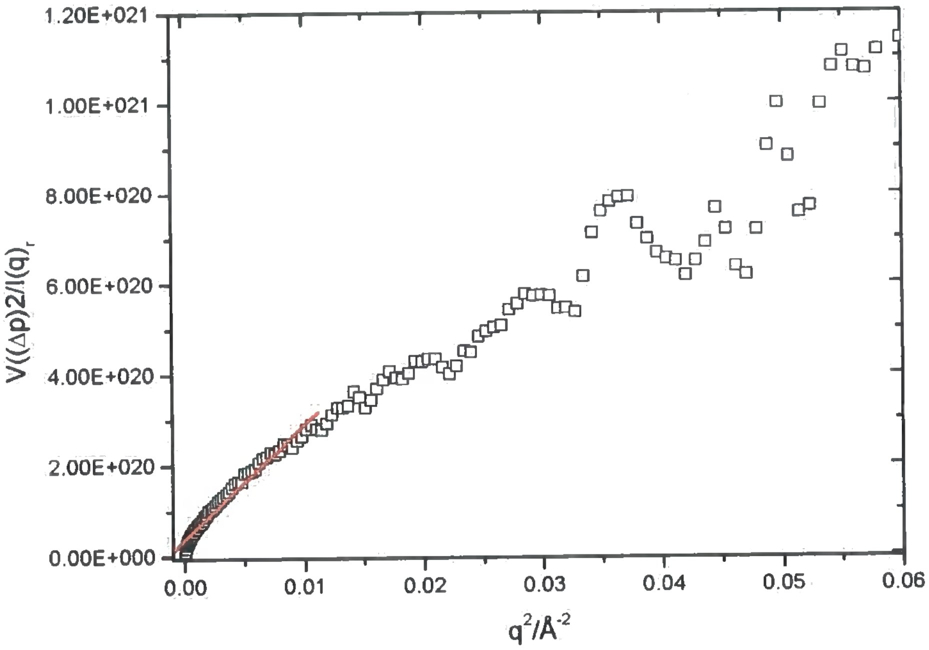

Figure 4.10 Calculation of *1/S(0)* for 6% by mass of 121100 gmol^{-1} DPEO in 213400 gmol^{-1} PMMA

The intercept with $q^2 = 0$ axis and Equation 4.9 can then be used to find χ_{eff}. Monomer volumes are assumed to be the same in the blend as in pure samples, so can be calculated using R_i and the densities. The condition $v_{PMMA} = v_{DPEO} = v_u$ does not hold, as the DPEO monomer is approximately 46% of the volume of a PMMA monomer. However, as PMMA is present at the higher volume fraction we define $v_{PMMA} = v_u$.

4.11 Results and discussion

Figure 4.11-4.14 show the variation of χ_{eff} with volume fraction of DPEO for various PMMA molecular weight blends. For all PMMA molecular weights χ_{eff} increases from a small negative value to a small positive value at approximately φ_{DPEO}=0.17, before decreasing again. The values of χ_{eff} indicate a homogeneous blend when $\varphi_{DPEO} < 0.17$ (and possibly above this value if a small positive χ is considered to provide a homogenous blend) at all temperatures in the range 343 K-373 K. Previous work has shown χ=-0.13 over the PMMA volume at 353 K for an unknown concentration of PEO in PMMA[2], which is not in good agreement with results here. Figure 4.13 shows unusual variation of χ_{eff} for 213400 gmol^{-1} PMMA samples, which is attributed to errors in two particular samples, possibly due to sample bubbling or defects.

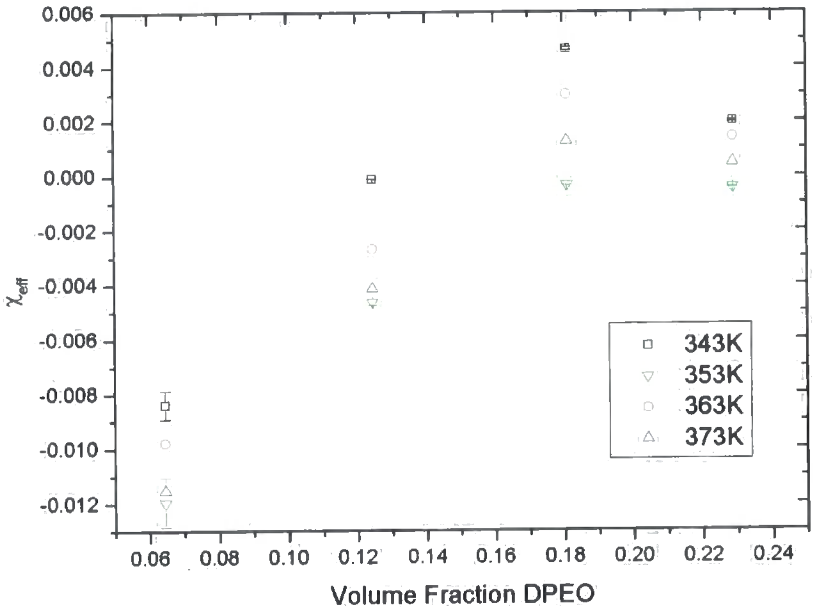

Figure 4.11 Plots of χ_{eff} for blends of 60200 gmol^{-1} PMMA and 121100 gmol^{-1} DPEO against volume fraction DPEO.

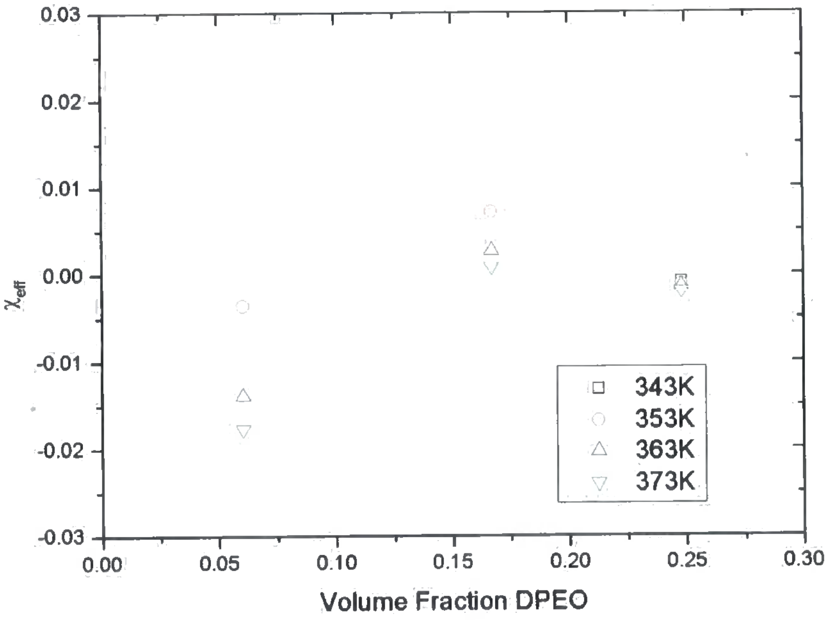

Figure 4.12 Plots of χ_{eff} for blends of 96200 gmol^{-1} PMMA and 121100 gmol^{-1} DPEO against volume fraction DPEO

Blends of DPEO and PMMA are known to be partially miscible which is confirmed by the composition dependence of χ_{eff}. The φ_{DPEO} above which the blend ceases to be homogenous[6,12] is typically given as ~0.3. The value of χ_{eff} for the highest concentration of DPEO (φ_{DPEO}=0.37), found here was small and indicated a homogenous blend. Previous SANS work[4] exhibited a slight downward curvature in the value of χ_{eff} at low φ_{DPEO} for 458 K-473 K, which became more obvious with increased *T*. In this study the composition dependence of χ_{eff} for a given blend appears to be the same for all temperatures. This is in contradiction to that found from previous work[4]. A composition dependence of χ_{eff} for polymer blends has been attributed to several factors. Flory-Huggins theory does not account for excess volumes of mixing for the two polymers in the blend. A negative volume change on mixing for PEO/PMMA blends has been found indicating that the two components of the blend are attractive[13] to each other but also indicating that Flory-Huggins theory may not be applicable. Another source of composition dependence of χ_{eff} values is the use of the random phase approximation with the assumption of incompressibility of polymer melts. It has been shown that volume changes from 0.05% on mixing produce significant composition dependence of χ_{eff} at the extremes of the concentration range[14]. Downward curvatures in the dependence of χ at the extremes of a composition scale indicate a negative excess volume and an attractive blend. The decrease in χ_{eff} as φ_{PEO} increases may be due to a change in polymer volume at that concentration.

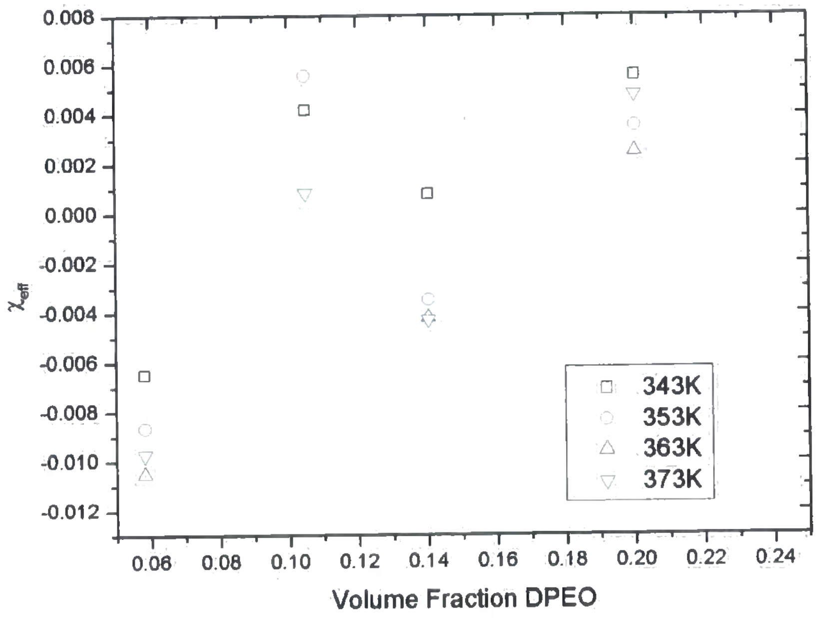

Figure 4.13 Plots of χ_{eff} for blends of 213400 gmol^{-1} PMMA and 121100 gmol^{-1} DPEO against volume fraction DPEO

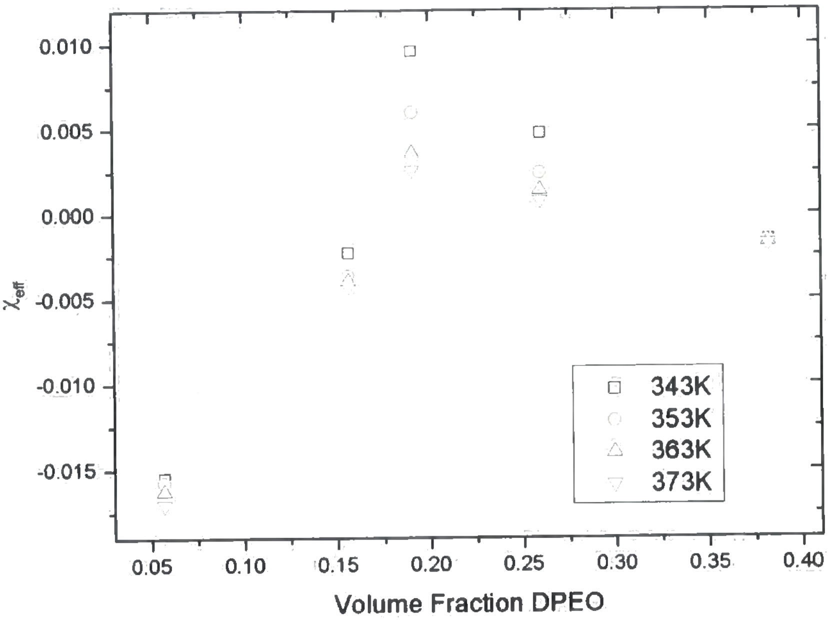

Figure 4.14 Plots of χ_{eff} for blends of 2016100 gmol^{-1} PMMA and 121100 gmol^{-1} DPEO against volume fraction DPEO

There is no physical basis for the interaction parameter being dependent on polymer molecular weight and χ is generally found experimentally to be independent of molecular weight.[15] Figure 4.15 shows the variation of χ_{eff} with molecular weight. There is no clear dependence on molecular weight and values are generally the same for all PMMA molecular weights utilised. From some neutron scattering experiments[3] it has been asserted that χ_{eff} has molecular weight dependence for blends of PMMA/DPEO but this is not supported here.

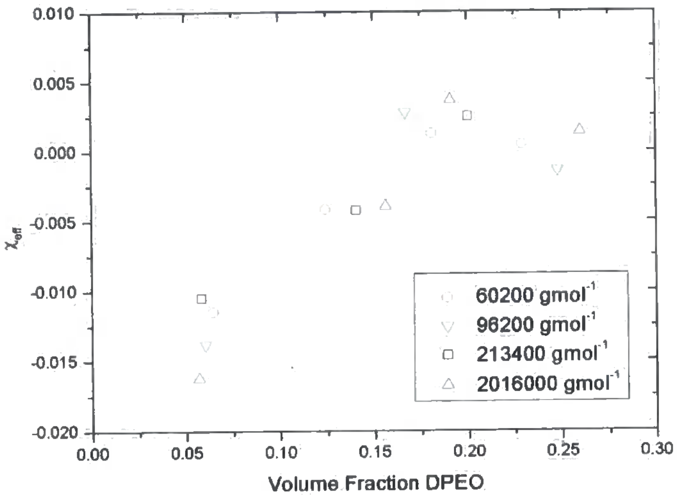

(A)

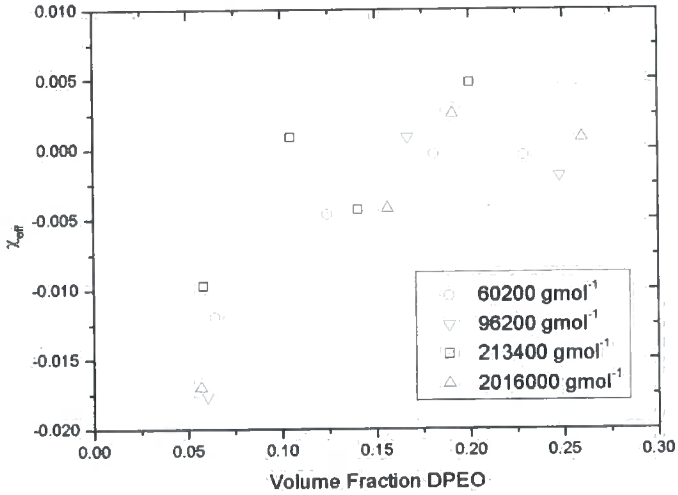

(B)

Figure 4.15 Plots of χ_{eff} against volume fraction for blends of various molecular weight PMMA and 121100 gmol^{-1} DPEO (A) 373 K and (B) 363 K

χ parameters from polymer blends are often found to be linear functions of reciprocal temperature ($1/T$)[15],

$$\chi(T) = A + \frac{B}{T} \qquad \text{Equation 4.13}$$

Sometimes the functions are non-linear and can be fitted with a quadratic[15],

$$\chi(T) = A + \frac{B}{T} + \frac{C}{T^2} \qquad \text{Equation 4.14}$$

A and B represent the enthalpic and entropic contributions respectively. Figure 4.16 and Figure 4.18 show the variation of χ_{eff} with $1/T$. χ_{eff} does not appear to vary linearly for all temperatures; hence for all concentrations of φ_{DPEO}, the variation of χ_{eff} with $1/T$ was fitted with both linear and polynomial forms and examples are shown in Figure 4.17 and Figure 4.19. All blends could be fit with a linear function, however non-linear fits often exhibited smaller errors (Figure 4.17 **A, B** and **D** and Figure 4.19 **C**). The curvature (and sign of A, B, C) were not consistent. If variation with $1/T$ is a quadratic, for all molecular weights and temperatures with the same φ_{DPEO} the sign of A, B, and C could be assumed to be the same. It was therefore assumed that the linear fit was the most reasonable.

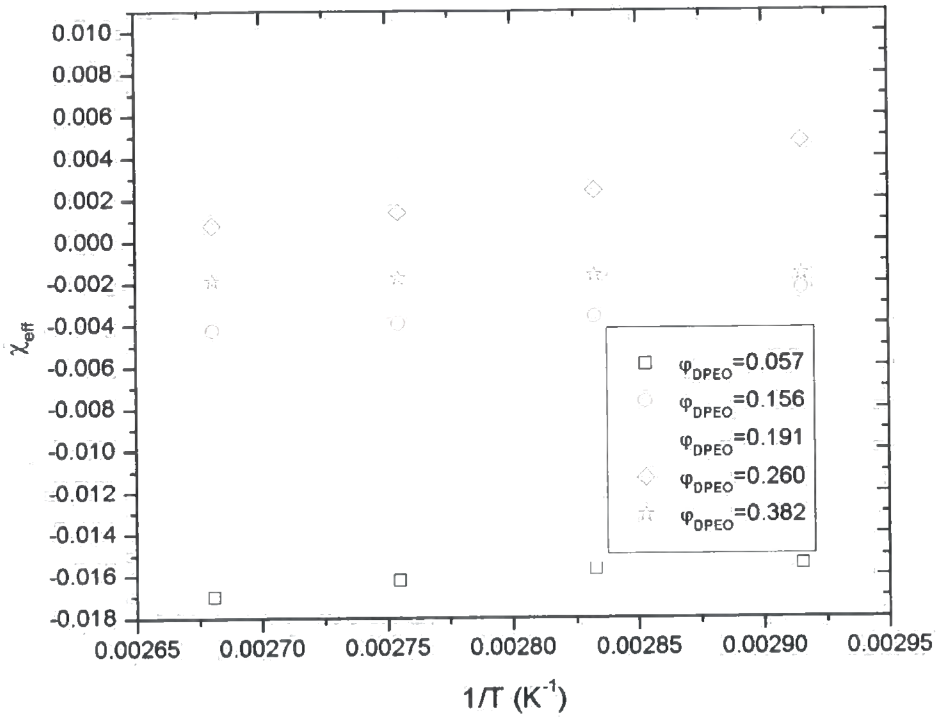

Figure 4.16 Plots of χ_{eff} against $1/T$ for 2016100 gmol^{-1} PMMA with various concentrations of 121100 gmol^{-1} DPEO

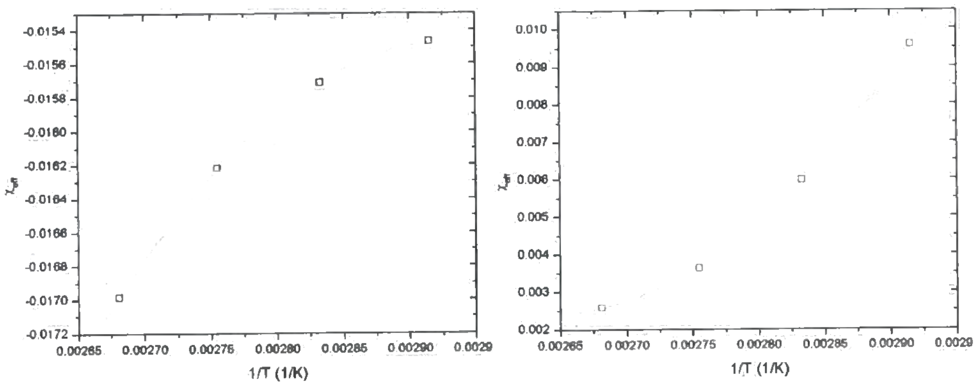

(A) (B)

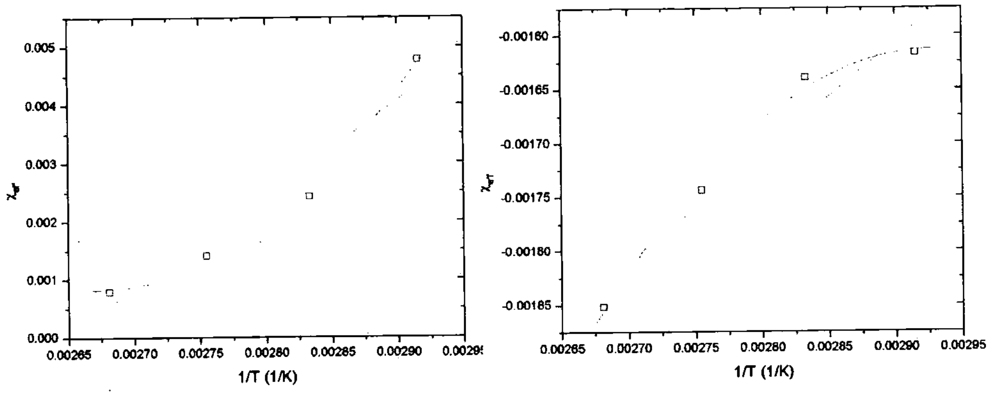

(C) (D)

Figure 4.17 Plots of χ_{eff} against 1/T for 2016100 gmol^{-1} PMMA and 121100 gmol^{-1} DPEO with linear (Equation 4.13) and non-linear fits (Equation 4.14). (A) 0.057=φ_{DPEO} (B) 0.19117=φ_{DPEO} (C) 0.2599=φ_{DPEO} (D) 0.38244=φ_{DPEO}

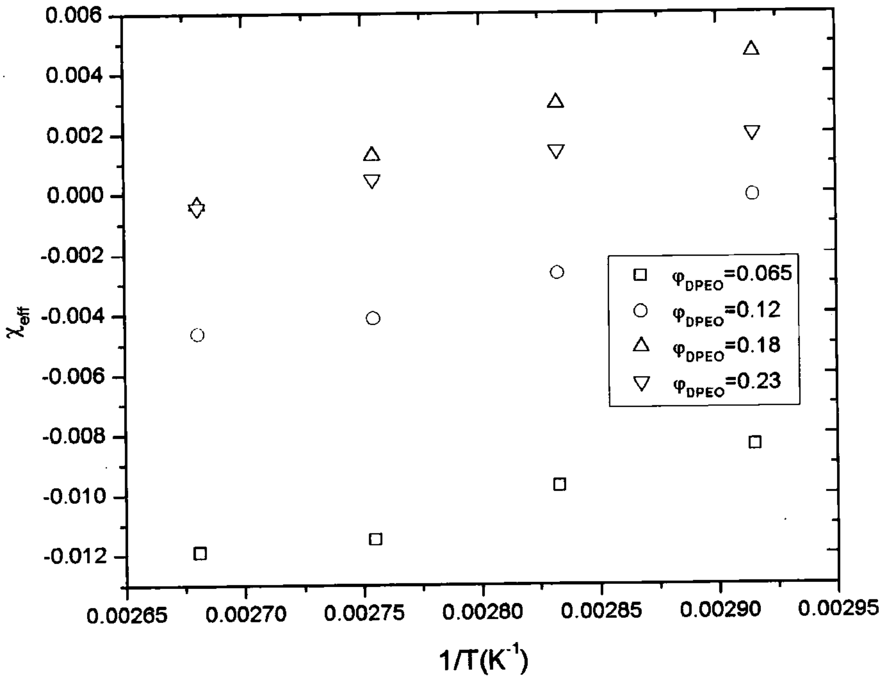

Figure 4.18 Plots of χ_{eff} against $1/T$ for 60200 gmol^{-1} PMMA with various concentrations of 121100 gmol^{-1} DPEO

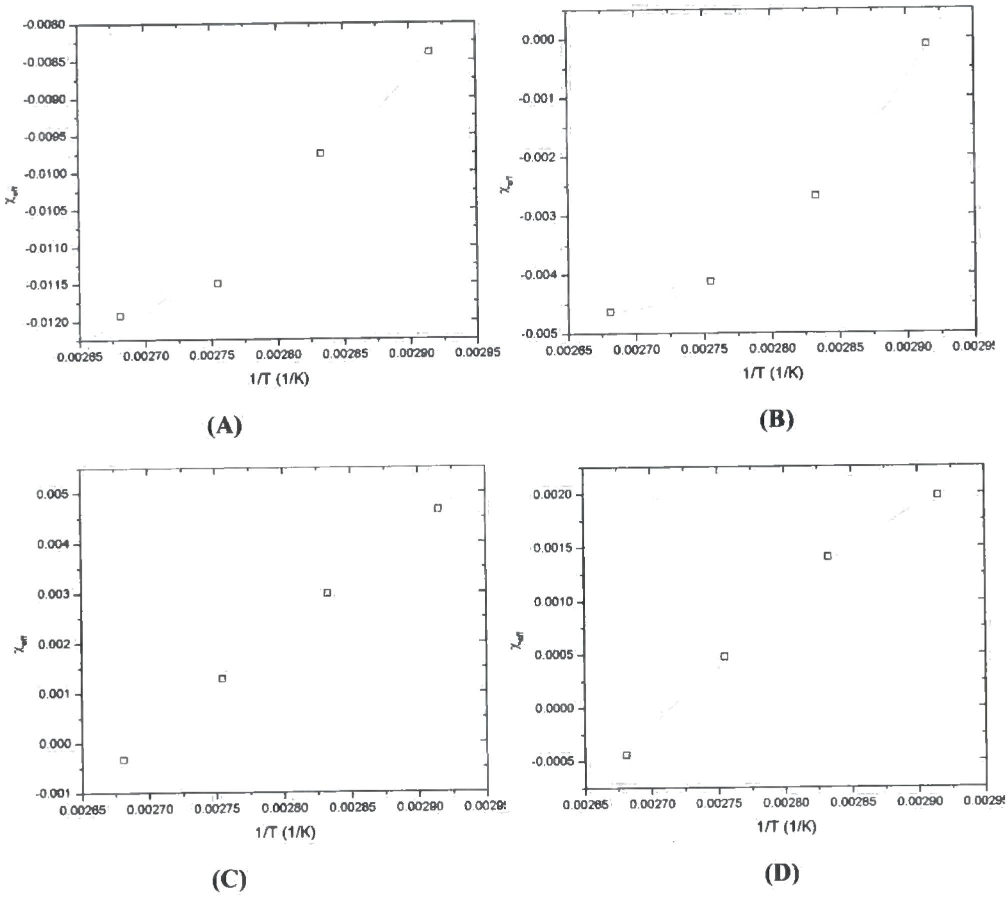

(A) **(B)**

(C) **(D)**

Figure 4.19 Plots of χ_{eff} against 1/T for 60200 gmol^{-1} PMMA and 121100 gmol^{-1} DPEO with linear (Equation 4.13) and non-linear fits (Equation 4.14) (A) 0.0645=φ_{DPEO} (B) 0.12449=φ_{DPEO} (C) 0.1811=φ_{DPEO} (D) 0.22896=φ_{DPEO}

Examples of A and B for linear fits, as calculated, are shown in Table 4.4 and Table 4.5. Linear fits gave the smallest errors in parameters A and B when $\varphi_{DPEO} \approx 0.18$ or the turning point of the χ_{eff} versus φ_{DPEO} plot. Should χ_{eff} increase non-linearly with $1/T$, the resultant phase diagrams will differ from that for linear variation with $1/T$, schematics of two of these phase diagrams are shown in Figure 4.20.

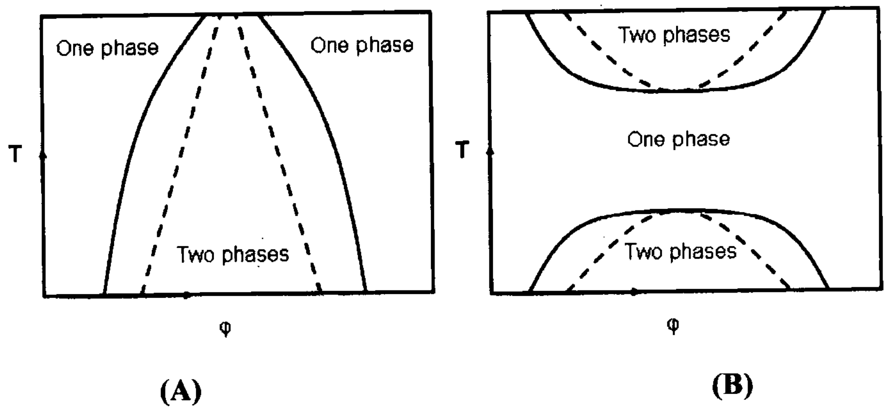

Figure 4.20 Schematics for predicted binodal (solid line) and spinodal (dashed line)[15] of blends with (A) positive χ that increases non-linearly with $1/T$ and $C \neq 0$ and (B) positive χ that is non-monotonic with temperature and $C > 0$

For negative C phase diagrams will display a 'neck' at high T; increasing temperature will result in relatively little increase in miscibility at higher temperatures. For a positive C, the phase diagram will abruptly flatten out and a sudden change in miscibility at a certain temperature for a broadened range of φ_{DPEO} will be observed[15].

φ_{DPEO}	A	B(K^{-1})
0.057	-0.034 ± 0.003	6 ± 1
0.084	-0.025 ± 0.006	8 ± 2
0.156	-0.08 ± 0.01	30.1 ± 0.2
0.191	-0.044 ± 0.009	17 ± 3
0.260	-0.005 ± 0.009	1.03 ± 0.2
0.382	-0.048 ± 0.006	13 ± 3

Table 4.4 Parameters of the temperature dependence of χ_{eff} for DPEO/PMMA, (PMMA= 2016100 gmol^{-1}) as described by (Equation 4.13)

φ_{DPEO}	A	B(K^{-1})
0.065	-0.055 ± 0.006	16 ± 2
0.124	-0.06 ± 0.01	19 ± 4
0.181	-0.057 ± 0.001	21.3 ± 0.3
0.229	-0.028 ± 0.001	10.4 ± 0.9

Table 4.5 Parameters of the temperature dependence of χ_{eff} for DPEO/PMMA, (PMMA= 60200 gmol^{-1}) as described by (Equation 4.13)

Linear fits were reasonable and the signs of A and B indicate that the system exhibited upper critical solution behaviour in agreement with previous work using SANS and similar data analysis[4] but in contradiction to other SANS work[3], pressure measurements[3] and states of matter theory[13,16] which predicted lower critical solution temperature behaviour (LCST). The value of χ_{eff} at the spinodal temperature, below which the blends phase separate instantly, is given by,

$$\chi_{eff}^{s} = \frac{v_u}{2}\left(\frac{1}{v_{DPEO}\varphi_{DPEO}N_{DPEO}} + \frac{1}{v_{PMMA}\varphi_{PMMA}N_{PMMA}}\right) \qquad \text{Equation 4.15}$$

For example, for φ_{DPEO}=0.5 and φ_{DPEO}=0.18 the values are calculated as shown in Table 4.6 using Equation 4.15 and values listed in Table 4.7. It can be seen that molecular weight has a larger influence on predicted spinodal values than volume fraction. However values are in near agreement with those previously calculated from SANS work[4] (320 ± 100 K).

PMMA molecular weight /gmol^{-1}	φ_{DPEO}=0.18 121100gmol^{-1} DPEO/ K	φ_{DPEO}=0.5 121100gmol^{-1} DPEO/ K	φ_{DPEO}=0.18 170700gmol^{-1} DPEO/ K
2016000	331	338	334
213400	330	336	333
96200	328	333	331
60200	326	330	329

Table 4.6 Showing the spinodal at various PMMA molecular weights and DPEO molecular weights at two concentrations

In previous work[3] it has been proposed that entropic contributions to χ_{eff} in mixtures of DPEO and PMMA are dominant. However, later work[17] showed that enthalpic interactions were dominant. This enthalpic contribution is attributed to the specific interaction between the negative oxygens in PEO and positive carbonyl carbons in PMMA. Values of χ_{eff} were similar for various molecular weights of PMMA as would be expected if χ_{eff} is molecular weight independent. An average over all molecular weights and compositions is given in Table 4.7 and is compared to a similar average from the work by Hopkinson[4] *et al*, whose work was carried out above the T_g of the PMMA component of the blend on similar molecular weight polymers. There was agreement with this work over the comparative size of enthalpic and entropic contributions. The similarity of the values obtained suggests that interactions in the samples may be considered the same above and below the T_g of PMMA.

	A	B(K^{-1})
Average	-0.06 ± 0.01	21.57 ± 4.11
Previous work	-0.055	16.75 ± 8.25

Table 4.7 Parameters of the temperature dependence of χ_{eff} for DPEO/PMMA, from this work and previous work[4]

4.12 Summary

SANS was used to find χ_{eff}. Values were in good agreement with previous work and suggest that the blend exhibits upper critical solution temperature behaviour. Enthalpic interactions are dominant for blends of PMMA and DPEO. χ_{eff} was found to be concentration dependent at the temperatures utilised for ion beam experiments (above the T_m of DPEO but below the T_g of PMMA).

4.13 References

(1) Liberman, S. A.; Gomes, A. D.; Macchi, E. M. *Journal of Polymer Science Part a-Polymer Chemistry* **1984**, *22*, 2809-2815.

(2) Cortazar, M. M.; Calahorra, M. E.; Guzman, G. M. *European Polymer Journal* **1982**, *18*, 165-166.

(3) Ito, H.; Russell, T. P.; Wignall, G. D. *Macromolecules* **1987**, *20*, 2213-2220.

(4) Hopkinson, I.; Kiff, F. T.; Richards, R. W.; King, S. M.; Farren, T. *Polymer* **1995**, *36*, 3523-3531.

(5) Achorn, P. J.; Ferrillo, R. C. *Journal of Applied Polymer Science* **1994**, *54*, 2033-2043.

(6) Li, X.; Hsu, S. L. *Journal of Polymer Science Part B-Polymer Physics* **1984**, *22*, 1331.

(7) Rieger, J. *Polymer Testing* **2001**, *20*, 199-204.

(8) Degennes, P. G. *Scaling Concepts in Polymer Physics*; Cornell University Press: Ithaca, New York, 1979.

(9) Doi, M. *Introduction to Polymer Physics*; Oxford University Press: Oxford, 1996.

(10) Roe, R.-J. *Methods of X-Ray and Neutron Scattering in Polymer Science*; 1st ed.; Oxford University Press, 2000.

(11) Karim, A.; Mansour, A.; Felcher, G. P.; Russell, T. P. *Physica B* **1989**, *156*, 430.

(12) Jin, X.; Zhang, S. H.; Runt, J. *Macromolecules* **2004**, *37*, 8110-8115.

(13) Privalko, V. P.; Petrenko, K. D.; Lipatov, Y. S. *Polymer* **1990**, *31*, 1277-1282.

(14) Kumar, S. K. *Macromolecules* **1994**, 260.

(15) Balsara, N. P. In *Physical Properties of Polymers Handbook*; Mark, J. E., Ed.; Woodbury: New York.

(16) Cimmino, S.; Martuscelli, E.; Silvestre, C. *Polymer* **1989**, *30*, 393-398.

(17) Russell, T. P.; Ito, H.; Wignall, G. D. *Macromolecules* **1988**, *21*, 1703-1709.

Chapter 5

Elastic Recoil Detection of diffusion of DPEO and PMMA

5.1 Introduction

Previous NRA experiments (chapter 3) have shown that diffusion of DPEO into PMMA displayed slowing down and unusual interfacial broadening. It is important therefore to see if the diffusion profile for PMMA can provide further information about the diffusion process. ERD, unlike NRA is sensitive to both ^1H and ^2H and is therefore a suitable tool for looking at DPEO and PMMA. To remove any possibility of thin film effects, a DPEO layer of >50 nm is required. Theories of case II diffusion often rely upon one component acting as a 'well' displaying no dilution, a DPEO film thickness >50 nm may allow this assumption to be taken and the diffusion more expansively investigated. Samples containing 300 nm of DPEO on bulk PMMA (>1 μm, but resolvable to ~400 nm) should be the limit of film thicknesses resolvable by ERD. It is necessary to make experimental refinements, such as optimising experimental geometry, beam energy and choice of stopper foil to allow these samples to be successfully profiled. Calculation of a depth profile from collected data requires the correct energy per channel, foil depth and stopping powers to be found and assessed. With variation of beam energy it is important to analyse the impact of beam damage on calculated depth profiles. Surface roughness must also be defined. With any interfaces present in the annealed samples corresponding to different regions of the ERD spectra (relating to both ^1H and ^2H peaks), interfaces present in depth profiles are defined and fitting methods discussed. Diffusion behaviour of both DPEO and PMMA is compared to Fickean and case II diffusion.

5.2 *Experimental refinement*

5.2.1 Experimental geometry

The traditional ERD[1] commonly used in polymer systems utilises a geometry where $\alpha_1=\alpha_2=15°$ and $\Phi=30°$, (Figure 2.2) a 3.0 MeV ^4He incident beam and a 10.6 μm Mylar™ foil which results in a depth of 800 nm being accessible with a depth resolution of 80 nm. The limit of depth resolution of this system is largely due to the straggling of ^2H and ^1H in the stopper foil. The resolution can be improved by decreasing E_{in}, allowing a thinner stopper foil, varying α_1, and using heavier projectiles. High E_{in} (>3.0 MeV) is required to analyse depths of up to 800 nm. If $\Phi=30°$, $\alpha_1=15°$, path lengths of the incoming and the outgoing beams are the same. When $\alpha_1>15°$, the path length of the outgoing particle is longer than the path length for the incident particle. As ^4He is most affected by the stopping power of the polymer sample, the range analysed is maximised by minimising the incident path length for the depth normal to the surface. ^1H and ^2H are less affected so a long path length is acceptable. Therefore an experimental geometry of $\Phi=30°$, $\alpha_1=19°$ was utilized for experiments here.

5.2.2 Stopping powers

For these experiments ions will pass through DPEO and PMMA. Calculation of stopping power by SRIM® requires both elemental stoichiometry and density, the density of DPEO depends on whether it is crystalline or amorphous. The stopping powers of PMMA for ^1H, ^2H and ^4He ions lie between the stopping powers for amorphous and crystalline PEO. Hence, the stopping powers for PMMA were treated as the bulk stopping powers for the sample.

5.2.3 Beam Energy

It is possible for resonances to occur at certain energies for some nuclei. The deuterium cross section is known[2] to have a resonance at 2.135 MeV. This resonance can result in significant inaccuracies in subsequent depth profiles. It is therefore preferable for ^{4}He to not exhibit energies near the resonance energy both at the surface and after subsequent energy loss from traversing the sample. The loss of energy of a ^{4}He ion as it passes through the sample can be described by the function of the stopping power with depth. Hence for incident energy of 3245 keV, the energy of ^{4}He (α_I=19°) at a depth 1 μm normal from the surface is 2795 keV. This value is sufficiently distant from the resonance value of 2135 keV for the resonance of the cross section of deuterium to be ignored.

5.2.4 Energy per channel

To create a depth profile, 'channels' needs to be converted to energy. The keV/ch (keV per channel) for the experimental beam energy can be calculated using a calibration sample of sub-nanometre depth layer of gold on silicon, a ^{4}He incident beam of 3.245 MeV with no foil present, Φ=150° and θ=0. The energy of ^{4}He recoiled from Au and Si, (E_{out}) can be calculated using (Equation 2.3), If E_{in} is known (3.245 MeV), E_{out} can be calculated when $\Phi = 30$. A linear function of calculated energy with channel found from the spectrum provides keV/ch as the gradient and the 'offset' as the intercept; so that keV/ch=2.4829, offset= 66.564 keV.

5.2.5 Stopper Foil

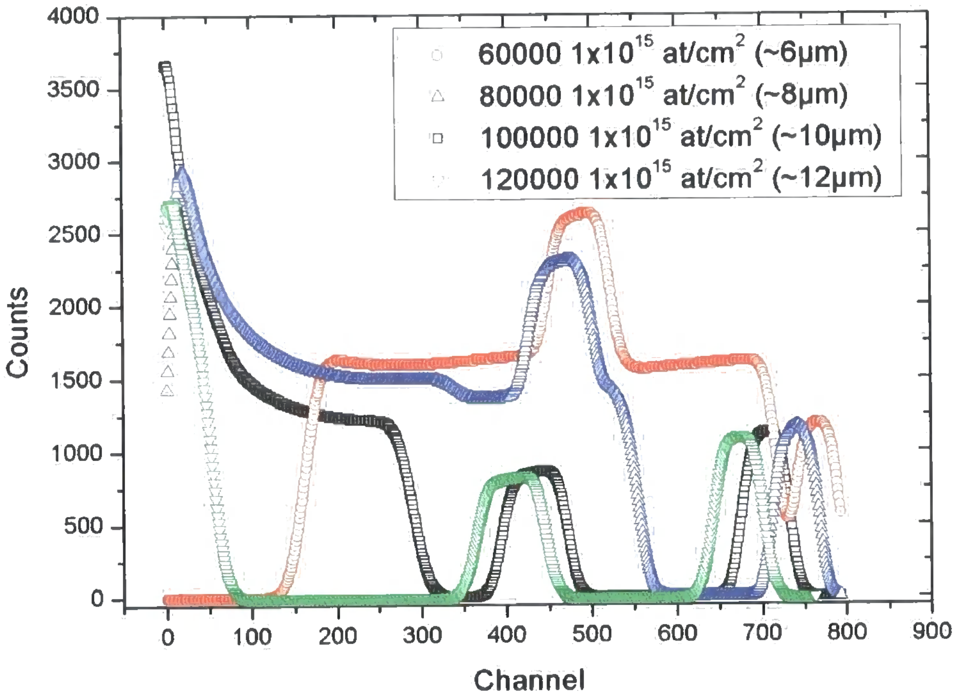

Figure 5.1 Simulation for various stopper foil thickness for a target of 3000 atoms/cm^2 (approx 300 nm) DPEO on 4800 at/cm^2 (approx 480 nm) PMMA on silicon block. E_{in}=3.245 MeV, α =19°, Φ=29.5°, Energy per channel 2.483 keV, detector resolution 50 keV.

The stopper foil is required to remove as much of the forward-scattered ^{4}He signal as possible, without blocking the recoiled ^{1}H and ^{2}H too significantly. With an energy of approximately 3.25 MeV chosen for the incident ^{4}He ions, SIMNRA was used to simulate the spectra for a typical sample (300 nm layer of DPEO over 400 nm PMMA on a silicon substrate), for various depths of Mylar^{TM}. Experimental optimisation required the ^{1}H and ^{2}H peaks to be distinct and separated by enough channels for peak broadening from polymer diffusion to be resolvable. Peaks should also not form a Gaussian shape, which indicates that depth information has been lost in the stopper foil, and have a clear edge at higher energies. The ^{4}He peak should still appear in the spectra at low energies but should be separated from the ^{1}H and ^{2}H peaks. From Figure 5.1 a foil of depth 10 µm was considered to be the best choice.

An effective depth of the stopper foil is needed for calculating the energy loss experienced by recoiled particles, and subsequently the depth of origin. The thickness can be calculated by using the Φ=30°, α=19° and ^{4}He incident energy 3.45 MeV with and without a foil for a sample of gold on silicon. The effective depth is 9.81 μm and this value is used in all energy to depth conversions for this experimental set-up.

5.2.6 Resolution and beam damage

For a system with perfect resolution, where stopping power and scattering cross-section are independent of incident ^{4}He energy the calculated volume fraction profile should resemble a 'top hat' function. The actual profile is a convolution of this shape with a Gaussian of root mean square deviation $\sigma_g(z)$ representing the finite system resolution,[3] which can be assumed constant at a given depth and hence each convoluted step is given by an error function, which can be approximated by a hyperbolic tangent,

$$\varphi(z) = \frac{1}{2} + \frac{1}{2}\tanh\left(\frac{z - z_i}{w_{tot}}\right) \quad i = 1,2 \qquad \text{Equation 5.1}$$

$\varphi(z)$ is the volume fraction of the deuterated polymer at depth z. z_1 is the position of the air/polymer interface and z_2 the polymer/silicon interface. A direct measure of the system resolution w_{tot} is related by, $w_{tot} = 1.1\sigma_g = \sqrt{(12/\pi)}$. The error in this approximation is negligible compared to the scatter of data points. w_{tot} can have several contributions including the broadening interface, surface roughness, Gaussian instrumental resolution and beam damage. Polymers are sensitive to exposure to ionising radiation which, depending on the type of polymer is capable of exciting electronic states of the polymer molecules and consequently causing chemical changes. These can include cross-linking, disintegration, chain scission and gas evolution.[4] At approximately 2-3 MeV ^{4}He ions cause polymer cross-linking and the polymer loses matter as small molecules ($^1H_2$, $^2H_2$ and $^1H^2H$) which are desorbed. These losses persist indefinitely.[5] Beam damage can be minimized by minimizing the energy of the incident ions, total charge deposited and environmental conditions such as atmosphere and temperature. The ion beam end station is fitted with a liquid nitrogen cooling system. A platinum resistance thermometer can be used to calculate the temperature of the sample rack and sample holder. Maintaining a temperature T, below 193 K, minimizes beam damage. With the energies required to probe up to 1 μm with ERD, beam damage should be significant. w_{tot} can thus be described,

$$w_{bd} = \sqrt{w_{tot}^2 - w_{res}^2} \qquad \text{Equation 5.2}$$

where w_{bd} is the width attributed to beam damage and w_{res} to instrumental resolution. The resolution of the system with depth was calculated using a range of depths of hydrogenous and deuterated polystyrene (HPS and DPS), spun onto silicon wafers. PS has a similar stopping power to PMMA and is known to have a better resilience to beam damage than PMMA or DPEO, hence beam damage can be ignored when calculating w_{tot}, so that $w_{tot} = w_{res}$. Spectra were obtained for doses of 0.5 μC and a cooling system was also utilized to minimize beam damage further. Spectra were normalized and placed on a depth scale as described in 2.3.5.1 and 2.3.5.2. Resolution was calculated by fitting the high and low energy fronts of ^{1}H and ^{2}H peaks respectively using Equation 5.1. w_{res} as a function of depth is plotted in Figure 5.2.

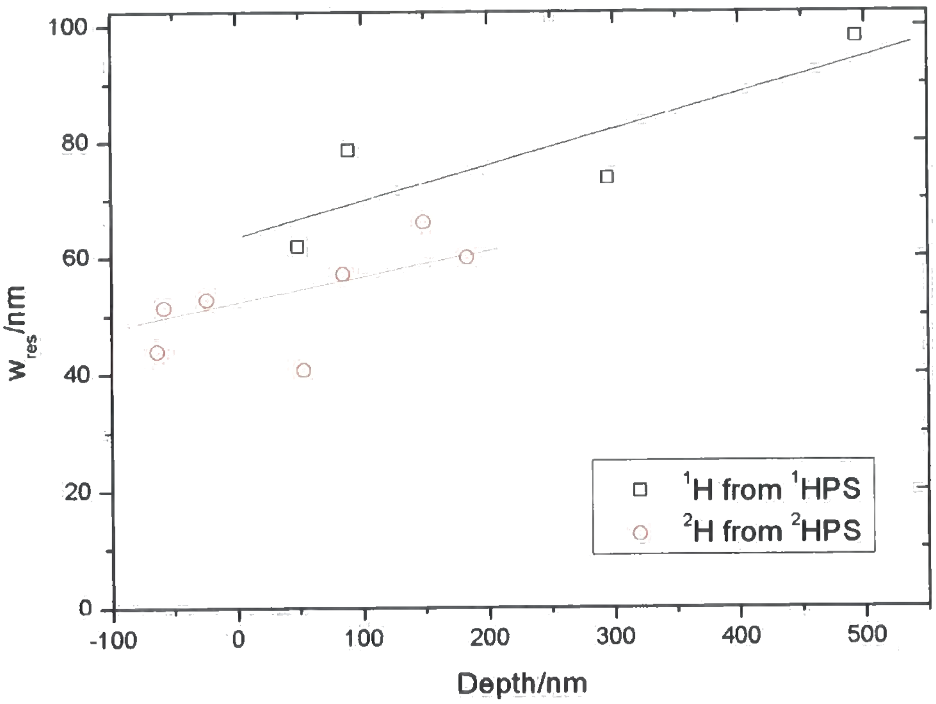

Figure 5.2 Showing resolution, w_{res} as a function of depth for ^{2}H and ^{1}H recoiled from DPS and HPS respectively as found from an ERD experiment with ^{4}He incident energy=3.245MeV, α =19°, Φ=30° and a 9.81μm stopper foil is placed in front of the detector The lines represent the best fit for a linear relation between resolution and depth.

w_{bd} can then be calculated for samples of DPEO and PMMA. Samples were exposed to sequential doses of 0.12 μC of ^{4}He beam on the same spot with the cooling system on. w_{tot} was then calculated for the DPEO top and bottom surface as well as the PMMA top surface, w_{res} is described by the linear fits described in Figure 5.2 and consequently w_{bd} was calculated according to Equation 5.2.

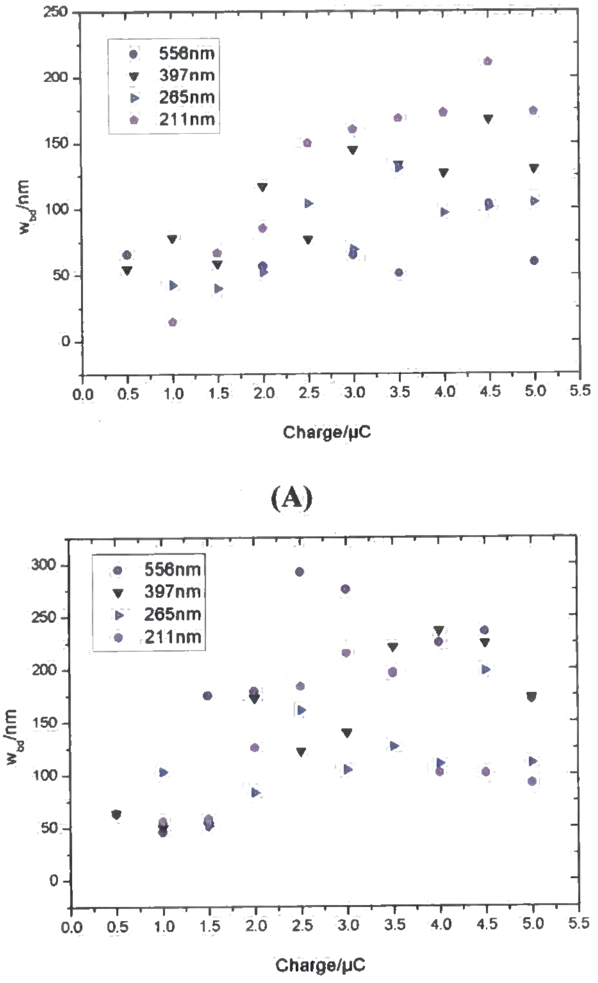

(A)

(B)

Figure 5.3 Plot of w_{bd} for (A) DPEO interface and for (B) PMMA interface against total charge for various depths of 77800 gmol^{-1} DPEO on >1μm 1600 gmol^{-1} PMMA. Using an ERD experiment where ^{4}He incident energy=3.245 MeV, α=19°, Φ=30°, a 9.81 μm stopper foil is placed in front of the detector and a cooling system maintains the sample rack at a temperature 188 K < T < 193 K

Figure 5.3 shows that appreciable beam damage occurs for samples at the energies utilized, especially for doses of >1 μC. There is no clear correlation between effective beam damage and dose although damage generally increases with dose. The dose needs to be minimized (for example to 0.5 μC) without losing information as a result of low counts and hence poor resolution. Low dose spectra can be added together to improve statistical significance.

There is no clear molecular weight dependence for beam damage. This is unsurprising as beam damage should only be influenced by the elemental stoichiometry and bond type. There is a relationship between beam damage and the depth of the interface. It is believed that this is due to the retention of released radicals or small molecules within thicker films due to further reaction with polymer chains whilst diffusing to the surface.[5] PMMA is believed to be more sensitive to ^{4}He radiation energies used in ERD than PEO.[4] PMMA has also been shown to lose ^{1}H faster than ^{2}H and this process is independent of initial bond type and atom environment.[4] For the system where PMMA is the 'substrate' it is hence afforded some protection by the PEO layer. The total contribution of beam damage to w_{tot} for various molecular weights is approximately 20%, a similar value to the resolution function. A straight line relation of beam damage to depth for the individual polymers can thus be determined and can be convoluted into calculations of w_{tot}. By comparing beam damage for the individual polymers for given depths, it can be seen that the PMMA receives comparatively higher damage than DPEO, despite being protected by the DPEO layer, as shown for one typical interface in Figure 5.4.

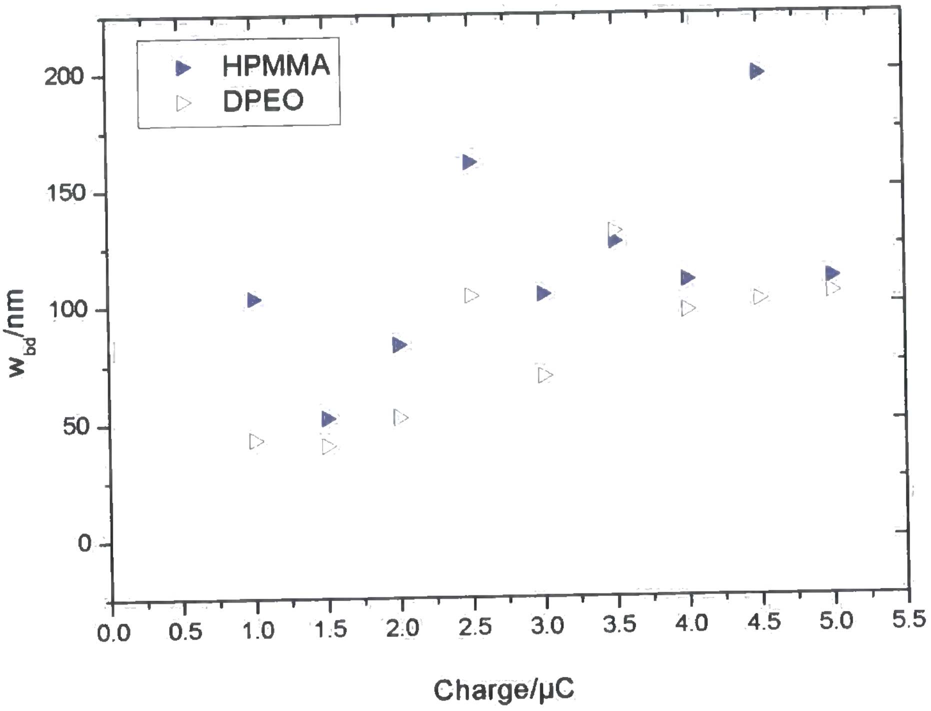

Figure 5.4 Plot of w_{bd} for PMMA/DPEO interface at a depth 265 nm from the surface against total charge. Molecular weights of 77800 gmol^{-1} DPEO and 1600 gmol^{-1} PMMA. Using an ERD experiment where ^{4}He incident energy=3.245 MeV, α=19°, Φ=30°, a 9.81 μm stopper foil is placed in front of the detector and a cooling system maintains the sample rack at a temperature 188 K < T < 193 K

5.2.7 Effect of surface roughness

During ion beam analysis a rough surface will affect the energies of particles entering and emerging from the sample as described in section 2.4.4. In order to assess the effect for ERD samples, the roughness thickness distribution of the sample surface needs to be found. Samples were made in a similar fashion to ERD experiments (section 5.3.2). Surface roughness was analysed using the digital instrument AFM Nanoscope IV as described in section 2.8. As with the NRA samples, surface roughness was found to never be more than approximately 10% of the initial DPEO depth. These values were then be used to simulate the effect of surface roughness on ion beam spectra.

SIMNRA[6] was used to simulate the ERD system using no roughness distribution, AFM measured values for roughness, and the 'worst case scenario'; simulations with a thickness distribution the same size as the DPEO film were created. These were then compared with experimental data. A typical example is shown in Figure 5.5. Where AFM shows the roughness to be 50 nm, the best fit for experimental data, including the 'tail' for both ^{1}H and ^{2}H peaks, gives a roughness of the layer >50 nm. Hence the surface roughness is an important factor in the shape of unannealed profiles and profiles after heating, but is not the major contribution to the experimentally observed 'tail', which is likely to indicate statistical error, instrumental resolution or beam damage as a greater factor.

As the change in surface roughness is not predictable with increasing heating times and therefore PEO distribution, it cannot be continuously accounted for when looking at diffusion widths. Compared to data for annealed samples, the surface roughness only accounts for a very small part of the diffused tail as shown in Figure 5.5 . With increased anneal time, surface roughness decreases, so for most annealed samples, roughness is a less significant contribution to effective width than beam damage or resolution. ERD surface roughness can be considered as a similar source of error in calculating width as statistical noise.

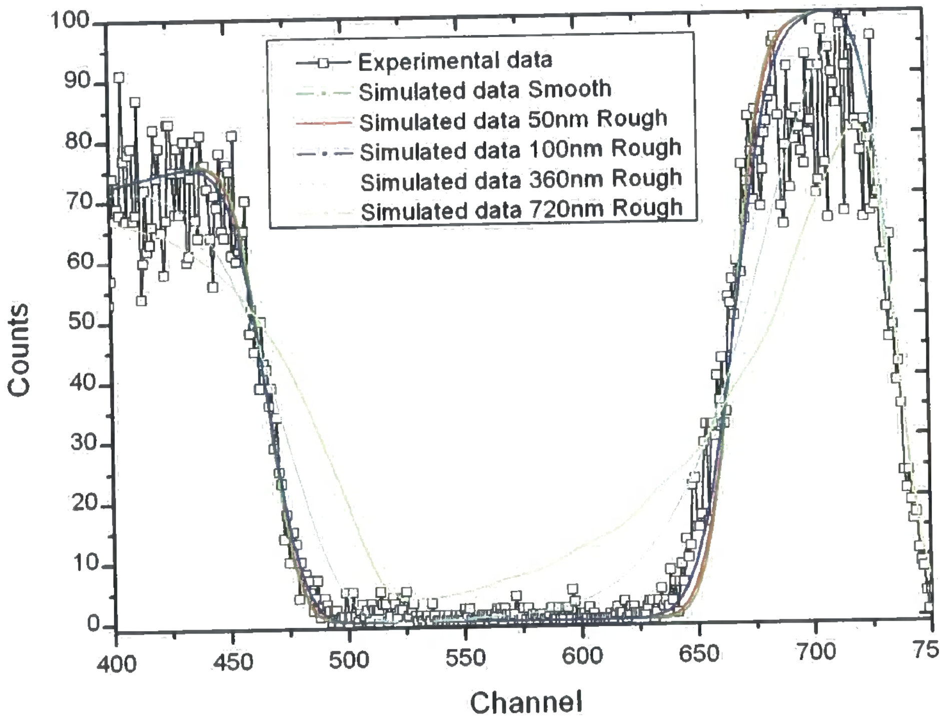

Figure 5.5 Experimental data and simulated data for ~300 nm DPEO, Mw= 77800 gmol^{-1}, on ~800 nm relaxed PMMA Mw=213400 gmol^{-1}, with various FWHM roughness.

5.3 *Experimental*

5.3.1 Materials

The polymers listed in Table 5.1 were utilised during this experiment, complete details of characterisation are in Appendix I. All polymers were above their individual entanglement molecular weight ($M_{e,PMMA}$=10000 gmol^{-1} and $M_{e,PEO}$=1700 gmol^{-1})[7]

Polymer	M_w/ gmol^{-1}	M_n/ gmol^{-1}	Polydispersity
DPEO	170700	165000	1.04
DPEO	121100	119100	1.02
DPEO	89217	82210	1.09
DPEO	17300	14800	1.03
PMMA	60200	59600	1.01
PMMA	96200	93000	1.03
PMMA	182400	153400	1.19
PMMA	213400	178000	1.20
PMMA	2016000	1903000	1.06

Table 5.1 Materials

5.3.2 Bilayer construction

Bilayers of all combinations of the polymers in Table 5.1 were constructed using spin coating. A thick film of ~1 μm PMMA was spun onto a silicon wafer from a solution in toluene. The PMMA was then relaxed by heating overnight at 413 K. After cooling, a thin film of DPEO approximately 300 nm thick was spun directly onto the PMMA from a solution in methanol. The wafers were then broken up into smaller pieces and heated in a vacuum oven at various anneal temperatures and times. Previous NRA experiments had demonstrated suitable temperatures and time regimes for annealing. Samples were heated at 373 K, 363 K, 353 K and 343 K for a range of times up to 48 hours. Temperature was measured by the digital oven display. Once removed from the vacuum oven, the samples were quenched on an aluminium block at ambient temperature. The time taken for the oven to evacuate and repressurise limited the anneal time to a minimum of 10 minutes. Samples were examined using an optical microscope to check for dewetting.

5.3.3 ERD measurements

Bilayers of the same type were placed on the same racks. Samples were analysed using a 3.245 MeV beam of ^{4}He ions. θ=70°,Φ≈30° and a Mylar^{TM} foil of 9.81 μm depth placed in front of the detector. Each sample was exposed to a charge of 0.5 μC on two separate areas. Counts for both samples were then summed. The temperature of the rack was maintained below 193 K throughout the measurement.

5.4 *Data Analysis*

5.4.1 Depth scale conversion and normalised yield

Channel was converted to depth using a spreadsheet discussed in section 2.3.5.1. To account for variation in forward scattering angle between samples, the surface channel was first defined by using least squares fitting and Equation 5.3 so the precise angle of the detector could be calculated. The volume fraction of a given species at a given depth was calculated as described in 2.3.5.2.

5.4.2 Raw data and interface definitions

Figure 5.6 shows typical raw data for bilayers that included 89217 gmol^{-1}, 121100 gmol^{-1} and 170700 gmol^{-1} DPEO.

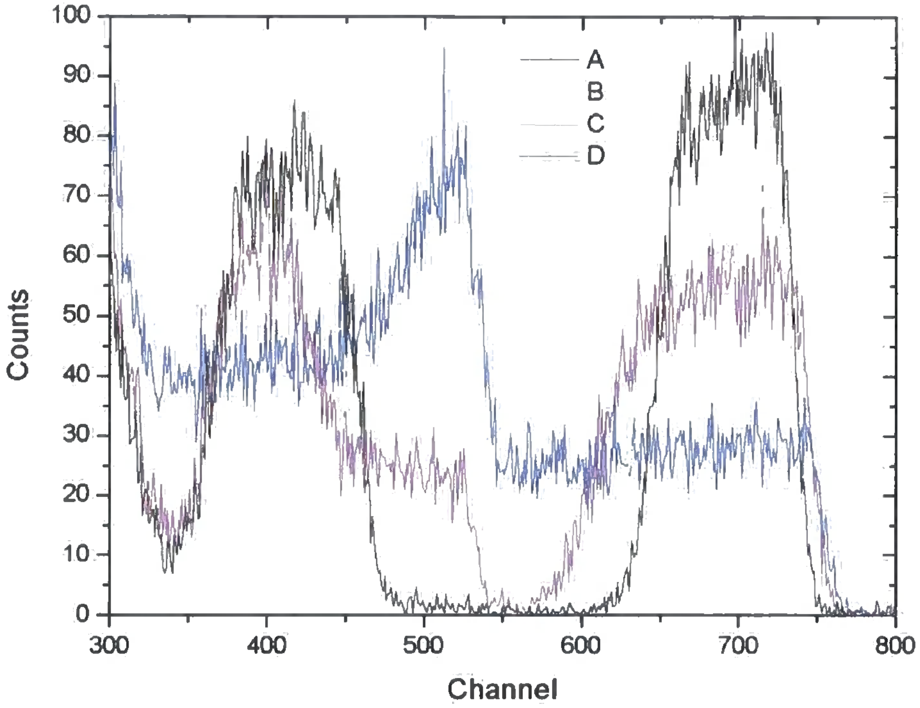

Figure 5.6 Raw data collected for a sample of approximately 300 nm 121100 gmol^{-1} DPEO on 2016000 gmol^{-1} PMMA annealed for various temperatures at 363 K.

A, an unannealed sample, shows two distinct peaks. The peak to the right between channels 750 and 650 is due to recoiled ^{2}H from DPEO, the peak to the left from channel 450, is due to recoiled ^{1}H from PMMA. The peak appearing below channel 350 is due to forward scattered ^{4}He. If the signals due to forward scattered ^{4}He and ^{1}H overlap then it is impossible to resolve the volume fraction data for the hydrogenous polymer. **D** indicates a sample that cannot be analysed as the ^{1}H and ^{2}H peaks have merged significantly. It may indicate a homogenous blend of PEO and PMMA. Only samples that included 2016000 gmol^{-1} PMMA had diffusion behaviour slow enough for resolvable peaks at 373 K. **B** and **C** show the development of a 'shoulder' on the ^{1}H (PMMA) peak. Subsequent heating shows the shoulder grows in counts (volume fraction) but does not move to higher energies (toward the surface depth). The bulk of the PMMA peak does not decrease in volume fraction noticeably. **B** and **C** also show the ^{2}H (DPEO) peak decrease in height (volume fraction) and extends to lower energies (greater depth within the bilayer) with anneal time. The DPEO peak did not smear out in a similar fashion to diffusion shown in Figure 2.4, instead it maintains a clear surface or 'front'.

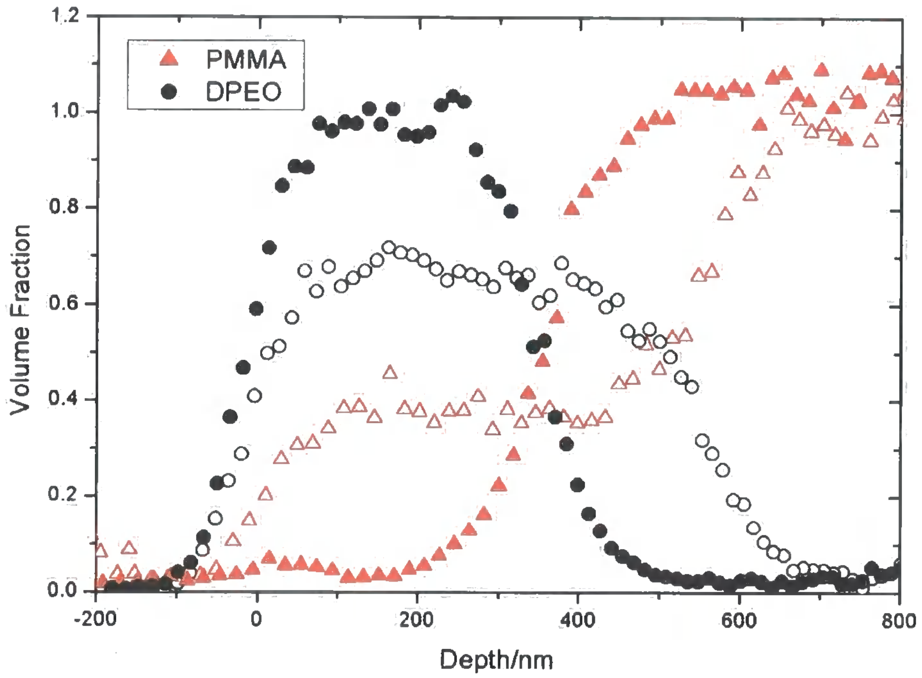

Figure 5.7 Normalised depth profiles for 89217 gmol^{-1} DPEO and 16000 gmol^{-1} PMMA at 343 K after 0 seconds (filled symbols) and 1919 seconds (open symbols) plotted on the same depth scale

Plotting normalised profiles on the same depth scale allows some of the movement to be understood. Figure 5.7 shows a typical plot. All the annealed data, showed a step-like profile formed on the PMMA layer, indicating that PMMA is present throughout the sample up to the air surface. A pure DPEO layer is not present, but the bilayer consists of a DPEO rich blend layer on top of PMMA. No spectra showed an intermediate step between the initial bilayer and the blend/PMMA bilayer. This implies that the rate of PMMA diffusion within the DPEO is in excess of that calculable by ion beam analysis. The formation of the blend layer may be analogous to PMMA being rapidly solvated in a liquid. As shown in Figure 5.8, $d_{interface}$ is thus the interface between the blend and PMMA for all annealing times where $t > 0$. When $t=0$, the $d_{interface}$ describes DPEO/PMMA interface. As the interface for the 'step' is sharp there is no concentration function to describe the PMMA within the blend. The concentration of PMMA is constant with depth throughout the blend. The growth in height of the step-like profile indicates an increase in volume fraction PMMA ($\varphi_{blend-PMMA}$) in the blend.

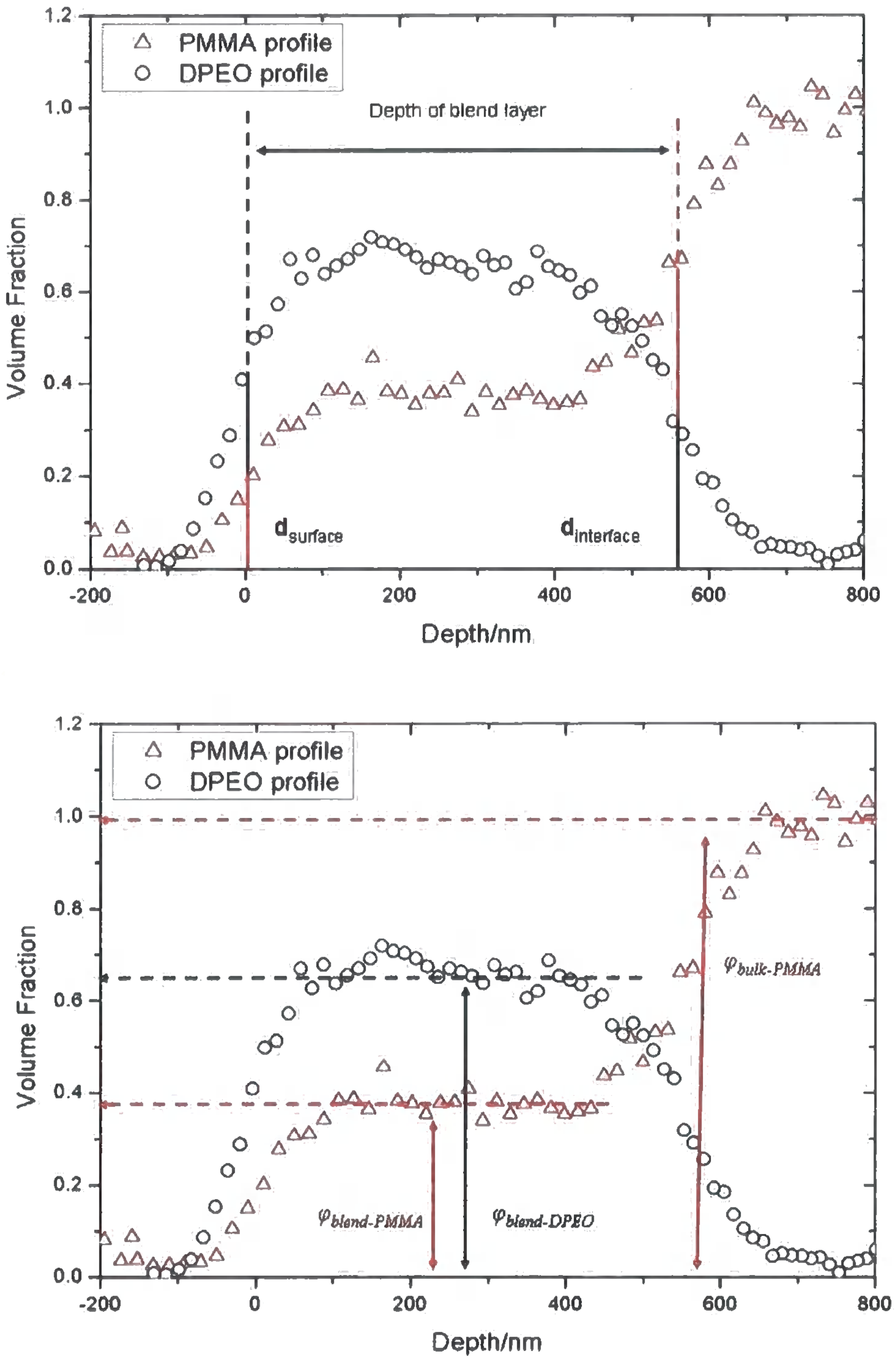

Figure 5.8 Schematic of definition of interfaces and volume fractions on superimposed PMMA and DPEO profiles

From Figure 5.7 it can also be seen that the DPEO peak decreased in volume fraction and $d_{interface}$ moved to greater depths with time. Whilst this indicates that DPEO diffused into the pure PMMA, DPEO is no longer in a homogenous

DPEO environment. The decrease in height of the DPEO peak indicates a decrease in volume fraction DPEO ($\varphi_{blend\text{-}DPEO}$) in the blend.

Some of the samples that included DPEO molecular weight >17300 $gmol^{-1}$ exhibited a further change in DPEO depth profile with time, an example is shown in Figure 5.9. At longer anneal times, subsequent to the development and growth of the ^1H surface excess and broadening of the ^2H peak, another step-like profile developed on the ^2H (DPEO) peak. This phenomenon was mostly, but not exclusively observed for samples that included lower molecular weight polymers, 60200 $gmol^{-1}$and 16000 $gmol^{-1}$ PMMA and 89217 $gmol^{-1}$ DPEO. This is probably not a molecular weight specific process, but was observed for those bilayers as the extent of diffusion was greater during the anneal time schemes utilised.

Plotting the PMMA and DPEO profiles on the same depth scale (Figure 5.9) revealed that the blend/PMMA interface $d_{interface}$ present in Figure 5.8 was still present at a similar depth in profiles with the DPEO surface excess and that the position of $d_{interface}$ varied with time. This indicated that the blend present between $d_{PMMA\text{-}surface}$ and $d_{interface}$ continued to swell with additional PMMA. Bulk PMMA lay next to blend PMMA as before, however a further DPEO rich layer was present at the surface, bordering the blend with the interface $d_{PMMA\text{-}surface}$. PMMA was not present at the surface of the sample in the same concentration present in the blend ($\varphi_{blend\text{-}PMMA}$). The sum of $\varphi_{blend\text{-}DPEO}$ and φ_{DPEO} was unity for all samples. $\varphi_{blend\text{-}DPEO}$ was considered to describe the volume fraction within the bulk blend as illustrated in Figure 5.8. It is unlikely that this profile was due to dewetting as all samples were checked with an optical microscope and dewetted samples would typically show the substrate (in this case the blend) at the surface, i.e. $d_{PMMA\text{-}surface} = d_{DPEO\text{-}surface}$.

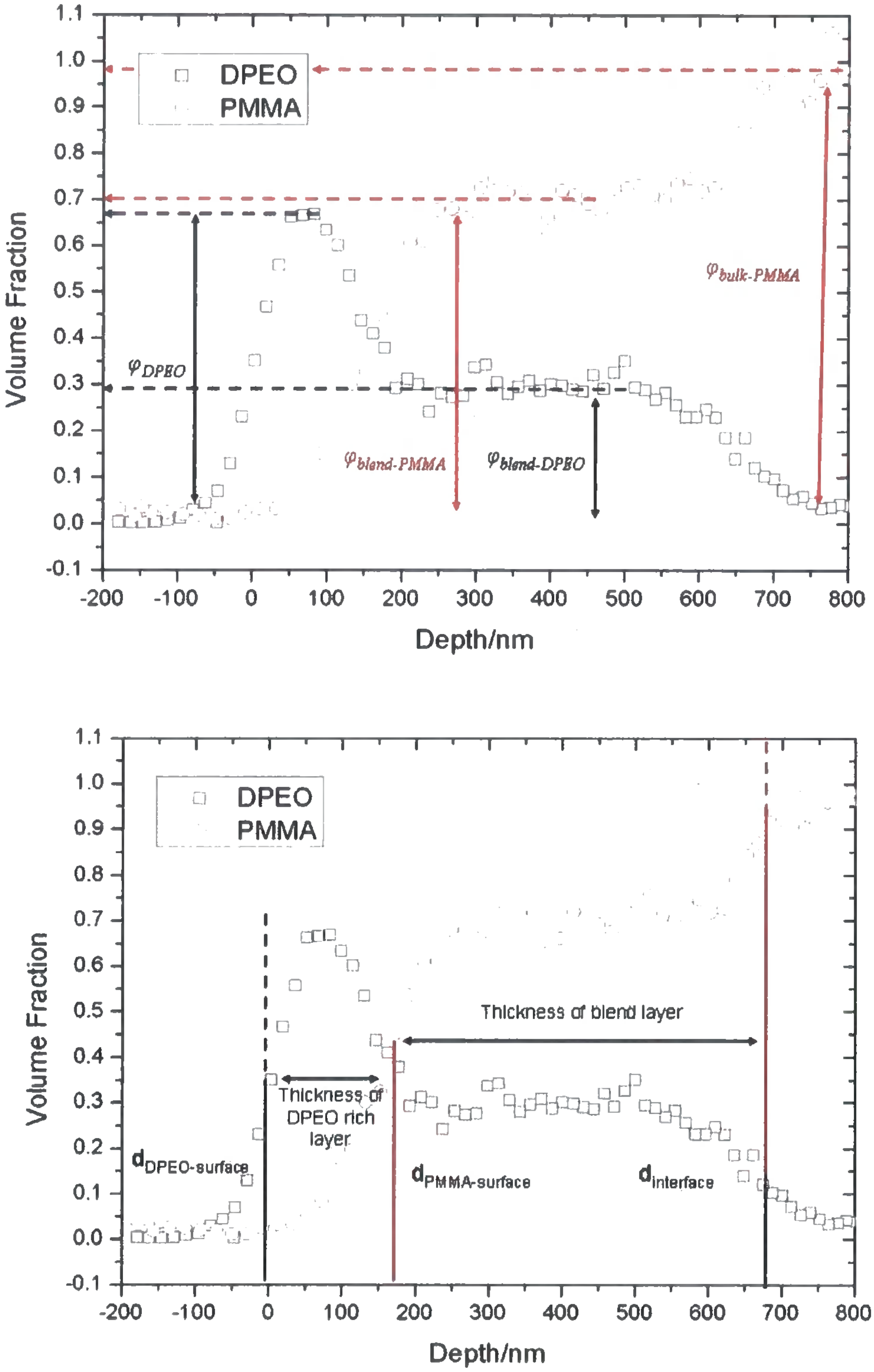

Figure 5.9 Schematic of definition of volume fractions and depths on superimposed PMMA and DPEO profiles for longer annealed samples showing DPEO step-like profile.

Samples that included 17300 gmol^{-1} DPEO behaved in a slightly different manner to those of higher DPEO molecular weight. A typical example of raw data is shown in Figure 5.10.

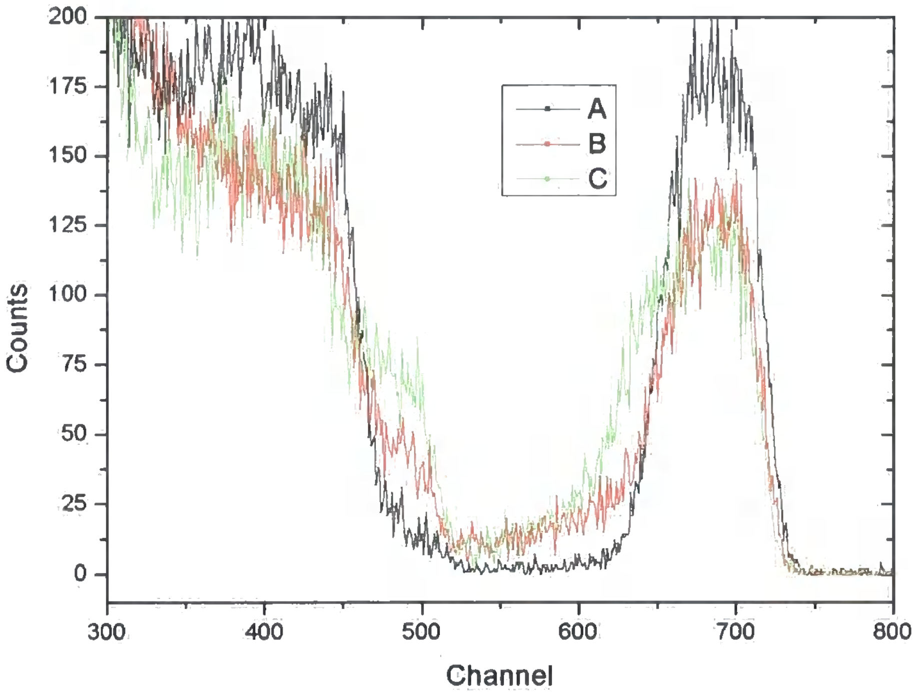

Figure 5.10 Raw data collected for a sample of approximately 300 nm 17300 DPEO on 2016000 PMMA annealed for various times at 353 K.

Figure 5.10 **A** shows the unannealed sample and **B** and **C** show the annealed samples. As with the higher DPEO molecular weight samples, the ^{1}H peak exhibits a shoulder upon annealing, indicating a surface excess that grows in volume fraction (counts) with time. The top of the shoulder is less flat than for samples characterised in Figure 5.6. This reflects the shape of the ^{2}H peak. Some samples at smaller anneal times appeared to exhibit a small tail precursor at greater channels (depths) next to the original DPEO peak (**B** is an example). The volume fraction in this tail dropped with depth. The peak 'slumps' with increasing angle with time (**C**). No shoulder as described in Figure 5.9 was apparent at later anneal times. This differed from the more well- defined box-like profiles with constant volume fraction with depth previously discussed for higher molecular weight DPEO.

5.4.3 Calculating diffusion profile

The position and broadening, of an interface can be described by a hyperbolic tangent, [3]

$$\varphi(d) = \varphi_i + \left(\varphi_i \tanh\left(\frac{d_i - d}{w_{tot}} \right) \right) \qquad \text{Equation 5.3}$$

w_{tot} represents the full width half maximum (FWHM) of the broadening interface. If w_{tot} is considered to only be due to beam damage (w_{bd}) and resolution (w_{res}) with no interfacial broadening Equation 5.2 applies, where w_{bd} and w_{res} are known as a function of depth. The value of d_i or depth for a given interface and volume fraction of a layer, φ (as defined in Figure 5.8 and Figure 5.9) can thus be determined using least squares fitting of Equation 5.3 to the normalised data. Figure 5.8 and Figure 5.9 show the typical DPEO and PMMA profiles, normalised, plotted on the same depth scale and defines interfaces. The PMMA peak was described by 2 hyperbolic tangents, one for each region, describing each interface as shown in Figure 5.11(A). As none of the spectra showed smearing, Equation 5.2 was applied. Figure 5.11 (B) and (C) show the DPEO peak initially described by 2 tangents and if the surface excess described in Figure 5.9 occurred, by 3 tangents. In the simpler case described in Figure 5.11 (B), the average φ of the two tangents was taken as the overall volume fraction for the blend present on top of the PMMA layer. The depth of the PMMA/blend interface $d_{interface}$ can be found from both PMMA and DPEO peaks as shown in Figure 5.8 and were generally in very good agreement therefore the value of $d_{interface}$ used for comparison between anneal times was an average of these two values. The values found for φ_{DPEO} , $\varphi_{blend\text{-}PMMA}$ and $\varphi_{blend\text{-}DPEO}$ for samples that matched Figure 5.11 (C) were treated separately to values of $\varphi_{blend\text{-}PMMA}$.

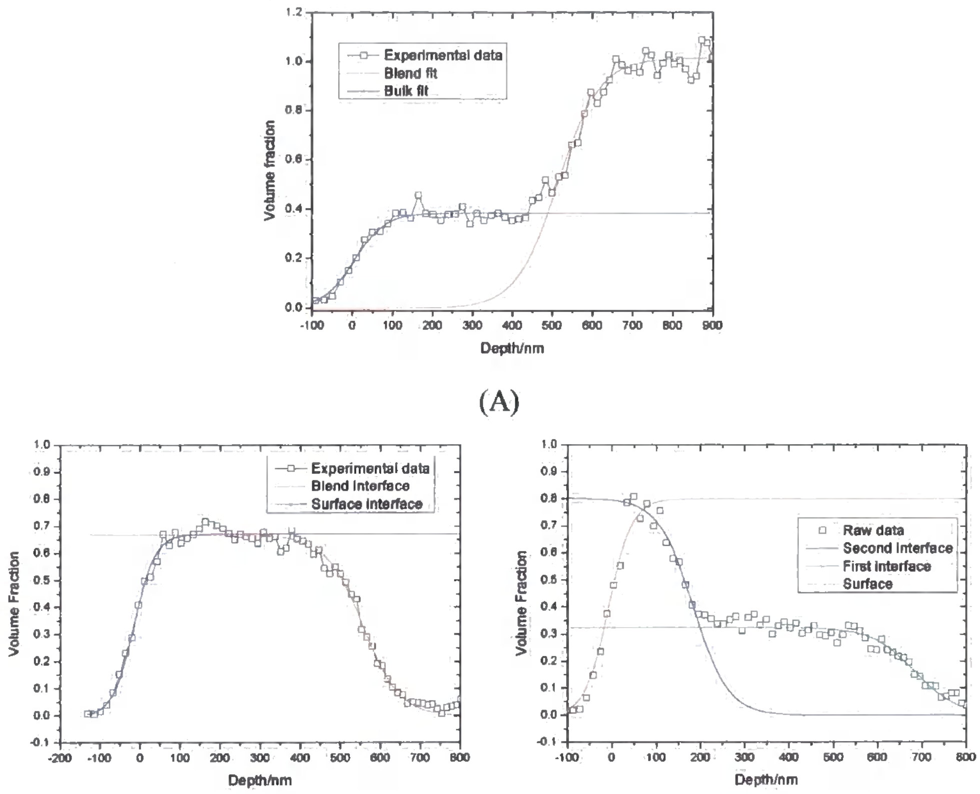

(A)

(B) (C)

Figure 5.11 Examples of hyperbolic tangents fitting PMMA, (A) and DPEO profiles (B and C)

(A) Annealed ^{1}H peak fitting $d_{surface}$ and $\varphi_{blend\text{-}PMMA}$ (blue) and $d_{interface}$ and $\varphi_{bulk\text{-}PMMA}$ (red)

(B) Annealed ^{2}H peak fitting $d_{surface}$ and $\varphi_{blend\text{-}DPEO}$ (blue) and $d_{interface}$ and $\varphi_{bulk\text{-}DPEO}$ (red)

(C) Annealed ^{2}H peak exhibiting step profile fitting $d_{DPEO\text{-}surface}$ and φ_{DPEO} (red) , $d_{PMMA\text{-}surface}$ and φ_{DPEO} (blue) and $d_{interface}$ and $\varphi_{blend\text{-}DPEO}$

It was found that neither of the two fitting regimes shown in Figure 5.11 (B and C) could be used to describe DPEO peaks for bilayers including 17300 gmol^{-1} DPEO. For these films $\varphi(d)$ varied gradually over the entire depth range and could not be described satisfactorily by Equation 5.3. The surface $d_{surface}$ was fitted using a hyperbolic tangent as before, with Equation 5.2. The unannealed sample's hidden interface was also fitted with Equation 5.3 and Equation 5.2 and the depth of initial $d_{interface}$ was found. For annealed profiles this value of d_i as described was kept the same and w_{tot} was varied. Where w_{tot} is described by,

$$w_{tot} = \sqrt{w_{bd}^2 + w_{res}^2 + w_{width}^2} \qquad \text{Equation 5.4}$$

which includes the broadening interfacial width, w_{width}. An example is shown in Figure 5.12

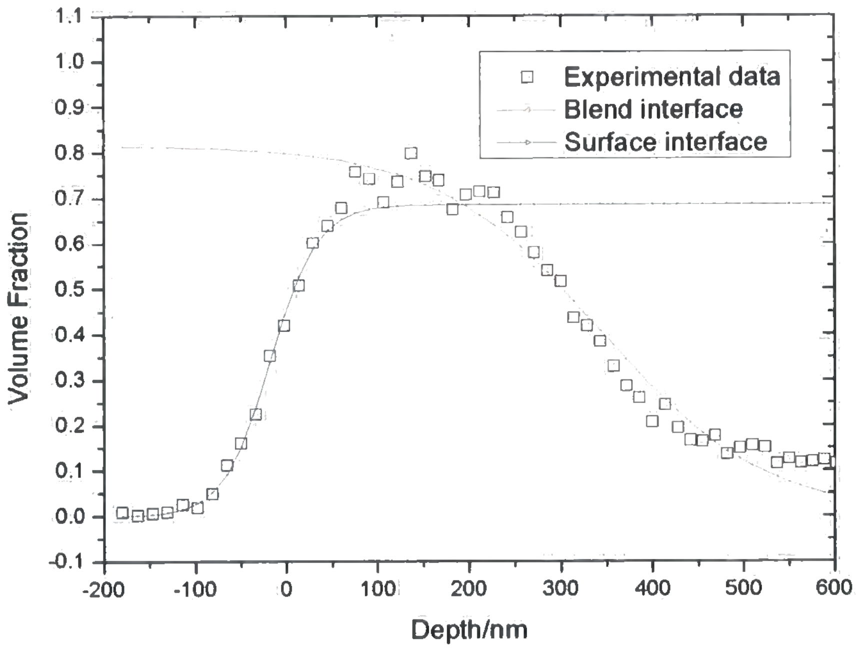

Figure 5.12 Example of hyperbolic tangent fitting DPEO profile for 17300 gmol^{-1} DPEO bilayer samples.

As the shape of the PMMA profile was so similar between 17300 gmol^{-1} and higher molecular weight DPEO bilayer samples, the ^{1}H profile was fitted in the same way as shown in Figure 5.11. The $\varphi_{blend\text{-}PMMA}$ and $d_{interface}$ values found were included in subsequent analysis of PMMA profiles.

5.5 *Discussion*

5.5.1 Rubbery/Glassy diffusion couples

Glassy PMMA is quickly dissolved into the molten DPEO and subsequently into DPEO/PMMA blend. There is no measurable concentration gradient within the blend (until the step-like profile forms in the DPEO profile) so the blend establishes a constant concentration with depth in times smaller than those analysed here. As such it is impossible to verify which component of the blend is faster moving. As PMMA is dissolved into the DPEO rich layer, the T_g of the blend layer will change with PMMA concentration (section 4.5). As long as the T_g of the blend remains below T, the operating temperature of the experiment (343-363 K), polymers should diffuse freely within the blend. At such temperatures, the PMMA bulk is glassy, for a PMMA molecule to diffuse into the blend it must first be placed in an environment where it can reptate. This can only occur at $d_{interface}$ where glassy polymers are in contact with mobile blend polymers.

Diffusion of long chain glassy entangled polymers into rubbery entangled polymers has been observed for polystyrene (PS) into polyphenylene oxide (PPO) above and below their T_g's respectively[8,9], rubbery poly(vinylmethylether) (PVME) into glassy PS [10]. Further studies of these two diffusing pairs have only included one entangled polymer with rubbery component below the entanglement molecular weight[11,12].

5.5.2 Diffusion regimes for rubbery/glassy bilayers

Typically, Fickean diffusion (2.1) is used to describe polymer/polymer diffusion, where Equation 3.1 is used to extract values for the interfacial width w_{width}. Plots of $w^2_{width}/4$ against t provide gradients equal to D^*_T the tracer diffusion coefficient for the component in the matrix. A description of Fickean diffusion based on a moving atomically thin layer of markers between diffusing components has been used to analyse polymer diffusion with gold markers[13-15]. For a diffusion couple, A and B; where direction of interface movement is towards the side with the fastest diffusing species, the intrinsic diffusion coefficients of the two components are D_A and D_B where $D_A > D_B$. Hence the velocity of the interface between the components v is towards the A rich side the diffusion equation. For comparison with the DPEO/PMMA system A= PMMA, B=DPEO.

$$\frac{\partial\varphi}{\partial t}=\frac{\partial}{\partial x_0}\left(D(\varphi)\frac{\partial\varphi}{\partial x_0}\right) \qquad \text{Equation 5.5}$$

can be written. Using the Boltzmann transformation to define the variable,

$$u=\frac{x_0}{\sqrt{t}} \qquad \text{Equation 5.6}$$

Equation 5.5 becomes,

$$-\frac{1}{2}u\frac{d\varphi}{du}=\frac{d}{du}\left[D(\varphi)\frac{d\varphi}{du}\right] \qquad \text{Equation 5.7}$$

Concentration φ is thus $\varphi=\Phi(u)$. The interface is thought to stay at constant composition $\varphi_0=\Phi(0)$ as time increases. When $\Delta D(\varphi)=D_A(\varphi)-D_B(\varphi)$, a shift in interface Δd will be determined by,

$$\Delta d=2\Delta D(\phi_0)\Phi'(0)t^{\frac{1}{2}} \qquad \text{Equation 5.8}$$

where $\Phi'(0)\equiv(d\Phi(u)/du)\big|_{u=0}$ hence regardless of the composition dependence of D_A-D_B the interface depth should vary linearly with $t^{0.5}$.

Diffusion into glassy matrices has mostly been considered in relation to penetration of small molecules, investigated by sorption techniques. The penetration of low molecular weight molecules, such as solvents, into glassy polymer does not exhibit Fickean behaviour. Under no external stresses the diluents penetrate the glassy polymer in the form of sharp swelling fronts. This can be described by case II diffusion. The polymer is in contact with an infinite reservoir of small molecules. The transport of these molecules into the glassy polymer is characterised by an induction period followed by the formation of a diffusion front with a steep concentration gradient between diluent rich and polymer material. The absorbed diluent /polymer zone is called the plasticised zone as the presence of the solvent allows mobility of the polymer to increase from glassy to rubbery. Figure 5.13 shows a schematic of the process. The front propagates at a constant velocity v, mass uptake of diluent is linear with time and there is no concentration gradient behind the diffusing front.

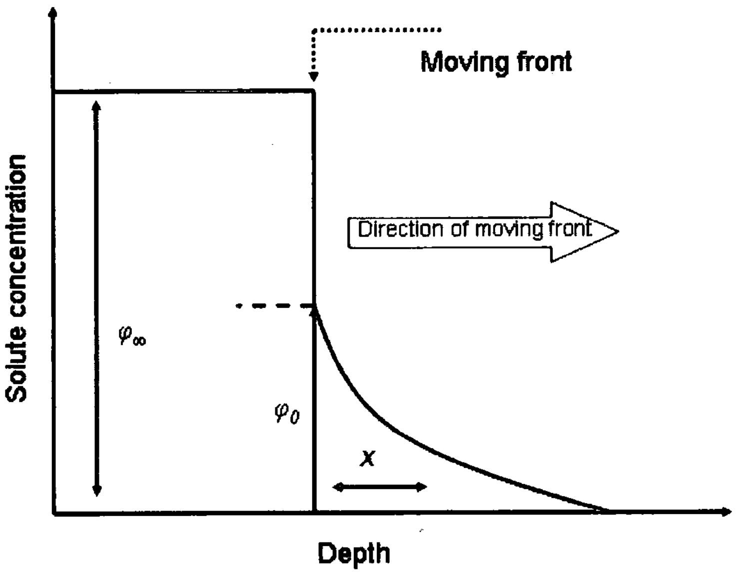

Figure 5.13 Schematic of case II front advancing toward right, preceded by a Fickean diffusion front.

These are the essential features of case II diffusion.[16] The case II diffusion front is always preceded by a Fickean precursor, or process zone, rising up to a given concentration φ_0 where the swelling induced stresses are sufficient to cause yielding and plastic flow in the mobile diluent rich polymer region. It has been shown [16,17] that in the initial stages of non-Fickean diffusion there was a critical volume fraction φ_c below which the characteristic diffusion front would not form. In this process zone, entangled glassy polymer chains are in close proximity to the mobile chains in the diluent material. The diffusion is driven by the stress generated ahead of the diffusing front and the time dependent mechanical response is the rate controlling step. The diffusion front advances linearly with time, in contrast to Fickean diffusion, which scales with the square root of time.

5.5.3 Blend volume fraction

In these systems PMMA is in excess of DPEO, therefore it could be expected that a homogenous sample, where diffusion is complete and the system has reached equilibrium would reflect the total amount of material of both components. For the samples analysed the volume fraction of PMMA in the PEO rich layer, now the 'blend', was measured up to $\varphi_{blend\text{-}PMMA}$= 0.5 for several samples. Whether the concentration ever increased beyond this level, to the stoichiometry of the sample as a whole, is unknown, as the system could not be further measured since ^{1}H and ^{2}H peaks overlapped. Figure 5.14 shows a typical plot of the change in volume fraction of the two components in the blend layer (between $d_{interface}$ and $d_{surface}$) with time. An increase of PMMA in the blend is matched by the decrease in DPEO as would be expected so that,

$$\varphi_{PMMA} + \varphi_{DPEO} = 1 \qquad \text{Equation 5.9}$$

Typically the change in volume fraction with time occurs faster for higher operating temperatures. This is not surprising as molecules should have more energy for movement with higher temperatures. The interaction parameter, χ of the blend is dependent on temperature T, which may also influence the movement of PMMA into the blend. The relationship between volume fraction and time is not linear, with the changes in $\varphi_{blend\text{-}PMMA}$ and $\varphi_{blend\text{-}DPEO}$ being greater at smaller anneal times and slowing at greater anneal times.

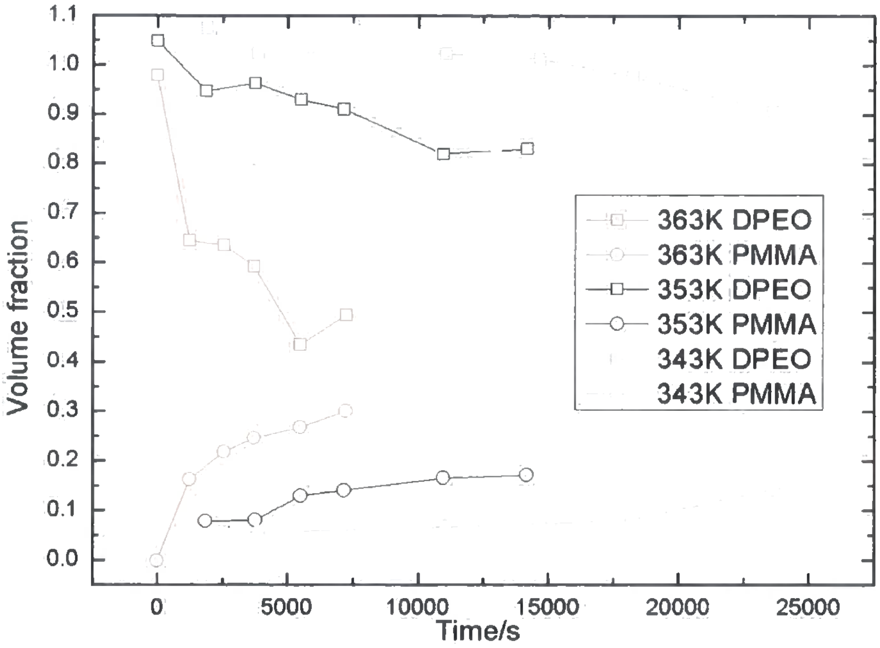

Figure 5.14 Plot of volume fraction of 96200 gmol^{-1} PMMA ($\varphi_{blend\text{-}PMMA}$) and 121100 gmol^{-1} DPEO ($\varphi_{blend\text{-}DPEO}$) between $d_{interface}$ and $d_{surface}$ against anneal time for various temperatures.

The interaction parameters for blends of DPEO and PMMA are known to be concentration dependent. It is typically believed that blends where $\varphi_{blend\text{-}DPEO} >\sim 0.3$ are not homogeneous. For the operating temperatures utilised in these experiments, the interaction parameter for the system (when $\varphi_{blend\text{-}DPEO} < 0.3$) was small and negative indicating a homogenous blend. Several samples analysed formed a blend layer with a composition where $\varphi_{blend\text{-}DPEO} > \sim 0.3$ and $\varphi_{blend\text{-}PMMA} > 0.3$

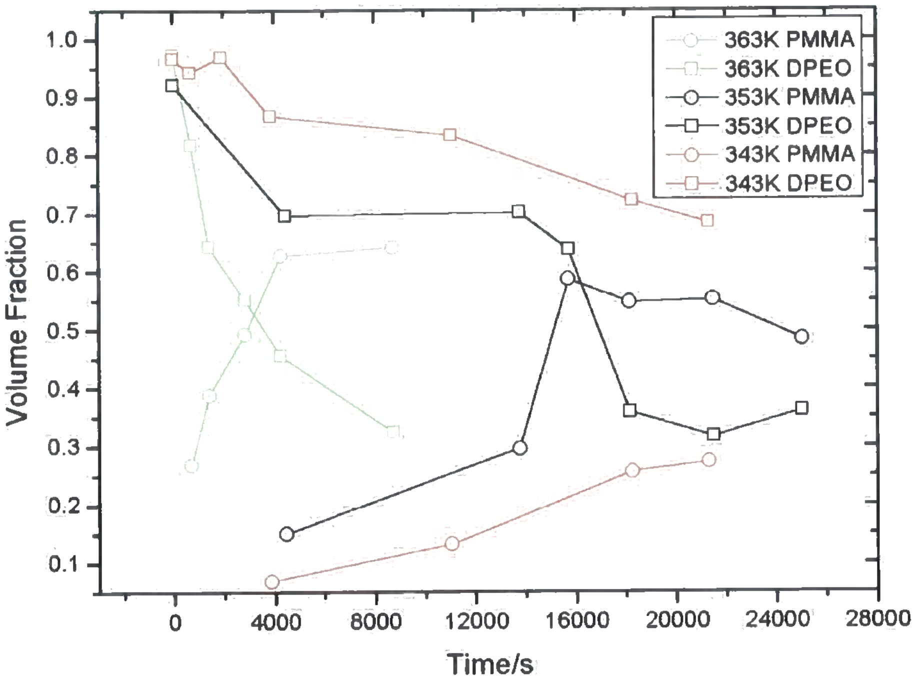

Figure 5.15 Plot of volume fraction of 60200 gmol^{-1} PMMA ($\varphi_{blend\text{-}PMMA}$) and 89217 gmol^{-1} DPEO ($\varphi_{blend\text{-}DPEO}$) between $d_{interface}$ and $d_{surface}$ against anneal time for various temperatures.

Figure 5.15 shows a typical plot of volume fraction against time for one of the samples that exhibited the development of the DPEO surface excess shown in Figure 5.9. The sum of $\varphi_{blend\text{-}DPEO}$ and $\varphi_{blend\text{-}PMMA}$ was unity. It can be shown that the DPEO step-like profile only develops for annealing times subsequent to $\varphi_{blend\text{-}DPEO}= \varphi_{blend\text{-}PMMA}= \sim 0.5$. Volume fractions then tend towards and equilibrate where $\varphi_{blend\text{-}DPEO}= 0.3$, the concentration at which the blend should still be homogeneous. Further evidence of the eventual value of $\varphi_{blend\text{-}DPEO}$ is lost as longer anneal times provide spectra with ^{1}H and ^{2}H signals overlap. PMMA and DPEO are known to have very different surface energies[18]and blend separation may occur at the air surface where surface tension effects[19] are important as opposed to within the blend where nucleation may be less likely. There are many cases of similar surface segregation in polymer blends.[20] It is likely that the PEO rich region at the surface is always present in the annealed systems, however cannot be resolved until $\varphi_{blend\text{-}DPEO} < 0.5$. As shown in Figure 5.14 and Figure 5.15 the volume fraction change with time shows similar curvature before and after $\varphi_{blend\text{-}DPEO}= \varphi_{blend\text{-}PMMA}=0.5$. This indicates that the flow of PMMA from the bulk continues in a similar fashion before and after the step-like profile is observed, also indicating that it may always be present in annealed samples. ATR-FTIR studies of diffusion PVME into glassy PS, also allowed determination of volume fraction of PVME against interdiffusion time for the blend[10]. An initial induction time for PVME to reach the IR beam penetration depth was found, then the PVME molar fraction increased rapidly and reached the equilibrium mole fraction of the PS/PVME blend. This may be similar to the system here, where the rate of change in volume fraction with time decreases as equilibrium is reached, however the PVME/PS couple does not have the same partial miscibility behaviour as DPEO/PMMA.

Figure 5.14 indicates the change in volume fraction with time for the two components in the 'blend' as defined by $d_{interface}$. This does not allow for the movement $d_{interface}$, and is not a measure of movement of material into an area of set dimensions, but movement of material into a volume of changing dimensions. A Matano interface describes a plane within a diffusion couple, across which interface equal amounts of volume diffuse in either direction (section 1.1). As the interface moves with time, a greater net volume of one component flows in one direction, therefore no interface can be defined whereby equal mass of DPEO flows in one direction whilst PMMA flows in the other. $d_{interface}$ could be defined as the interface over which increase in PMMA on one side is matched by decrease on PMMA on the other. However this implies that the DPEO and PMMA occupy the same volume on both sides of the interface. As one side is rubbery and the other glassy, and in completely different chemical environments, this is unlikely.

It is useful to analyse the volume fraction as the number of molecules of each component within the blend. With interface movement, the volume occupied by the blend increases and hence the total amount of material present in the blend increases with time. To calculate the flux of quantifiable material the volume fraction is multiplied by the depth of the interface, which equates to multiplying by the volume of the blend. Definition of this interface is hard, bilayers analysed did not include a blend $\varphi_{PMMA} > 0.5$, the interface between the PMMA and blend could be assumed to contain the co-ordinate depth for $0.5=\varphi_{PMMA}$. This assumption may not be true for all anneal times. Using the densities of the polymers, depth in nm can be converted to atoms per cm^2. Density for PMMA is very similar to, and lies between that of, crystalline and amorphous DPEO hence this was assumed to be the density of the polymers in the blend. Using molecular weights as described in section 5.3.1 the number of polymer molecules can then be calculated for each component. The 'flux' is defined as the number of PMMA polymers per cm^2 per second crossing the interface where $\varphi_{blend\text{-}PMMA} \approx 0.5$. Polymer diffusion is typically measured in units of cm^2s^{-1}, comparisons are therefore hard between these calculated fluxes and previous work on other polymer couples.

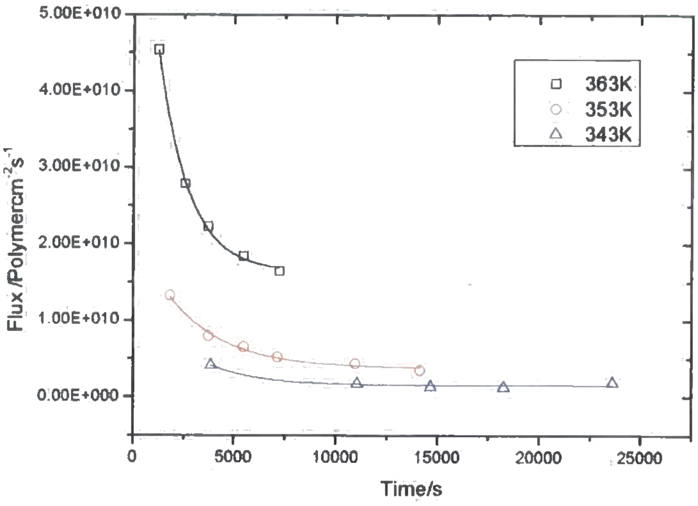

(A)

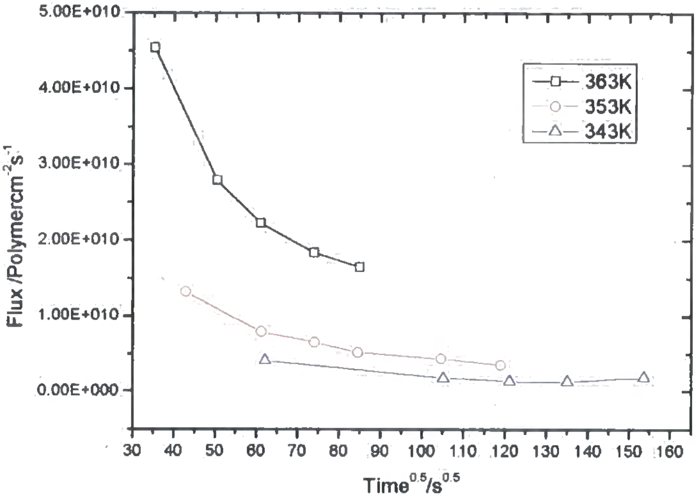

(B)

Figure 5.16 Plot of flux of polymer of 96200 gmol^{-1} PMMA into 121100 gmol^{-1} DPEO rich blend against anneal (A) time *t* and (B) $t^{0.5}$ for various temperatures. Plots against t are fitted with a first order exponential. Plots against t are fitted with first order exponentials.

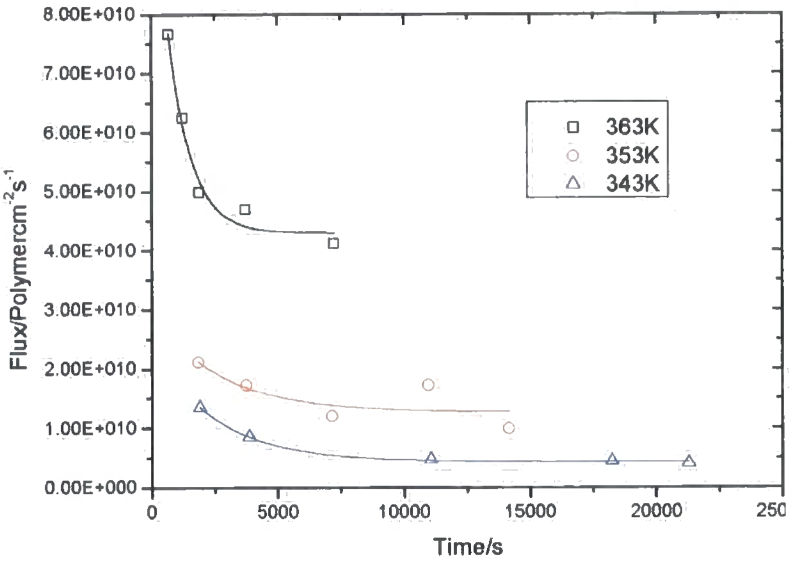

(A)

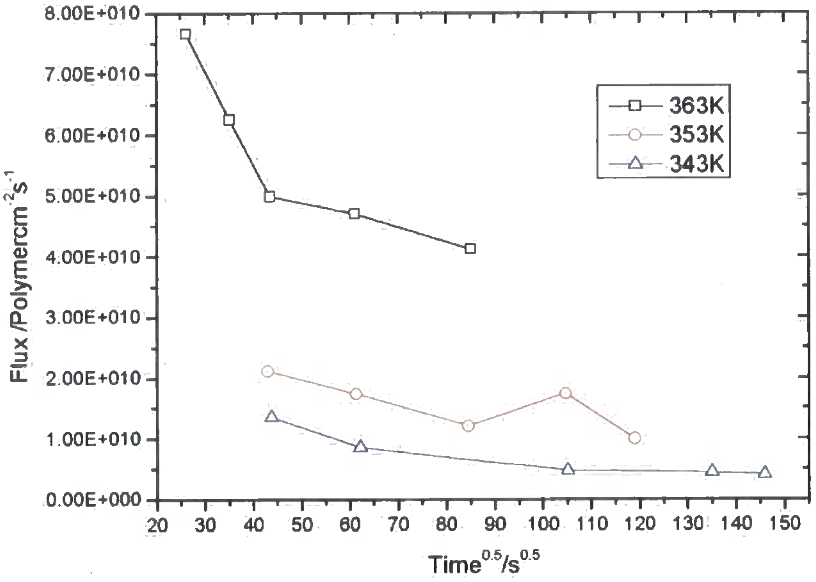

(B)

Figure 5.17 Plot of flux of polymer of 60200 gmol^{-1} PMMA into 121100 gmol^{-1} DPEO rich blend against anneal time (A) *t* and (B) $t^{0.5}$ for various temperatures. Plots against t are fitted with first order exponentials.

Figure 5.16 (A) and Figure 5.17 (A) show typical plots of fluxes of PMMA with time *t*, which show that flux does not vary linearly with time. A linear relationship between polymer flux and time is expected for Fickean diffusion. Plots of flux vs. $\sqrt{t}$ are not linear either. The flux of material may be inhibited with time due to the changing concentration of the blend. This change in concentration may explain a kinetic or a thermodynamic slowing. With increase in PMMA concentration the blend local T_g decreases, thus blend viscosity decreases and prevents glassy PMMA polymers from diffusing as rapidly into the blend. Thermodynamic slowing down, the process where the interdiffusion coefficient approaches zero as the critical point of demixing is approached from the one-phase region, has been observed for several blends such as the interdiffusion of polystyrene and poly(α-methylstyrene) .[21] The change in concentration will also affect χ, the interaction parameter, leading to a blend that is not homogenous and an unfavourable thermodynamic environment for glassy PMMA chains. The flux of PMMA is temperature dependent where $T > T_g$ of the blend. If the dissolution of glassy polymers into the blend is dependent on blend polymer activity at $d_{interface}$, higher temperatures will provide higher blend mobility. Looking at the displacement of curves in Figure 5.17 with temperature the flux is not linearly dependent on temperature. An exponential dependence in time, in line with the WLF equation might be expected, but there are insufficient temperatures to create reasonable statistical evidence.

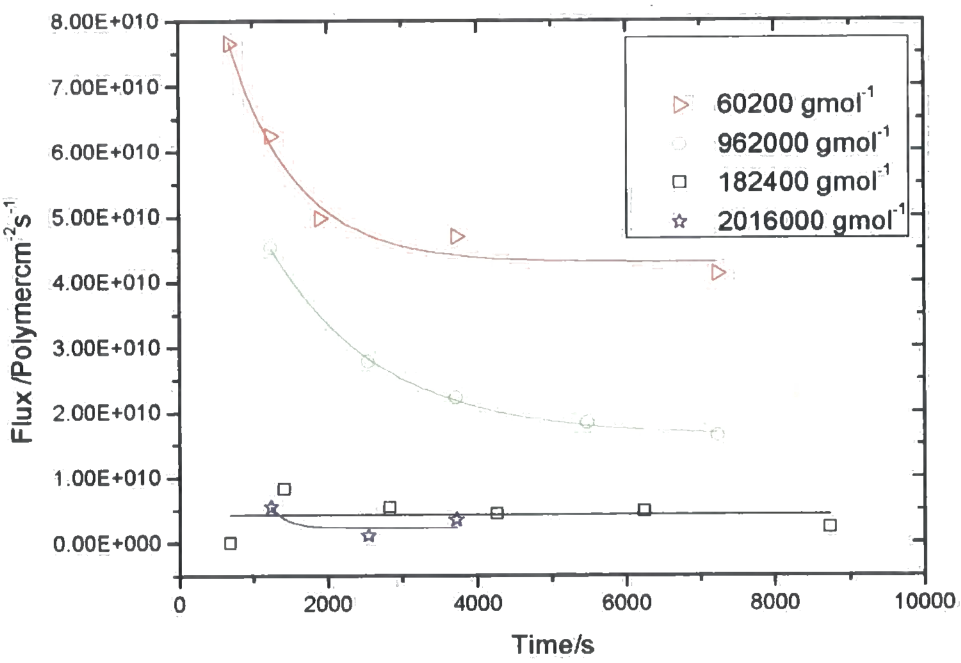

Figure 5.18 Plot of flux of various molecular weight PMMA polymers into 121100 gmol^{-1} DPEO rich blend against anneal time t at 363 K. Plots are fitted with first order exponentials.

The movement of the PMMA within the blend should be similar to that described by tracer or mutual diffusion.[8,14,22,23] The blend is above the T_g and the polymers should diffuse by reptation and constraint release as all the polymers utilised have molecular weights above the entanglement molecular weight. The time taken for the complete dissolution of the PMMA polymers, forming a homogenous blend with DPEO, t_{diss} is associated with polymer reptation and constraint release within this blend and the molecular weight of the components should affect the diffusion coefficients of PMMA within the blend. No concentration gradient is apparent within the blend even for the highest molecular weight PMMA (2016000 gmol^{-1}) so t_{diss} is smaller than can be measured by this experimental set up.

Figure 5.18 shows typical molecular weight dependencies of flux of PMMA into the blend at given temperatures. The higher molecular weight PMMA has a smaller flux of polymer with time. Previous work (section 4.11) has shown no molecular weight dependence of χ so thermodynamic effects are not responsible for the molecular weight dependence of flux. Kinetic effects within the blend are considered to be too fast to control the flux as shown here. The molecular weight dependence of flux of polymer into the blend is thus due to action at the interface between the blend and the PMMA. For a PMMA molecule to cease being 'glassy' it needs to be exposed to sufficient comparatively more mobile molecules. This will occur either by contact with mobile blend molecules at the surface or by contact with mobile polymers diffusing into spaces in the glassy bulk. As the higher molecular weight polymers have a larger chain to be exposed to, a larger contact over time is required before the once glassy PMMA molecule can be considered 'mobile', leading to a comparatively lower flux for high molecular weight polymers.

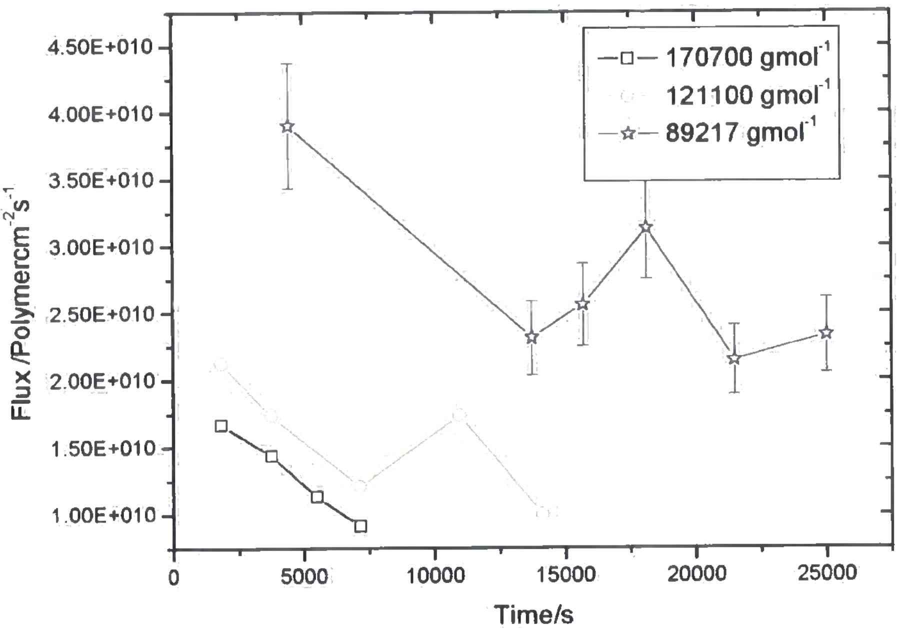

Figure 5.19 Plot of flux of 60200 gmol^{-1} PMMA polymers into various DPEO molecular weight rich blends against anneal time *t* at 353 K

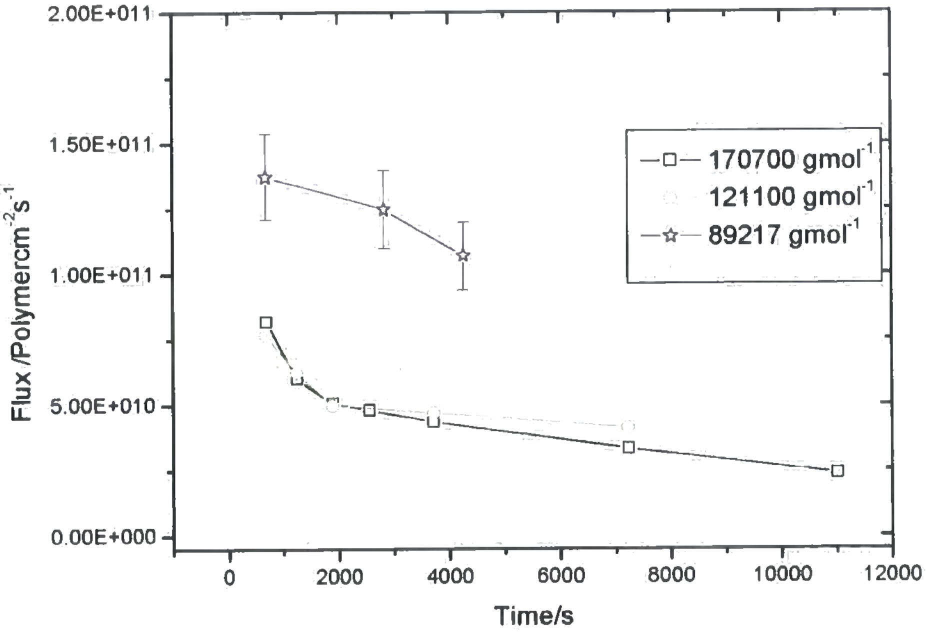

Figure 5.20 Plot of flux of 60200 gmol^{-1} PMMA polymers into various DPEO molecular weight rich blends against anneal time *t* at 363 K

Figure 5.19 and Figure 5.20 show typical molecular weight dependencies of PMMA flux into the blend at given temperatures for various DPEO molecular weights. In general the higher molecular weight DPEO has a smaller flux of PMMA polymer with time. Smaller DPEO molecules will have a greater number of highly mobile ends near the glassy PMMA. This may lead to greater exposure of the glassy PMMA molecules to an environment with mobile polymers and encourage dissolution from the bulk. Alternatively smaller DPEO molecules may be better suited to diffusing into spaces in the glassy bulk, again enhancing PMMA exposure to mobile polymers. As shown in Figure 5.20 flux does not always display clear DPEO molecular weight dependence, a similar contradiction was observed for the PMMA weight dependence. The PMMA chain may not distinguish between DPEO chain ends and only an environment rich in DPEO monomers is required, thus making DPEO molecular weight less significant to action at the interface, however T_g varies with molecular weight and could explain the variation of flux with molecular weight shown in Figure 5.20.

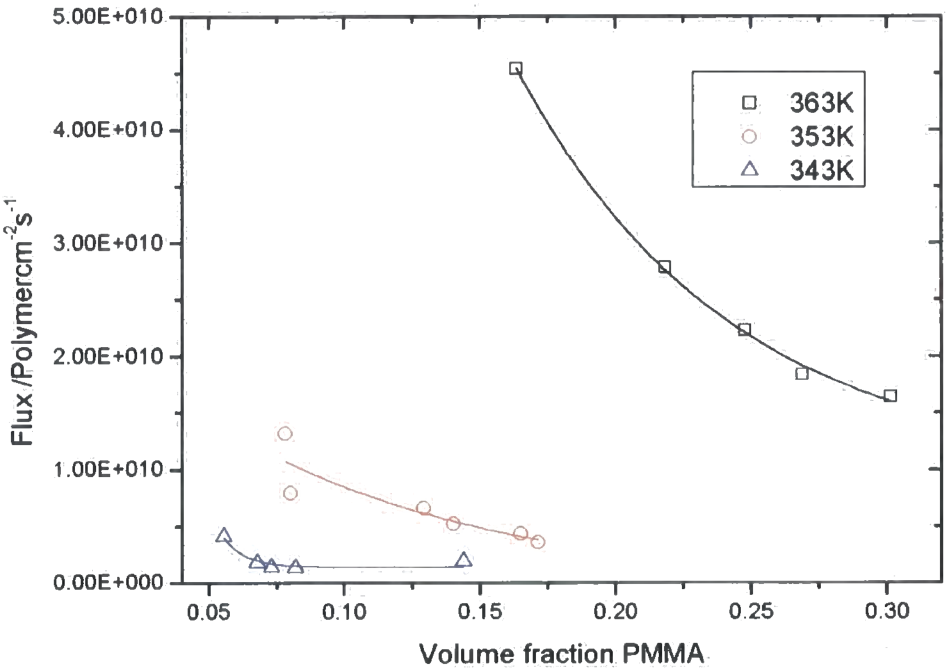

Figure 5.21 Plot of flux of 96200 gmol^{-1} PMMA molecules into 121100 gmol^{-1} DPEO rich blend against PMMA volume fraction in the blend $\varphi_{blend\text{-}PMMA}$. Data is fitted with first order exponentials.

From Figure 5.21 the flux of PMMA can be seen to be non-linear with change in volume fraction, although the curvature of the plot is less pronounced than for plots against time. Figure 5.22 and Figure 5.23 show polymer fluxes with volume fraction for various molecular weights of both PMMA and DPEO. Smaller polymers exhibit faster fluxes of material into the blend.

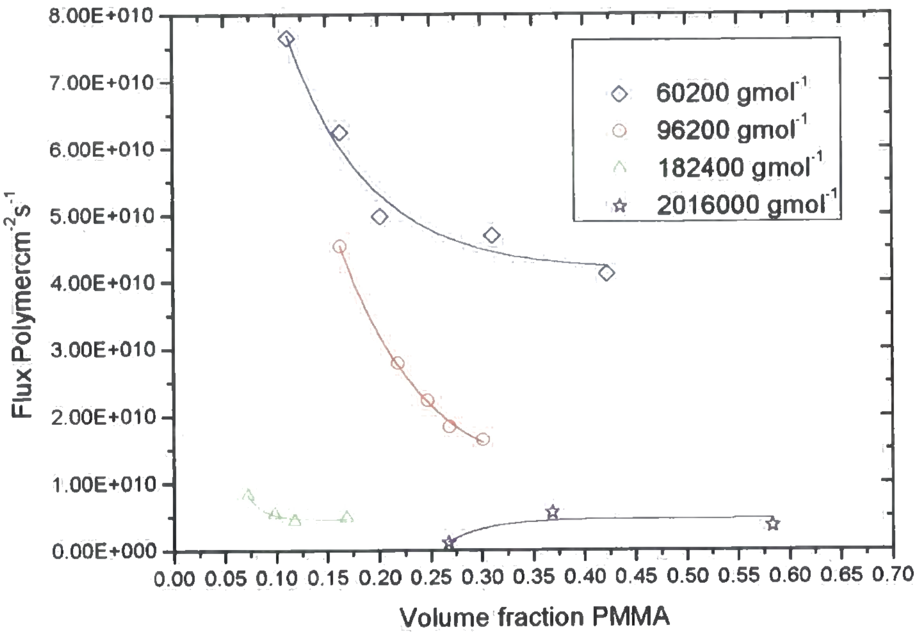

Figure 5.22 Plot of flux of various molecular weight PMMA polymers into 121100 gmol^{-1} DPEO rich blend against PMMA volume fraction in the blend ($\varphi_{blend\text{-}PMMA}$) at 363K. Plots are fitted with first order exponentials.

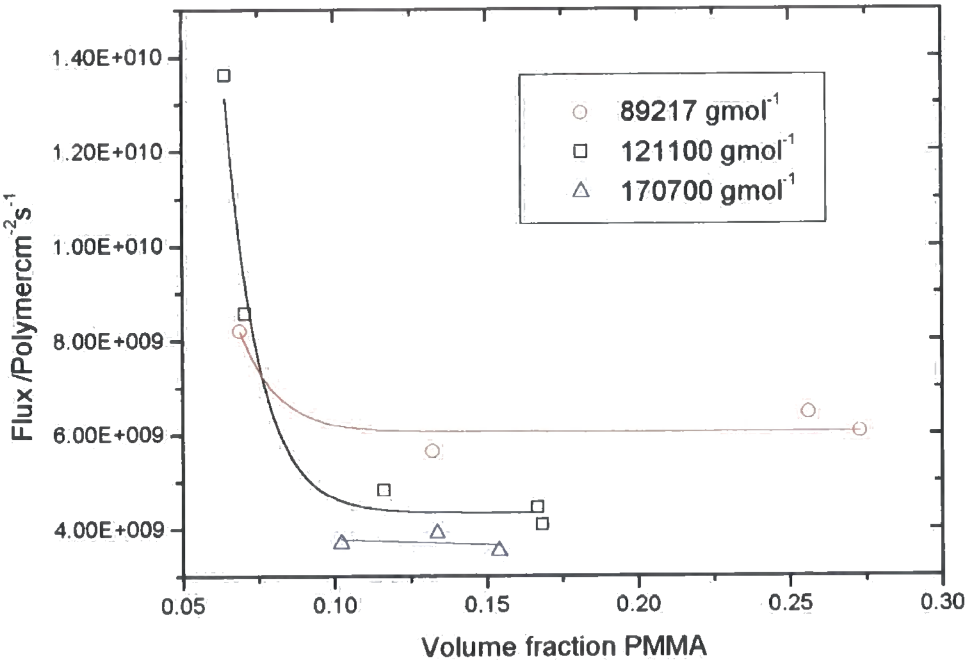

Figure 5.23 Plot of flux of 60200 gmol^{-1} PMMA polymers into various DPEO molecular weight rich blends against PMMA volume fraction in the blend ($\varphi_{blend\text{-}PMMA}$) at 343 K.

There did not appear to be a linear relationship between molecular weight and PMMA flux. The 2016000 gmol^{-1} PMMA exhibited polymer fluxes of the same order as polymers 10 times smaller. However 16000 gmol^{-1} PMMA flux was often an order of magnitude higher than the nearest molecular weights. This was surprising as all polymers were above the entanglement molecular weight.

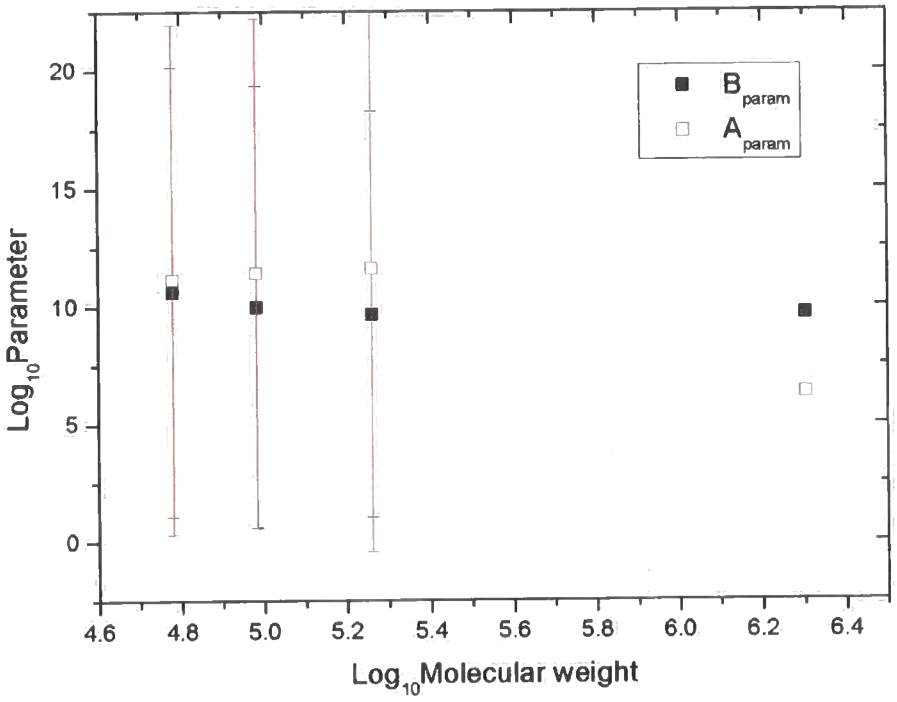

Figure 5.24 Double log plots displaying variation of parameters relating to behaviour of flux with volume fraction, for fits shown in Figure 5.22 (Flux=B_{param}+Aparam * $e^{(-\varphi_{PMMA}/t1)}$) and PMMA molecular weight.

Typical double log plots, as shown in Figure 5.24, did not produce a consistent value for a scaling relationship between flux and molecular weight.

5.5.4 Application of Fickean diffusion

If the bilayers diffused by Fickean diffusion, the raw data should have shown broadening of the polymer-polymer interface, characterised by an increase in w_{width} as shown in Figure 2.4. It would also have been possible to fit the depth profiles by adding an extra w term (w_{width}) as described in Equation 5.5. However fits without w_{width} were very good, as shown in Figure 5.25, indicating that for all DPEO molecular weights examined >17300 gmol^{-1}, Fickean diffusion could not describe the movement of the interface or polymer between the blend and pure PMMA.

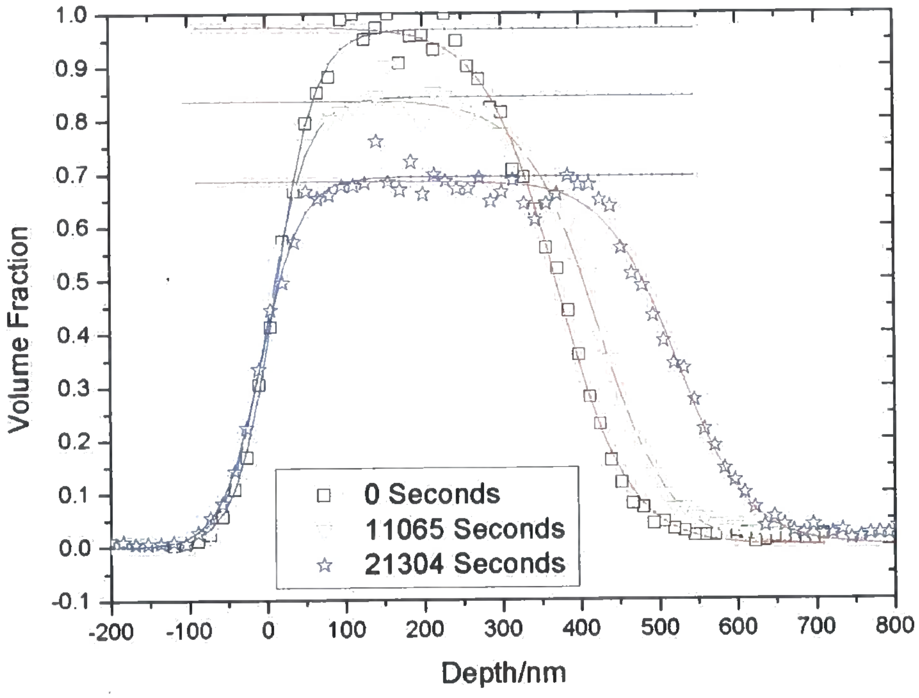

Figure 5.25 Depth profiles and hyperbolic tangent fits for approximately 300 nm 89217 gmol^{-1} DPEO on 2016000 gmol^{-1} PMMA, for various anneal times at 343 K. The value of w_{tot} used includes beam damage and resolution functions only.

Fits for bilayers containing 17300 gmol^{-1} DPEO required the inclusion of w_{width}. An example of this fitting regime is shown in Figure 5.26. Although more suitable than early the fitting regime discussed in Figure 5.11, the fits are not perfect at early anneal times. Plots of $w_{width}^2/4$ versus time as described in Equation 3.1, were found to give reasonable straight lines, and diffusion coefficients were extracted from the gradients (Figure 5.27).

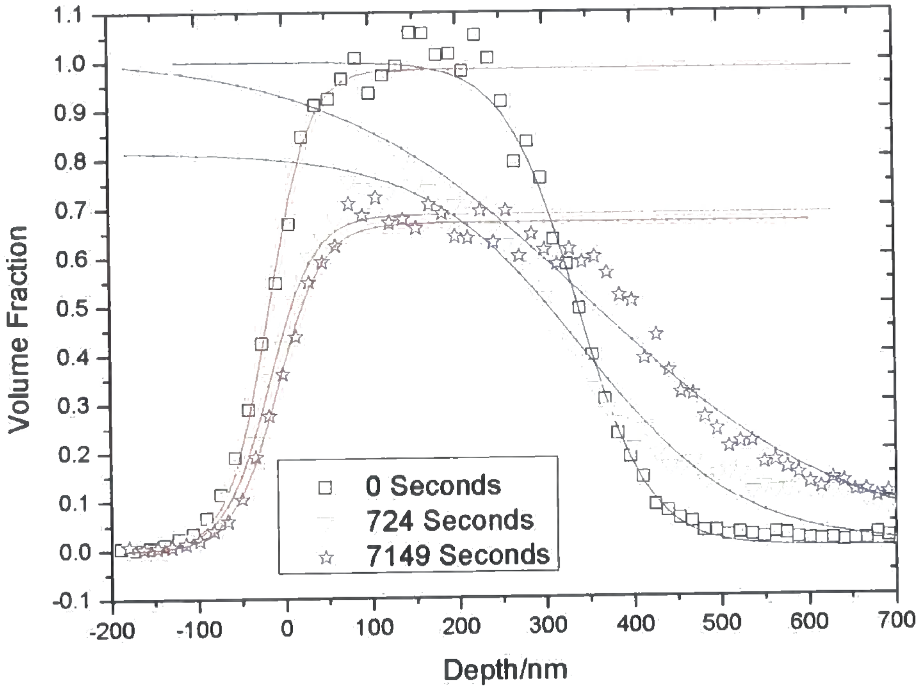

Figure 5.26 Depth profiles and hyperbolic tangent fits for approximately 300 nm 17300 gmol^{-1} DPEO on 2016000 gmol^{-1} PMMA annealed for various temperatures at 353 K Where w_{tot} includes beam damage, resolution functions and interfacial widths.

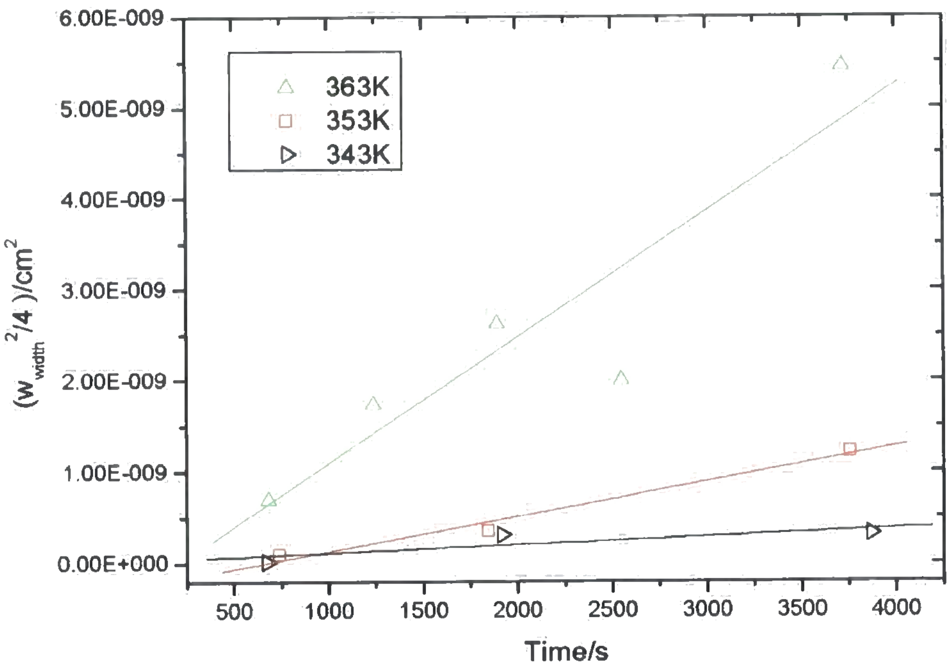

Figure 5.27 **Plot interfacial width $w_{width}^2/4$ of the interface between 60200 gmol^{-1} PMMA and 17300 gmol^{-1} DPEO against time for various temperatures. Straight line fits where the gradient is equivalent to the diffusion coefficient in cm^{2}s^{-1}.**

The values of diffusion coefficients D^*_{DPEO} are of order 10^{-14} cm^{2}s^{-1}. The tracer diffusion coefficients[10] for entangled polymers above the T_g are typically 10^{-9}-10^{-14}cm^{2}s^{-1}.

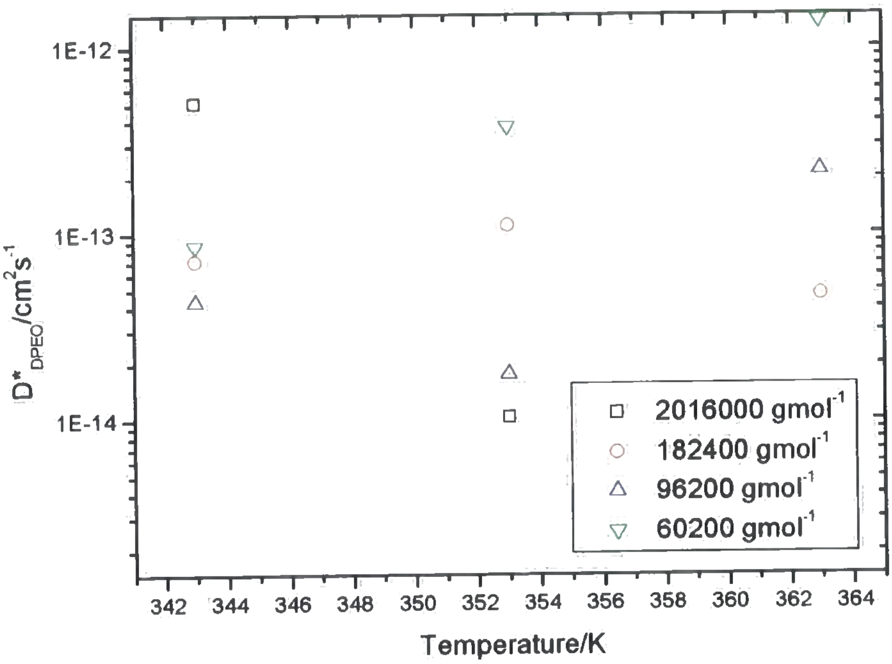

Figure 5.28 Plot of diffusion co-efficient with temperature for various PMMA molecular weight bilayers including 17300 gmol^{-1} DPEO.

Figure 5.29 shows that the diffusion coefficient exhibited a dependence on temperature, higher temperatures should result in faster moving molecules. Molecular weight dependence was inconsistent for any given temperature; however, this may be due to the statistically small number of molecular weights analysed.

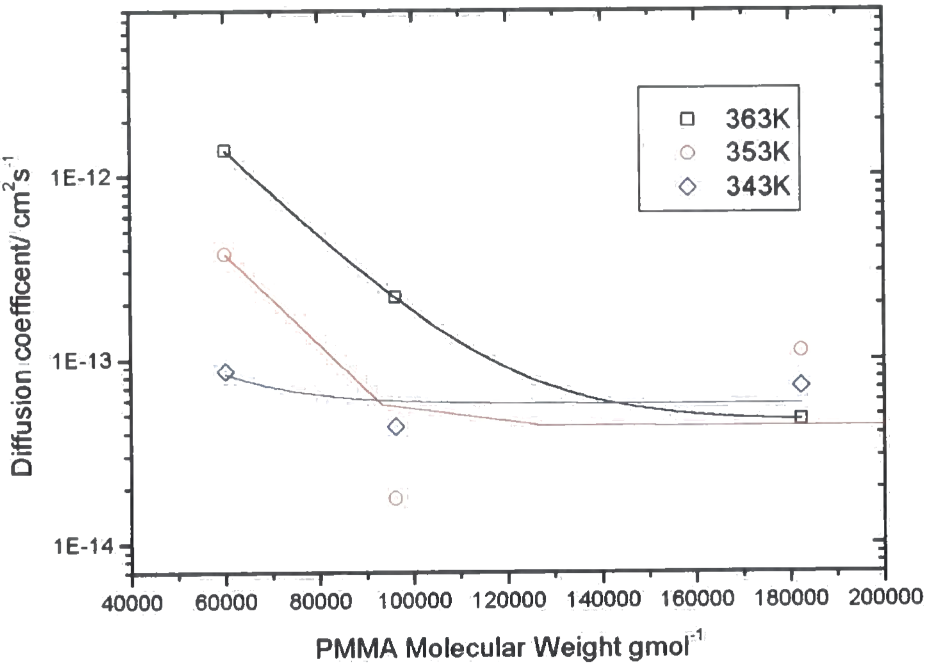

Figure 5.29 Plot of diffusion co-efficient with PMMA molecular weight for bilayers including 17300 gmol^{-1} DPEO. Various temperatures fitted with first order exponential.

Displacement of the interface $d_{interface}$ with time is linear for case II diffusion. For Fickean diffusion, interface displacement varies linearly with $t^{0.5}$ when one component is faster than the other (Equation 5.8). This relationship requires that the interface has a constant concentration, which is not true at $d_{interface}$, although it could be said to always contain the concentration $\varphi_{blend-PMMA}$=0.5. Figure 5.30 - Figure 5.32 show typical plots for bilayers. Graphs of depth against $t^{0.5}$ of the interface could be considered straight line graphs, however there is sufficient deviation from the straight line to imply some curvature in behaviour, notably for smaller molecular weights at longer anneal times. The diffusion front velocity is not independent of time and only instantaneous front velocities can be calculated as a function of concentration.

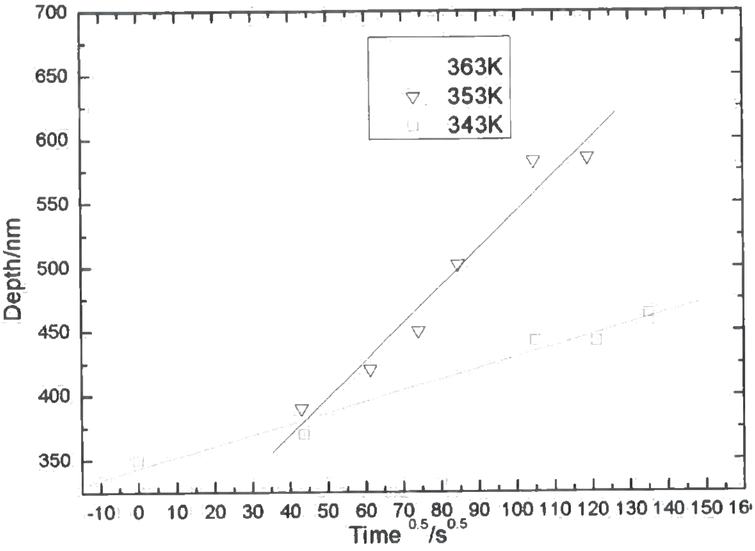

(A)

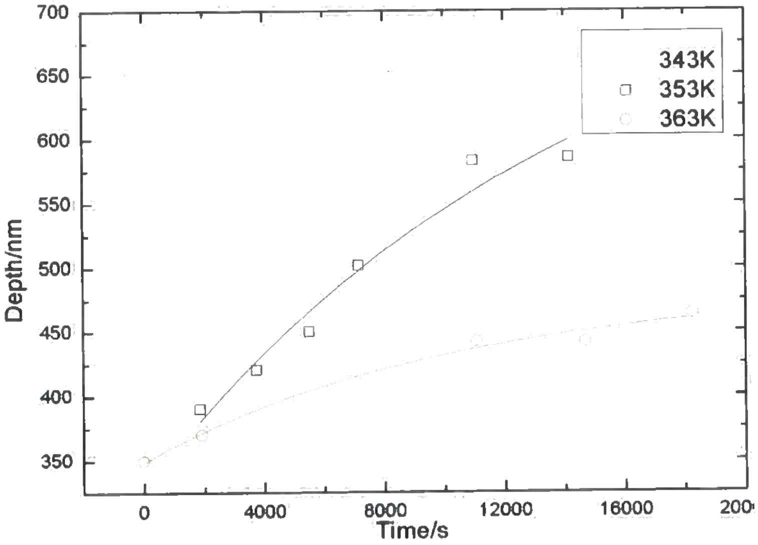

(B)

Figure 5.30 Plot of depth of interface $d_{interface}$ between 2016000 gmol^{-1} PMMA its blend with 170700 gmol^{-1} DPEO with time (A) $t^{0.5}$ and (B) t

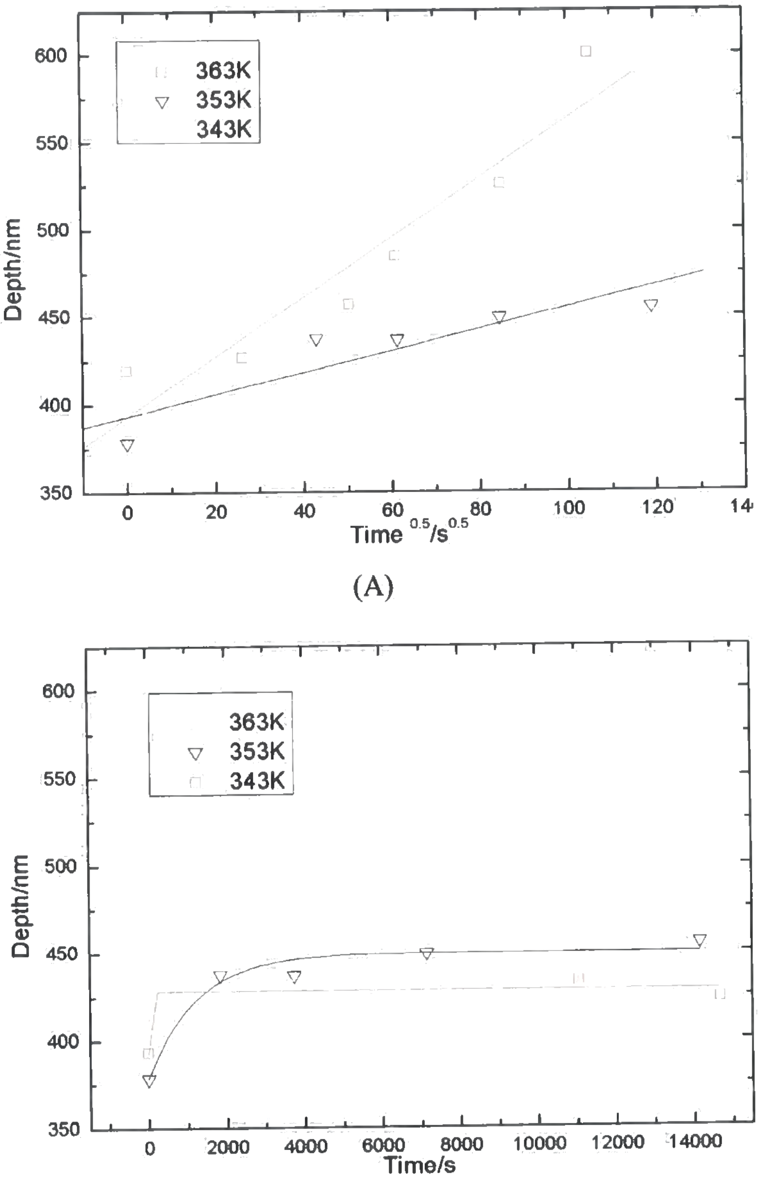

(A)

(B)

Figure 5.31 1 Plot of depth of interface $d_{interface}$ between 96200 gmol^{-1} PMMA its blend with 121100 gmol^{-1} DPEO with time (A) $t^{0.5}$ and (B) t

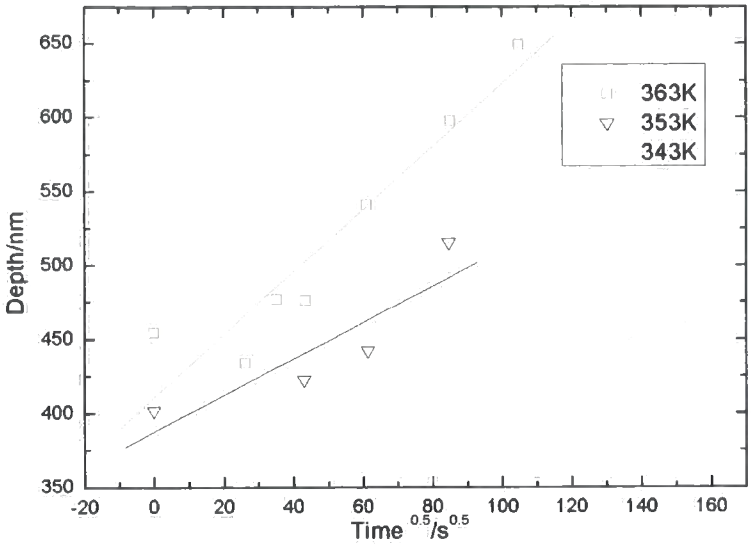

(A)

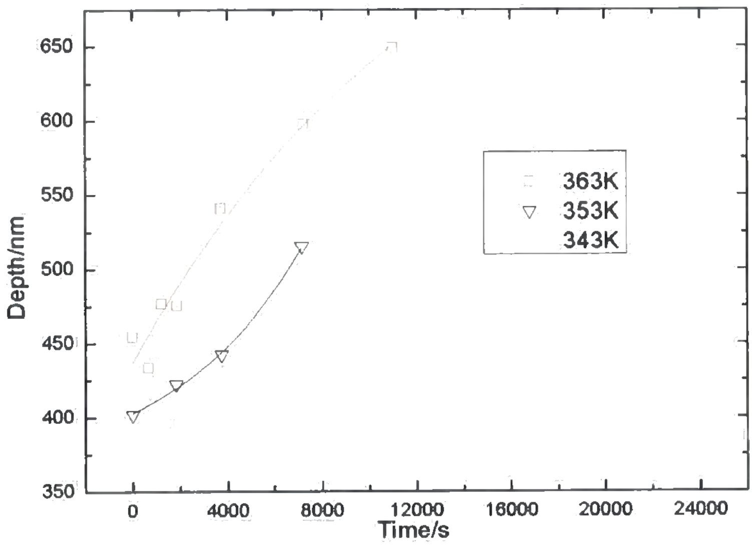

(B)

Figure 5.32 Plot of depth of interface $d_{interface}$ between 60200 gmol^{-1} PMMA its blend with 170700 gmol^{-1} DPEO with time (A) $t^{0.5}$ and (B) t

The gradient of straight lines of depth versus $t^{0.5}$should be proportional to $C^*\sqrt{D_{PMMA}}$ (Equation 5.9). The typical relationship of this parameter and PMMA molecular weight is shown in Figure 5.33. $C^*\sqrt{D_{PMMA}}$ is of the order of 10^{-7} $cm^2s^{0.5}$, diffusion of polystyrene of molecular weights 33000 to 943000, above the T_g of polystyrene[14] was of the order 10^{-7} $cm^2s^{0.5}$, again indicating similar diffusion times to other entangled polymers.

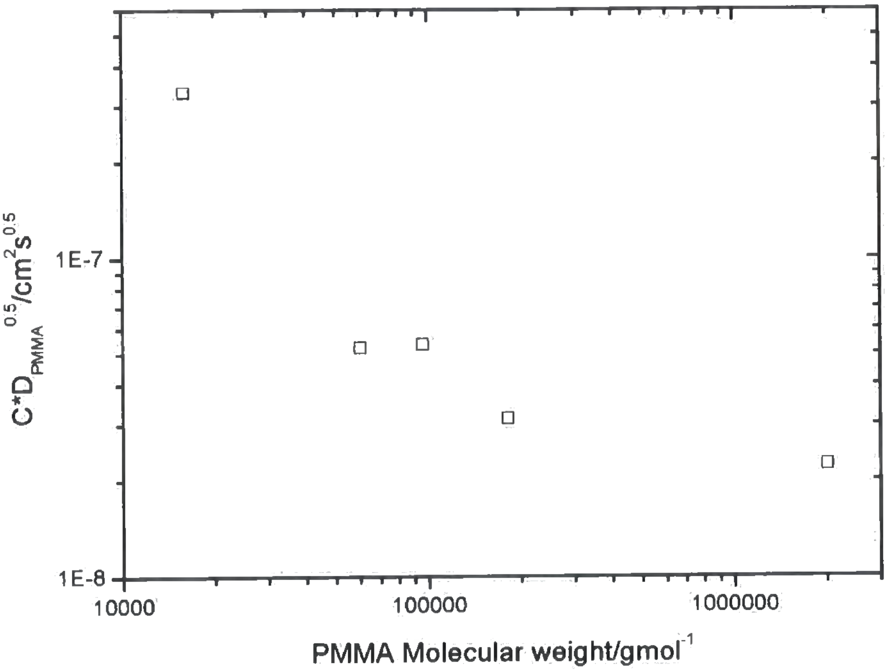

Figure 5.33 Plot of $C\sqrt{D_{PMMA}}$ (as found from straight line plots of interface displacement against $t^{0.5}$) versus PMMA molecular weight for 121100 $gmol^{-1}$.DPEO at 343 K

5.5.5 Application of Case II diffusion

Some authors[9,10] extend case II processes to describe the diffusion of rubbery polymers into glassy polymers (above the entanglement molecular weight) of similar size to here (~100000 $\mathrm{gmol^{-1}}$), showing that the process is controlled by the mechanical response of the glassy polymer. Others point out that large molecules in liquid state are associated with low osmotic pressures, insufficient to trigger a mechanism of mechanically controlled penetration.[12] The diffusion process for liquid polymer (PS) into a PS/PPO couple does not change when the temperature T_g of the PPO is reached, giving diffusion processes that were similar for liquid/glassy and liquid/liquid couples.[12,24] The mixing of the liquid and glassy polymers has been considered to be diffusion controlled as observed in liquid-liquid polymer diffusion.

Lin *et al* analysed rubbery PS into glassy PPO using SIMS. They discovered an interface with a sharp transition from $\varphi_{PPO} = 1$ to $\varphi_{PPO}=0.2$ over a thin transition zone of 20-30 nm. After annealing, a Fickean diffusion profile was created in the PS region apparently due to PPO diffusing into the PS. The PPO concentration in PS was then constant with depth, indicating a homogenously mixed sample past the Fickean tail. The driving force for the dispersion of PPO in the PS was believed to be mainly due to the large negative enthalpy of mixing for the two polymers. The PPO concentration in the PPO layer remained at $\varphi_{PPO}=1$, undiluted with PS molecules. The sharp interface was displaced with time towards the PPO bulk, effectively thinning the PPO bulk. This movement of the interface was considered to be a strong indication of case II behaviour in the location of the interface.

There are several similarities with the DPEO/PMMA system. The once glassy PMMA molecules are also quickly dissolved into the bulk liquid DPEO. A front is clearly observed for the glassy PMMA being dissolved by the DPEO and PMMA also maintains $\varphi_{PMMA}=1$ behind the interface. However, there is no clear evidence of a Fickean tail of dissolved PMMA in the DPEO although the Fickean process is widely regarded as the dominant diffusion mechanism in polymer melts. This could be due to the PMMA being dissolved faster in liquid DPEO than PPO into liquid PS or having greater mobility in DPEO than can be measured, so the Fickean profile exists on a time scale not resolvable by the methods utilised here. The dissolution of PMMA in DPEO is more analogous of a glassy polymer with a good solvent than two polymers in a melt.

For the PS/PPO case investigated by SIMS, the velocity of the interface started to slow with time. As the interface was still sharp this was taken to indicate that there had not been a change in chain diffusion mechanism but instead was attributed to a decrease of the chemical potential differences of the polymer molecules across the glassy/rubbery interface. The interface itself was found to broaden with time. Interfacial broadening was not detected for the high molecular weight PMMA/DPEO interface. When observed, interfacial broadening has been attributed to a plasticising region, but is not apparent for this system. It is possible that the plasticising region is too small to be seen as it is lost in the effective widths ascribed to beam damage and resolution.

The characteristic moving front is distinguishable for the bilayers investigated here however the application of case II diffusion is complex. In this system, the penetrant molecule could be considered to be the liquid DPEO and the glassy matrix the PMMA. The PMMA is quickly solvated into the DPEO, the reservoir of penetrant is thus no longer pure. Instead the penetrant is DPEO in a blend with PMMA. If mobile polymers are the penetrant phase, it may be possible that part or complete PMMA molecules flow back into the glassy bulk. This process could not be distinguished as the only observable quantity is the net displacement of polymers. If the driving force for mixing is the concentration dependent favourable enthalpy between the two polymers, then the 'backflow' of PMMA is unlikely. If the driving force is entropic, then 'backflow' is important in describing diffusion as the DPEO molecules. Case II diffusion does not account for this movement.

A sharp diffusion front is always apparent in systems where DPEO molecular weight > 17300 gmol^{-1}. The interface borders the PMMA and PMMA/DPEO blend and the position of the interface on the depth scale varies with time, *t*. The volume fraction of the blend changes with time and thus the front does not represent the boundary between pure PMMA and a blend of given concentration φ_0 as shown in Figure 5.13. There does not appear to be a Fickean precursor present in the system shown here. If present, the fits to $d_{interface}$ on the DPEO and PMMA peaks (Figure 5.25) would be poor, with broadening indicating that w_{width} should be fitted as shown in Equation 5.5. However fits were good for DPEO molecular weight >17300 gmol^{-1}, it is possible that the depth of the Fickean precursor (x in Figure 5.13) was of a similar or smaller scale to the effective widths of the instrumental resolution and beam damage and could not be distinguished, such an effective width w_{width} would be ~30 nm, so if present the precursor will involve $x < 30$ nm.

Contrary to the requirements of case II diffusion as described by Thomas and Windle,[16,17] both polymer components are in limited supply. Conservation of mass of penetrant requires the concentration of penetrant in the plasticised zone, (in this case, both are equivalent and indicate the blend) to decrease systematically with time and diffusion depth. The properties of the material behind the diffusion front will therefore alter with time and penetration depth, continuously varying the local driving forces that advance the diffusion front. Experiments with small molecules[25] as the limited supply diluent have shown that the concentration of the diluent in the plasticized region dropped monotonically from some initial level to a final level φ_{final} at which point the case II front stalled. φ_{final} occurs when the glass transition temperature for the plasticized region that matches the temperature of the system and the process zone thus encounters a sudden increase in deformation resistance, leading to the stalling of the front. The diffusion front in this system, does not appear to 'stall' but the front velocity slows with time. Stalling may not be exhibited because the system does not have sufficient depth range to detect the process. The diffusion behaviour displayed by a thinner film (50 nm) of DPEO on PMMA (chapter 3), where DPEO was in greater limited supply than shown here, included a slowing down of diffusion or stalling.

The early increases of volume fraction of PMMA in the DPEO rich region are linear with time. The volume fraction with time relationship is not linear as the system approaches approximately $\varphi_{PMMA}=0.5$. It is possible that case II diffusion can only be applied to the early stages of diffusion, where volume fraction gain is linear and defined. The PEO-rich region does not always display a homogenous concentration; a surface excess was observed at later anneal times, as described in Figure 5.9. This could indicate some form of concentration gradient was present behind the moving front. Theoretical studies of case II diffusion have shown that, at high penetrant concentration,[26] such that the concentration of the diluent rich blend is sufficiently high, the polymers remain mobile and do not apply 'back stress' on the moving front, and the diffusion front velocity is relatively insensitive to changes in the concentration of the plasticised (diluent rich) layer. The mobility required for the back stress to be negligible is unknown, hence an assumption that volume fraction of penetrant is always too high for a back stress to not occur may not be reasonable. The presence at longer anneal times of a concentration gradient (the DPEO surface excess characterised in Figure 5.9) complicates the application of case II diffusion but could possibly be ignored if only early diffusion is analysed.

From Figure 5.16 and Figure 5.17 the linear gain in PMMA in the DPEO rich layer with time is not apparent; this may reflect the non-linear displacement of the interface. It is unclear whether the slowing down of PMMA volume fraction gain is a reflection of mechanical osmotic pressure and the loss in mobility of the DPEO and consequent 'back stresses' or the change in thermodynamic compatibility with concentration. The system observed here may also be limited supply case II diffusion.

The shape of the depth profiles formed implies that the 17300 gmol^{-1} DPEO bilayers comes the closest to displaying a case II Fickean precursor. The small shoulder pre-cursor could be the Fickean precursor to the front. For most samples a small shoulder in the concentration profile appeared close to $d_{interface}$ and eventually the broadening peak maintained a constant shoulder at 0.1 volume fraction within the PMMA rich layer.

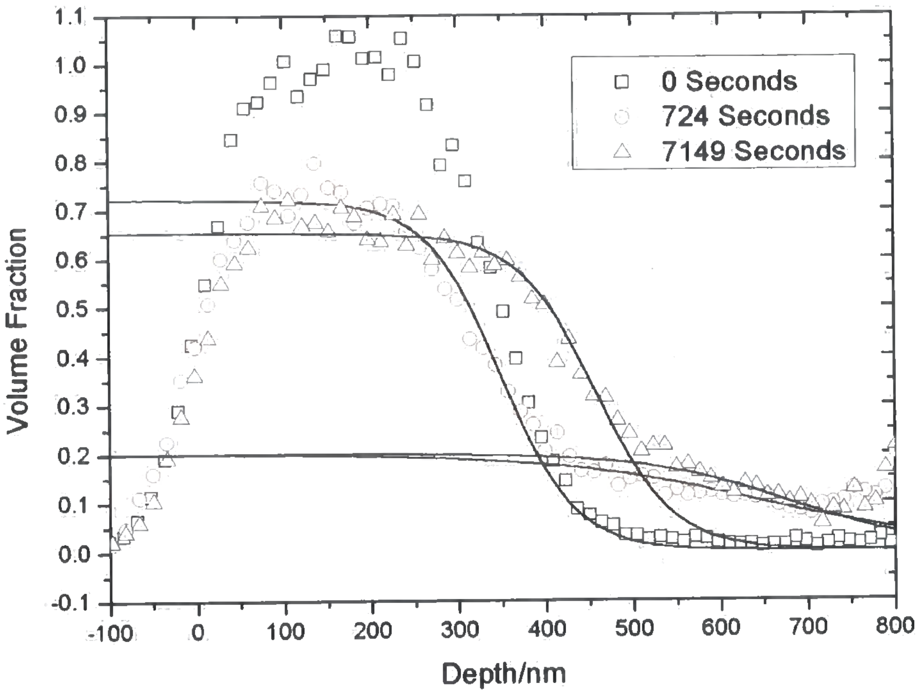

Figure 5.34 Depth profiles and hyperbolic tangent fits for approximately 300 nm 17300 DPEO on 2016000 PMMA annealed for various temperatures at 353 K

As can be seen from Figure 5.34 the profile at 724 seconds does not show a displacement of the DPEO bulk or front. This could be because the Fickean pre-cursor had to be developed to φ_c before case II diffusion could begin. Such a small shoulder is close for many samples to background noise and it is very hard to clearly distinguish or fit. An attempt, allowing two hyperbolic tangents with varying values of $d_{interface}$ and w_{width} is shown in Figure 5.34.

5.6 *Summary*

The DPEO/PMMA diffusion couple could be said to exhibit both Fickean and case II characteristics. Plots of interface movement with $t^{0.5}$ were not strictly linear and the non-linear relationship of interface displacement with t could reflect limited supply case II characteristics rather than Fickean diffusion being the overiding diffusion regime. Many characteristics of limited supply case II diffusion were exhibited in profile shape especially for bilayers containing 17300 gmol^{-1} DPEO. The different behaviour of 17300 gmol^{-1} DPEO could be attributed to the higher mobility of the DPEO compared to other samples. This mobility may allow the DPEO to form a Fickean precursor within the glassy PMMA, although the PMMA itself behaves in the same general fashion irrespective of molecular weight. The characteristic slowing down associated with limited supply case II diffusion was further complicated by the concentration dependence of the interaction parameter for PMMA and DPEO blends. Diffusion of PMMA could be said to follow limited supply case II processes at the resolution available to the experimental system. The diffusion is controlled by action at the interface.

5.7 References

(1) Composto, R. J.; Walters, R. M.; Genzer, J. *Materials Science & Engineering R-Reports* **2002**, *38*, 107-180.

(2) Genzer, J.; Rothman, J. B.; Composto, R. J. *Nuclear Instruments & Methods in Physics Research Section B- Beam Interactions with Materials and Atoms* **1994**, *86*, 345-354.

(3) Kerle, T.; Scheffold, F.; Losch, A.; Steiner, U.; Schatz, G.; Klein, J. *Acta Polymerica* **1997**, *48*, 548-552.

(4) Patnaik, A. *Metals Materials and Processes* **1995**, *6*, 245-262.

(5) Abel, F.; Quillet, V.; Schott, M. *Nuclear Instruments & Methods in Physics Research Section B- Beam Interactions with Materials and Atoms* **1995**, *105*, 86-90.

(6) Mayer, M. *Nuclear Instruments & Methods in Physics Research Section B- Beam Interactions with Materials and Atoms* **2002**, *194*, 177-186.

(7) Fetters, L. J.; Lohse, D. J.; Richter, D.; Witten, T. A.; Zirkel, A. *Macromolecules* **1994**, *27*, 4639-4647.

(8) Composto, R. J.; Kramer, E. J. *Journal of Materials Science* **1991**, *26*, 2815-2822.

(9) Lin, H. C.; Tsai, I. F.; Yang, A. C. M.; Hsu, M. S.; Ling, Y. C. *Macromolecules* **2003**, *36*, 2464-2474.

(10) Jabbari, E.; Peppas, N. A. *Macromolecules* **1993**, *26*, 2175-2186.

(11) Tomba, J. P.; Carella, J. M.; Garcia, D.; Pastor, J. M. *Macromolecules* **2001**, *34*, 2277-2287.

(12) Tomba, J. P.; Carella, J. M.; Pastor, J. M. *Macromolecules* **2005**, *38*, 4355-4362.

(13) Reiter, G.; Huttenbach, S.; Foster, M.; Stamm, M. *Macromolecules* **1991**, *24*, 1179-1184.

(14) Green, P. F.; Palmstrom, C. J.; Mayer, J. W.; Kramer, E. J. *Macromolecules* **1985**, *18*, 501-507.

(15) Kramer, E. J.; Green, P.; Palmstrom, C. J. *Polymer* **1984**, *25*, 473-480.

(16) Hui, C. Y.; Wu, K. C.; Lasky, R. C.; Kramer, E. J. *Journal of Applied Physics* **1987**, *61*, 5137-5149.

(17) Hui, C. Y.; Wu, K. C.; Lasky, R. C.; Kramer, E. J. *Journal of Applied Physics* **1987**, *61*, 5129-5136.

(18) Walton, D. G.; Soo, P. P.; Mayes, A. M.; Allgor, S. J. S.; Fujii, J. T.; Griffith, L. G.; Ankner, J. F.; Kaiser, H.; Johansson, J.; Smith, G. D.; Barker, J. G.; Satija, S. K. *Macromolecules* **1997**, *30*, 6947-6956.

(19) Jones, R. A. L.; Norton, L. J.; Kramer, E. J.; Bates, F. S.; Wiltzius, P. *Physical Review Letters* **1991**, *66*, 1326-1329.

(20) Geoghegan, M.; Jones, R. A. L.; van der Grinten, M. G. D.; Clough, A. S. *Polymer* **1999**, *40*, 2323-2329.

(21) Composto, R. J.; Kramer, E. J.; White, D. M. *Macromolecules* **1992**, *25*, 4167-4174.

(22) Green, P. F.; Mills, P. J.; Kramer, E. J. *Polymer* **1986**, *27*, 1063-1066.

(23) Tomba, J. P.; Carella, J. M.; Garcia, D.; Pastor, J. M. *Macromolecules* **2004**, *37*, 4940-4948.

(24) Nealey, P. F.; Cohen, R. E.; Argon, A. S. *Polymer* **1995**, *36*, 3687-3695.

(25) Argon, A. S.; Cohen, R. E.; Patel, A. C. *Polymer* **1999**, *40*, 6991.

Chapter 6

Elastic Recoil Detection analysis of bilayers of DPEO and PS-PMMA block copolymer

6.1 Introduction

The diffusion of PMMA and DPEO was found by ERD and NRA to display both case II and Fickean characteristics. For annealed bilayer films, PMMA diffused rapidly into DPEO, forming a blend layer adjacent to the film surface. There was no evidence of a concentration gradient within the blend, indicating that the diffusion of PMMA within the blend was too fast to measure. Even very high molecular weight PMMA 2016000gmol^{-1} was too fast to measure. It would therefore be advantageous to slow down the PMMA or DPEO components. Block copolymers composed of two distinct polymer chains chemically bound together exhibit rich phase behaviour and have applications in compatibilizing immiscible polymer blends, stabilising colloidal particles and nanocomposites. The diffusion coefficient of a PS-PMMA diblock copolymer into PS and PMMA homopolymer of various molecular weights, demonstrated diffusion coefficients orders of magnitude less than those of homopolymer chains of the same degree of polymerisation diffusing into the same environments.[1-3] This difference is attributed to the monomeric friction coefficient of PMMA into PS, ζ_{PMMA}(PS), being many orders of magnitude larger than that of PS into PS ζ_{PS}(PS).[4] The very high value of the effective friction coefficient controls the diffusion of the probe copolymer. Hence the behaviour of the host chains that control the tube the copolymer is contained by, becomes an important issue. The temperature dependence of the diffusion coefficient was found to be controlled by the viscoelastic relaxations of the host polymers.[4] A block copolymer of PS-PMMA could replace the PMMA as the glassy matrix; The PMMA and DPEO components should still have favourable enough interactions whilst the PS part of the chain should slow the diffusion process. The copolymer will need to be characterised to find the glass transition temperature, transmission electron microscopy can be used to establish the morphology of PS and PMMA in a thin film. Experimental refinements to the ERD methods, taking into account surface roughness and the changes to stopping powers from PS present and any subsequent adjustments to the data conversion used in chapter 5, can be made. PMMA/DPEO bilayers were compared to both Fickean and case II diffusion; any interfaces and interfacial growth between the copolymer and DPEO films can be characterised and similarly compared. By utilising the same DPEO molecular weights comparisons can then be made to the PMMA/DPEO system with an emphasis on the effect of changing the interaction parameter of the system.

6.2 Copolymer background

The diffusion of copolymer into homopolymers has not been extensively studied. It has been proposed[4] that if the block whose translation process is energetically more favourable in a given phase, moves forward first then the attached block with a greater friction coefficient will impede further motion. If both processes are considered independent then an effective friction factor ζ_{eff} can be written,

$$\zeta_{A-B}(A)=\zeta_{eff}=N_{n,A}\zeta_A(A)+N_{n,B}\zeta_B(A) \qquad \text{Equation 6.1}$$

where $N_{n,i}$ are the degrees of polymerisation and ζ_i are the individual monomeric friction coefficients for polymers, ζ_{eff} can then be used in reptation equations to describe behaviour in the blend (section 1.2.3-4). The interaction parameter for PS and PEO has been found[5] to be $\chi_{PS\text{-}PEO}$=-0.0067+25.26/T whereas PS and PMMA has an interaction parameter[6] $\chi_{PS\text{-}PMMA}$=0.0129+1.96/T. Isotopic labelling of polymers is known to have a small effect on the interaction parameter,[7] however, as no direct measure of the interaction parameter for DPEO and hydrogenous PS are known, the hydrogenous parameters will have to suffice.

The difference due to isotopic labelling is minimal compared to the polymer type. Resultant values of the interaction parameters at relevant temperatures are shown in Table 6.1, $\chi_{\mathrm{DPEO\text{-}PMMA}}$ is composition dependent as discussed in chapter 4, and hence a range of values is quoted. $\chi_{DPS\text{-}PEO} > \chi_{PS\text{-}PMMA} > \chi_{DPEO\text{-}PMMA}$ means that the PS component of the copolymer chain will prefer the copolymer environment to that of the DPEO blend.

T/K	χ DPS-PEO	χ PS-PMMA	χ DPEO-PMMA[a]
343	0.067	0.019	-0.002 to 0.006
353	0.065	0.018	-0.004 to 0.004
363	0.063	0.018	-0.006 to 0.003
373	0.061	0.018	-0.005 to 0.006

Table 6.1 Showing interaction parameters for PS, PMMA and PEO.

[a] A range of values as measured in chapter 4 between 6% and 40% DPEO

The formation of micelles by the block copolymers complicates the diffusion process. It is know that within the bulk, copolymer micelles will form.[2] As $\chi_{DPS\text{-}PEO} > \chi_{PS\text{-}PMMA}$ this is unlikely to occur within the PEO blend. Diffusion of micelles would be expected to be slower than for free chains. The behaviour of PS-PMMA in DPEO might also encourage the PS segment to form a collapsed coil in order to minimise interactions with PMMA or DPEO.

The T_g of the copolymer was found to be ~140°C, as can be seen from the DMA trace in section 4.6 and the PMMA molecular weight with the nearest T_g was 182400 gmol^{-1}, ($T_{gE''}$= 132 °C and $T_{g\tan\sigma}$=141 °C). The systems have very similar glass transitions, this indicates that any differences in diffusion behaviour are due to the difference in interaction parameters between the copolymer and the pure homopolymer. At annealing temperatures greater than 118°C the DPS and PMMA tracer diffusion coefficients for unentangled DPS and PMMA in the blend are considered to be near equality (at 134 °C $D_{DPS}^{*} = D_{PMMA}^{*} = 1.2\times10^{-12}\ \mathrm{cm^2s^{-1}}$)[8]. Both polymers had T_g of approximately 70 °C, so for equality of diffusion coefficient the temperature must be well in excess of the T_g. In this work T was never above the T_g of the pure copolymer but above the T_g of the blend. It can be assumed that the diffusion coefficients of the components if separated are different.

6.3 Experimental

6.3.1 Materials

The DPEO molecular weight polymers and PS-PMMA copolymer in Appendix I were utilised during this experiment. All polymers were above their individual entanglement molecular weight (PMMA=10000 gmol^{-1}, PS=14000 gmol^{-1} and PEO=1700 gmol^{-1})[9]

6.3.2 Bilayer construction

In the same procedure detailed in section 5.3.2 bilayers that included various DPEO molecular weights on copolymer were constructed using spin coating. Thick films of PS-PMMA were spun onto silicon wafers from a solution in toluene and relaxed by heating overnight at 413 K in a similar fashion to PMMA films. Samples were heated at 373 K, 363 K, 353 K and 343 K for a range of times up to 48 hours. Samples were examined using an optical microscope to check for dewetting.

6.3.3 Transmission electron microscopy

The size and formation of micelles within PS-PMMA can be measured using transmission electron microscopy (TEM). A 50 nm thick film of copolymer was spun from a solution of toluene on to a glass slide. This was annealed at 140 °C for 24 hours in a similar fashion to the treatment of samples used in ERD experiments. The film was then floated off the slide and picked up on copper grids. The film was then stained with RuO_4 in an enclosed gas chamber. The stained films were then observed using a transmission electron microscope. RuO_4 stains only PS,[10] thus only the PS portion of block copolymers appeared darker in brighter field images.

6.3.4 ERD measurements

The same ion beam set up was utilised for studying the diffusion of DPEO into PS-PMMA as for DPEO into PMMA, so that the same analysis could be used and results would be comparable. Bilayers of the same molecular weight were placed on the same racks.

6.4 *Data Analysis*

6.4.1 Depth scale conversion and normalised yield

Channel was converted to depth using the same spreadsheet discussed in 5.4.1 and 2.3.5.1. It is assumed that the stopping powers of PS-PMMA were the same as for PMMA. This is reasonable since the bulk of the copolymer was PMMA and PS varies only slightly in stopping powers from PMMA. Hence the assumption should introduce no greater error than using DPEO stopping powers as equivalent to PMMA as shown in Figure 6.1.

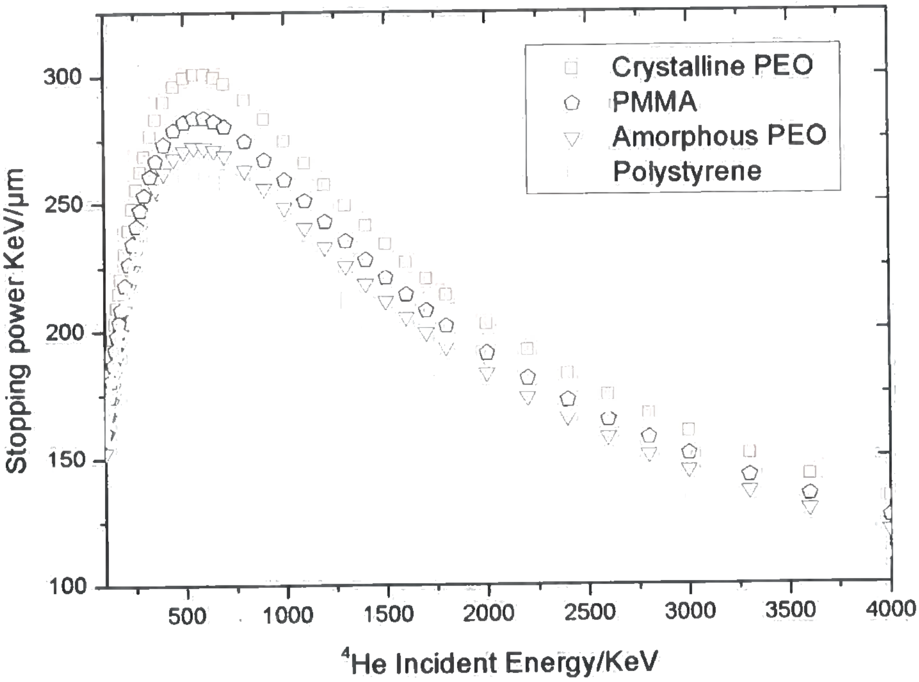

Figure 6.1 Plot of stopping power in KeV/ μm against energy of ^{4}He/ KeV, as calculated using SRIM® for PMMA, amorphous and crystalline PEO, (density of 1.120 gcm^{-3} and 1.238 gcm^{-3} respectively) and polystyrene

The volume fraction of a given species at a given depth was calculated as described in 2.3.5.2.

6.4.2 Surface roughness, resolution and beam damage

As shown in section 5.2.7, surface roughness was dominated by the effect of crystallinity within the DPEO layer. Roughness in general decreased with increasing PMMA concentration within the DPEO layer. AFM measurements showed no difference in the behaviour of DPEO/copolymer bilayers to that of PMMA layer. Polystyrene only accounted for approximately 10% of the PMMA bilayer; the difference in surface roughness between pure PMMA bilayer samples and copolymer bilayer samples should therefore be negligible compared to larger contributions to the effective interfacial width such as beam damage and resolution.

The resolution function with depth was also considered to be identical to that of the PMMA bilayers. The function of effective width due to beam damage, w_{bd} , against depth was considered to be the same as for the PMMA bilayers. Although PMMA is considered to be more sensitive to the effect of ^{4}He radiation, it was protected by a similar amount of DPEO. The polystyrene in the copolymer layer exposed to the radiation should be more resilient to beam damage however it only accounts for 10% of the copolymer and relative effect should be minimal

6.4.3 Raw data and interface definitions

Only samples that included 121100 gmol^{-1}and 170700 gmol^{-1} DPEO had diffusion behaviour slow enough for resolvable peaks to be observed at 373 K.

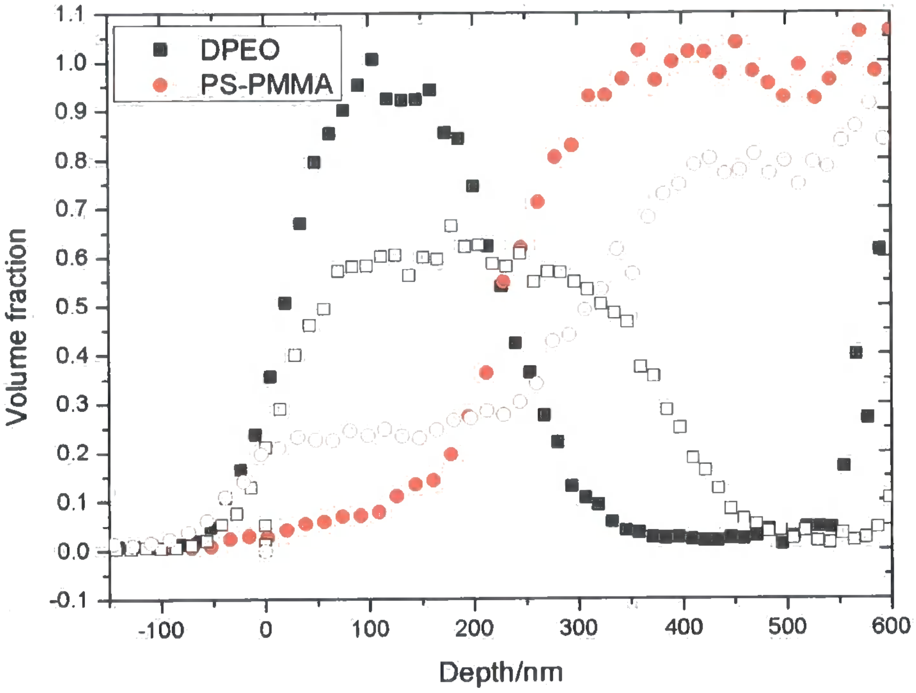

Figure 6.2 Normalised depth profiles for 121100 gmol^{-1} DPEO and PS-PMMA at 373 K after 0 seconds (closed) and 7200 seconds (open) plotted on the same depth scale

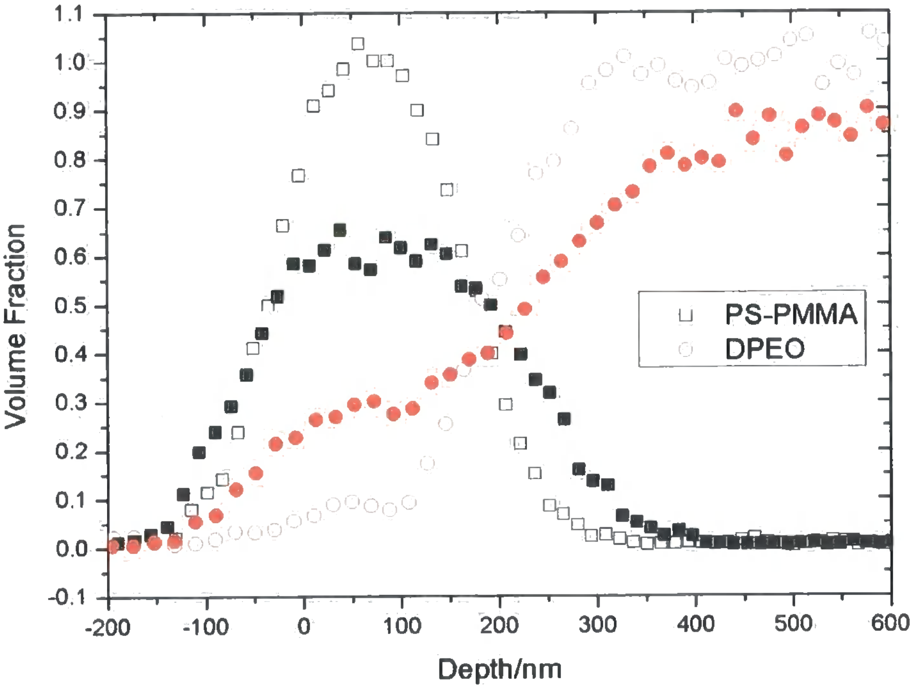

Figure 6.3 Normalised depth profiles for 170700 gmol^{-1} DPEO and PS-PMMA at 363 K after 0 seconds (open) and 25184 seconds (closed) plotted on the same depth scale

Figure 6.2 and Figure 6.3 show normalised DPEO and PS-PMMA profiles on the same depth scale. All the spectra exhibited a step-like profile of PS-PMMA, indicating ^{1}H present throughout the sample up to the air surface ($d_{surface}$ as defined in Figure 6.4). This can be taken to indicate that PS-PMMA is present throughout the DPEO layer. PS and PMMA are indistinguishable using ERD as both are hydrogenous. The radius of gyration of a chain of PS-PMMA (<50 nm) is much smaller than the total depth of the DPEO layer (~300 nm) thus there can be no surface enrichment, with the PS part of the copolymer remaining inside the PS-PMMA bulk and the PMMA part diffusing into the DPEO. Such a situation would result in ^{1}H signal reaching only part way into the DPEO layer. Thus although PS and DPEO do not have a favourable interaction parameter and would not be expected to mix, both PS and PMMA are present within the DPEO layer. A pure DPEO layer is not present, but the bilayer subsequent to annealing consists of a DPEO rich blend layer on top of PS-PMMA. No spectra showed an intermediate step between the initial bilayer and the blend/PS-PMMA bilayer implying that the diffusion co-efficient of PS-PMMA within the DPEO is in excess of that measurable by ion beam analysis. This may be analogous to PS-PMMA being rapidly solvated in a liquid. $d_{interface}$ is thus the depth of the interface between the blend and PS-PMMA for all annealing times where $t > 0$. When t=0, the $d_{interface}$ describes DPEO/PS-PMMA interface. Unlike the PMMA bilayers not all $d_{interface}$ were sharp. This can be seen in Figure 6.2 and Figure 6.3, where Figure 6.3 shows a slightly sloped interface between the blend and the PS-PMMA. There is a visible increase in width relative to the annealed sample that cannot be due to instrumental factors alone. The slope is generally only seen in later annealed samples and for copolymer bilayers with PS-PMMA substrates that were <1 μm. If PS-PMMA is no longer in excess then the diffusion observed will show characteristics of this limited supply. The growth in height of the 'step' in the step-like profile indicates an increase in volume fraction PS-PMMA ($\varphi_{blend\text{-}PS\text{-}PMMA}$) in the blend.

The DPEO peak decreased in volume fraction and $d_{interface}$ moved to greater depths with time. This indicates the net movement of the blend to greater depths, however the free movement across $d_{interface}$ of both DPEO and now mobile PS-PMMA molecules may occur.

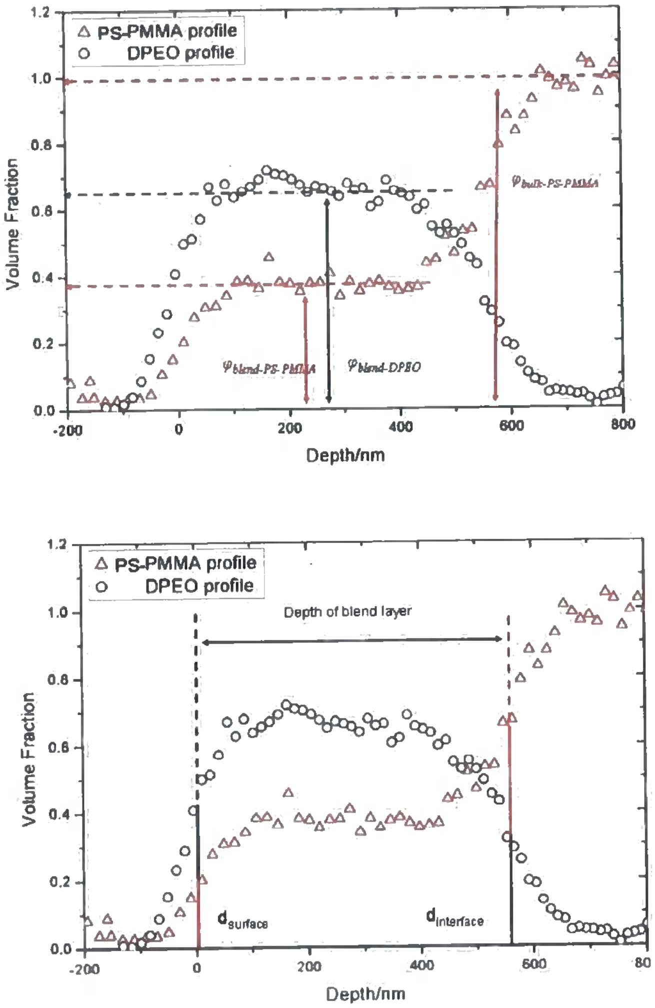

Figure 6.4 Schematic of definition of interfaces and volume fractions on superimposed PS-PMMA and DPEO profiles

As with the DPEO/PMMA bilayers some of the samples that included DPEO with a molecular weight >17300 $gmol^{-1}$ exhibited the development of a second step-like profile, an example is shown in Figure 6.5. The DPEO profile exhibited a region of high concentration of DPEO at the air surface and a region with lower φ_{DPEO} within the sample. This phenomenon was mostly observed for samples that included 89217 $gmol^{-1}$ DPEO. This was probably not a molecular weight specific process, but was observed for those bilayers as the extent of diffusion was greater during the annealing time schemes utilised. The displacement of the deepest interface of the DPEO was found to vary with time. Plotting the two profiles on the same depth scale (Figure 6.6) revealed a similar phenomenon to that observed for PMMA. A surface excess was observed in the DPEO-rich 'blend' layer. The sum of $\varphi_{blend\text{-}DPEO}$ and φ_{DPEO} was unity for all samples. $\varphi_{blend\text{-}DPEO}$ was considered to describe the volume fraction within the bulk blend as illustrated in Figure 6.4. As with PMMA bilayers it is unlikely that this profile may be due to dewetting.

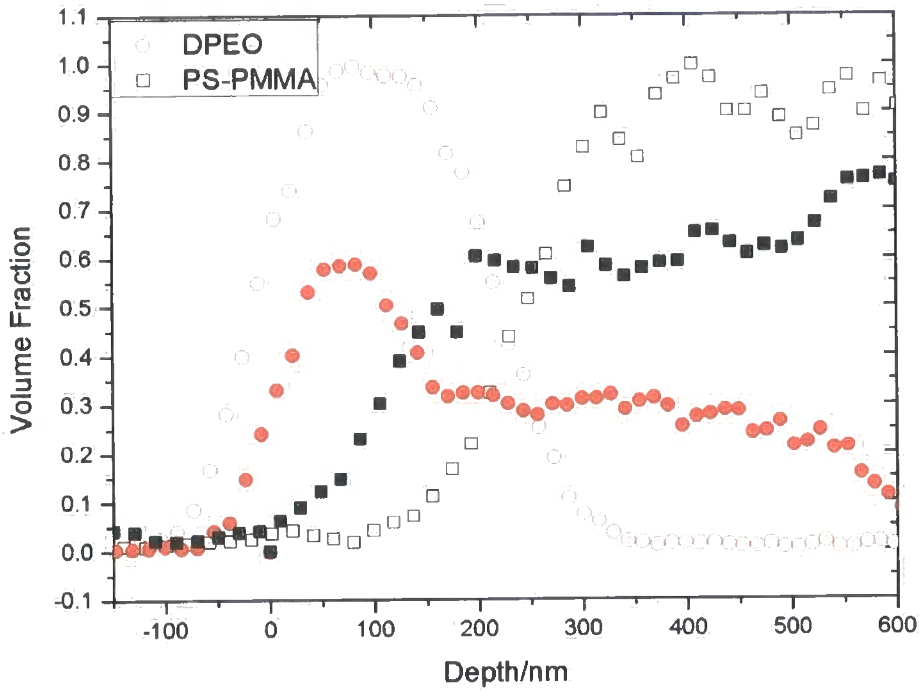

Figure 6.5 Normalised depth profiles for approximately 300 nm 89217 gmol^{-1} DPEO on PS-PMMA after 0 seconds (open) and 83509 seconds (closed) plotted on the same depth scale

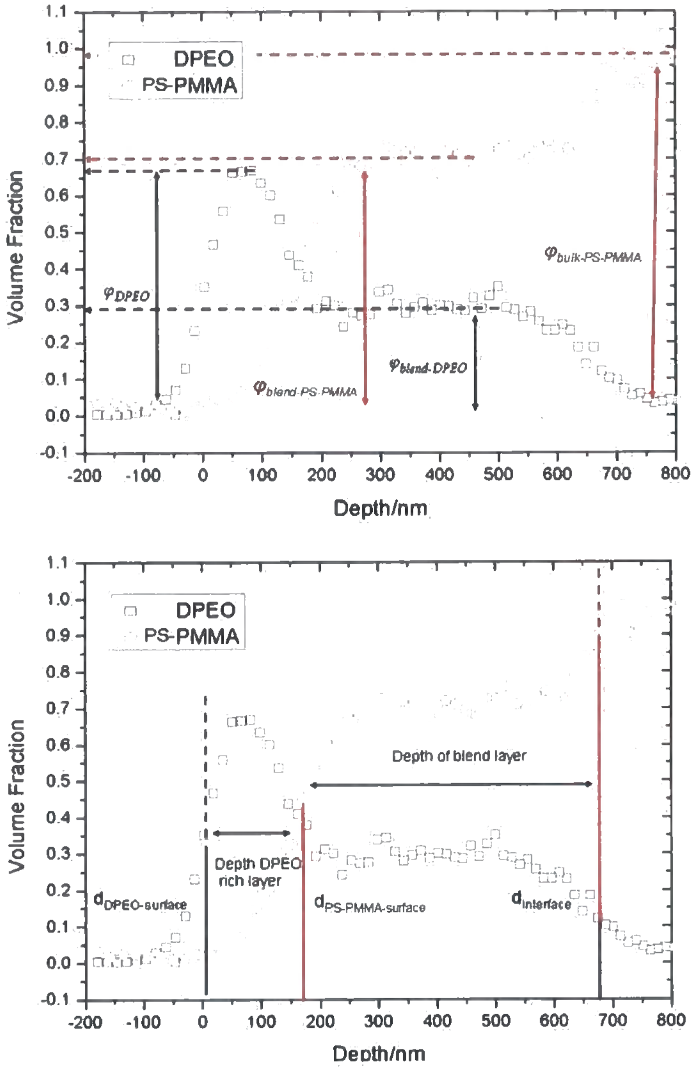

Figure 6.6 Schematic of definition of volume fractions and depths on superimposed PS-PMMA and DPEO profiles for longer annealed samples which exhibited a DPEO shoulder.

The PMMA bilayer samples that included 17300 gmol^{-1} DPEO behaved in a different manner to those of higher DPEO molecular weight. Annealed bilayers containing 17300 gmol^{-1} DPEO and PS-PMMA were visibly dewetted when viewed under an optical microscope. Diffusion information about the movement of PMMA could not be determined for these samples, as the PMMA was already exposed to the surface, and surface roughness effects would have interfered with any resolvable values of w_{eff}.

6.4.4 Calculating diffusion profile

The position, and broadening, of the interfaces were described by a hyperbolic tangent[11] as described in section 5.4.3 for the PMMA samples. With no interfacial broadening, w_{tot} is described by w_{bd} *and* w_{res} (Equation 5.2). The value of d_i or depth for a given interface was thus defined using least squares fitting. d_i (typically $d_{surface}$ and $d_{interface}$) and φ can be found for a given interface, Figure 6.7 shows the typical fits. The values of $d_{surface}$, $d_{interface}$ and φ were the result of averages between tangents in the same fashion as described for the PMMA bilayers (Figure 6.4 and Figure 6.6). As fits for bilayers containing DPEO >17300 gmol^{-1} were reasonable using the depth functions of w_{bd} and w_{res} used for PMMA bilayers, the assumption that surface roughness and beam damage were equivalent for the two types of bilayer appears justifiable. Figure 6.9 shows typical fits, the majority of samples fitted well.

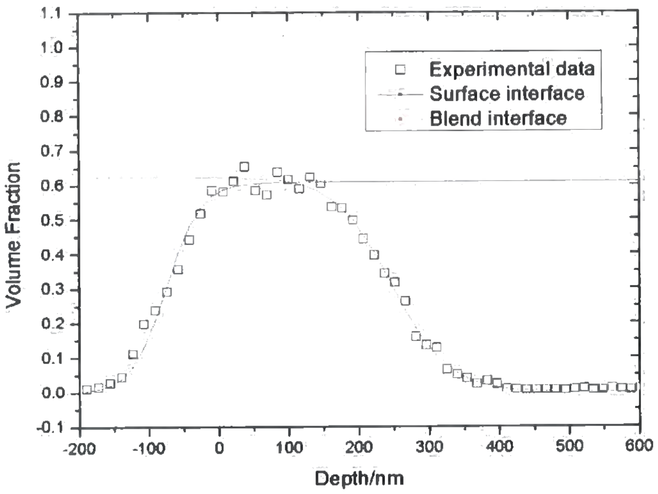

(A)

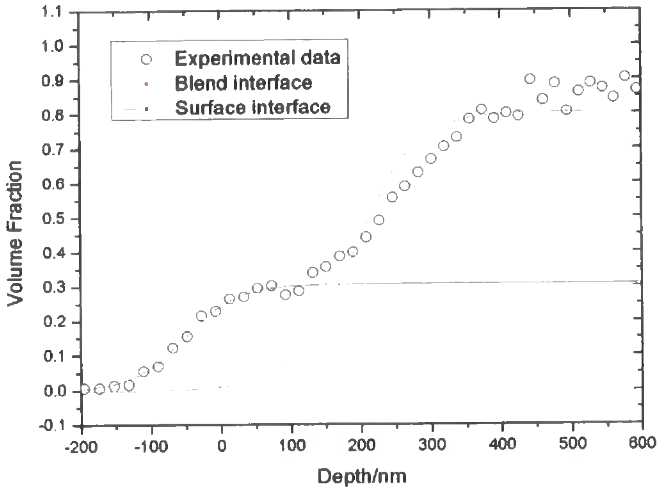

(B)

Figure 6.7 Example of hyperbolic tangent fitting DPEO profile (A) and PS-PMMA profile (B)

6.5 Discussion

6.5.1 TEM results

Transmission electron microscopy images for a 50 nm film of PS-PMMA copolymer are shown in Figure 6.8.

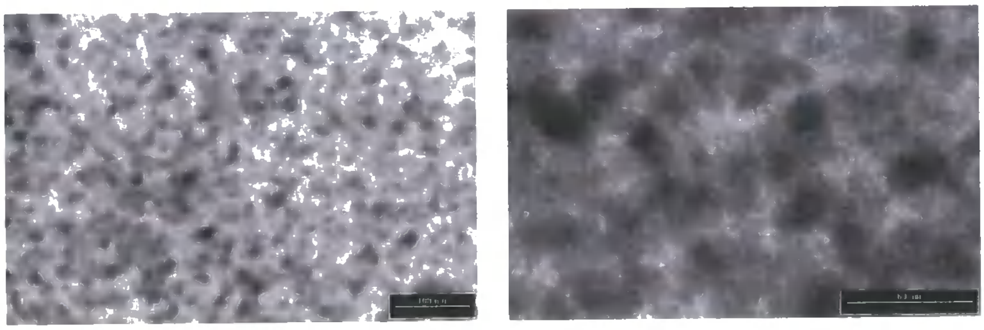

Figure 6.8 TEM images for PS-PMMA copolymer, using RuO_4 staining. Dark areas indicate polystyrene.

An average micelle diameter of 21.5 nm was found from Figure 6.8. Micelles can be seen at the surface and are presumably present throughout the sample. Mixtures of block copolymers and homopolymers in thin films and the bulk have been previously analysed.[3] Mixtures of PEO and PS-PMMA above the entanglement molecular weight are known to phase separate into macrodomains when $\varphi_{DPEO} > 0.4$.[3] For PS-PMMA copolymer within PS, micelles were also observed[2].

6.5.2 Rubbery/Glassy diffusion couples

Previously, glassy PMMA has been observed to be quickly dissolved into the molten DPEO and subsequently into DPEO/PMMA blend. The blend establishes a constant concentration with depth in times smaller than could be analysed using ERD. A PS-PMMA copolymer contains a portion of polymer that does not have a favourable interaction parameter with DPEO, this was expected to inhibit the movement of PMMA into DPEO or to affect the diffusion established between DPEO and PMMA. PS-PMMA was found to dissolve into the DPEO without surface enrichment, implying complete solvation for both the PS and PMMA block, in times faster than could be measured using ERD. No concentration gradient within the blend was apparent. If the PS-PMMA diffused only in the form of micelles or with a collapsed coil of PS it did not affect the diffusion of the once glassy molecules in the blend sufficiently for the action at the interface to be faster than diffusion through the blend. Without a concentration gradient it is impossible to verify which component of the blend is the faster moving. As the diffusion of copolymer into the DPEO was not several orders of magnitude slower than linear homopolymer, the copolymer may be assumed to diffuse as a single chain. Several other examples of diffusion of long chain glassy entangled polymers into rubbery entangled polymers has been observed, however there has not been a clear understanding of the method of diffusion utilised with samples often exhibiting both case II and Fickean behaviour[12,13] [14]. Further studies have only included one entangled polymer with rubbery component below the entanglement molecular weight[15,16].

As PS-PMMA is dissolved into the DPEO rich layer, the T_g of the blend layer will increase with PS-PMMA concentration. This process should be nearly identical to that of the pure PMMA as the T_g of the copolymer and PMMA are very similar. As long as the T_g of the blend remains below T, the operating temperature of the experiment (343-373 K), the blend layer will be liquid and polymers should diffuse freely within the blend. A PS-PMMA molecule will only be mobile in a PS-PMMA environment of lower local T_g or an environment of higher mobility polymers such as at $d_{interface}$.

6.5.3 Dewetting of low molecular weight DPEO

All bilayers that included 17300 gmol^{-1} DPEO showed, under an optical microscope, visible dewetting after annealing. This appeared as small circles of differing colour on the sample surface. The samples were analysed using the ion beam, typical raw spectra are shown in Figure 6.9.

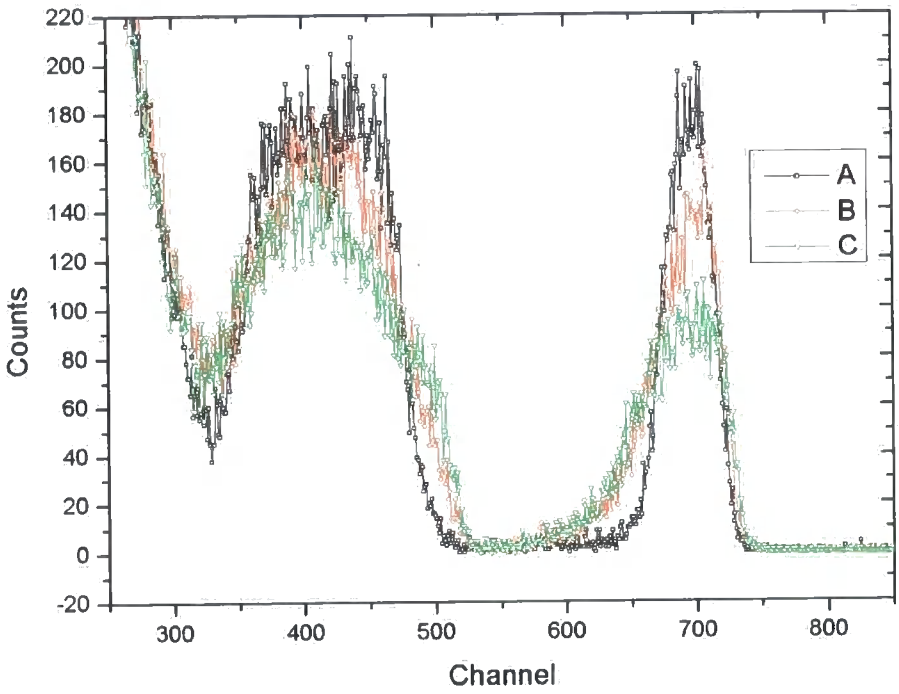

Figure 6.9 Plot of 17300 gmol^{-1} DPEO on PS-PMMA, after annealing 1324 seconds and 166118 seconds

Initially the shape of the spectra appears similar to that of 17300 gmol^{-1} DPEO on PMMA. The DPEO peak has a tail and the PMMA has a small shoulder indicating that the PS-PMMA has reached the surface. However, the PMMA/DPEO bilayers showed no sign of dewetting. It is possible that whilst some of the PEO dewetted some also diffused into the sample. Dewetting occurs in thin films[17] because of the comparably favourable interactions between the DPEO molecules compared to the substrate molecules and differing surface tensions of the polymer layers. It is unlikely that the timescale of dewetting is too slow to be observed for the PMMA/DPEO bilayers as opposed to PS-PMMA/DPEO bilayers, as diffusion for the PS-PMMA bilayers has been shown to be a similar scale to that of PMMA, if not slower. The action of DPEO diffusing into the sample would also decrease the depth of the DPEO layer on the surface, perhaps creating a critical depth or PS-PMMA concentration at which film instabilities were sufficient to precipitate dewetting. Dewetting may only be observed for the PS-PMMA samples because the PS may render the surface less compatible with the DPEO, the micelles at the surface may also act as nucleation sites for dewetting. The PS and DPEO have strongly unfavourable interactions which might encourage phase separation and dewetting at the interface. It is surprising that dewetting only occurs for the 17300 gmol^{-1} sample as all DPEO polymers have the same interaction parameter and very similar T_g. Whilst this polymer is the most mobile of those analysed, this would imply it has a greater ability to penetrate the copolymer substrate whilst the higher molecular weight DPEO, having the greater entropic barrier to interlayer diffusion, could be expected to dewet. Interactions at the interface are the rate determining step for diffusion for PMMA/DPEO bilayers; if action at the interface is independent of DPEO molecular weight, then the smaller DPEO polymers would be expected to have the mobility to retract and dewet on top of the substrate.

6.5.4 Blend volume fraction

For the samples analysed, $\varphi_{blend\text{-}PS\text{-}PMMA}$ was only measured up to $\varphi_{blend\text{-}PS\text{-}PMMA}=0.6$. Whether the concentration increased beyond this, to the stoichiometry of the sample or to another equilibrium concentration, is unknown, as the system could not be measured further. Figure 6.10 shows a typical plot of change in volume fraction of the two components in the blend layer (between $d_{interface}$ and $d_{surface}$) with time. Increase of PS-PMMA in the blend is matched by the decrease in DPEO as would be expected so that; $\varphi_{PS\text{-}PMMA\text{-}blend} + \varphi_{DPEO\text{-}blend} = 1$. Typically the change in volume fraction with time occurs faster for higher operating temperatures. The relationship between volume fraction and time is not linear, with the changes in $\varphi_{blend\text{-}PS\text{-}PMMA}$ and $\varphi_{blend\text{-}DPEO}$ being greater at smaller annealing times and slowing at greater annealing times. It can be assumed that, as PMMA is the main component of the PS-PMMA utilised, the interaction parameter χ exhibits similar temperature dependence to that found between DPEO and pure PMMA. Hence the behaviour of PS-PMMA in the DPEO blend might be similarly related to temperature.

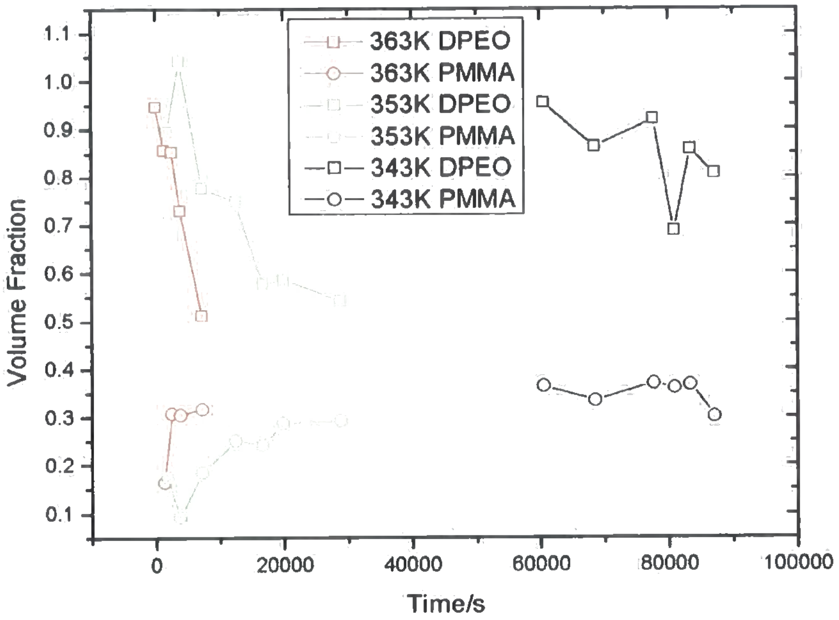

Figure 6.10 Plot of volume fraction of PS-PMMA ($\varphi_{blend\text{-}PS\text{-}PMMA}$) and 89217 gmol^{-1} DPEO ($\varphi_{blend\text{-}DPEO}$) between $d_{interface}$ and $d_{surface}$ against annealing time for various temperatures.

The interaction parameters for blends of DPEO and PMMA are known to be concentration dependent. It is typically believed that blends are not homogeneous where $\varphi_{blend\text{-}DPEO} > 0.3$. For the operating temperatures utilised in these experiments the interaction parameter when $\varphi_{blend\text{-}DPEO} < 0.35$, was small and negative for blends of PMMA and DPEO indicating a homogenous blend. The interaction parameter between PS and DPEO is positive at all concentrations, so repulsive interactions between the PS block should remain constant whilst the interactions with PMMA change. Several samples analysed formed a blend layer with a composition where $\varphi_{blend\text{-}DPEO} > \sim 0.3$ and $\varphi_{blend\text{-}PS\text{-}PMMA} > 0.3$. This could be considered to indicate that the concentration dependence of the interaction parameter and semi-miscible nature of the DPEO/PMMA components has been inhibited by the presence of the PS. The PS would be expected to increase the unfavourable interactions between the copolymer and the blend, limiting the range of blend compositions observed. The range of concentrations for the blend was similar to those found for DPEO/PMMA.

Figure 6.10 shows volume fraction against time for one of the samples that exhibited the development of the DPEO surface excess shown in Figure 6.5. The surface excess is only observed for annealing times subsequent to

$\varphi_{blend\text{-}DPEO}=\varphi_{blend\text{-}PS\text{-}PMMA}$ ~0.5. Volume fractions then tend towards and equilibrate where $\varphi_{blend\text{-}DPEO}=$ 0.3, the concentration at which PMMA/DPEO blends should still be homogeneous. PMMA and DPEO are known to have very different surface energies[18] and separation of phases with different concentrations may occur at the air surface where surface tension effects[19] are important. The critical concentration at which the second shoulder is observed is very similar ($\varphi_{blend\text{-}PS\text{-}PMMA}$ ~0.5) to that of the PMMA/DPEO bilayer. The diffusion of PS-PMMA into the blend continued during the appearance of the DPEO excess at the surface indicating that the surface excess may always be present in annealed samples. There are many cases of similar surface segregation in polymer blends[20]. It is likely that the PEO rich region at the surface is always present in the annealed systems, however cannot be resolved until $\varphi_{blend\text{-}DPEO} < 0.5$. As shown in Figure 6.10, the change in volume fraction change with time exhibits some curvature similar to that observed for the PMMA/DPEO sample.

To calculate the flux of quantifiable material (PS-PMMA) the volume fraction is multiplied by the depth of the $d_{interface}$, which equates to multiplying by the volume of the blend. Using the densities of the polymers, depth in nm can be converted to atoms per cm^2. Using molecular weights as described in Appendix I the number of polymer molecules can then be calculated for each component The 'flux' is defined as the number of PS-PMMA polymers per cm^2 crossing the interface where $\varphi_{blend\text{-}PS\text{-}PMMA}$ ~0.5 per second.

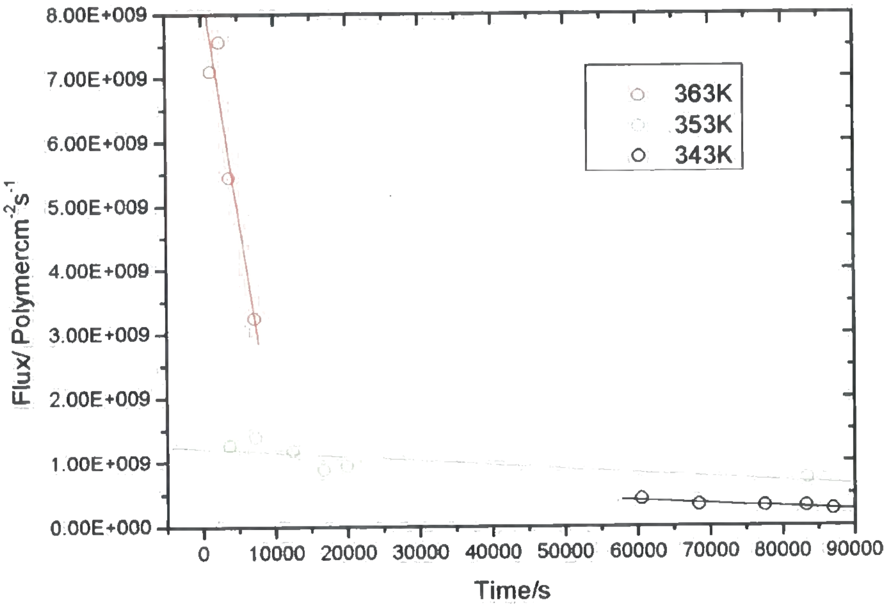

Figure 6.11 Plot of flux of polymer of PS-PMMA into 89217 gmol^{-1} DPEO rich blend against annealing time *t* for various temperatures. Data are fitted with a straight line

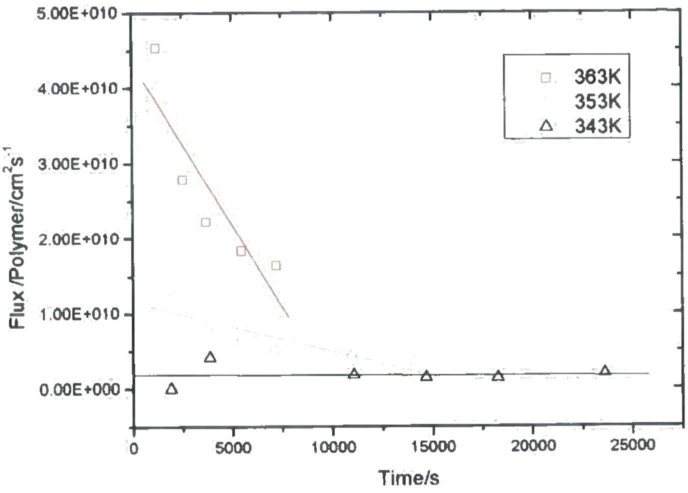

(A)

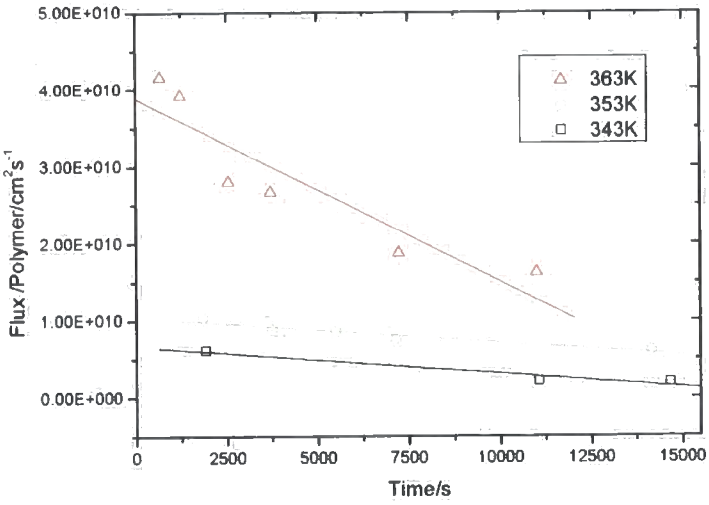

(B)

Figure 6.12 Plot of flux of polymer of 96200 gmol^{-1} PMMA into (A) 121100 gmol^{-1} and (B) 170700 gmol^{-1} DPEO rich blend against annealing time *t* for various temperatures. Plots against t are fitted with a straight line with gradients displayed in Table 6.2

T/K	DPEO M_w/gmol^{-1} in 96200gmol^{-1} PMMA	Gradient /polymer/cm^{2}s^{-2}	% error
363	121100	-4.35E+06	30.7
353	121100	-6.56E+05	29.5
363	170700	-2.38E+06	21.6
353	170700	-3.31E+05	17.3
343	170700	-3.56E+05	24.5
	In PS-PMMA		
363	89217	-7.35E+05	22.8
353	89217	-6.45E+03	42.9
343	89217	-5.10E+03	20.2

Table 6.2 For a straight line relationship between flux and time the gradient and associated errors for various bilayers.

Figure 6.11 and Figure 6.13 display typical plots of PS-PMMA flux of with time, *t*. Taking data sets that include the largest number of data points, Table 6.2 shows the gradients and errors of the linear fits to these plots and to PMMA/DPEO bilayers displayed in Figure 6.12. Whilst linear relationships could be applied to all flux against time plots only the PMMA/DPEO bilayers could be fitted with first order exponential curves. Linear relationships exhibited similar percentage errors for both the PMMA and PS-PMMA bilayers, however linear fits were marginally better for the copolymer bilayer. This may imply that unlike the flux of PMMA into DPEO, PS-PMMA is not inhibited with time due to the changing concentration of the blend. With an increase in PS-PMMA concentration, the blend local T_g increases and blend mobility decreases preventing glassy PS-PMMA polymers from diffusing as rapidly into the blend. The interaction parameter for the blend is also concentration dependent, leading at certain concentration ranges to a blend with an unfavourable thermodynamic environment for glassy PS-PMMA chains to diffuse into.

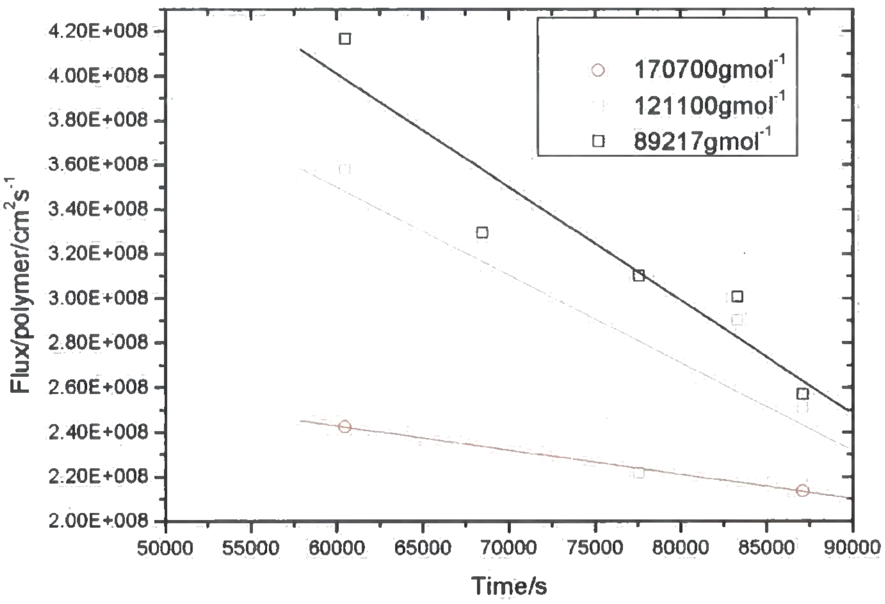

Figure 6.13 Plot of flux of polymer of PS-PMMA into DPEO rich blend against annealing time *t* for various molecular weight DPEO at 343 K

The movement of the PMMA within the blend should be similar to that described by tracer or mutual diffusion,[12,21-23] movement of PS-PMMA may be different. The time taken for the dissolution of the PS-PMMA polymer within the blend, t_{diss} is associated with polymer reptation, constraint release and the molecular weight of the components should affect the diffusion coefficients of PS-PMMA within the blend. No concentration gradient is apparent as with PMMA blends, so t_{diss} is smaller than can be measured by this experimental set up.

Figure 6.13 shows typical DPEO molecular weight dependencies of PS-PMMA flux into the blend at given temperatures. The higher molecular weight DPEO has a smaller flux of polymer with time. Taking the gradients of linear fits shown in Figure 6.13, the relationship between copolymer flux and DPEO molecular weight is Flux=(0.05±0.006) $M_{w,DPEO}$-9720 at 343 K. Further relationships between DPEO molecular weight and flux cannot be calculated due to the limited number of complete data sets. Previous work has shown no molecular weight dependence of χ for PMMA/DPEO blends. If PS-PMMA/DPEO is analogous then thermodynamic effects are not responsible for the molecular weight dependence of flux. Kinetic effects within the blend are considered to be too fast to control the flux. The molecular weight dependence of flux of polymer into the blend is thus due to action at the interface between the blend and the PS-PMMA. For a PS-PMMA molecule to cease being 'glassy' it needs to be exposed to enough of the more mobile molecules. Smaller DPEO molecules will have a greater number of highly mobile ends near the glassy PS-PMMA. This may lead to greater exposure of the glassy PS-PMMA molecules to an environment with mobile polymers and encourage dissolution from the bulk. Alternatively smaller DPEO molecules may be better suited to diffusing into spaces in the glassy bulk, again enhancing PS-PMMA exposure to mobile polymers. It is expected that the PS section of the polymer chain might hinder this process as it has unfavourable interactions with DPEO. However, if mobile molecules include PS-PMMA and DPEO chains in the blend, the unfavourable interactions between mobile and glassy components would be expected to be less. Hence with increasing $\varphi_{blend\text{-}PS\text{-}PMMA}$ within the blend, the release of glassy molecules from the PS-PMMA bulk might accelerate. This process is not observed; implying that the process at the surface is either independent of polymer type or the PS section of the copolymer is too small to influence the process. A DPEO molecular weight dependence of flux was not definitive for PMMA/DPEO blends but was clearer for the copolymers. This may be due to the greater importance of DPEO constraint release in conferring mobility to the copolymers. The contribution of uninhibited PMMA reptation, may lessen the impact of DPEO molecular weight constraint release upon the diffusion behaviour of PMMA/DPEO bilayers.

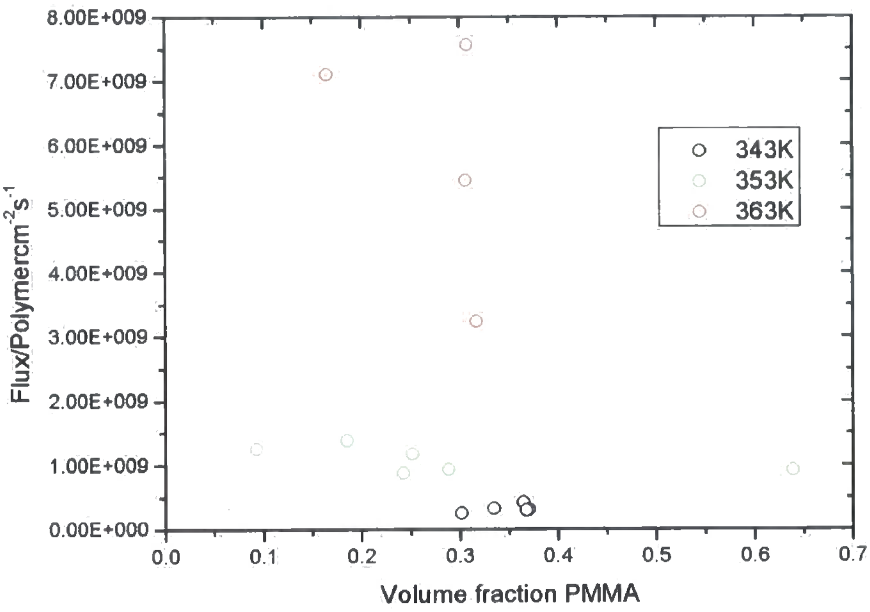

Figure 6.14 Plot of flux of PS-PMMA molecules into 89217 gmol^{-1} DPEO rich blend against PS-PMMA volume fraction in the blend $\varphi_{blend\text{-}PS\text{-}PMMA}$

The flux of PS-PMMA appears to change randomly with volume fraction within the blend, (Figure 6.14) unlike the relationship between fluxes of PMMA into its subsequent blend, which showed some curvature. The dependence of the flux on temperature may be attributed to both the extra energy available to the polymers at higher *T* but also to a possible change in interaction parameter, so that at higher temperatures it becomes energetically more favourable for PS-PMMA to enter the blend.

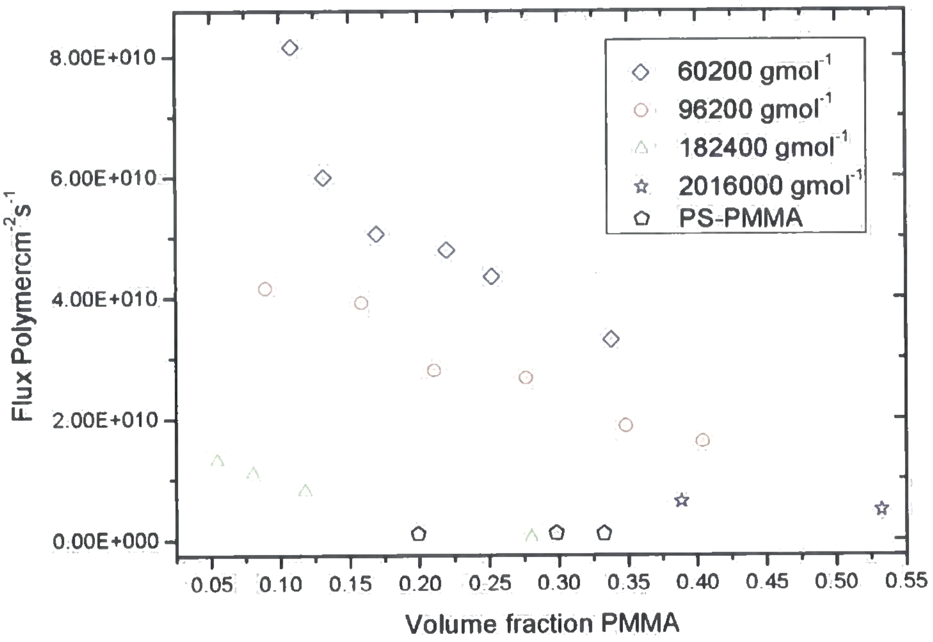

Figure 6.15 Plot of flux of various molecular weight PMMA polymers and PS-PMMA into 170700 gmol^{-1} DPEO rich blend against PMMA (PS-PMMA) volume fraction in the blend at 363 K

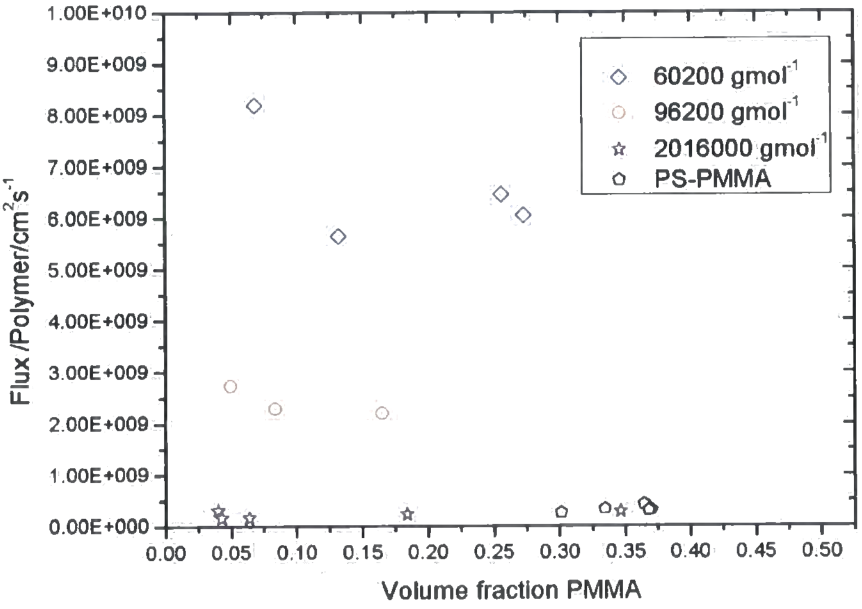

Figure 6.16 Plot of flux of various molecular weight PMMA polymers and PS-PMMA into 89217 gmol^{-1} DPEO rich blend against PMMA (PS-PMMA) volume fraction in the blend at 343 K

A linear relationship between molecular weight and PMMA flux was not found for the PMMA/DPEO blend (section 5.5.3). Figure 6.15 and Figure 6.16 show the PMMA flux with changing volume fraction including the copolymer. If PS-PMMA was expected to behave in the same way as PMMA the flux might be expected to fit in between 2016000 $gmol^{-1}$ and 182400 $gmol^{-1}$. This was not always observed, in Figure 6.16 where PS-PMMA exhibited fluxes of closer equivalence to 2016000 $gmol^{-1}$ indicating that the PS present inhibits the movement of the copolymer. However, in Figure 6.15 the copolymer's behaviour is closely related to that of 2016000 $gmol^{-1}$ and 182400 $gmol^{-1}$PMMA. This suggests that in couples of high molecular weight DPEO (Figure 6.15) and high molecular weight PMMA, the DPEO dictates diffusional behaviour, whereas at lower molecular weight DPEO (Figure 6.16) the PMMA molecular weight is the dominating factor. A quantifiable molecular weight dependence of flux was not observed for PMMA blends, so it is hard to draw conclusions by comparing them with PS-PMMA.

6.5.5 Application of Fickean diffusion

If the system analysed here exhibited Fickean diffusion the raw data should have shown the characteristic 'slump' shown in section (5.5.4).Like the PMMA/DPEO couple this was not apparent. For DPEO molecular weight >17300 gmol^{-1}, no measurable increase in the width of the polymer-polymer interface, w_{width}, was evident as shown in Figure 6.17, where w_{width}=0.

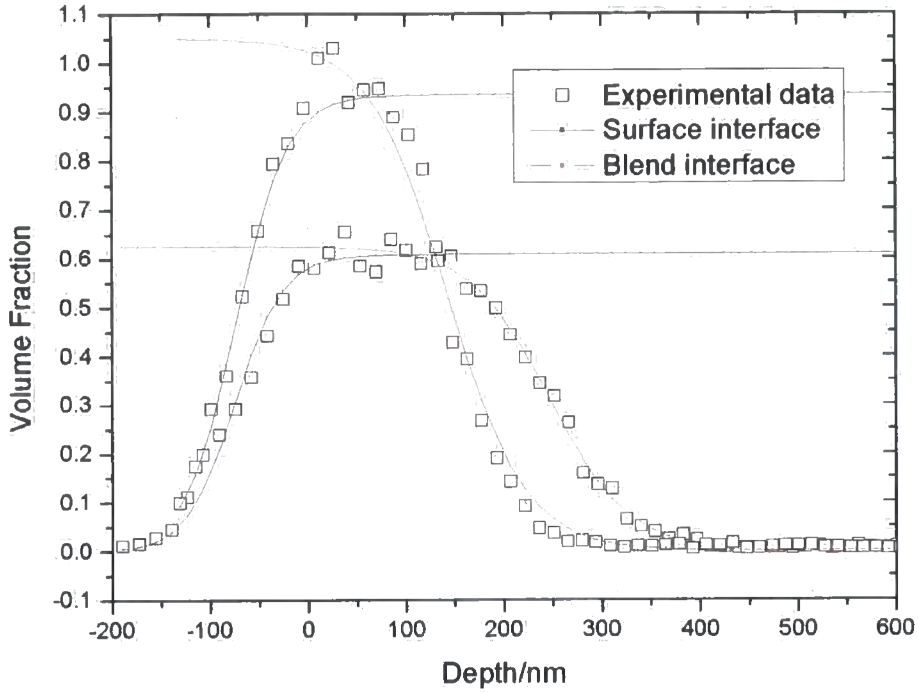

Figure 6.17 Depth profiles and hyperbolic tangent fits for approximately 300 nm 170700 gmol^{-1} DPEO on PS-PMMA, for various annealing times of 1324 seconds and 25185 seconds at 363 K. Where w_{tot} includes beam damage and resolution functions only.

Concentration is not constant at $d_{interface}$, although it could be said to always contain the concentration $\varphi_{blend\text{-}PS\text{-}PMMA}$=0.5. Figure 6.18-Figure 6.19 show typical plots for bilayers of PS-PMMA/DPEO and PMMA/DPEO. There was very little difference between the plots of $t^{0.5}$ and t, indicating that for the PS-PMMA couple either or neither case II or Fickean diffusion could apply. This is in contrast to PMMA couples where curvature is more pronounced for plots of depth against t.

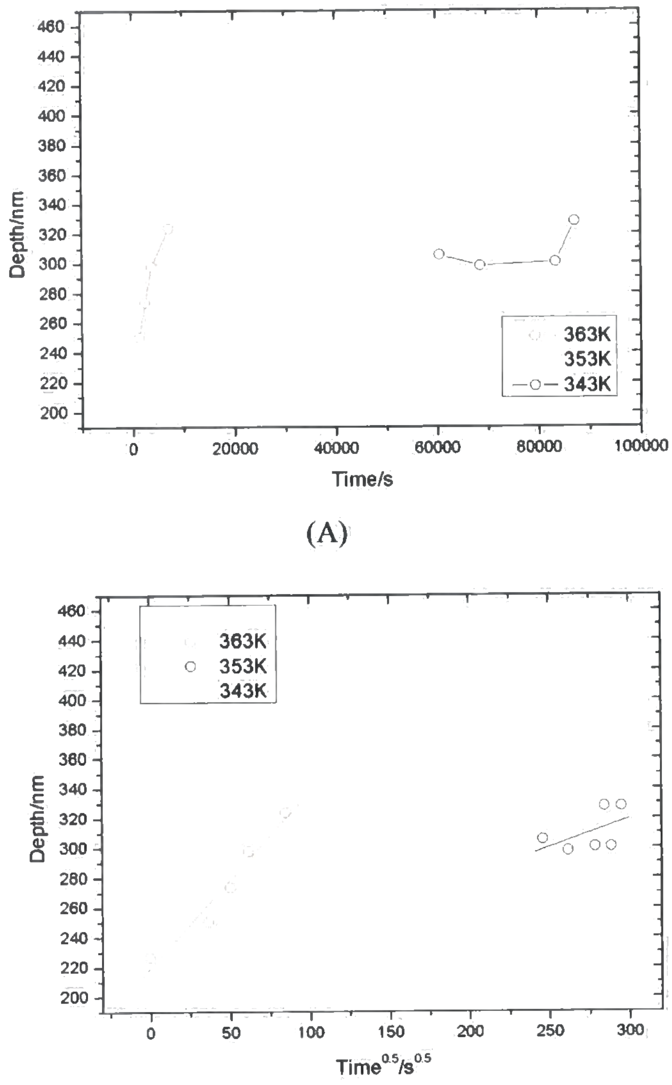

(A)

(B)

Figure 6.18 Plot of depth of interface $d_{interface}$ between PS-PMMA it's blend with 89217 gmol^{-1} DPEO with time t (A) and $t^{0.5}$ (B). The gradients of straight lines with are *343 K* (2.444x10^{-7} cm^{2}s$^{0.5}$) *353 K* (8.663x10^{-8} cm^{2}s$^{0.5}$) *363 K* (8.663x10^{-8} cm^{2}s$^{0.5}$)

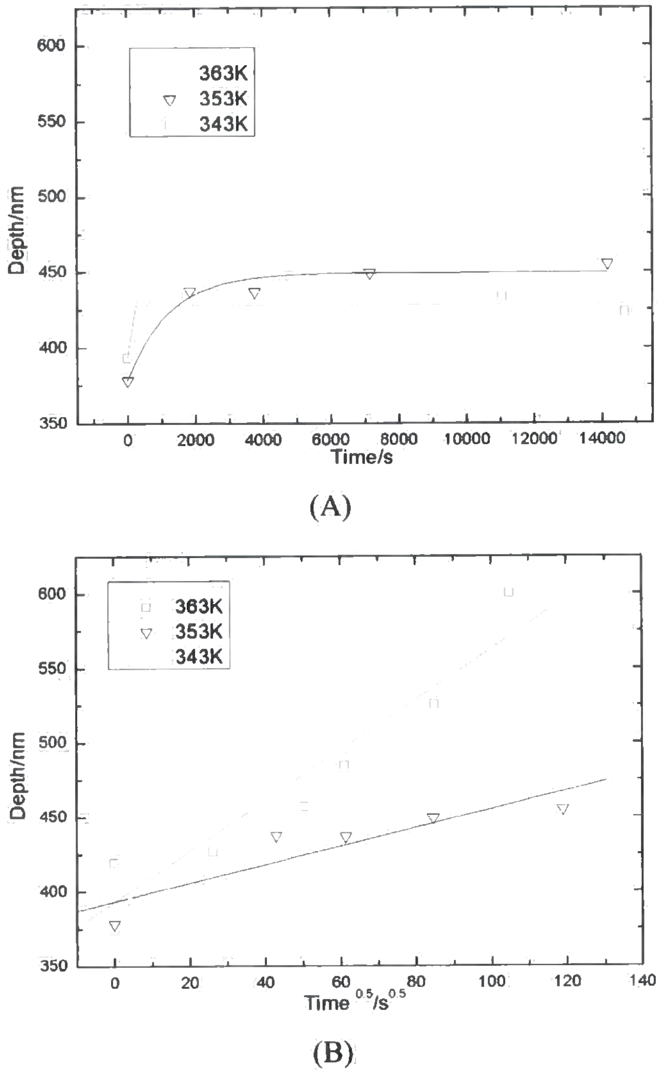

Figure 6.19 Plot of depth of interface $d_{interface}$ between 96200 gmol^{-1} PMMA and it's blend with 121100 gmol^{-1} DPEO with time t (A) and $t^{0.5}$ (B).

The gradient of straight lines of depth versus $t^{0.5}$should be proportional to diffusion coefficient as demonstrated in Equation 5.9. $C^*\sqrt{D_{DPEO}}$ are typically of the order of 10^{-7} cm^{2}s$^{0.5}$ for diffusion of DPEO into PMMA. $C^*\sqrt{D_{DPEO}}$ for DPEO into PS-PMMA are very similar and of the order 10^{-7} cm^{2}s$^{0.5}$.

6.5.6 Application of Case II diffusion

Case II diffusion has been applied to the DPEO/PMMA system. The once glassy PMMA molecules are also quickly dissolved into the bulk liquid DPEO. A front is clearly observed for the glassy PMMA being dissolved by the DPEO. PMMA maintains φ_{PMMA}=1 behind the interface. A plasticising region, if present, was too small to be seen, lost in the effective widths ascribed to beam damage and resolution.

A sharp diffusion front is always apparent in systems where DPEO molecular weight > 17300 gmol^{-1}. The penetrant molecule could be considered to be the liquid DPEO and the glassy matrix; the PS-PMMA. The PS-PMMA is quickly solvated into the DPEO, leaving the reservoir of penetrant DPEO in a blend. If mobile polymers are the penetrant phase, it may be possible that part or complete PS-PMMA molecules flow back into the glassy bulk. A process that might be favourable for the PS segments of the copolymer. This process could not be distinguished as the only observable quantity is the net displacement of polymers. If the driving force for mixing is the concentration dependent favourable enthalpy between the two polymers then the 'backflow' of PS-PMMA is unlikely. If the driving force is entropic, then 'backflow' is as important in describing diffusion as the DPEO molecules.

The position of the interface $d_{interface}$ varies with time, t. The volume fraction of the blend changes with time and thus the front represents the boundary between pure PMMA and a blend of given concentration as shown in Figure 6.4. The steep drop in concentration includes various volume fractions including the volume fraction associated with thermodynamic equilibrium of the blend (if there is one) and φ=0.5. Like the DPEO/PMMA bilayer, a Fickean precursor does not appear to be present. If present the fits to $d_{interface}$ on the DPEO peak and PMMA (Figure 6.17) would be poor with broadening indicating that w_{width} should be fitted as discussed earlier. However, fits were good for DPEO molecular weight >17300 gmol^{-1} as shown in Figure 6.17. It is possible that the depth of the Fickean precursor was of a similar or smaller scale to the effective widths of the instrumental resolution and beam damage and could not be distinguished. For the fit to be considered poor w_{width} should be ~30 nm, so if present the precursor will be <30 nm.

The penetrant DPEO is in limited supply, contrary to the typical requirements of case II diffusion. Conservation of mass of penetrant requires the concentration of penetrant in the plasticised zone, (in this case, blend) to decrease systematically with time and diffusion depth. The properties of the material behind the diffusion front will therefore alter with time and penetration depth, continuously varying the local driving forces that advance the diffusion front. Eventually the concentration of diluent in the plasticized region will drop monotonically from some initial level to a final level φ_{final} causing the case II front to stall. φ_{final} results when the glass transition temperature of the plasticized region matches the temperature of the system and the process zone thus encounters a sudden drop in mobility, leading to the stalling of the front. The diffusion front in this system, like the PMMA/DPEO does not appear to 'stall' however unlike the PMMA/DPEO system the front does not so conclusively slow with time, indicating that the process may be χ rather than T_g dependent as PS-PMMA/DPEO and PMMA/DPEO have similar T_g relationships.

Linear gain is indicated in the early increases of volume fraction of PS-PMMA in the DPEO rich region. The volume fraction with time relationship is not linear as the system approaches approximately $\varphi_{PS\text{-}PMMA}=0.5$. It is possible that non-supply limited case II diffusion can only be applied to the early stages of diffusion, where volume fraction increase is linear with time. As with the PMMA/DPEO couple, the DPEO rich region does not always display a homogenous concentration; a surface excess developed later in the diffusion as shown in Figure 6.5, which would indicate some form of concentration gradient behind the moving front or a reluctance of DPEO to leave the surface. The presence at longer annealing times of a concentration gradient (the DPEO shoulder characterised in Figure 6.6) complicates the application of case II diffusion but could possibly be ignored if only early diffusion is analysed.

From Figure 6.11 and Figure 6.13 a linear increase of PS-PMMA in the DPEO rich layer (and conversely allowing the flow of volume across the interface to be equal and opposite, DPEO loss) with time is not apparent, this may reflect the non-linear displacement of the interface with time. The interaction parameter can be assumed to be concentration dependent and the non-linear volume fraction increase may even reflect this relationship. Hence it is unclear whether the slowing down of PMMA volume fraction gain is a reflection of mechanical osmotic pressure and the loss in mobility of the DPEO and consequent 'back stresses' or the change in thermodynamic compatibility.

6.6 Summary

The DPEO/PS-PMMA diffusion couple could be said to exhibit both Fickean and case II characteristics in a similar fashion to the DPEO/PMMA. Plots of interface movement with $t^{0.5}$ were not strictly linear and the non-linear relationship of interface displacement with t could reflect limited supply case II characteristics rather than Fickean diffusion being the overiding diffusion regime. Deviation from linear behaviour is less pronounced than that for PMMA. The characteristic deceleration associated with limited supply case II diffusion was further complicated by the concentration dependence of the interaction parameter for PMMA and DPEO blends.The diffusion is controlled by behaviour at the interface. Values of polymer flux were of a similar order to that of pure PMMA although similar in behaviour to higher molecular weight than the PMMA block present. The dewetting behaviour of 17300 gmol^{-1} DPEO could be attributed to the presence of micelle nucleation sites on the copolymer interface.

6.7 References

(1) Arlen, M. J.; Dadmun, M. D.; Hamilton, W. A. *Journal of Polymer Science Part B-Polymer Physics* **2004**, *42*, 3235-3247.

(2) Green, P. F.; Barbour, J. C. *Journal of Non-Crystalline Solids* **1998**, *235*, 640-644.

(3) Jeong, U.; Ryu, D. Y.; Kho, D. H.; Lee, D. H.; Kim, J. K.; Russell, T. P. *Macromolecules* **2003**, *36*, 3626-3634.

(4) Green, P. F. *Macromolecules* **1995**, *28*, 2155-2158.

(5) Frielinghaus, H.; Mortensen, K.; Almdal, K. *Macromolecular Symposia* **2000**, *149*, 63-67.

(6) Callaghan, T. A.; Paul, D. R. *Macromolecules* **1993**, *26*, 2439-2450.

(7) Hopkinson, I.; Kiff, F. T.; Richards, R. W.; King, S. M.; Farren, T. *Polymer* **1995**, *36*, 3523-3531.

(8) Shearmur, T. E.; Clough, A. S.; Drew, D. W.; vanderGrinten, M. G. D.; Jones, R. A. L. *Physical Review E* **1997**, *55*, R3840-R3843.

(9) Fetters, L. J.; Lohse, D. J.; Richter, D.; Witten, T. A.; Zirkel, A. *Macromolecules* **1994**, *27*, 4639-4647.

(10) Adedeji, A.; Lyu, S.; Macosko, C. W. *Macromolecules* **2001**, *34*, 8663-8668.

(11) Kerle, T.; Scheffold, F.; Losch, A.; Steiner, U.; Schatz, G.; Klein, J. *Acta Polymerica* **1997**, *48*, 548-552.

(12) Composto, R. J.; Kramer, E. J. *Journal of Materials Science* **1991**, *26*, 2815-2822.

(13) Lin, H. C.; Tsai, I. F.; Yang, A. C. M.; Hsu, M. S.; Ling, Y. C. *Macromolecules* **2003**, *36*, 2464-2474.
(14) Jabbari, E.; Peppas, N. A. *Macromolecules* **1993**, *26*, 2175-2186.
(15) Tomba, J. P.; Carella, J. M.; Garcia, D.; Pastor, J. M. *Macromolecules* **2001**, *34*, 2277-2287.
(16) Tomba, J. P.; Carella, J. M.; Pastor, J. M. *Macromolecules* **2005**, *38*, 4355-4362.
(17) Reiter, G.; Huttenbach, S.; Foster, M.; Stamm, M. *Macromolecules* **1991**, *24*, 1179-1184.
(18) Walton, D. G.; Soo, P. P.; Mayes, A. M.; Allgor, S. J. S.; Fujii, J. T.; Griffith, L. G.; Ankner, J. F.; Kaiser, H.; Johansson, J.; Smith, G. D.; Barker, J. G.; Satija, S. K. *Macromolecules* **1997**, *30*, 6947-6956.
(19) Jones, R. A. L.; Norton, L. J.; Kramer, E. J.; Bates, F. S.; Wiltzius, P. *Physical Review Letters* **1991**, *66*, 1326-1329.
(20) Shull, K. R. *J.Chem.Phys* **1991**, *94*, 5723.
(21) Composto, R. J.; Kramer, E. J.; White, D. M. *Macromolecules* **1992**, *25*, 4167-4174.
(22) Green, P. F.; Mills, P. J.; Kramer, E. J. *Polymer* **1986**, *27*, 1063-1066.
(23) Green, P. F.; Palmstrom, C. J.; Mayer, J. W.; Kramer, E. J. *Macromolecules* **1985**, *18*, 501-507.

Chapter 7

Neutron reflectivity studies of the interface between DPEO and PMMA and PS-PMMA copolymers

7.1 Introduction

ERD experiments have shown swelling of DPEO with PMMA and movement of the interface between the resultant blend into the PMMA layer. Interfacial broadening was observed for the lowest entangled (17300 gmol^{-1}) DPEO molecular weight studied. A better resolution than that available with ion beam techniques is required to explore the mechanism at the interface between molten DPEO and glassy PMMA. A Fickean precursor to case II diffusion, if present, could not be resolved using ERD. It is unknown whether DPEO molecules initially enter the glassy matrix before PMMA is sufficiently mobile to move into the molten DPEO, or whether exposure of PMMA chains at the interface to the mobile DPEO is sufficient to loosen PMMA chains. If PMMA is replaced with a block copolymer, PS-PMMA, the PMMA and DPEO exhibit enough favourable interactions to diffuse whilst the PS portion of the chain is expected to slow the diffusion process. The two diffusion couples (PS-PMMA/DPEO and PMMA/DPEO) have very similar glass transition temperatures, so any differences in diffusion behaviour are due to the difference in interaction parameters between the copolymer and the pure homopolymer and the microstructure present in the block copolymer phase. ERD experiments demonstrated that the DPEO/PS-PMMA diffusion couple exhibit both Fickean and case II characteristics, in a similar fashion to the DPEO/PMMA. Values of polymer flux were of a similar order to that of pure PMMA although similar in behaviour to a higher molecular weight than the PMMA block present. Bilayers that included 17300 gmol^{-1} DPEO, in contradiction to the behaviour of the PMMA analogue bilayer, dewetted. This could be attributed to the presence of nucleation sites, in the form of PS micelles, at the copolymer interface.

7.2 Experimental refinement

Neutron reflectivity requires a strong contrast in scattering length density between the components in a bilayer. DPEO, PMMA and PS have a scattering length density of 6.89×10^{-6} Å^{-2}, 1.06×10^{-6} Å^{-2} and 1.2×10^{-6} Å^{-2} respectively, which makes the DPEO/PMMA and DPEO/PS-PMMA bilayers very suitable for neutron reflectivity experiments. Neutron reflectivity, like ion beam analysis is sensitive to surface roughness. Unlike ion beam analysis, where surface roughness was found to give a minimal contribution to measuring the interface broadening, neutron reflectivity is more sensitive. He exposed DPEO surface on DPEO and PMMA bilayers are known to have surface roughness of the order of 10% of the total thickness due to the crystallinity in DPEO. Instead of bringing the neutron beam through the rough surface, the beam can pass through the silicon substrate to the DPEO/PMMA interface before encountering the crystalline rough DPEO surface as shown in Figure 7.1. Interfacial broadening leads to damping of the Keissig fringes so for unannealed samples these fringes should be well resolved. Simulated data showed that for resolvable Keissig fringes to be seen, the hydrogenated layer should be approximately 60 nm thick with a much thicker layer of DPEO.

Neutron reflectivity has been used to analyse the change in interfacial profile between interdiffusing polymers. The most common approach utilised is the 'anneal-quench' procedure where the sample is heated and then rapidly quenched, before a reflection profile is collected[1-6]. In-situ, real-time measurements have also been carried out where the sample is placed on a pre-heated stage and reflectivity measurements begin. The upper limit of diffusion rate observable by this method is determined by the neutron flux limited count time per reflectivity profile[7,8]. Real time experiments can only explore a limited Q range during measurement. Since we are dealing with a system in which the development of the interfacial profile is not well characterised; maximum possible Q range is required, so the anneal-quench approach was adopted instead.

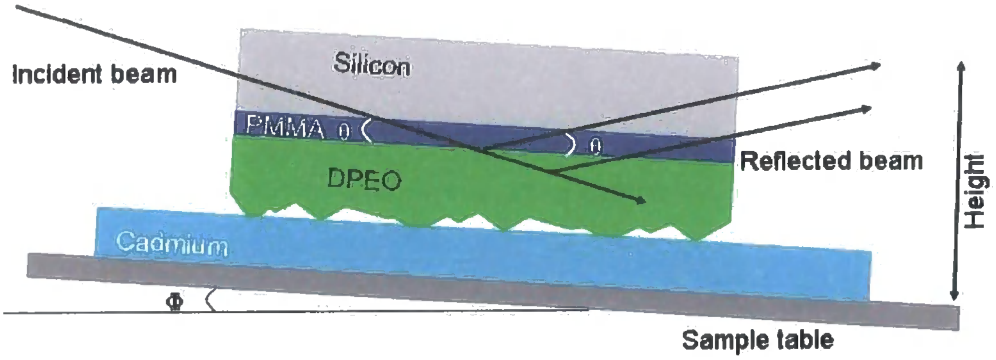

Figure 7.1 Schematic of sample geometry used during this neutron reflectivity experiment

7.3 Experimental

7.3.1 Materials

Complete details of the polymers were utilised during this experiment, are in Appendix I. All polymers were above their individual entanglement molecular weight (PMMA=10000 gmol^{-1}, PS=14000 gmol^{-1} and PEO=1700 gmol^{-1}) [9]

Polymer	M_w/gmol^{-1}	M_n/gmol^{-1}	Polydispersity
DPEO	170700	165000	1.04
DPEO	121100	119100	1.02
DPEO	89217	82210	1.09
DPEO	17300	14800	1.03
PMMA	96200	93000	1.03
PMMA	213400	178000	1.20
PMMA	2016000	1903000	1.06
PS-PMMA	PS= 29200 PMMA=285100		1.08

Table 7.1 Showing materials utilised

Bilayers that included 121100 gmol^{-1} molecular weight DPEO on all PMMA molecular weights in Table 7.1, 1211100 gmol^{-1} /170700 gmol^{-1} /89217 gmol^{-1}

DPEO molecular weights as on 96200 gmol^{-1} PMMA and all DPEO molecular weights on copolymer were constructed using spin coating. Bilayers were constructed in the same fashion described in including a thin film of approximately 50 nm of PMMA or PS-PMMA and a DPEO film of over 300 nm DPEO/PMMA samples were annealed for a range of times at 343 K in a vacuum oven and then quenched on an aluminium block at ambient temperature. Unannealed DPEO/PS-PMMA samples were measured using SURF and were consequently heated at 343 K for a range of times, quenched on a metal block and replaced in the reflectometer. Subsequently the DPEO/PS-PMMA samples were replaced in the oven and further annealed and quenched.

7.3.2 SURF measurements

Samples were placed in the orientation shown in Figure 7.1, on a cadmium block on the sample rack. Samples were aligned for height and Φ using a laser and then using neutrons. For each sample three angles were analysed (0.25°, 0.5° and 1.2°) measured for 60, 90 and 165 μAhours respectively, (μAhours are proportional to the integrated neutron flux) these settings have previously been established to give adequate statistics with samples of similar dimensions and composition[10].

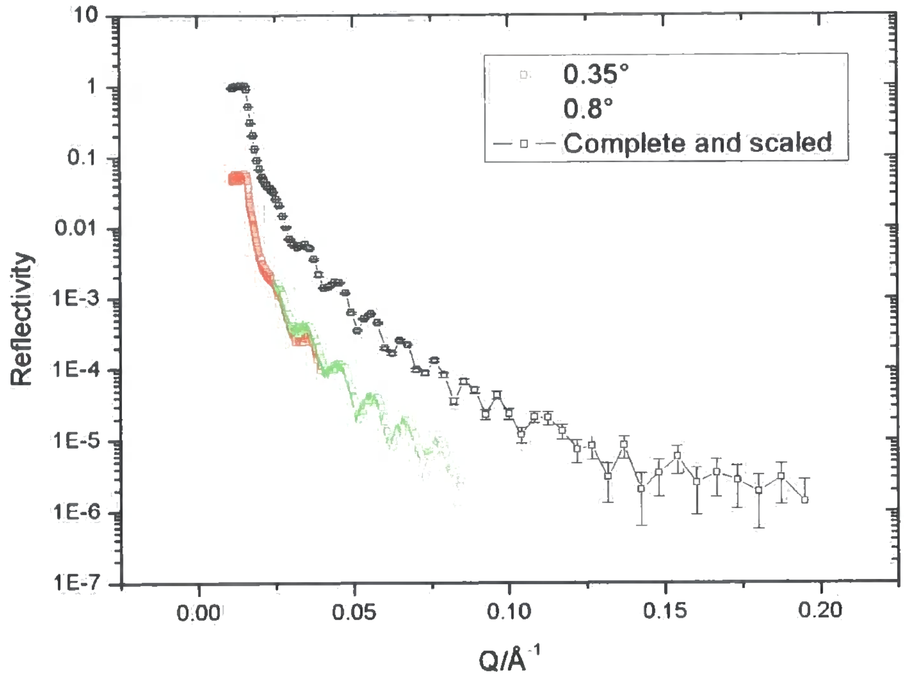

Figure 7.2 Typical plot of reflectivity against Q, showing data gathered from two angles and the scaled and stitched data used for analysis.

After the first few samples were analysed, there was found to be sufficient clarity and overlap to reasonable Q with the first two angle measurements, subsequently the samples were analysed for two angles (0.35° and 0.8°) measured for 60 and 160μAhours respectively. The transmission of both the air and the silicon block was measured for 35μAhours, with θ=0 and Φ =0.

7.4 Data analysis

7.4.1 Data reduction and raw data

For each angle reflectivity versus Q and errors are recorded. Scattering profiles from different angles are then stitched together into one continuous profile as shown in Figure 7.2. Data is then scaled to unity below the critical angle as shown in Figure 7.2 and can be imported into various model fitting software.

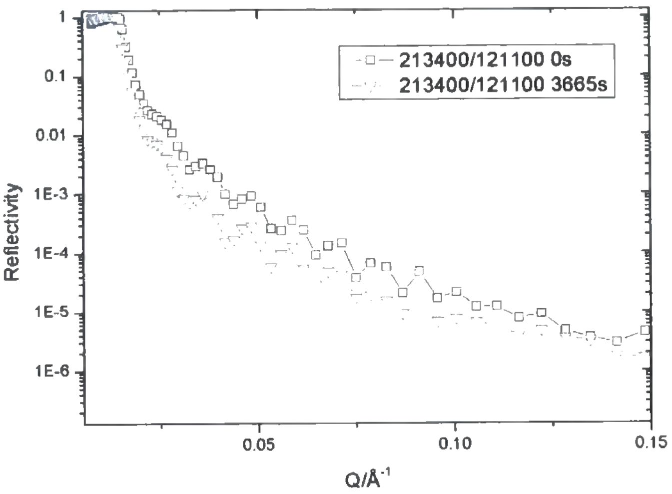

(A)

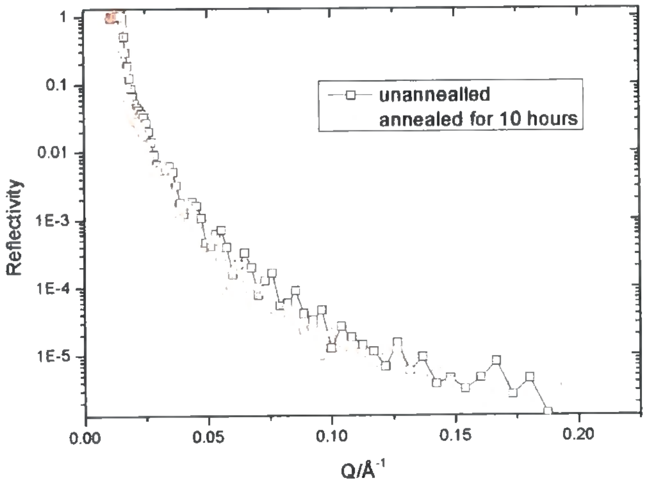

(B)

Figure 7.3 Raw reflectivity data for a bilayer of 213400 gmol^{-1} PMMA and 121100 gmol^{-1} DPEO annealed at 343 K for 0 seconds and 3665 seconds (A) and a bilayer of 89217 gmol^{-1} DPEO on PS-PMMA copolymer annealed at 343 K for 0 seconds and 36000 seconds (B)

Figure 7.3 shows typical reflectivity data for unannealled and annealed samples. The comparatively low absolute reflectivity for the annealled samples indicate a lower contrast in scattering length densities between DPEO and PMMA layers. The higher frequency of Keissig fringes for the annealed sample demonstrates an increase in PMMA layer thickness, indicating that PMMA has been swollen with DPEO.

7.4.2 PARRATT

PARRATT* is model fitting software that can be used for analysing X-ray and neutron reflectivity data. Reflectivity calculations are carried out by means of Parratt's dynamical approach[11]. The calculation is based on stratified media where only the refractive index differences perpendicular to the surface are considered. The calculation of the scattering length density includes the roughness for the interfaces. Roughness is calculated by an error function formalism where 'roughness' is the FWHM of the Gaussian in the scattering length density gradient at a given interface[12]. Only roughnesses that are small compared to the layer thickness are correctly calculated. The model is fitted to reflectivity data by using chi squared minimization. This is implemented as a simplified one dimensional Newton-Raphson method[13], which converges quadratically into the nearest minimum. By varying a chosen parameter more local minima can be found. A model containing various layers can be built. For every layer in the model, the layer thickness $d/Å$, the real part of the scattering length density $\rho/Å^{-2}$, the imaginary part of the scattering length density $Imp/Å^{-2}$, the roughness of the layer $\sigma/Å$, can be determined.

Data collected in this experiment demonstrated greater errors when $Q > 0.15$ Å^{-1} (Figure 7.2) and therefore fitting regimes only included $0 < Q < 0.15$ Å^{-1}. During model fitting, instrumental background reflectivity, down to which the reflectivities can be measured, was set to a constant $2x10^{-6}$, and the resolution (δQ) for Q up to 0.15 Å^{-1} was set to 0.003 Å^{-1}. The profile of scattering length density against depth was described by several steps with step size 10Å. The model used to describe unannealled samples included the silicon substrate, a layer of silicon oxide approximately 17 Å thick, a layer of PMMA or PS-PMMA and a thicker layer of DPEO. A roughness of 5 Å was added to all layers. A greater surface roughness is added to the interface between PMMA or PS-PMMA and DPEO to account for crystallinity and artifacts of polymer spinning. Unannealled samples are fitted first and then specific parameters were varied for subsequent annealed samples. It is assumed that as samples were constructed in the same fashion that the initial layer thickness of PMMA, DPEO and silicon

---

* PARRAT v.1.5.2 (Christian Braun, HMI Berlin)

oxide were identical. The fits for calculated reflectivity and experimental data, for unannealed samples, were good, indicating that diffusion or film degradation had not occurred during bilayer preparation. Examples are shown in Figure 7.4.

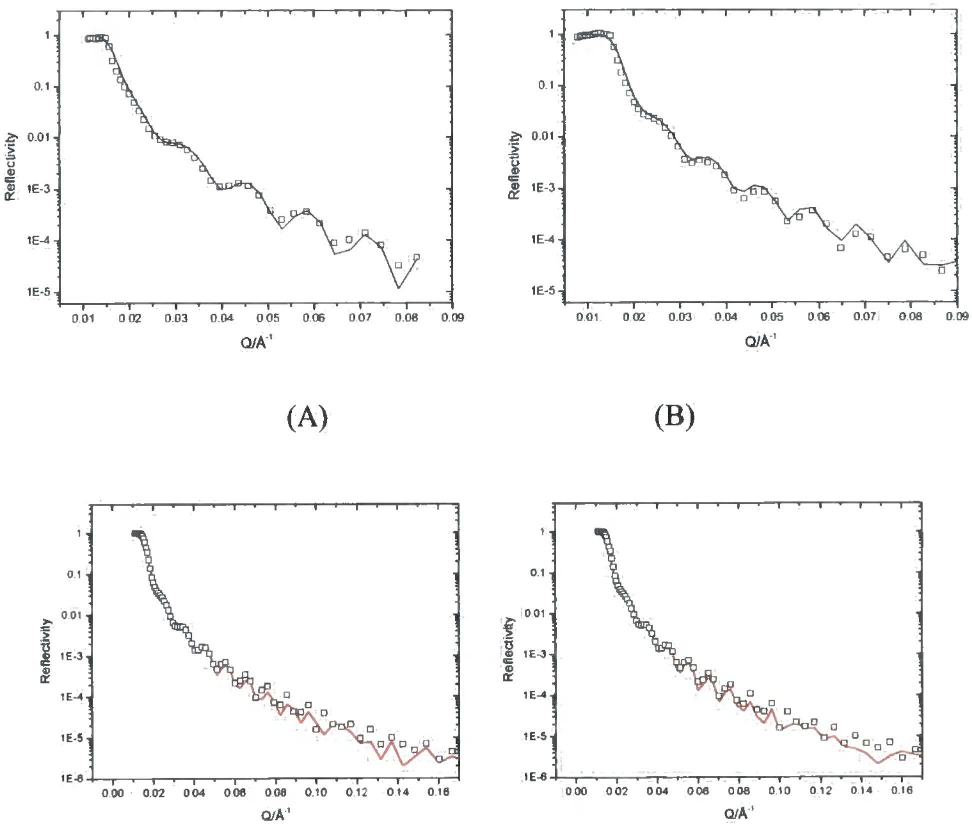

(A) (B)

(C) (D)

Figure 7.4 Reflectivity and fits for layer combinations: DPEO (170700 gmol^{-1}) and PMMA (96200 gmol^{-1}) (A) DPEO (121100 gmol^{-1}) and PMMA (2016000 gmol^{-1}) (B), PS-PMMA and DPEO (17300 gmol^{-1}) (C) PS-PMMA and DPEO (121100 gmol^{-1}) (D)

7.4.3 Interfacial models

The following models were applied to annealed reflectivity data. The fits as found are plotted together for comparison in Figure 7.9-7.17.

7.4.3.1 Varying composition of polymer layers (SLD)

Unannealled samples were fitted to reflectivity profiles as described in 7.4.2. The thickness of the two polymer layers and layer roughness, as found from the unannealled samples were maintained and reflectivity was fitted for annealed samples by varying the scattering length density (SLD) of the polymer layers.

This model allows for variation in the scattering length density of the two layers; thus, accounting for diffusion in both directions across the interface.

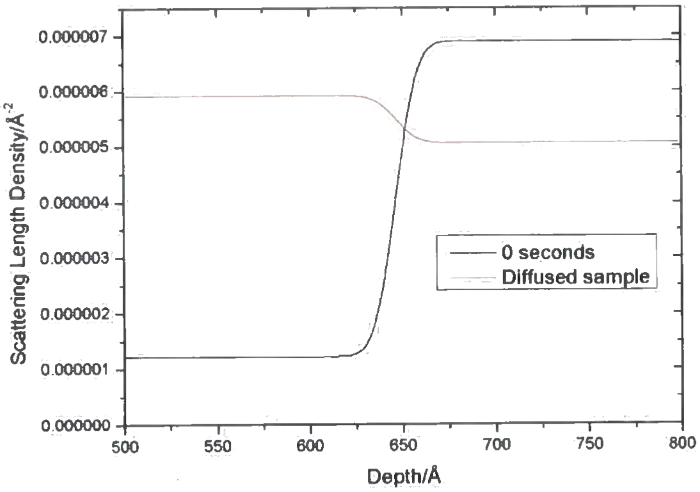

Figure 7.5 Example of scattering length density against depth profile for varying composition model (7.4.3.1)

7.4.3.2 Modelling interfacial roughness only

Unannealled samples were fitted to reflectivity profiles as described in 7.4.2. The subsequent samples were fitted by varying the roughness between the two polymer layers. Roughness between the polymer layers is considered to be equivalent to interfacial width. Roughness between the silicon and air layers was at the value determined for the unannealled samples. Scattering length densities of the polymer layers were maintained as for pure samples.

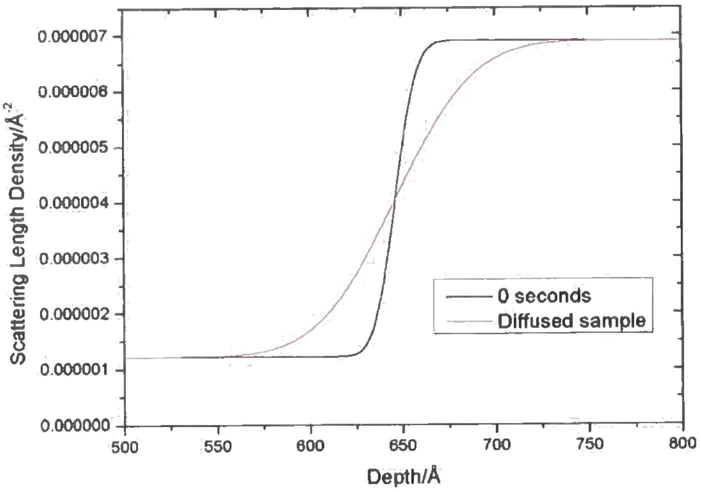

Figure 7.6 Example of scattering length density against depth profile for interfacial roughness model (7.4.3.2)

7.4.3.3 Modelling by inclusion of an additional layer

Unannealled samples were fitted to reflectivity profiles as described in 7.4.2. For subsequent annealed samples an extra 'mix' layer was added between the two polymer layers. Scattering length densities of the original polymer layers were maintained as for pure samples. The scattering length density and thickness of the 'mix' layer was varied. The thickness of the DPEO layer was found to have a negligible effect on the reflectivity provided 2500 Å < $thickness_{DPEO}$< 5000Å, however the thickness of the PMMA or PS-PMMA layer varied, to account for the movement of material into the mix layer.

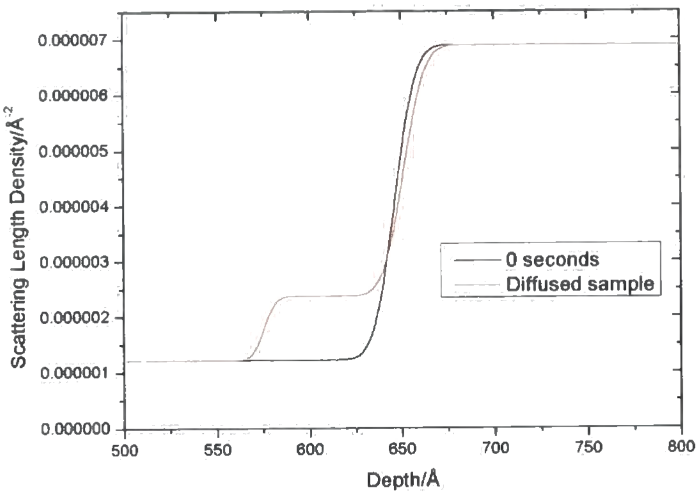

Figure 7.7 Example of scattering length density against depth profile for additional layer model (7.4.3.3)

7.4.3.4 Additional layer and roughness

Unannealled samples were fitted to reflectivity profiles as described in 7.4.2. Taking the model found from 7.4.3.3, surface roughness between the additional layer and the DPEO was varied; subsequent to the minimum found using PARRAT's fitting regime, the scattering length density and the depth of the mix layer were varied. PMMA or PS-PMMA thickness was then varied. Scattering length densities of the original polymer layers were maintained as for pure samples. The depth of the DPEO layer was found to have a negligible effect on the reflectivity provided 2500 Å < $depth_{DPEO}$ < 5000 Å, however the thickness of the PMMA or PS-PMMA layer was varied, to account for the movement of material into the mix layer to possibly compensate for the increased roughness.

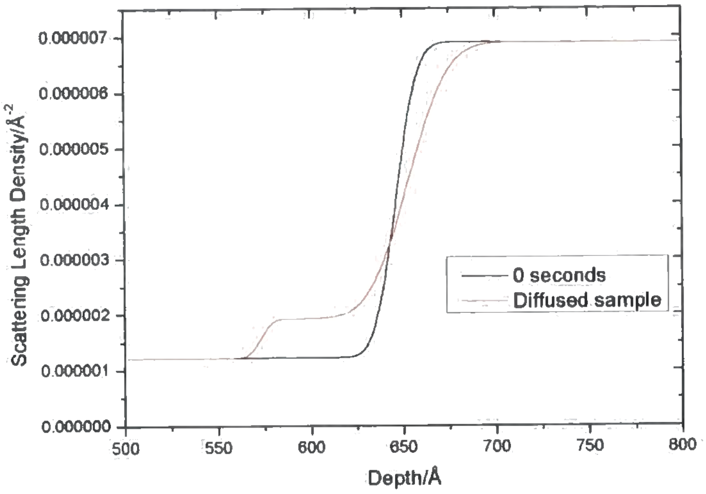

Figure 7.8 Example of scattering length density against depth profile for additional layer and roughness model (7.4.3.4)

To confirm the description of the unannealled samples, all the unannealled reflectivity data was also fitted with the same variables as the annealled data. This tended to give exactly the same description of the bilayers as described in 7.4.2. For the 'mix layer' models (7.4.3.3 and 7.4.3.4) this indicated a mix layer depth of 0nm at *t*=0.

7.5 PMMA bilayer results

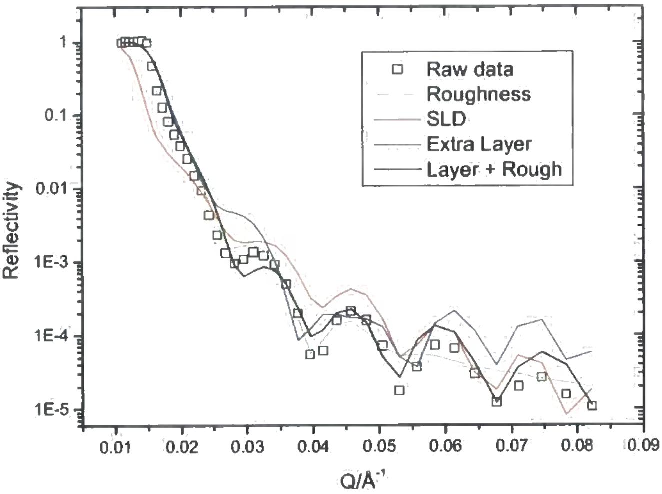

Figure 7.9 Experimental reflectivity for PMMA (96200 gmol^{-1}) and DPEO (170700 gmol^{-1}) bilayers heated at 343 K for 2500 s. Calculated reflectivites are for the four models; roughness (interfacial width) (7.4.3.2), SLD (7.4.3.1), extra layer (7.4.3.3) and extra layer with roughness(7.4.3.4).

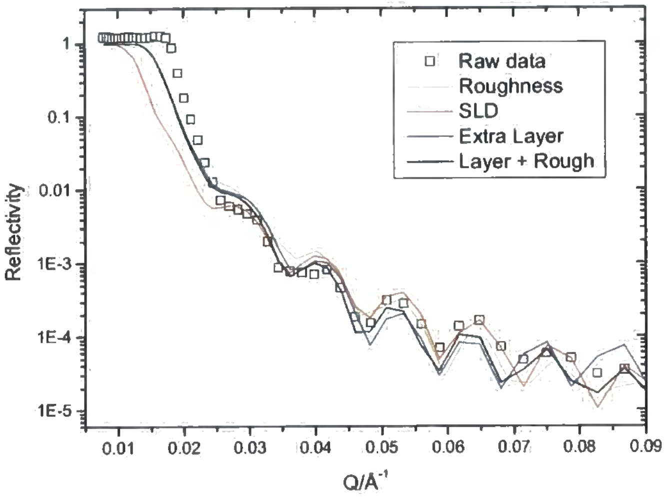

Figure 7.10 Experimental reflectivity for DPEO (121100 gmol^{-1}) and PMMA (96200 gmol^{-1}) bilayers heated at 343 K for 3661 s. Calculated reflectivites are for the four models; roughness (interfacial width) (7.4.3.2), SLD (7.4.3.1), extra layer (7.4.3.3) and extra layer with roughness(7.4.3.4).

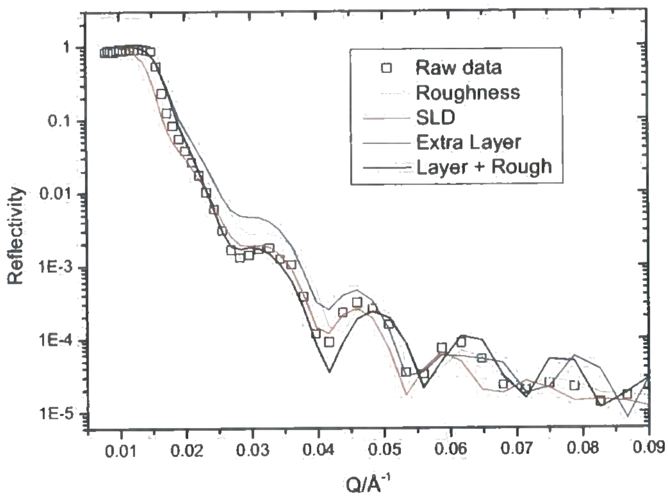

(A)

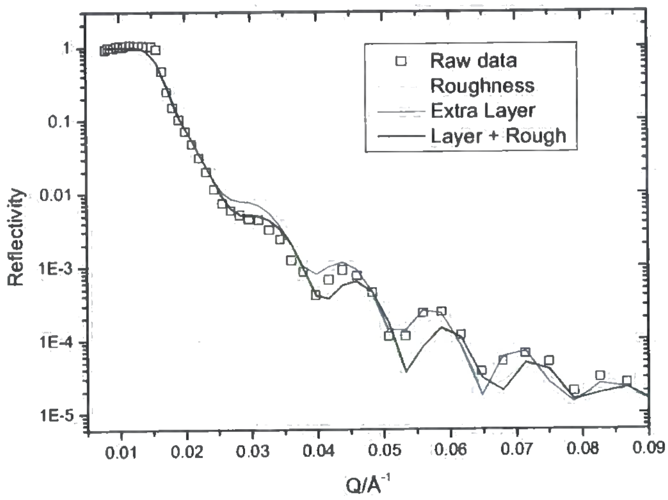

(B)

Figure 7.11 Experimental reflectivity for DPEO (89217 gmol^{-1}) and PMMA (96200 gmol^{-1}) bilayers heated at 343 K for (A) 1320 s and (B) 2500 s. Calculated reflectivites are for the four models; roughness (interfacial width) (7.4.3.2), SLD (7.4.3.1), extra layer (7.4.3.3) and extra layer with roughness(7.4.3.4).

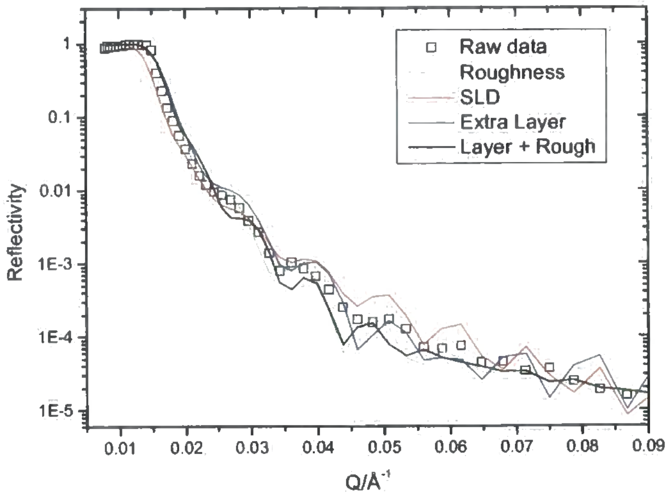

(A)

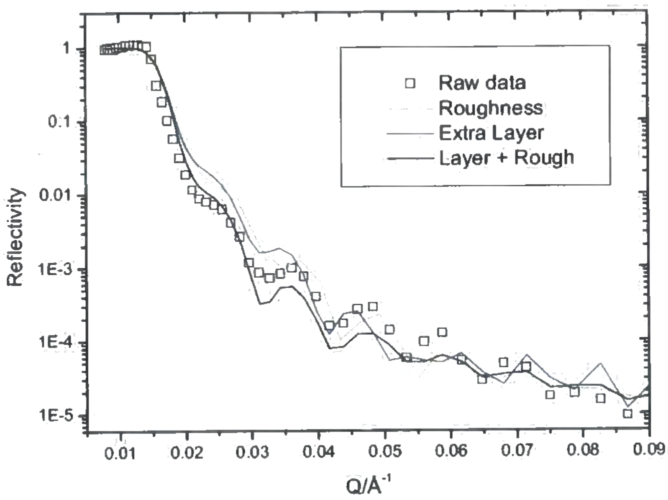

(B)

Figure 7.12 Experimental reflectivity for DPEO (121100 gmol^{-1}) and PMMA (213400 gmol^{-1}) bilayers heated at 343 K for (A) 630 s and (B) 3661 s Calculated reflectivites are for the four models; roughness (interfacial width) (7.4.3.2), SLD(7.4.3.1), extra layer(7.4.3.3) and extra layer with roughness(7.4.3.4).

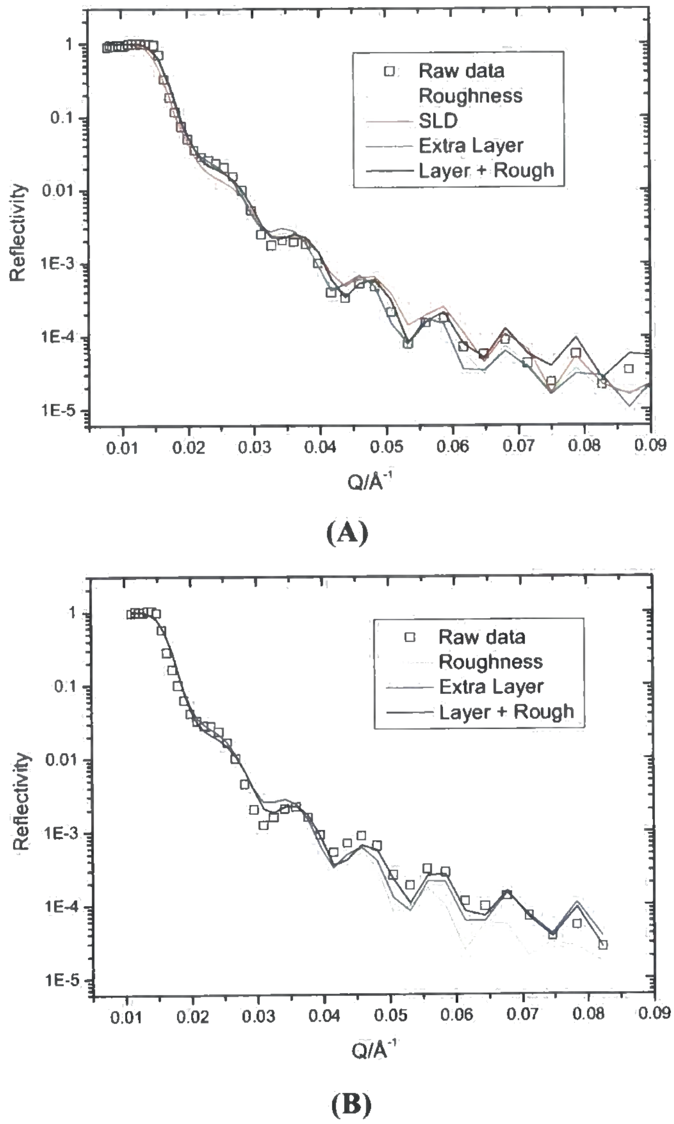

Figure 7.13 Experimental reflectivity for DPEO (121100 gmol^{-1}) and PMMA (2016000 gmol^{-1}) bilayers heated at 343 K for (A) 649 s and (B) 5628.s Calculated reflectivites are for the four models; roughness (interfacial width) (7.4.3.2), SLD (7.4.3.1), extra layer (7.4.3.3) and extra layer with roughness(7.4.3.4).

7.6 PS-PMMA bilayer results

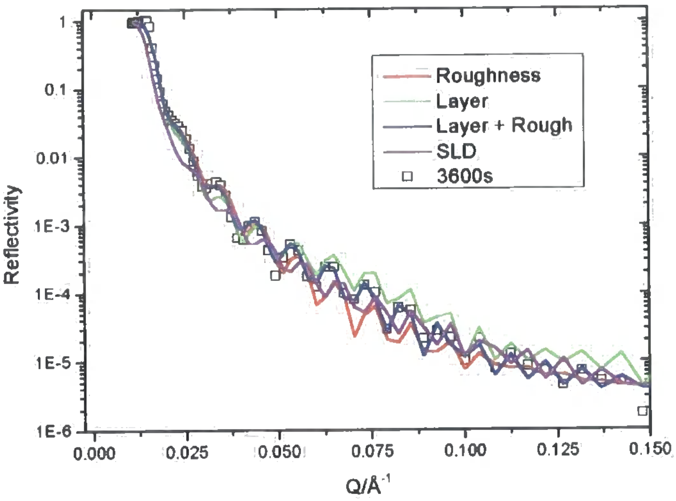

(A)

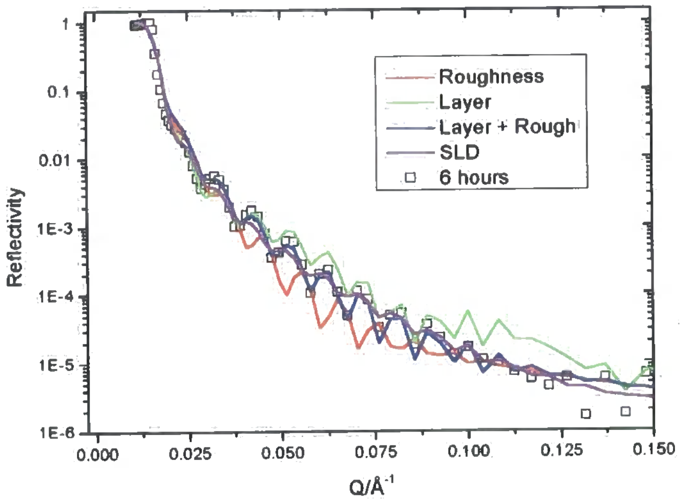

(B)

Figure 7.14 Experimental reflectivity for PS-PMMA and DPEO (89217 gmol^{-1}) bilayers heated at 343 K for (A) 3600 s and (B) 21600 s. Calculated reflectivities are for the four models; roughness (7.4.3.2), SLD (7.4.3.1), extra layer (7.4.3.3) and extra layer with roughness(7.4.3.4).

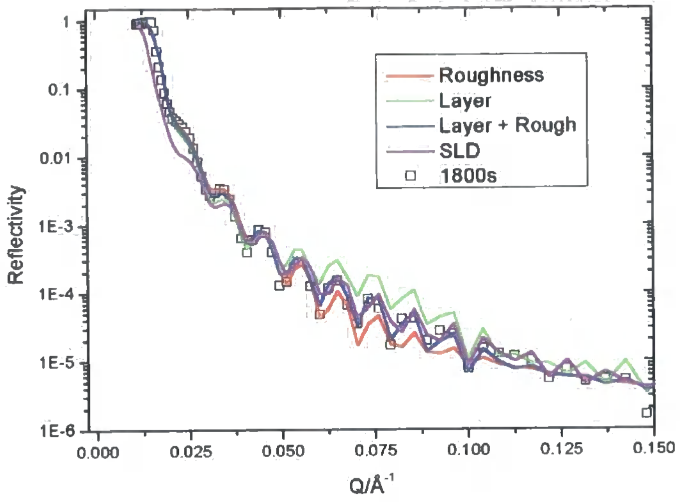

(A)

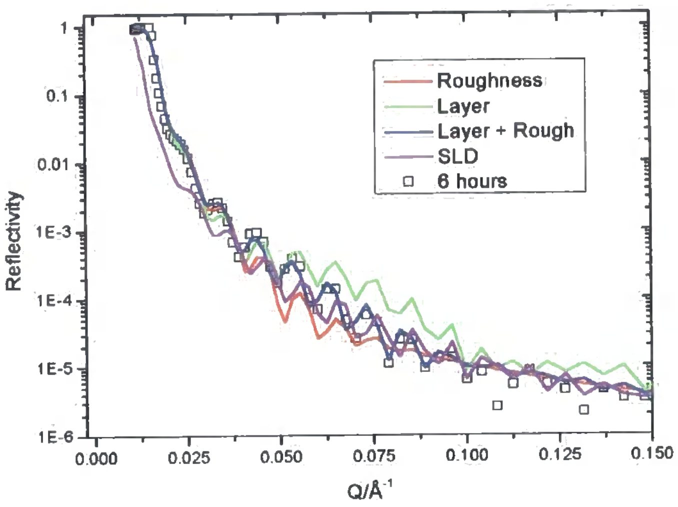

(B)

Figure 7.16 Experimental reflectivity for PS-PMMA and DPEO (170700 gmol^{-1}) bilayers heated at 343 K for (A) 1800 s and (B) 21600 s. Calculated reflectivities are for the four models; roughness (7.4.3.2), SLD (7.4.3.1), extra layer (7.4.3.3) and extra layer with roughness (7.4.3.4).

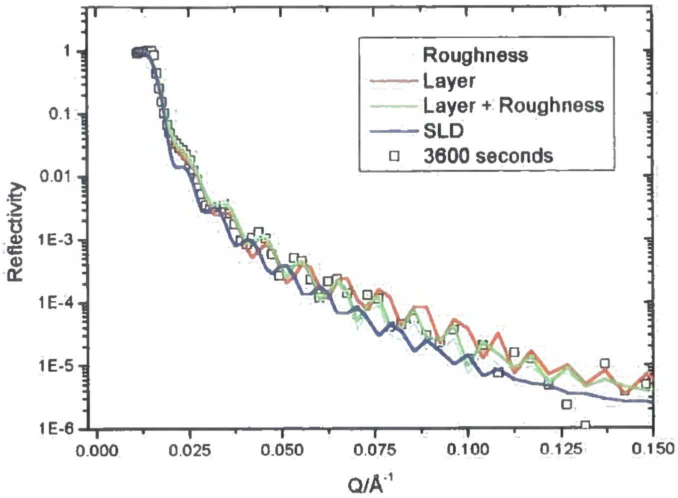

(A)

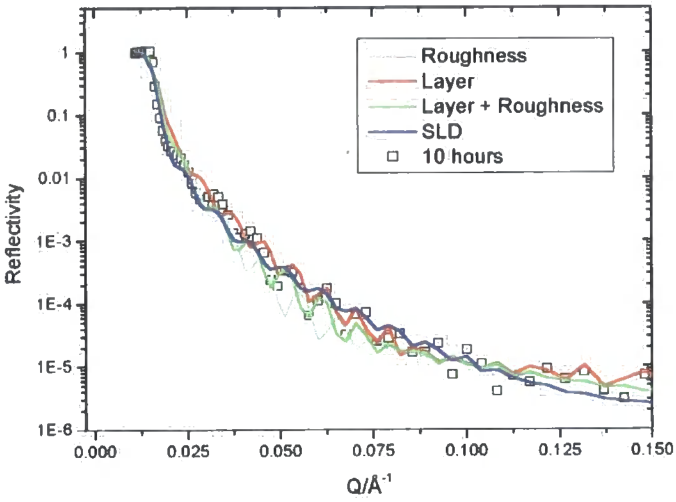

(B)

Figure 7.17 Experimental reflectivity for PS-PMMA and DPEO (17300 gmol^{-1}) bilayers heated at 343 K for (A) 3600 s and (B) 36000 s. Calculated reflectivities are for the four models; roughness (7.4.3.2), SLD (7.4.3.1), extra layer (7.4.3.3) and extra layer with roughness (7.4.3.4).

7.7 Discussion

It is known that nanoconfinement of polymers, say in thin films, can cause deviation in the glass transition temperature from bulk T_g. The length scale at which polymers deviate from the bulk T_g ranges from <100 nm in the absence of attractive substrate interactions[14] to values exceeding 100 nm in the presence of strongly attractive substrate interactions[15]. This means that a PMMA film of

~60 nm, may have a reduced T_g compared to that found from DMA or DSC, which only measure bulk T_g. Behaviour of PS-PMMA and PMMA films may differ from that of ~1 μm thick films used in ion beam analysis experiments so precise kinetics may vary.

Table 7.2 shows the radius of gyration for the polymers utilised in these experiments in theta solvents as found using the viscosity–molecular weight relationship[16]. All PMMA/PS-PMMA layers were found by both ellipsometry and reflectivity data to be larger than the radius of gyration. This indicates a degree of free movement for the PMMA/PS-PMMA molecules, not bound by specific interactions at the Si/SiO_2 interface. The radii of gyration of the two components of the copolymer are shown as individual polymers. The radius of gyration for the complete copolymer is not available so the Gaussian sum of the individual components may be used as an estimate.

Polymer	M_w/ gmol^{-1}	r_0/ Å	R_g/ Å
DPEO	170700	310	127
DPEO	121100	261	107
DPEO	89217	224	91
DPEO	17300	99	40
PMMA	96200	199	81
PMMA	213400	296	121
PMMA	2016000	682	278
PMMA	285100	342	140
PS	29200	115	47

Table 7.2 Unperturbed mean end-to-end distance of polymers utilised (r_0) and radius of gyration (R_g)[16].

Polymer	M_e/ gmol^{-1}	r_0/ Å	**R_g/ Å**
DPEO	1700	31	**13**
PMMA	10000	64	**26**
PS	**14000**	**79**	**32**

Table 7.3 Unperturbed mean end-to-end distance of entanglements for polymers utilised (r_0) and radius of gyration (R_g)[16].

7.7.1 PMMA bilayers

As can be seen from Figure 7.9-7.13 of the three models used, none clearly described all of the reflectivity data. Figure 7.18 shows the volume fraction of PMMA for the polymer layers as found using the volume fraction variable model described in 7.4.3.1. A minimum of three annealing times was run for each molecular weight combination. In general, the scattering length density (and hence volume fraction) of the DPEO layer decreased with time, indicating a dilution of the DPEO with a lower scattering length density polymer, PMMA. The scattering length density (and hence volume fraction) of the PMMA layer increased with time, indicating a dilution of the PMMA with a higher scattering length density polymer, DPEO (Figure 7.18). This clearly confirms the movement of polymers across the interface in opposite directions. Though a general trend of increase or decrease could be distinguished the data points appeared to have a wide spread due to the limited accuracy of this very simple model.

The DPEO layer is considerably thicker than the PMMA layer; hence one molecule of PMMA entering the DPEO phase should have a smaller impact on the volume fraction of the layer than one molecule of DPEO entering the thinner PMMA layer. The bilayer that is described best by the composition variation model is 2016000 gmol^{-1} PMMA/121100 gmol^{-1} DPEO (Figure 7.13). From Figure 7.18(B) the PMMA volume fraction also increases rapidly with time whilst the DPEO volume fraction remains only slightly modified. It might be expected that lower molecular weight combinations would show a greater change in volume fraction with time, however this was not observed, and the 2016000 gmol^{-1} PMMA/121100 gmol^{-1} DPEO bilayer exhibited the fastest increase in DPEO volume fraction within the PMMA layer. As can be seen from Table 7.2 the 2016000 gmol^{-1} PMMA polymer has a radius of gyration of the order of the layer thickness and hence it may be expected that the movement of this PMMA molecular weight be inhibited.

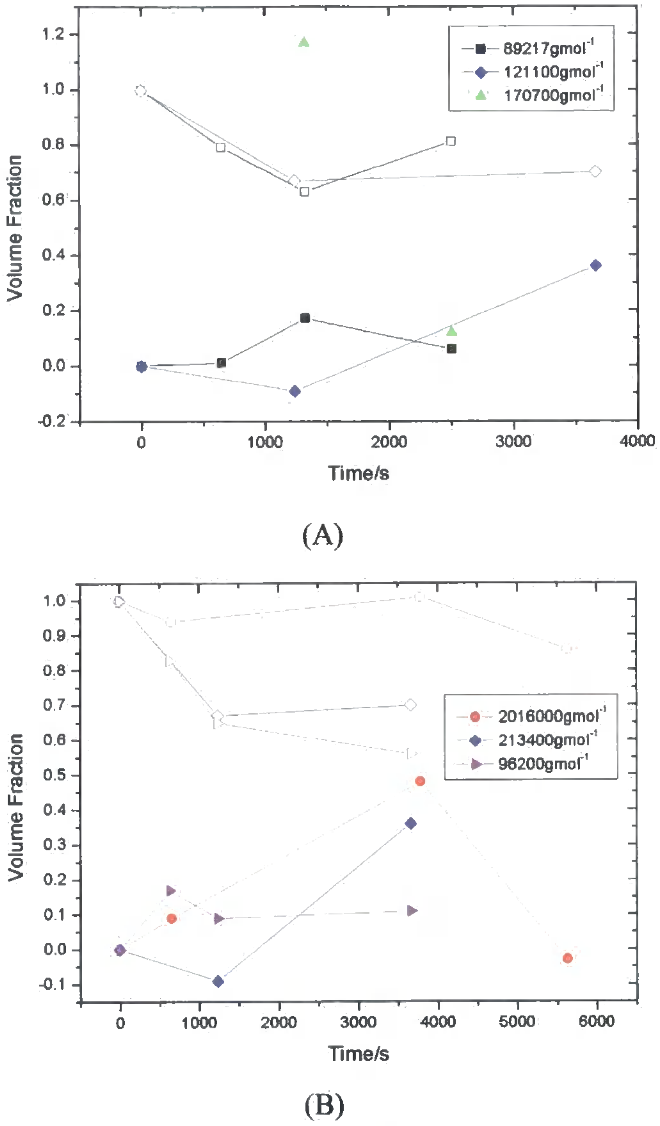

Figure 7.18 Plots of the volume fraction of PMMA rich (open symbols) and DPEO rich (closed symbols) layers with time for all bilayers. (A), describes various DPEO molecular weight bilayers with 96200 gmol^{-1}PMMA. (B) describes various PMMA molecular weight bilayers with 121100 gmol^{-1} DPEO.

Figure 7.19 shows change in interfacial width of PMMA/DPEO interfaces with time for all bilayers as described by the 'roughness' (interfacial width) model (7.4.3.2). In general the interfacial width increased with time. Figure 7.20 shows the variation of the PMMA layer thickness with time when fitted with the roughness model. Typically the PMMA thickness does not vary with change in interfacial width and consequently the interfacial width could be considered the only variable. An increase in interfacial width can indicate the movement of both PMMA and DPEO across the interface, and was of the order 50 Å, which is smaller than the unperturbed dimensions of the polymer chains utilized (Table 7.2). This indicates that with the annealing times and temperatures explored, the broadening of the interface corresponded to partial mixing of chains. However, calculated reflectivity fits were generally imperfect, the best fits being for the combinations: PMMA (96200 $gmol^{-1}$) with DPEO (170700 $gmol^{-1}$) and DPEO (89217 $gmol^{-1}$) with PMMA (96200 $gmol^{-1}$). Both of these combinations also exhibited the most systematic relationship between roughness and time as shown in Figure 7.19. The larger PMMA molecular weight polymers did not exhibit a retarded rate of interfacial width change with time; if the model described reflectivity data well longer chains would be expected to have longer reptation and constraint release times. The roughness model is analogous with previous models, used to describe interfacial broadening of DPMMA/PMMA interfaces, analysed using neutron reflectivity[5]. That fits are poor indicates that diffusion of PMMA into DPEO is quite different to that within a matrix of chemically identical polymers.

Previous experiments investigating the diffusion of thicker films of PMMA and DPEO have shown that diffusion may occur via the case II process. If case II diffusion occurs as described in 5.5.5, a Fickean tail is expected to build in front of a case II moving front to allow the once glassy polymers sufficient mobility to move into the molten penetrant polymers. Interfacial broadening might be the best model of a Fickean precursor and, if present, may be expected to occur at earlier times, however, this was not observed.

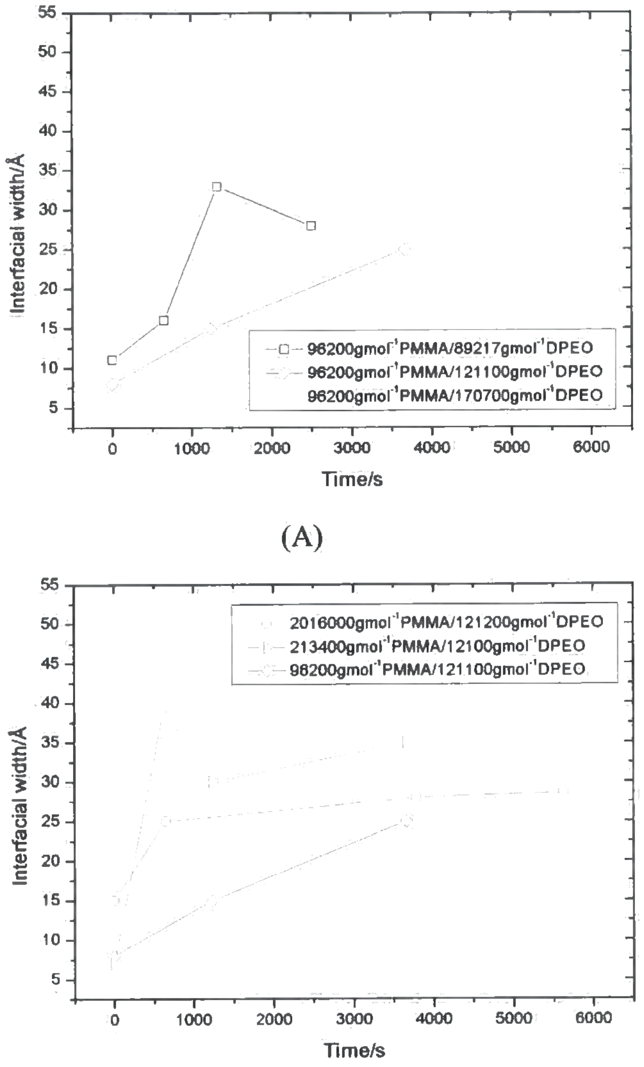

Figure 7.19 Plots of interfacial width of PMMA/DPEO interface with time for all bilayers. (A) Shows bilayers of various DPEO molecular weights with 96200 gmol^{-1} PMMA. (B) Shows bilayers of various PMMA molecular weights with 121100 gmol^{-1} DPEO.

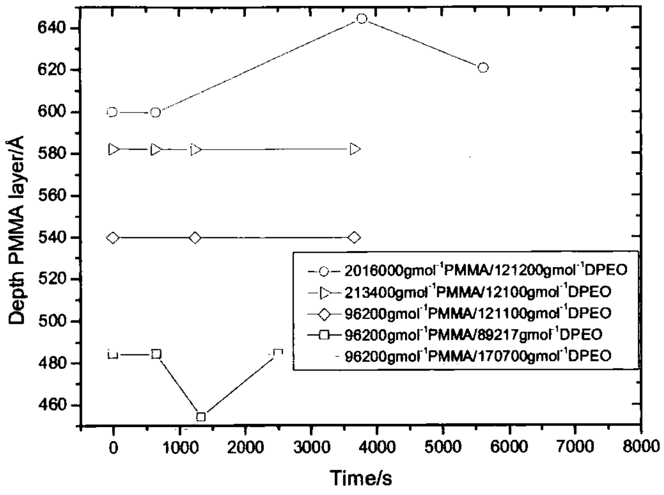

Figure 7.20 Plot of PMMA thickness with time, when fitted with interfacial roughness

Figure 7.21 shows the change of thickness with time, of a 'mix' layer added between PMMA and DPEO as described by the model (7.4.3.3). In general, the mix layer thickness increased with time, although at later times the layer thickness decreased or plateaued. The calculated fits were better for the extra layer model than for those described in 7.4.3.1 and 7.4.3.2.

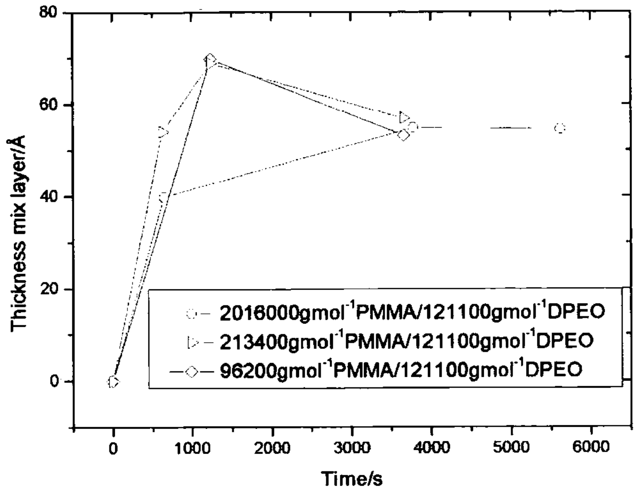

(A)

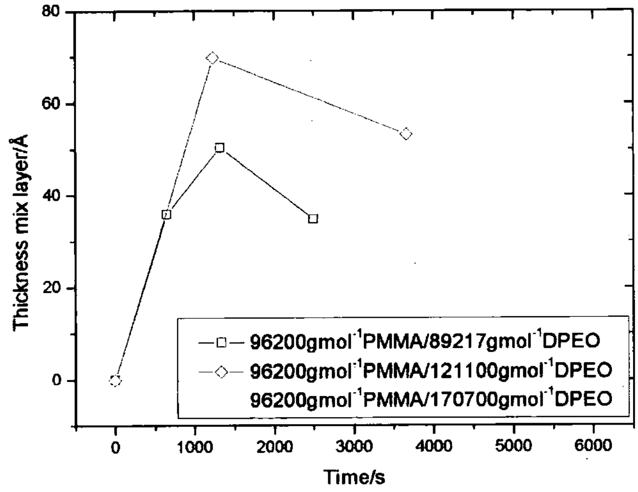

(B)

Figure 7.21 Plots of the thickness the 'mix layer' with time for all bilayers. (A) Shows bilayers of various PMMA molecular weights with 121100 gmol^{-1} DPEO. (B) Shows bilayers of various DPEO molecular weights with 96200 gmol^{-1} PMMA.

The change in mix layer thickness with time has minimal molecular weight dependence. The thickness of the mix layer, like the roughness model is slightly smaller than the unperturbed molecule dimensions. Again this may indicate that only a portion of both PMMA and DPEO polymer chains are present in the 'mix' layer. This may also indicate that the behaviour observed is a composite of the mix layer and roughness models, the similarities of the profiles are shown in Figure 7.22.

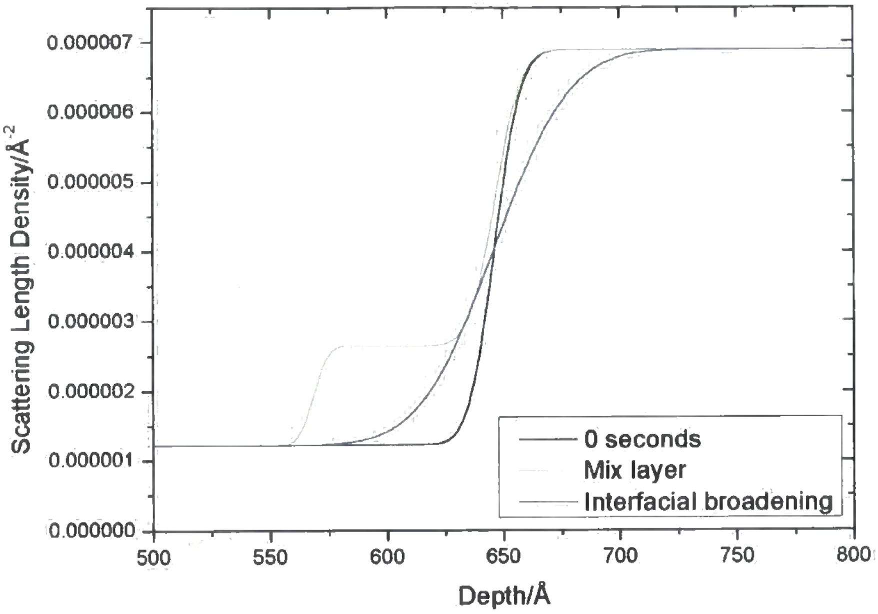

Figure 7.22 Profiles of mix layer and interfacial broadening models for 121100 gmol^{-1} DPEO on copolymer heated at 343 K for5400 s

A plateau was observed for variation of mix layer Figure 7.21(A) at ~52 Å, equivalent to approximately the radius of gyration of 3 PMMA entanglements or 2-3 DPEO entanglements and very similar to the unperturbed mean end-to-end distance of one entanglement. This plateau may represent a non-equilibrium state that eventually disappears. PMMA was glassy at 343 K, whilst DPEO was molten, for the PMMA to become mobile it should be in an environment surrounded by DPEO or other mobile chains, as the mix layer contains entanglements of both components, this is supported. The mix layer thus represents a plasticising zone, where sufficient mobility is imparted to PMMA molecules, by exposure to sufficient DPEO monomers at a constant volume fraction. This mix layer may also represent the film width required to lower the T_g of PMMA molecules in comparison to bulk behaviour. Previous diffusion investigations (chapter 5) with PMMA and DPEO have shown non linear relationships between the movement of the interface between the PMMA and DPEO rich phase with time, as exhibited in Figure 7.21, a plot of mix layer thickness with the square root of time, shows no linearity (Figure 7.23).

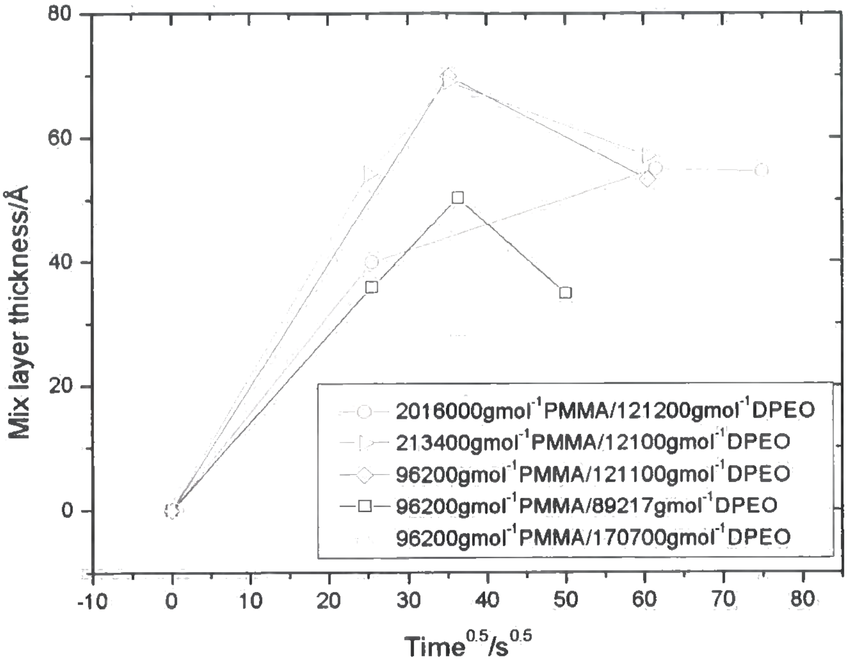

Figure 7.23 Plots of the thickness of the 'mix layer' with the square root of time for all bilayers

To form the mix layer, the PMMA and DPEO layers should be depleted, DPEO should be in such excess that depletion is negligible. To allow for the depletion of PMMA, the thickness of the PMMA layer was also fitted in the model. The variation of thickness of this PMMA layer with time is shown in Figure 7.24. There was no distinct trend in PMMA loss. It would be expected that loss of PMMA would be matched by an increase of scattering length density attributed to PMMA in the mix layer. Table 7.4 shows the values of the mix layer thickness and PMMA thickness for each annealed sample. There was no clear relation between the mix layer volume fraction and loss of PMMA.

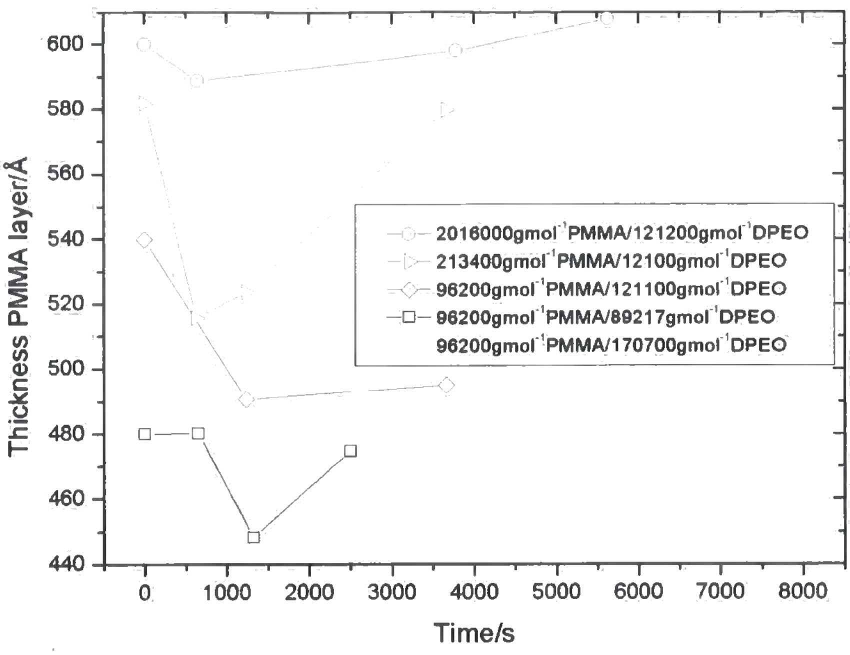

Figure 7.24 Plot of the thickness of PMMA layer with time, when fitted with a 'mix' layer

PMMA/ gmol^{-1}	DPEO/gmol^{-1}	Annealing time /s	SLD of mix layer/ Å^{-2}	φ_{DPEO}	Thickness mix layer/Å	Thickness reduction of PMMA layer/ Å
213400	121100	630	3.21E-06	0.37	54	67
213400	121100	1237	2.33E-06	0.22	69	59
213400	121100	3661	2.79E-06	0.30	57	2
2016000	121100	649	3.50E-06	0.42	40	11
2016000	121100	3786	2.44E-06	0.24	55	2
2016000	121100	5628	4.91E-06	0.66	55	-8
96200	121100	1237	2.42E-06	0.23	70	49
96200	121100	3661	3.26E-06	0.38	53	45
96200	170700	1320	3.24E-06	0.37	29	15
96200	170700	2500	4.90E-06	0.66	57	1
96200	89217	649	3.49E-06	0.42	36	4
96200	89217	1320	3.65E-06	0.44	50	36
96200	89217	2500	3.21E-06	0.37	35	10

Table 7.4 Showing, for annealed samples, the scattering length density, equivalent volume fraction of components and thicknesss of the 'mix' layer and reduction in thickness of the PMMA layer as compared to the unannealled bilayer.

Diffusion is annealing time and molecular weight dependent, therefore the scattering length density of the 'mix layer' might be expected to display a trend between samples. Scattering length density is invariant with respect to both thickness of the mix layer and time annealed with an average scattering length density of $3.34\times10^{-6} \pm 0.82\times10^{-6}$ Å^{-2}. This indicates an average DPEO volume fraction 0.39±0.14. It is possible that with further annealing this volume fraction would change. The variation present may be statistical and a mix layer of $\varphi_{PEO}\approx0.4$ may exist for all annealing times. Miscibility is limited by the phase boundary and this may dictate the concentrations found in the mix layer[17-19](4.11). A similar neutron reflectivity experiment that utilised DPMMA and oligomeric PEO (polyethylenegylcol (PEG)), with PEG molecular weight 640 gmol^{-1} displayed[8] a linear time dependence of DPMMA layer thickness reduction. A clear intermediate layer was observed between PEG and DPMMA with a volume fraction of $\varphi_{PEG}=0.35$, believed to indicate the solubility limit of PEG in DPMMA. The interdiffusion layer found here was not as well defined as that for PEG, but the volume fraction $\varphi_{DPEO}=0.39$ was quite similar. That molten PEO behaves in a similar fashion to PEG at room temperature, indicates a mobility for the PEO chains similar to that of unentangled oligomers.

A roughness (interfacial width) can be added to the mix layer model as described in 7.4.3.4. Fits were marginally better than previous models as described in Figure 7.9-7.13. A typical scattering length density profile for this model is shown in Figure 7.25, the mix layer thickness increased with time and interfacial broadening between the mix layer and DPEO also increased with time The profile indicates asymmetric diffusion between PMMA and DPEO.

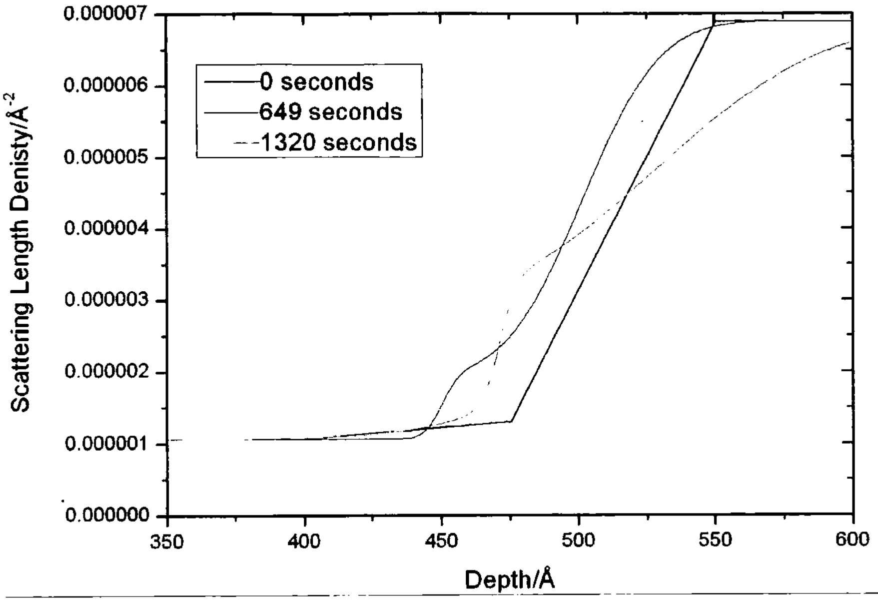

Figure 7.25 Example of a scattering length density against depth profile using the additional layer and roughness model, for a 96200 gmol^{-1} PMMA and 89217 gmol^{-1} DPEO bilayer

The mix layer generally increased with time as shown in Figure 7.26. Despite the limited anneal times for each sample; a plateau is reached for some of the bilayers. This slowing down may occur because of the composition dependence of the interaction parameter or glass transition temperature. Plateaus generally occur at ~70 Å, approximately the radius of gyration of 2-3 entanglements of either polymer which may indicate a limit of diffusion between the polymers before reptation is the dominant diffusive process.

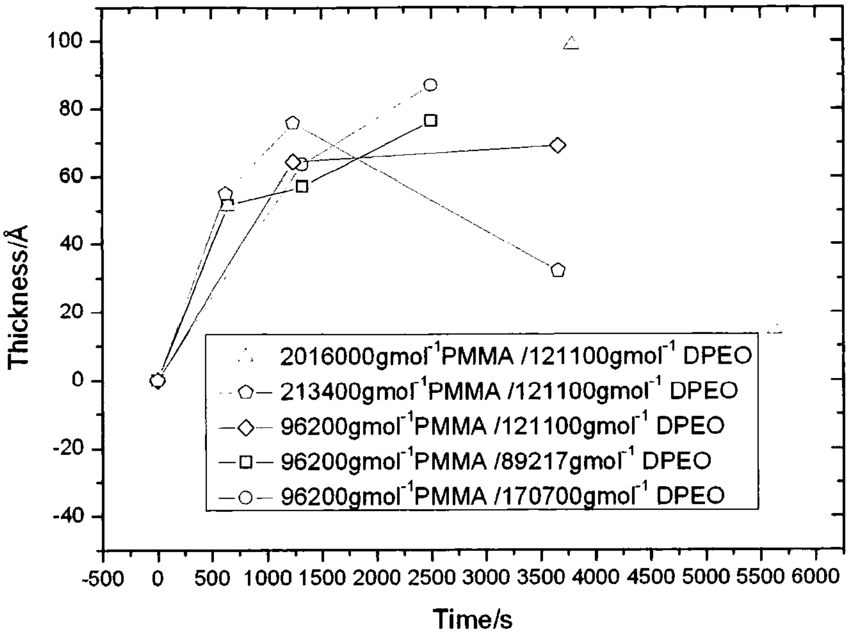

Figure 7.26 Using additional layer and roughness model the calculated mix layer thickness as a function of time, for DPEO/PMMA bilayers.

The interfacial width generally increased with time but was independent of polymer molecular weight as shown in Figure 7.27 . The interfacial widths are of the order of a few entanglements of either polymer, so molecular weight may not be an important factor.

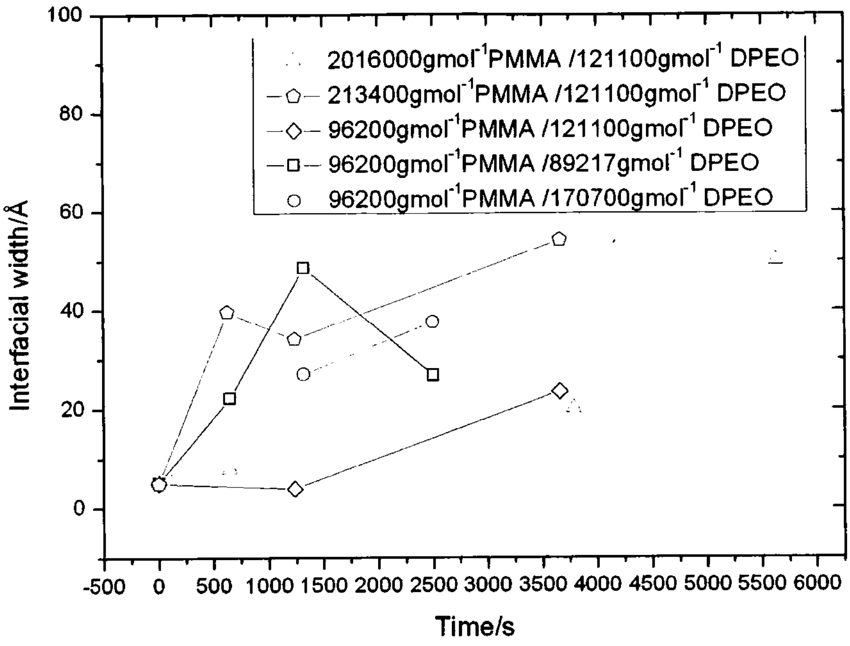

Figure 7.27 Using additional layer and roughness model the calculated interfacial width as a function of time, for DPEO/PMMA bilayers with various DPEO molecular weights.

It is expected that in a similar fashion to The PMMA layer may decrease with time to compensate for the movement of polymer chains into DPEO. From Figure 7.28 it can be seen that in general the PMMA thickness decreased with time but was inconsistent between molecular weights.

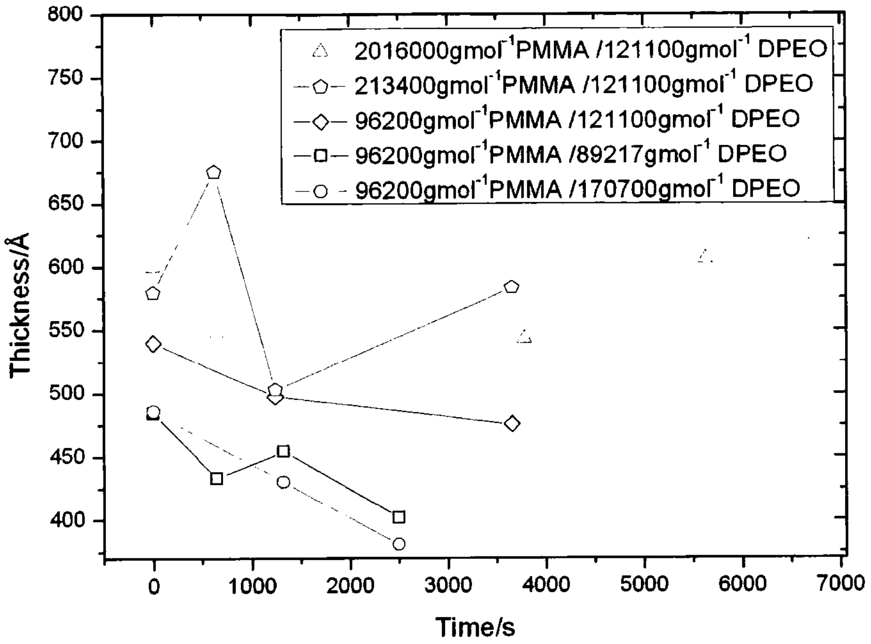

Figure 7.28 Using additional layer and roughness model the calculated PMMA layer thickness as a function of time, for DPEO/PMMA bilayers with various DPEO molecular weights.

The mix layer scattering length density and hence volume fraction did not exhibit a consistent increase or decrease with time, instead indicating a statistical variation where the mix layer φ_{DPEO}=0.19±0.05. This differs from the mix layer without interfacial broadening described in 7.4.3.3, where φ_{DPEO}=0.39±0.14, a value consistent with miscibility behaviour of DPEO and PMMA.

7.7.2 PS-PMMA bilayers

Sequential annealing and quenching of the bilayers, caused some deteriation of the samples, visible to the naked eye, at the edges of the silicon block. This was especially true of the 17300 gmol^{-1} DPEO samples, where as was found for the ion beam experiments dewetting became evident at later annealing times and quenches. The silicon block is exposed to a wide neutron beam so that inhomgeneities, especially at the edge of the sample should not impact on collected reflectivity data. However, the poor relationship between calculated reflectivities and experimental data at the longest anneal times from 17300 gmol^{-1} bilayers (Figure 7.17) indicates that this may not be the case. Previous experiments (6.5.3) have shown that bilayers that included 17300 gmol^{-1} DPEO dewetted and this may be the process observed here at later annealing times. Due to the time constraints of experimental work at ISIS a minimum of 5 bilayers were run for each molecular weight combination. As can be seen from Figure 7.14-7.17, of the four models used, none perfectly described all the reflectivity data.

Figure 7.29 shows a typical profile of a PS-PMMA bilayer with time, as fitted with the composition variation model (7.4.3.1). There was no regular variation of layer composition with time. The greatest change in layer composition appeared to at timescales less than the shortest annealing time. The scattering length density of the PS-PMMA layer indicates a dilution of the PS-PMMA with a higher scattering length density polymer: DPEO. The decrease in the scattering length density of the DPEO layer also indicates copolymer is present in the DPEO layer and the movement of polymers across the interface in opposite directions.

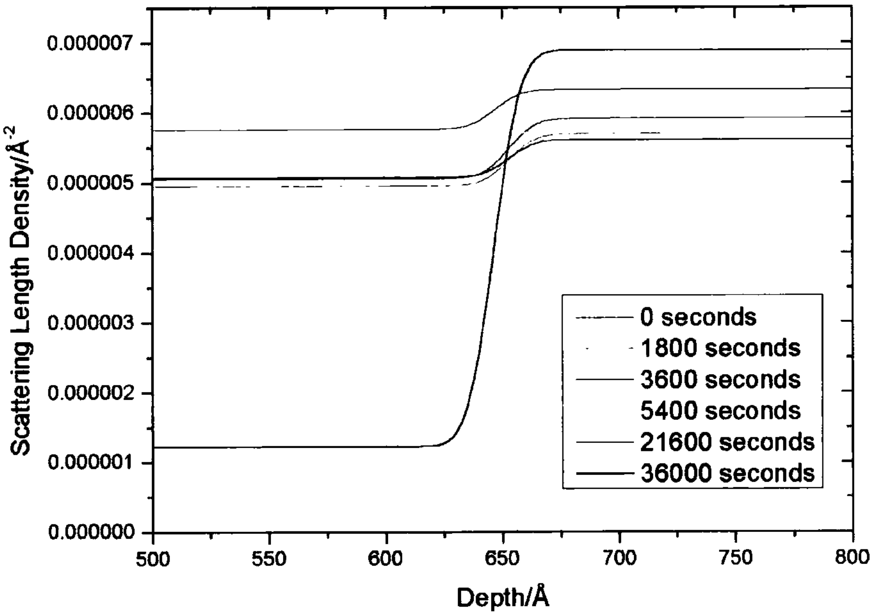

Figure 7.29 Example of a scattering length density against depth profile using the composition variation model, for 121100 gmol^{-1} DPEO/PS-PMMA bilayer.

Figure 7.30 shows there was no consistent variation of scattering length density within both polymer layers with time and this is reflected in the poor agreement of calculated reflectivity and experimental data. The proportionately smaller change in scattering length density of the DPEO rich layer, compared to the PS-PMMA rich layer, is expected as DPEO is in excess compared to PS-PMMA.

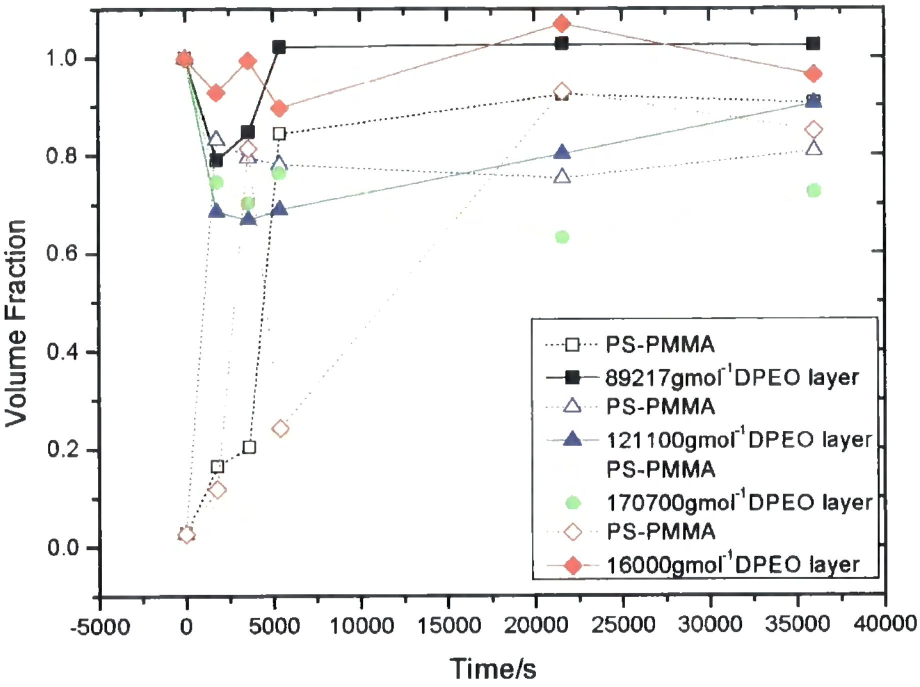

Figure 7.30 Plot of layer volume fraction DPEO as a function of time, for DPEO/PS-PMMA bilayers with various DPEO molecular weights

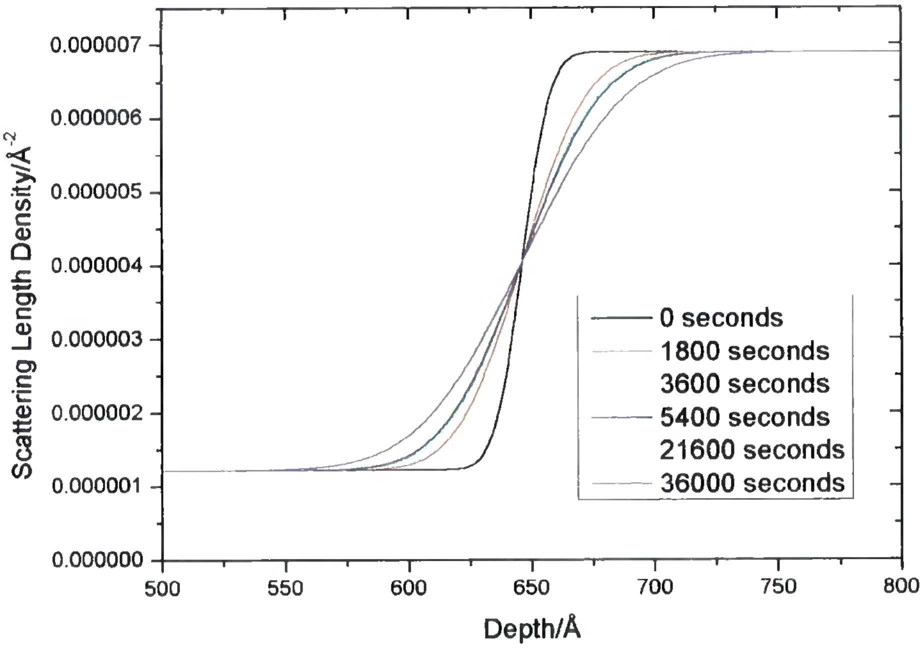

Figure 7.31 Example of a scattering length density against depth profile using the interfacial roughness model, for 121100 gmol^{-1} DPEO/PS-PMMA bilayer.

Figure 7.31 shows a typical profile of a PS-PMMA bilayer with time as fitted with the roughness model (7.4.3.2). The interfacial width increases with time as shown in Figure 7.32, however the square of interfacial width did not increase linearly with time. An increase in interfacial width can indicate the movement of both PS-PMMA and DPEO across the interface. Interfacial widths were found to be up to 35 Å, which is only a small portion of the unperturbed dimensions of the polymer chains (Table 7.2). This indicates that it is unlikely that a complete chain has crossed the DPEO/PS-PMMA interface, but several smaller parts of the chain. As shown in Figure 7.32 the interfacial width plateaued at ~25-35 Å, which corresponds to the radius of gyration for one PMMA entanglement or 2-3 DPEO entanglements. It is unlikely that PS entanglements would be preferentially solvated in DPEO, and if present would then collapse to a smaller coil that the theta solvent radius of gyration. Calculated reflectivity fits were generally poor, the best fits were for early annealing times, with greater disparity to experimental data at annealing times of 6 and 10 hours. It is possible that for early annealing times interfacial broadening is a good description of action at the interface, with a non-linear increase of interfacial width with time. At later annealing times this action is not such a good description of behaviour when an asymmetric interface may be a better approximation and is expected for a system that exhibits case II diffusion including a Fickean pre-cursor.

The larger molecular weight DPEO did not exhibit a retarded rate of interfacial width growth with time. This might be expected if the model described reflectivity data well. The 17300 gmol^{-1} DPEO bilayer appeared to behave in a similar fashion to other bilayers, despite displaying generally poor fits to all models. Bilayers that included PMMA instead of PS-PMMA, exhibited interfacial widths of the order 50 Å, at shorter annealing times to those used here. However, calculated reflectivities did not reflect the experimental data, so comparisons may not be reasonable. The smaller interfacial widths exhibited by the copolymer may be due to the polystyrene block inhibiting movement of either the PMMA or DPEO across the interface compared to the homopolymer bilayers.

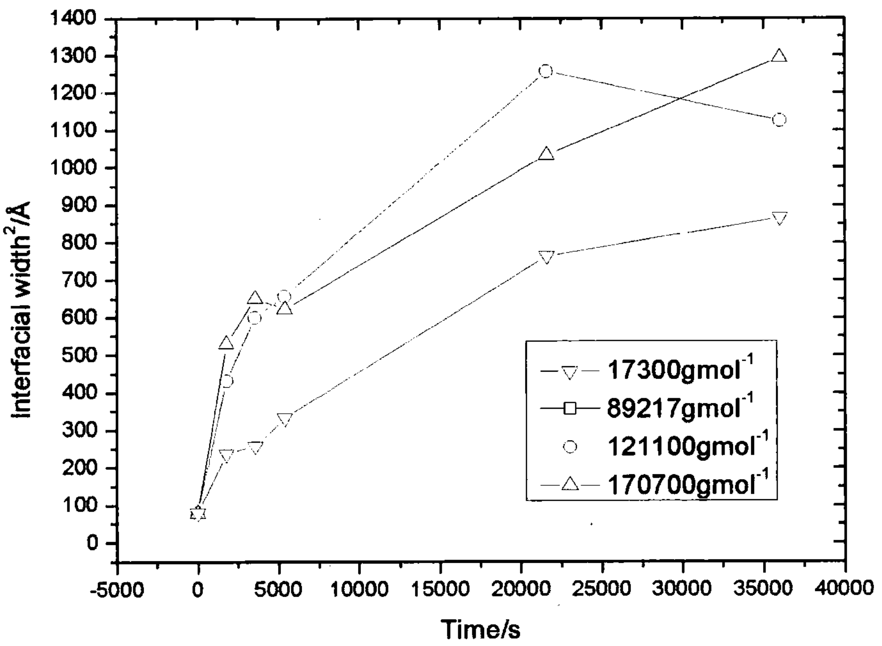

Figure 7.32 Plot of roughness^2 (interfacial width^2) as a function of time, for DPEO/PS-PMMA bilayers with various DPEO molecular weights.

Figure 7.33 shows a typical profile of a PS-PMMA bilayer with time as fitted with the additional layer model (7.4.3.3). The scattering length density of the extra layer is approximately invariant for all annealing times. The thickness of the extra layer varies with time. Layer thickness was >50 Å, which indicates the radius of gyration of 1-2 entanglements of either polymer chain. In the blend environment, due to the unfavourable interactions between PS and DPEO, PS may collapse leaving a total radius of gyration for the copolymer, equivalent to just the PMMA component. The average scattering length density of the mix layer, for all DPEO molecular weights (except 17300 gmol^{-1}) is equivalent to DPEO volume fraction of 0.22±0.07. When this model was applied to PMMA/DPEO bilayers the additional layer also exhibited an invariant scattering length density, equivalent to φ_{DPEO}= 0.39±0.14. This is higher than the value found here and bore closer resemblance to the behaviour of PMMA with PEG[8] and to known phase behaviour of PMMA/PEO (5.5.3). The presence of PS in the bilayer should interfere with PMMA/DPEO phase behaviour. Approximately 10% of the glassy matrix is attributed to PS, however the volume fraction of the mix layer is not equivalent to 90% of that found from PMMA/DPEO bilayers. This may indicate that PS is present in the mix layer and influencing the solubility of the components and hence volume fraction of the mix layer. The relationship between the layer thickness and time is shown in Figure 7.34. In general, the mix layer thickness increased with time towards a plateau value of 100 Å. The 17300 gmol^{-1} DPEO bilayer did not exhibit this trend; however this sample exhibited the greatest degradation from heating and may not give consistent results.

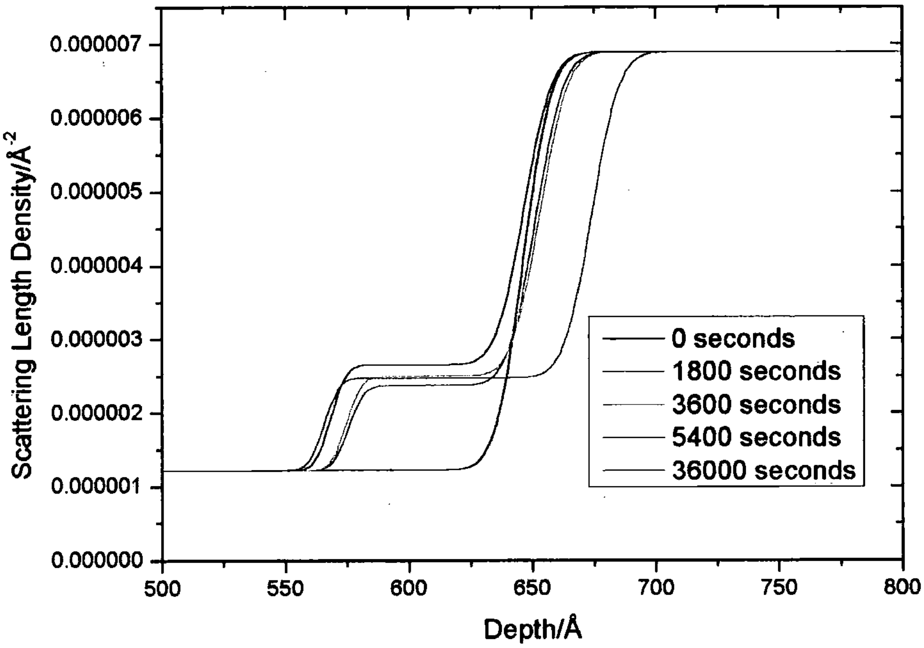

Figure 7.33 Example of a scattering length density against depth profile using the additional layer model, for 121100 gmol^{-1} DPEO/PS-PMMA bilayer.

The relationship between mix layer thickness, or interface depth with the square root of time is displayed in Figure 7.35, if polymer diffusion was Fickean, interface displacement should be linear with $t^{0.5}$.

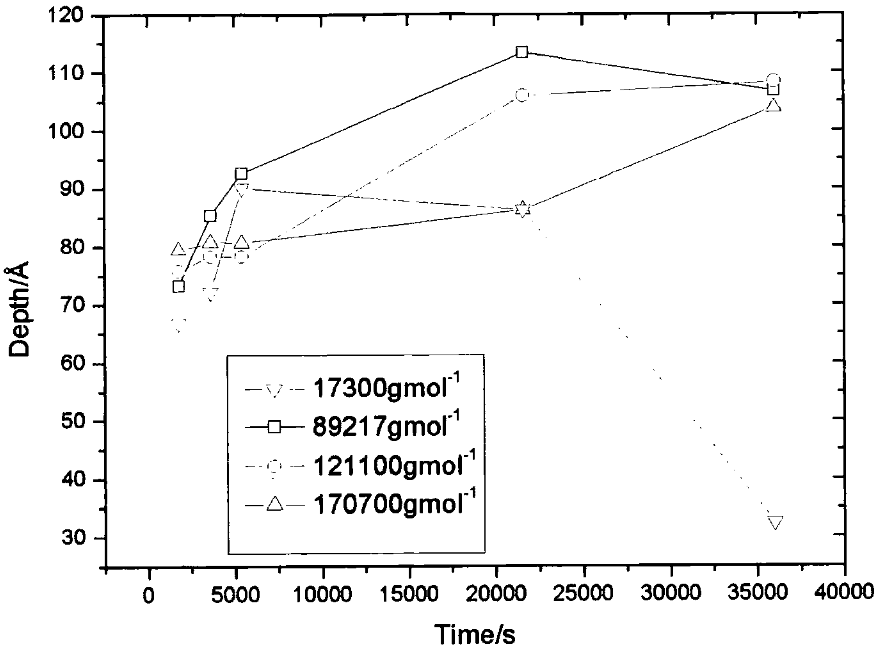

Figure 7.34 Using additional layer model the calculated mix layer thickness as a function of time, for DPEO/PS-PMMA bilayers with various DPEO molecular weights. Dashed line indicates the most degraded sample.

The rate of increase of mix layer thickness with time is the slope in Figure 7.35 which is within uncertainty similar for 89217 gmol^{-1} and 121100 gmol^{-1} and slightly slower for 170700 gmol^{-1} greater for the smaller () DPEO combinations. The calculated reflectivities exhibited the same fringes as the experimental data, but were at an elevated reflectivity. From Figure 7.14-7.17 it can be seen that additional layer fits were better at longer annealing times. A better fit was achieved by including an interfacial roughness (extra interfacial broadening) between the mix layer and the DPEO.

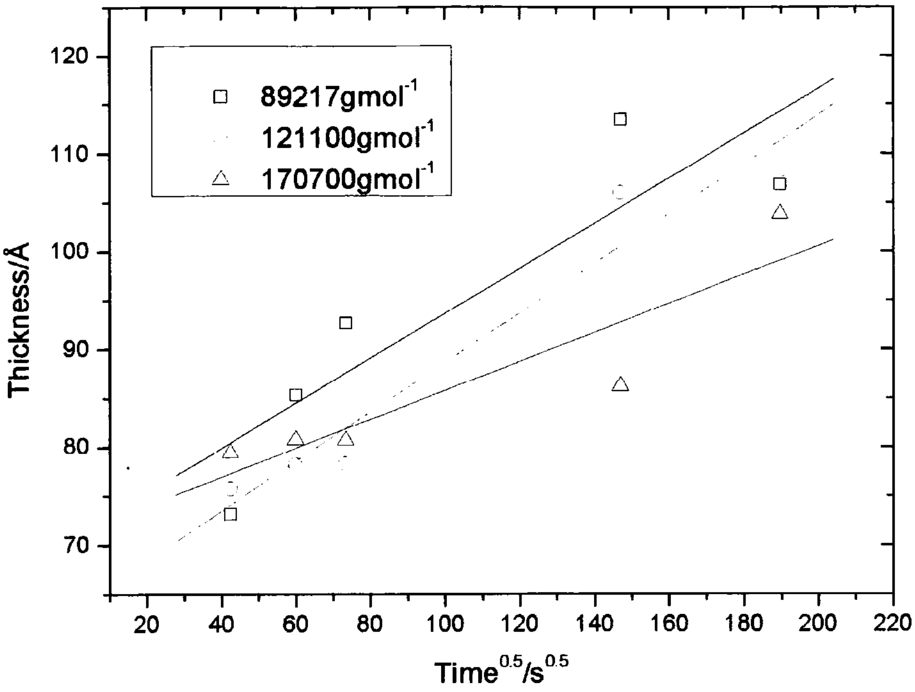

Figure 7.35 Using additional layer model the calculated mix layer thickness as a function of the square root of time, for DPEO/PS-PMMA bilayers with various DPEO molecular weights

The best model was the additional layer and roughness model (7.4.3.4). This was particularly effective at describing reflectivity for bilayers at later annealing times. Figure 7.36 shows a typical profile of a PS-PMMA bilayer with time as fitted with the roughness model, this demonstrates an asymmetric diffusion profile between the polymers.

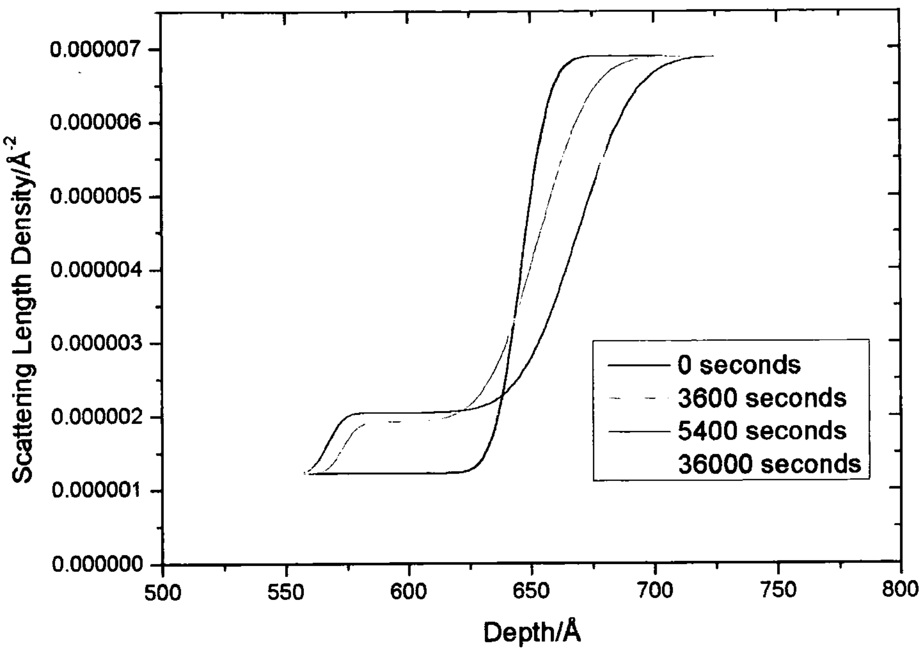

Figure 7.36 Example of a scattering length density against depth profile using the additional layer and roughness model, for 121100 gmol^{-1} DPEO/PS-PMMA bilayer.

Figure 7.37 shows the variation of the mix layer thickness with time. The mix layer thickness increases with time and the rate of increase in thickness is greater for smaller molecular weight DPEO. The variation of mix layer thickness with time is non-linear for the smaller DPEO molecular weights, this observation may also be true for the large DPEO molecules if longer annealing times were observed. The mix layer thickness variation with $t^{0.5}$ was non- linear hence indicating non-Fickean diffusion into the mix layer. The scattering length density of the mix layer is invariant with time and the equivalent volume fraction for all molecular weights was φ_{DPEO}=0.09±0.07. For calculated reflectivities that only gave good fits to experimental data (exempting 89217 gmol^{-1} DPEO at 6hours and 170700 gmol^{-1} DPEO at 5400s) φ_{DPEO}=0.12±0.03. This volume fraction was smaller than that found for the additional layer model and was consistent with the mix layer volume fraction found for the PMMA/DPEO bilayer using the mix layer and roughness model. This may indicate that the volume fraction of the mix layer is not indicative of a solubility limit between the polymers.

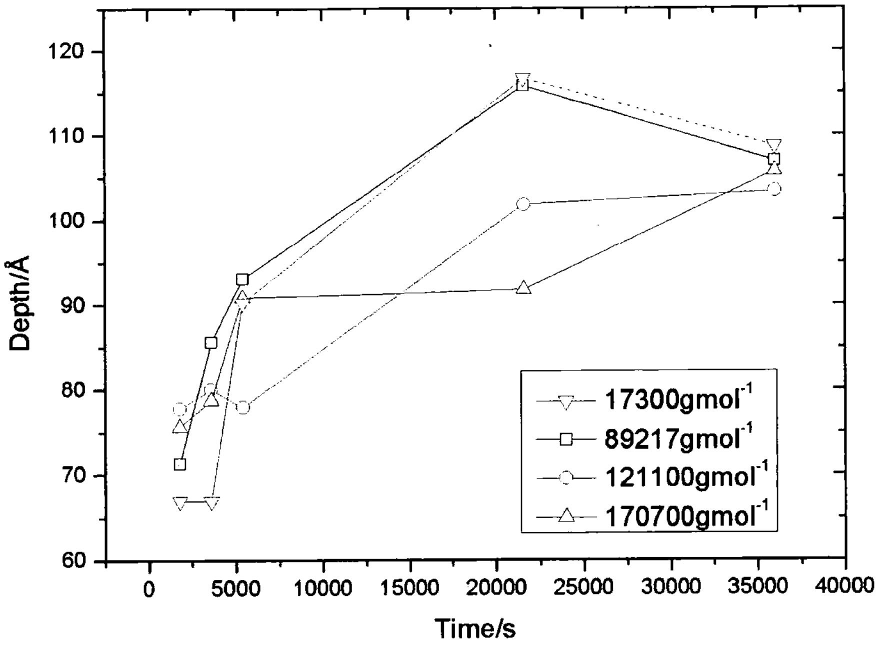

Figure 7.37 Using additional layer and roughness model the calculated mix layer thickness as a function of time, for DPEO/PS-PMMA bilayers with various DPEO molecular weights. Dashed line indicates the most degraded sample.

Figure 7.38 shows the variation of the pure PS-PMMA layer thickness with time. If PS-PMMA molecules diffuse out of the PS-PMMA bulk into the DPEO, then the copolymer layer must decrease with time, as material moves across the interface. After the initial decrease in thickness, the PS-PMMA thickness remains constant at approximately 550 Å, a decrease of ~70 Å which is equivalent to the radius of gyrations of approximately 3 entanglements of PMMA chains. No constant PMMA layer thickness was observed for the PMMA/DPEO bilayers when fitted with this model, however the PMMA bilayers may have exhibited the later stages of the processes not observed here. The combination of extra interfacial broadening and additional layer indicates a concentration gradient at the interface, one that reflects a higher concentration of PS-PMMA near the PS-PMMA bulk and a more diffuse region in the DPEO layer.

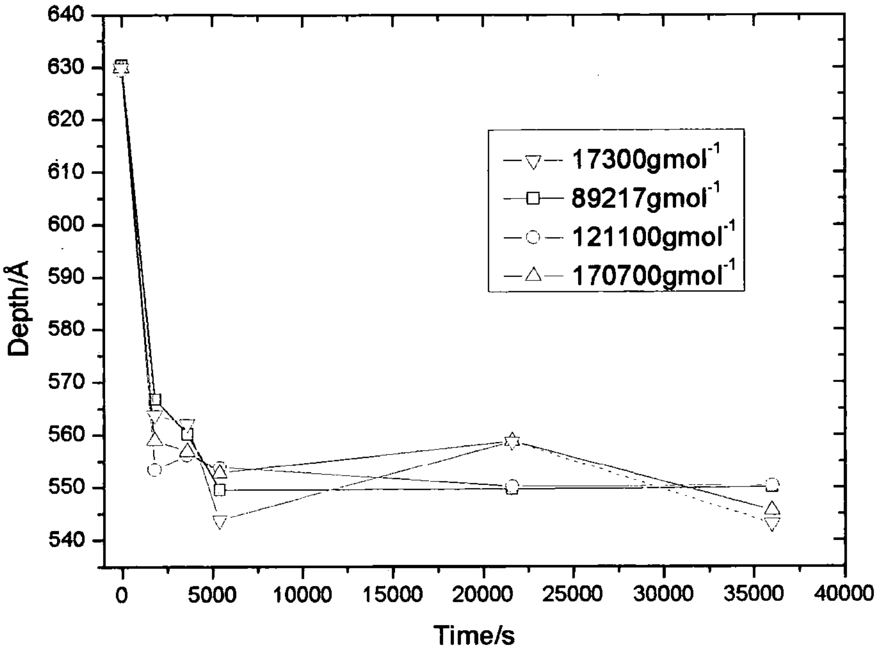

Figure 7.38 Using additional layer and roughness model the calculated PMMA layer thickness as a function of time, for DPEO/PS-PMMA bilayers with various DPEO molecular weights. Dashed line indicates the most degraded sample.

Table 7.5 shows the extra interfacial broadening added to the additional layer. For all molecular weights the interfacial broadening did not vary consistently with time, instead showing statistical variation with annealing time, with an average interfacial width of 17 ± 5 Å. This differed from behaviour observed for the DPEO/PMMA bilayers, where interfacial broadening generally increased with time, possibly exhibiting earlier or later behaviour than that observed for the PS-PMMA bilayer. The average interfacial width for each molecular weight combination increases with increasing DPEO molecular weight. Taking into account the errors in the calculated averages, such a relationship is tentative. 17 ± 5 Å is close to the R_g of one DPEO entanglement.

Time/s	DPEO: 89217gmol^{-1} Interfacial width / Å	DPEO: 121100gmol^{-1} Interfacial width / Å	DPEO: 170700gmol^{-1} Interfacial width / Å	DPEO: 17300gmol^{-1} Interfacial width / Å
1800	13.3	29.5	17.3	12.5
3600	14.2	16.7	16.3	12.8
5400	8.25	14.6	24.2	14.3
21600	17.5	18.5	21.2	25.5
36000	15.5	15.0	22.2	21.8
Average	13.7 ± 3.5	18.9 ± 6.2	20.2 ± 3.3	17.4 ± 5.9

Table 7.5 Using additional layer and roughness model the calculated extra interfacial widths and average with time, for DPEO/PS-PMMA bilayers with various DPEO molecular weights

7.8 Summary

Simple models including symmetric diffusion (interfacial broadening) failed to describe diffusion between PMMA/DPEO and PS-PMMA/DPEO bilayers. An extra mix layer model analogous to previous work with a PEG diffusion system displayed similar volume fraction behaviour[8]. Longer annealing times may have provided greater polymer movement, which may have led to more disparate reflectivity and clearer relationships to the models suggested. A more complicated model that attempted to combine the individual models to produce an asymmetric profile provided the most reasonable fits. Bilayers could be fitted by a mix layer of $\varphi_{DPEO} \sim 0.1$ and extra interfacial broadening between this layer and DPEO. The thickness of mix layers are within the scale that would allow glass transition depression of the polymers near an interface,[20] and several polymer entanglements to cross the interface. Most of the models imply a diffusion width of approximately 1 entanglement, indicating a miscibility between the polymers that is hindered by the onset of entangled and reptation behaviour. Allowing the 'roughness' model to describe the initial stages of diffusion, material from both the PS-PMMA and DPEO flows in opposite directions across the interface, which does not support a flux of vacancies, or the movement of only the most mobile (DPEO) chains. As with ion beam analysis, neither case II nor Fickean diffusion of DPEO and PS-PMMA or PMMA was found to completely describe the data, although elements of Fickean diffusion could be applied to early diffusion times and case II diffusion to later times. This case II diffusion may be mirrored in the moving front behaviour of the thicker films used in ion beam analysis.

7.9 References

(1) Karim, A.; Felcher, G. P.; Russell, T. P. *Macromolecules* **1994**, *27*, 6973.

(2) Karim, A.; Mansour, A.; Felcher, G. P.; Russell, T. P. *Physica B* **1989**, *156*, 430.

(3) Fernandes, M. L.; Higgins, J. S.; Penfold, J. *Makromolekulare Chemie-Macromolecular Symposia* **1992**, *62*, 103.

(4) Fernandes, M. L.; Higgins, J. S.; Penfold, J.; Shackleton, C. *Journal of the Chemical Society-Faraday Transactions* **1991**, *87*, 2055.

(5) Kunz, K.; Stamm, M. *Macromolecules* **1996**, *29*, 2548-2554.

(6) Sivaniah, E.; Sferrazza, M.; Jones, R. A. L.; Bucknall, D. G. *Physical Review E* **1999**, *59*, 885.

(7) Bucknall, D. G.; Butler, S. A.; Higgins, J. S. *Macromolecules* **1999**, *32*, 5453-5456.

(8) Bucknall, D. G.; Higgins, J. S.; Butler, S. A. *Chemical Engineering Science* **2001**, *56*, 5473.

(9) Fetters, L. J.; Lohse, D. J.; Richter, D.; Witten, T. A.; Zirkel, A. *Macromolecules* **1994**, *27*, 4639-4647.

(10) Hopkinson, I.; Kiff, F. T.; Richards, R. W.; Affrossman, S.; Hartshorne, M.; Pethrick, R. A.; Munro, H.; Webster, J. R. P. *Macromolecules* **1995**, *28*, 627-635.

(11) Parratt, L. G. *Physical Review* **1954**, *95*, 359.

(12) Nevot, P.; Croce *Revue de physique appliquée* **1980**, *15*, 761.

(13) Press, W.; Flannery, B.; Teukolsky, S.; Vetterling, W. *Numerical Recipes*; Cambridge Univ Press: Cambridge, 1986.

(14) Kawana, S.; Jones, R. A. L. *Physical Review E* **2001**, *6302*, art. no.-021501.

(15) vanZanten, J. H.; Wallace, W. E.; Wu, W. L. *Physical Review E* **1996**, *53*, R2053-R2056.

(16) Brandrup, J.; Immergut, E. H. *Poymer Handbook*; 3rd ed.; John Wiley & Sons, 1989.

(17) Silvestre, C.; Cimmino, S.; Martuscelli, E.; Karasz, F. E.; Macknight, W. J. *Polymer* **1987**, *28*, 1190-1199.

(18) Privalko, V. P.; Petrenko, K. D.; Lipatov, Y. S. *Polymer* **1990**, *31*, 1277-1282.

(19) Ito, H.; Russell, T. P.; Wignall, G. D. *Macromolecules* **1987**, *20*, 2213-2220.

(20) Ellison, C. J.; Torkelson, J. M. *Nature Materials* **2003**, *2*, 695-700.

Chapter 8

Conclusions and Further work

8.1 Conclusions and further work

Nuclear reaction analysis has been used to observe the diffusion of molten DPEO into glassy PMMA where both components are entangled. The observed slowing down of diffusion of DPEO could be attributed to both the concentration dependent changes in interaction parameter and blend glass transition temperature, T_g. Further understanding of the concentration dependence of the diffusion could be achieved by utilising rheology and shift factors to describe blend behaviour at a given concentration. Small angle neutron scattering was used to find the interaction parameter, χ at the temperatures above the melting temperature (T_m) of DPEO but below the T_g of PMMA. The blend exhibited upper critical solution temperature behaviour, enthalpic interactions were dominant and χ was found to be concentration dependent. Small angle neutron scattering could be used to establish the interaction parameter χ of blends of PS-PMMA/DPEO and conformation within the blend. This may assist in comparing results of diffusion behaviour between PMMA and PS-PMMA with DPEO.

Elastic recoil detection showed that glassy PMMA was quickly dissolved into molten DPEO and subsequently into the evolving DPEO/PMMA blend. The rate of increase of blend PMMA volume fraction (φ_{PMMA}) decreases with increasing volume fraction. Differences in surface tension meant that within the changing blend, surface segregation occurred and a blend of higher DPEO concentration was maintained at air surface. DPEO/PMMA diffusion couples can be described by both Fickean and limited supply case II diffusion. It is likely that diffusion is a combination of both these processes and that behaviour is limited by both the concentration dependence of the interaction parameter and the glass transition temperature. The lowest molecular weight of DPEO (17300 $gmol^{-1}$) utilised in this study displayed different behaviour, a study of bilayers with larger range of molecular weights may allow the onset of this behaviour to be established. Action at the interface was established to be the rate determining step in PMMA disssolution.

PMMA was substituted with a block copolymer polystyrene-b-poly(methylmethacrylate) (PS-PMMA). Polystyrene is immiscible with DPEO and PMMA, however diffusion behaviour was similar to that of pure PMMA with DPEO, exhibiting the same similarities to case II and Fickean diffusion. This indicates that a variation in the blend thermodynamic compatibility with minimal alteration in the glass transition temperature, did not alter diffusion behaviour but altered diffusion behaviour with time. This may indicate that the freedom of movement of mobile polymer molecules dominated the diffusion process. The PS-PMMA flux into the growing blend was found to be similar to that of a higher molecular weight PMMA chain, than the PMMA block present. In contradiction to the homopolymer system, dewetting was observed for 17300 $gmol^{-1}$ DPEO again indicating the importance of relative surface tensions and interactions at the interface to the bilayer's diffusion.

Neutron reflectivity was employed to analyse polymer diffusion at the interface of both PMMA/DPEO and PS-PMMA/DPEO bilayers. Models applied demonstrated that no simple model could describe behaviour at the interface. A hybrid model of both interfacial broadening and the addition of a mix layer gave the best correlation with experimental data. The volume fraction profiles of the interface show that diffusion was limited to the radius of gyration of 1-3 entanglements of either component polymer chain. This indicates miscibility between repeat units, whilst one component was molten and one glassy was possible, but behaviour was limited by entanglements and the onset of polymer repatation. The growing precursor layer was found to have $\varphi_{DPEO} \sim 0.1$ for both systems, which may indicate that interactions were not dominated by the interaction parameter, for which $\varphi_{DPEO} \sim 0.3$ may be expected.

To understand whether DPEO or PMMA first penetrates the opposite phase one polymer component could be crosslinked or composed of a highly entangled system such as star polymers. This could be investigated by both ion beam analysis and neutron reflectivity techniques. Crosslinking polymers to form a network should produce a matrix that inhibits diffusion and mobile molecules may not be able to penetrate the polymers that are anchored. The DPEO may therefore be unable to lower the T_g of the PMMA and instigate diffusion. Although there are several polymer systems that are partially miscible or contain one semi-crystalline component, none are available that exhibit such different glass transitions as DPEO/PMMA, so behaviour cannot be directly compared.

Further evidence of the flux of material across the PMMA/DPEO interface could be established from gold marker experiments. Gold markers placed between two films of polystyrene[1] have shown that the Au islands are displaced towards the more mobile side of the interface. The net flux of polymers at the interface can thus be approximated by the movement of Au islands. The movement of these gold markers can be followed using Rutherford back scattering RBS[2]. It is possible to extract tracer diffusion coefficients from the marker spectra and gold marker experiments can analyse the flux of particles.

Mutual diffusion can only be measured using two blends of slightly different concentration placed next to each other. DPEO/PMMA blends cannot be spun on top of each other and PEO blends cannot be floated on water. However, it may be possible to float PEO blends on mercury or another non-solvent. This method has inherent risks in handling the material used to float the film on.

Real time measurements of polymer diffusion have been taken using neutron reflectivity[3]. Using high energy helium beams, data collection is fast using ion beam analysis. It is therefore possible to take real time measurements of polymer diffusion. The ion beam endstation includes a platinum thermistor to measure sample rack temperature but no dedicated heating system. However the cooling system may be altered to achieve a constant elevated temperature as measured by the thermocouple. This may allow the early stages of diffusion between DPEO and PMMA to be measured and compared to neutron reflectivity results and establish a new technique for analysing interfacial and thin film behaviour.

8.2 References

(1) Reiter, G.; Huttenbach, S.; Foster, M.; Stamm, M. *Macromolecules* **1991**, *24*, 1179-1184.
(2) Green, P. F.; Palmstrom, J. W.; Kramer, E. J. *Macromolecules* **1985**, *18*.
(3) Bucknall, D. G.; Butler, S. A.; Higgins, J. S. *Macromolecules* **1999**, *32*, 5453-5456.

Appendix I

Polymers Utilised

Molecular weights were measured using size exclusion chromatography and glass and melting transitions found using differential scanning calorimetry and dynamic mechanical analysis. Results are displayed in Table I.1,

Polymer	Source	Mn/gmol^{-1}	Mw/gmol^{-1}	Mw/Mn	T_g from DSC/K	T_m from DSC/K	T_g from DMA tanδ /K	T_g from DMA E" /K	Average T_g from DMA /K
DPEO	LRH	119100	121100	1.02			222	219	220
DPEO	LRH	75400	77800	1.03	215	330			
DPEO	LRH	16900	17300	1.03	227	337	243	249	246
DPEO	LRH	165000	170700	1.04			220	222	221
DPEO	LRH	65200	76000	1.17					
DPEO	Polymer labs	82210	89200	1.09					
PMMA	LRH	178000	213400	1.20	404				
PMMA	LRH	153400	182400	1.19	405		414	405	410
PMMA	LRH	93000	96200	1.03	405		405	392	399
PMMA	LRH	59600	60200	1.01	406		413	401	407
PMMA	LRH	14800	16000	1.08	408				
PMMA	Polymer labs	1903000	2016000	1.06			420	409	414
PS-PMMA	Polymer source		PS= 29200 PMMA=285100	1.08			417	409	413

Table I.1 Showing polymers utilised in experiments. LRH indicates polymers synthesised by Lian Hutchings.

Appendix II

Glossary of Terms

F	rate of transfer of material per unit area,
C	concentration of the diffusing material
x	distance measured in the direction of diffusion
D	diffusion coefficient
A_1	an arbitrary constant
t	time
M_g	total amount of material present
ξ_C	As described in Equation 1.5
η	$\xi_C/2\sqrt{(Dt)}$
h_0	original depth of interface
B_{mob}	mobility coefficient
μ	chemical potential
S_p	partial stress tensor in one dimension
s	constant
v_1	constant $=B_m s$
ψ	Boltzman similarity variable
X_M	reference plane between diffusing couples
C_L and C_R	concentrations of blocks on left (L) and right hand side(R)
C'	as illustrated in figure
T_g	glass transition temperature
T_m	melting temperature
$M_{e,i}$	entanglement molecular weight
G_N^0	plateau modulus
ρ_d	polymer density
N_a	Avagadro constant
T	temperature
k_B	Boltzman constant
v_n	number of chains per unit volume
L	chain length
Λ_i	the effective bond length or Kuhn step length of polymer i

D_A*	tracer diffusion of polymer A
a	separation between Rouse beads (step length)
K_A	a constant for species A
v	velocity of a bead
$\zeta_{0,\mathrm{i}}$	monomeric friction coefficient of polymer i
M_i	molecular weight of chain i
M_0	molecular weight of the monomer
N_r	number of relaxation times τ_l
τ_l	relaxation time
D_{RO}	Rouse dynamics self-diffusion coefficient
$<R_g^2>$	mean end-to end distance
L_c	contour length
a_2	step length
N_i	number of primitive chain steps for polymer i
ξ	tube diameter
$D_{R,A}$	reptation diffusion coefficient of A
$D_{Ro,A}$	Rouse diffusion coefficient of A
$\tau_{\mathrm{R,A}}$	time taken for the chain to abandon it's original path
$F_A(t)$	fraction of the original tube still occupied by a reptating polymer
W_i	weight fraction of component i
τ_w	waiting time
P_A	molecular weight of a matrix of A chains
$D_{CR,A}$	constraint release diffusion coefficient for A chain
ΔG^M	free energy of an A-B mixture
χ	interaction parameter
N_i	number of monomers per polymer i
φi	volume fraction of i in the blend
χ_C	critical interaction parameter
φ_C	critical concentration
ΔG_{mix}^{ex}	Gibbs free energy of mixing per segment
D_M	mutual diffusion coefficient
χ_s	interaction parameter at the spinodal point
$<R_B^2>^{0.5}$	root mean square end-to-end distance of B chains
D_T	transport diffusion coefficient
D_{coop}	cooperative diffusion coefficient
S_{coop}	$S_{AA}+2S_{AB}+S_{BB}$
S_{ij}	static structure factor for combinations of ij
$S\varphi_i(q)$	equilibrium fluctuations in Fourier space about the mean concentration φ_i
T_C	critical temperature
φ_{dc}	critical concentration
V_{amorph}	the molar volume of an amorphous polymer
V_{crys}	the molar volume of a crystalline polymer
ΔH_{Crys}	heat of fusion per mole of the crystalline polymer
E_0	incident monoenergetic beam of $^4He^{++}$ ions
N_d	atomic number density
m_i	mass of particle i
Z_t	target ion's atomic number
$E_{in,0}$	incident particle energy

v	ion velocity
I	excitation energy of an electron
α	angle with respect to the sample surface
Φ	scattering angle
δE_s	energy loss passing through the Mylar stopper foil
δE_{ss}	energy loss travelling out of sample
N	number of layers
Δx	layer thickness
$S_{out,j}$	function of energy loss with depth as evaluated at $E_{out,j}$
V_{cm}	velocity of the centre of mass
δx	depth resolution
ΔE_D	detector energy resolution
ΔE_M	energy broadening due to multiple scattering
ΔE_S	energy straggling in the sample
ΔE_F	energy straggling in the stopper foil for ERD only
ΔE_G	geometrical broadening
θ	neutron scattering angle
L_{sd}	distance from the sample to the detector
$\mathbf{k}_s$	scattered wavevector
$\mathbf{Q}$	scattering vector
Q	modulus of $\mathbf{Q}$,
n_j	neutron refractive index
d	molecular level length scale
$I(Q)$	flux of neutrons
$\Delta\Omega$	solid angle element defined by the size of a detector pixel
η_d	detector efficiency
I_T	transmission of the sample
V_s	volume of the sample exposed to the beam
N_{conc}	number concentration of scattering centres
V	individual volume
B	background signal
ρ	neutron scattering length density
$n_{d,i}$	number density of a species i
b_i	coherent scattering length, interaction between the neutron and nucleus i
$P(Q)$	form factor
R	radius of a homogeneous sphere
$R_{g,i}$	radius of gyration of polymer i
$S(Q)$	structure factor
$g(r)$	density distribution function
r	distance of the nearest neighbour co-ordination shell
σ	force (F) applied per unit area A
A	unit area
ε	strain
l	original length
Δl	the change in length
E	tensile modulus
E''	loss modulus
E'	storage modulus
T_{gDMA}	glass transition found using DMA

T_{gDSC}	glass transition found using DSC
θ	reflectivity angle
j	medium
λ	neutron wavelength
σ_a	adsorption cross section
θ_c	critical angle
z	perpendicular component
$\mathbf{R}$	perpendicular reflectivity
$r_{j,j+1}$	Fresnel reflection coefficient
$r^*_{j,j+1}$	complex conjugate
$\mathbf{q}$	Neutron momentum transfer
q_{zj}	momentum transfer normal to the surface
q_c	critical value of momentum transfer
β_m	phase factor
d_m	path length
n_m	refractive index
Δq_i	difference between successive minima
κ_m	$n_m \sin\theta_m$
M	overall sample matrix
w_{width}	diffused width of the deuterated polymer
Img.Ra	arithmatic average of the absolute values of the surface height deviations measured from the mean plane
Img.Rms	root mean square average of height deviations taken from the mean data plane
v_i	volumes of polymer repeat units for polymer *i*
v_u	volume of a solvent molecule
V	the scattering volume
$D(x)$	the Debye function
ξ_l	correlation length
χ_{eff}	the effective interaction parameter
I	transmitted flux
I_0	incident flux
σ_T	the total cross section (the sum of incoherent and coherent cross sections for each atom)
t_h	the thickness of SANS sample
$I(q)_r$	reduced elastic coherent scattering intensity
$I(q)$	sum of elastic coherent and background scattering
C_i	weighted sum of the background scattering from pure components
R_i	the molecular mass of the monomer *i*
A, B	enthalpic and entropic contributions to polymers mixing
d_0	depth normal to the surface
$\sigma_g(z)$	gaussian of root mean square deviation
$\varphi(z)$	the volume fraction of polymer at depth *z*
$\theta(z)$	step functions at depth *z*
z_1	air/polymer interface
z_2	polymer/silicon interface
w_{tot}	effective width of interface
w_{bd}	effective width attributed to beam damage
w_{res}	effective width attributed to instrumental resolution
φ_0	concentration where the swelling induced stresses are sufficient

	to cause plastic flow
t_{diss}	time taken for the dissolution of the PMMA polymer into the blend
$C^*\sqrt{D_{PMMA}}$	as defined in Equation 5.10
$\zeta_{PMMA}(\mathrm{PS})$	monomeric friction coefficient of PMMA into PS
$\zeta_{PS}(\mathrm{PS})$	monomeric friction coefficient of PS into PS
ζ_{eff}	effective monomeric friction factor
$Imp/\mathring{A}^{-2}$	the scattering length density,
σ_r	roughness of the layer
$<r^2>_o$	unperturbed mean square end-to-end distance

Appendix III

Glossary of Acronyms

Page numbers indicate first use of acronym. Page numbers in brackets indicate complete description of term.

PEO	Polyethylene oxide	(24)
DPEO	Deuterated polyethylene oxide	(24)
PMMA	Poly(methylmethacrylate)	(24)
LCST	Lower critical solution temperature behaviour	16(16)
UCST	Upper critical solution temperature behaviour	16(16)
PVDF	Poly(vinylidene fluoride)	18
ATR-FTIR	Attenuated total reflectance fourier spectroscopy	22
PS	Polystyrene	22
PVME	Poly(vinyl methyl ether)	22
PXE	Poly(xylenyl ether)	23
PS/PXE	Blend of Polystyrene and Poly(xylenyl ether)	23
PVC	Polyvinyl chloride	23
PCL	Polycaprolactone	23
PVC/PCL	Blend of Polyvinyl chloride and Polycaprolactone	23
RBS	Rutherford Back Scattering	23
ERD	Elastic recoil detection analysis	23(37)
SIMS	Dynamic secondary ion mass spectrometry	23
PVC/PMMA	Blend of Polyvinyl chloride and Poly(methylmethacrylate)	24

aPMMA	Atactic PMMA	24
iPMMA	Isotactic PMMA	24
sPMMA	Syndiotactic PMMA	24
SANS	Small angle neutron scattering	25(50)
NMR	Nuclear Magnetic Resonance	26
PS-PMMA	diblock copolymer of polystyrene and Poly(methylmethacrylate) (polystyrene-b-poly(methyl methacrylate))	29
PET	Poly(ethylene teraphalate)	37
SAXS	Small angle X-ray scattering	27
DMA	Dynamic Mechanical Analysis	61
DSC	Differential Scanning Calorimetry	64
AFM	Atomic Force Microscopy	65
TEM	Transmission electron microscopy	66
FWHM	Full width half maximum	140
SLD	Scattering length density	216(52)

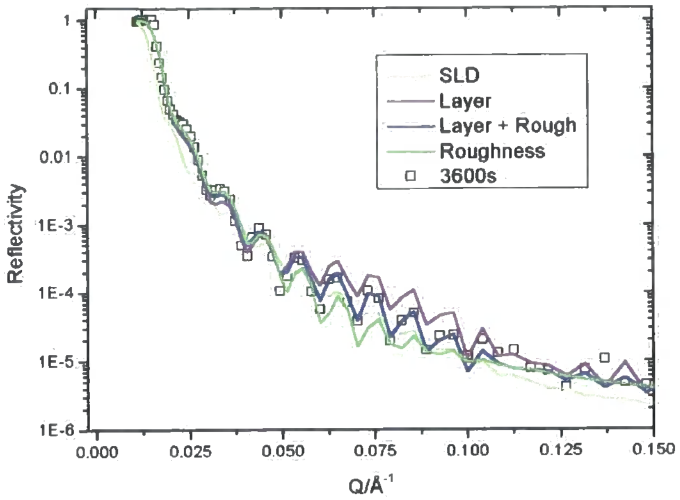

(A)

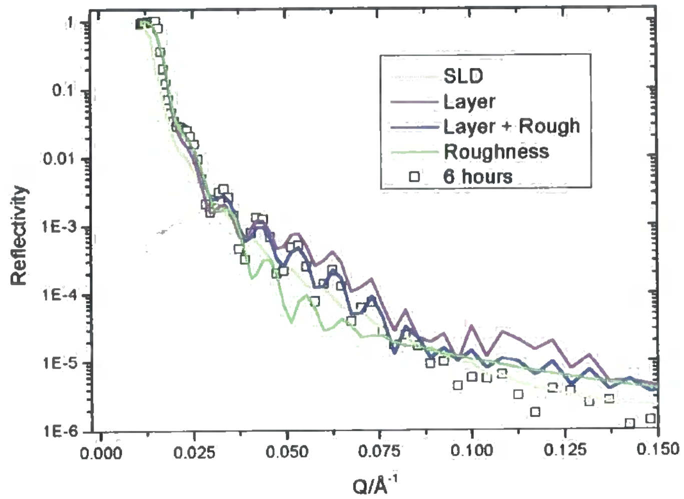

(B)

Figure 7.15 Experimental reflectivity for PS-PMMA and DPEO (121100 gmol^{-1}) bilayers heated at 343 K for (A) 3600 s and (B) 21600 s. Calculated reflectivities are for the four models; roughness (7.4.3.2), SLD (7.4.3.1), extra layer (7.4.3.3) and extra layer with roughness(7.4.3.4).